

**A NUMERICAL AND EXPERIMENTAL INVESTIGATION INTO
PRESSURE SCREEN FOIL ROTOR HYDRODYNAMICS**

by

SEAN DELFEL

B.S., Aeronautical and Astronautical Engineering, The University of Washington, 2002

A THESIS SUBMITTED IN PARTIAL FULFILLMENT OF
THE REQUIREMENTS FOR THE DEGREE OF

DOCTOR OF PHILOSOPHY

in

THE FACULTY OF GRADUATE STUDIES

(Mechanical Engineering)

THE UNIVERSITY OF BRITISH COLUMBIA

(Vancouver)

OCTOBER 2009

© Sean Delfel, 2009

Abstract

Pressure screens are an effective way to remove contaminants from a pulp stream and to fractionate the pulp, or separate the fibres by length, both of which improve the quality of the end-product paper. In this thesis, seven experimental and numerical studies were conducted to investigate the hydrodynamics of pressure screen foil rotors and the effects of rotor design on the overall performance of a pressure screen. Additionally, this knowledge was applied to the development of a high performance foil rotor for both out-flow and in-flow screens.

A multi-element foil rotor was developed using computational fluid dynamics (CFD), laboratory experiments, pilot plant trials, and a full scale mill trial. It was found that varying the shape and configuration of the foil affected both the pressure pulses generated by the rotor and the maximum capacity of the pressure screen. The multi-element foil (MEF) was found to be capable of generating a 126% higher magnitude negative pressure pulse, a 31% increase in screen capacity at a given rotor power consumption and a 43% reduction in power consumption without affecting capacity compared to state of the art single element rotors.

The effect of varying the frequency of the pressure pulses, by changing the number of foils on the rotor, the diameter of the cylinder, and slot velocity on rotor performance was also studied. Adding foils to the rotor was found to reduce the velocity of the fluid relative to the foils and the magnitude of the pressure pulses generated by the rotors, leading to a reduction in overall screen performance. Increasing the diameter of the screen slightly reduces the performance of the foils. Increasing slot velocity did not affect the pressure pulses generated by the rotor for fully attached flows, but caused the foils to stall and a higher tip speed.

Finally, factors affecting rotor power consumption other than rotor speed were investigated experimentally and analytically. The cylinder slot geometry, flow rates, and

the design of the inlet to the screen were all found to have significant effects on rotor power consumption.

Table of Contents

Abstract	ii
Table of Contents	iv
List of Tables	viii
List of Figures	ix
List of Symbols	xviii
Acknowledgements	xxi
Co-Authorship Statement.....	xxii

Chapter 1: Introduction	1
1.1 Background	1
1.2 Literature Survey	5
1.2.1 Rheology of Pulp Fiber Suspensions	5
1.2.2 Screening Theory	10
1.2.3 Cylinder Geometry and Hydrodynamics	18
1.2.4 Pressure Screen Rotor Studies	20
1.2.5 Airfoil Development	26
1.2.6 Inverted Foils in Ground Effect	28
1.3 Research Objectives.....	29
1.3.1 A Numerical Investigation into the Effectiveness of Multi-Element Pressure Screen Rotor Foils.....	30
1.3.2 Experimental Measurement of Pressure Pulses from a Pulp Screen Rotor	31
1.3.3 High Performance Multi-Element Foil (MEF) Pulp Screen Rotor - Pilot and Mill Trials	31
1.3.4 High Performance Foil Rotor Improves De-Ink Pulp Screening.....	31
1.3.5 Effect of Pulse Frequency and Cylinder Diameter on Pressure Screen Rotor Performance	32
1.3.6 A Numerical Study of Multi-Element Pressure Screen Rotor Foils with In-Flow Cylinders.....	32
1.3.7 Influence of Cylinder Design and Other Factors on Capacity and Power Consumption in a Pressure Screen.....	32
1.4 References	34

Chapter 2: A Numerical Investigation into the Effectiveness of Multi-Element Pressure Screen Rotor Foils	42
2.1 Introduction.....	42
2.2 Numerical Method	45
2.3 Computational Domain and Mesh Generation	46
2.4 Boundary Conditions	47

2.5 Grid Independence and Model Validation	48
2.5 Results and Discussion	50
2.5.1 Lip Length.....	51
2.5.2 Angle-of-Attack	53
2.5.3 Flap Angle.....	56
2.5.4 Flap Positioning	61
2.6 Conclusions.....	67
2.7 References.....	68

Chapter 3: Experimental Measurement of Pressure Pulses from a Pulp Screen

Rotor.....	70
3.1 Introduction.....	70
3.2 Experimental Setup.....	74
3.3 Experimental Results and Discussion	78
3.3.1 Error Analysis	78
3.3.2 Effect of Tip Speed	79
3.3.3 Effect of Varying MEF Geometry	86
3.3.4 Effect of Slot Velocity	91
3.4 Numerical Methods.....	98
3.5 Numerical Results and Discussion.....	100
3.6 Conclusions.....	105
3.7 References.....	107

Chapter 4: High Performance Multi-Element Foil (MEF) Pulp Screen Rotor – Pilot

and Mill Trials.....	109
4.1 Introduction.....	109
4.2 Pilot Screening Trials.....	113
4.3 Results and Discussion	116
4.4 Mill Application.....	121
4.5 Conclusions.....	124
4.6 References.....	126

Chapter 5: High Performance Foil Rotor Improves De-Ink Pulp Screening 127

5.1 Introduction.....	127
5.2 Rotor Design and Experimental Setup.....	130
5.3 Mill Application Results	132
5.4 Conclusions.....	138
5.5 References.....	139

Chapter 6: Effect of Pulse Frequency and Cylinder Diameter on Pressure Screen	
Rotor Performance	140
6.1 Introduction.....	140
6.2 Numerical Method	143
6.3 Numerical Results and Discussion.....	145
6.4 Experimental Setup.....	153
6.5 Experimental Results	155
6.6 Conclusions.....	159
6.7 References.....	160
 Chapter 7: A Numerical Study of Multi-Element Pressure Screen Rotor Foils with	
In-Flow Cylinders	162
7.1 Introduction and Background	162
7.2 Numerical Method	165
7.3 Results and Discussion	167
7.4 Conclusions.....	176
7.5 References.....	178
 Chapter 8: Influence of Cylinder Design and Other Factors on Capacity and Power	
Consumption in a Pressure Screen.....	180
8.1 Introduction.....	180
8.2 Analysis.....	182
8.3 Experimental Procedure.....	186
8.4 Experimental Results	188
8.5 Conclusions.....	193
8.6 References.....	195
 Chapter 9: Conclusions and Recommendations for Future Work	197
9.1 Introduction.....	197
9.2 Discussion and Analysis	197
9.3 Conclusions.....	211
9.2 Recommendations for Future Work.....	215
9.3 References.....	217
 Appendix A: Numerical Methods.....	219
A.1 Introduction.....	219
A.2 Turbulence Modeling.....	220
A.3 Domain Discretization and Boundary Conditions	222
A.4 Convergence Criteria	225
A.5 References.....	226

Appendix B: Details of Analysis	227
B.1 Introduction	227
B.2 Analysis	227
B.3 References	229

List of Tables

Table 3.1:	Test parameters and foil configurations studied experimentally.	78
Table 3.2:	Test conditions used in the simulations.	99
Table 7.1:	Fluid and geometric properties used in the study.	166
Table 8.1:	Wire geometries studied.	188
Table 8.2:	Physical parameters for the UBC MR8 pressure screen with an AFT EP rotor and wire cylinder with 0.6mm contour height and 3.2mm wire width.	191
Table 9.1:	Trial details of the two experiments.....	198
Table 9.2:	Slope of the best fit curve, m , and correlation coefficient, S , of maximum slot velocity as a function of minimum pressure at various tip speeds...	204
Table 9.3:	Slope of the best fit curve, m , and correlation coefficient, S , of maximum slot velocity as a function of maximum pressure at various tip speeds. .	207
Table 9.4:	Slope of the best fit curve, m , and correlation coefficient, S , of maximum slot velocity as a function of integrated force at various tip speeds.	210

List of Figures

Figure 1.1:	An illustration of a modern pressure screen.	3
Figure 1.2:	A schematic illustrating (a) out-flow screens and (b) in-flow screens.	4
Figure 1.3:	A typical contoured slot design with key dimensions identified [80].	18
Figure 1.4:	Airfoil nomenclature for a single-element foil.	27
Figure 2.1:	Computational domain and a typical mesh.	47
Figure 2.2:	Experimental and numerical results for pressure traces on the screen cylinder for a NACA 8312 rotor foil at $Re = 5 \times 10^5$, an angle-of-attack of $\alpha = 0$ deg, a chord of $c = 4$ cm, and a gap of $g = 3$ mm.	50
Figure 2.3:	Multi-element rotor foil with specific foil parameters defined.	51
Figure 2.4:	Pressure contours and streamlines for a multi-element foil with varying main foil trailing edge lip length: (A) $l = 0.10 \cdot c$, (B) $l = 0.25 \cdot c$, and (C) $l = 0.50 \cdot c$. The foil is at $\alpha = 0$ deg. and the flap is at $\delta = 7$ deg. for all cases.	52
Figure 2.5:	Pressure traces on the screen cylinder for a multi-element foil with varying main foil trailing edge lip length l . The foil is at $\alpha = 0$ deg. and the flap is at $\delta = 7$ deg. for all cases.	53
Figure 2.6:	Pressure contours and streamlines for a multi-element foil at (A) $\alpha = 0$ deg., (B) $\alpha = 2$ deg., (C) $\alpha = 4$ deg., (D) $\alpha = 5$ deg., (E) $\alpha = 7$ deg., and (F) $\alpha = 10$ deg. The flap is at $\delta = 7$ deg. and $l = 0.5 \cdot c$ for all cases.	55
Figure 2.7:	Pressure traces on the screen cylinder for a multi-element foil at varying angles-of-attack. The flap is at $\delta = 7$ deg. and $l = 0.5 \cdot c$ for all cases.	56
Figure 2.8:	(A) Maximum wall pressure coefficient on the screen cylinder and (B) minimum wall pressure coefficient on the screen cylinder vs. foil angle-of-attack The flap is at $\delta = 7$ deg. and $l = 0.5 \cdot c$ for all cases.	57
Figure 2.9:	Pressure contours and streamlines for a multi-element foil at (A) $\delta = 7$ deg., (B) $\delta = 15$ deg., (C) $\delta = 22$ deg., (D) $\delta = 29$ deg., and (E) $\delta = 36$ deg. The foil is at $\alpha = 7$ deg. and $l = 0.5 \cdot c$ for all cases.	58
Figure 2.10:	Pressure traces on the screen cylinder for a multi-element foil at varying flap angles. The foil is at $\alpha = 0$ deg. and $l = 0.5 \cdot c$ for all cases.	59

Figure 2.11:	(A) Maximum wall pressure coefficient at the screen cylinder and (B) minimum wall pressure coefficient at the screen cylinder vs. flap angle for various angles-of-attack. $l = 0.5*c$ for all cases.....	60
Figure 2.13:	Pressure contours and streamlines for a multi-element foil with varying x-positions for the flap leading edge. The flap leading edge is at (A) $x = 0.00 * c$, (B) $x = -0.02 * c$, (C) $x = -0.03 * c$, (D) $x = -0.05 * c$, (E) $x = -0.06 * c$, and (F) $x = -0.08 * c$. In all cases the flap leading edge is at $y = -0.05 * c$, $\alpha = 1 \text{ deg.}$, $\delta = 15 \text{ deg.}$, and $l = 0.5*c$	63
Figure 2.14:	Pressure contours and streamlines for a multi-element foil with varying y-positions for the flap leading edge. The flap leading edge is at (A) $y = -0.04 * c$, (B) $y = -0.05 * c$, (C) $y = -0.07 * c$, (D) $y = -0.09 * c$, and (E) $y = -0.11 * c$. In all cases the flap leading edge is at $x = 0.04 * c$, $\alpha = 1 \text{ deg.}$, $\delta = 15 \text{ deg.}$, and $l = 0.5*c$	64
Figure 2.15:	Surfaces of (A) maximum wall pressure coefficient and (B) minimum wall pressure coefficient vs. flap leading edge x- and y-position. The foil is at $\alpha = 1 \text{ deg.}$, $\delta = 15 \text{ deg.}$, and $l = 0.5*c$ for all cases.	66
Figure 3.1:	Cross section of the MEF with angle-of-attack (α), flap angle (δ), and chord length defined.	73
Figure 3.2:	The MR-8 laboratory pressure screen with key components called out..	75
Figure 3.3:	Installation of the pressure sensor in the wedge wire cylinder.	76
Figure 3.4:	A sample of the raw pressure pulse data collected. The red lines illustrate how the data was split between the two foils for averaging.	76
Figure 3.5:	The ensemble average pressure pulse and 99% confidence intervals for the EP rotor at $V_s = 0 \text{ m/s}$ and (a) $V_t = 7 \text{ m/s}$, (b) $V_t = 11 \text{ m/s}$, and (c) $V_t = 15 \text{ m/s}$. The 99% confidence intervals shown are representative of those found throughout the study.	80
Figure 3.6:	Pressure traces for EP rotor at various tip speeds and $V_s = 0 \text{ m/s}$	81
Figure 3.7:	Pressure traces for the MEF rotor at $(\alpha, \delta) = (4, 17) \text{ deg.}$, at various tip speeds, and at $V_s = 0 \text{ m/s}$	82
Figure 3.8:	Traces of non-dimensional pressure coefficient for the EP rotor at various tip speeds and $V_s = 0 \text{ m/s}$	82

Figure 3.9:	Traces of non-dimensional pressure coefficient for the MEF rotor at $(\alpha, \delta) = (4, 17)$ deg., at various tip speeds, and at $V_s = 0$ m/s.	83
Figure 3.10:	(a) Minimum pressure coefficient and (b) maximum pressure coefficient plotted as a function of Reynolds number for the EP rotor at $V_s = 0$ m/s. The solid line represents the average of values above $Re = 60,000$	83
Figure 3.11:	Minimum pressure coefficient plotted as a function of Reynolds number for the MEF rotor at (a) $(\alpha, \delta) = (4, 12)$ deg., (b) $(\alpha, \delta) = (4, 17)$ deg., and (c) $(\alpha, \delta) = (4, 22)$ deg. at $V_s = 0$ m/s. The solid line represents the average of values above $Re = 60,000$	84
Figure 3.12:	Maximum pressure coefficient plotted as a function of Reynolds number for the MEF rotor at (a) $(\alpha, \delta) = (4, 12)$ deg., (b) $(\alpha, \delta) = (4, 17)$ deg., and (c) $(\alpha, \delta) = (4, 22)$ deg. at $V_s = 0$ m/s. The solid line represents the average of values above $Re = 60,000$	85
Figure 3.13:	Effect of varying angle-of-attack on the non-dimensional pressure trace for the MEF at a constant flap angle ($\delta = 17$ deg.). The tip speed is $V_t = 13$ m/s and the slot velocity is $V_s = 0$ m/s.	87
Figure 3.14:	Effect of varying flap angle on the non-dimensional pressure trace for the MEF at a constant angle-of-attack ($\alpha = 4$ deg.). The tip speed is $V_t = 13$ m/s and the slot velocity is $V_s = 0$ m/s.	88
Figure 3.15:	Effect of varying the MEF flap angle on the minimum pressure coefficient, with lines of constant angle-of-attack, at $V_s = 0$ m/s and (a) $V_t = 7$ m/s, (b) $V_t = 11$ m/s, and (c) $V_t = 13$ m/s.	89
Figure 3.16:	Effect of varying the MEF flap angle on the maximum pressure coefficient, with lines of constant angle-of-attack, at $V_s = 0$ m/s and (a) $V_t = 7$ m/s, (b) $V_t = 11$ m/s, and (c) $V_t = 13$ m/s.	90
Figure 3.17:	Effect of varying slot velocity on the non-dimensional pressure trace for the EP rotor at (a) $V_t = 5$ m/s, (b) $V_t = 7$ m/s, (c) $V_t = 9$ m/s, (d) $V_t = 11$ m/s, (e) $V_t = 13$ m/s, and (f) $V_t = 15$ m/s.	93
Figure 3.18:	Effect of varying slot velocity on the non-dimensional pressure trace for the MEF rotor at $(\alpha, \delta) = (2, 17)$ deg. at (a) $V_t = 5$ m/s, (b) $V_t = 7$ m/s, (c) $V_t = 9$ m/s, (d) $V_t = 11$ m/s, (e) $V_t = 13$ m/s, and (f) $V_t = 15$ m/s.	94

Figure 3.19:	Minimum pressure coefficient as a function of slot velocity for the EP rotor at various tip speeds.	95
Figure 3.20:	Minimum pressure coefficient as a function of slot velocity for the MEF rotor at (a) $(\alpha, \delta) = (6, 12)$ deg., (b) $(\alpha, \delta) = (6, 17)$ deg., and (c) $(\alpha, \delta) = (6, 22)$ deg., at various tip speeds.....	96
Figure 3.21:	Effect of varying the MEF flap angle on the minimum pressure coefficient, with lines of constant angle-of-attack, at $V_t = 7$ m/s and (a) $V_s = 0$ m/s, (b) $V_s = 1$ m/s, (c) $V_s = 2$ m/s, and (d) $V_s = 3$ m/s.....	97
Figure 3.22:	Computational domain used in the study and a typical mesh with boundary conditions labeled.	100
Figure 3.23:	Experimental and numerical non-dimensional pressure traces for the MEF at $(\alpha, \delta) = (0, 22)$ deg.	102
Figure 3.24:	Numerically predicted minimum pressure coefficient on the cylinder wall for varying MEF geometry. The results were obtained using the k- ϵ turbulence model.....	103
Figure 3.25:	Numerically generated pressure contours and streamlines for the MEF at (a) $\alpha = 0$ deg., (b) $\alpha = 2$ deg., (c) $\alpha = 4$ deg., and (d) $\alpha = 6$ deg., and a flap angle of $\delta = 12$ deg.....	104
Figure 3.26:	Numerically predicted maximum pressure coefficient on the cylinder wall for varying MEF geometry. The results were obtained using the k- ϵ turbulence model.....	105
Figure 4.1:	MEF showing angle-of-attack, α , and flap angle, δ	111
Figure 4.2:	Pressure contours and streamlines for a multi-element foil at (A) $\delta = 15.8$ deg., (B) $\delta = 23.8$ deg., (C) $\delta = 30.83$ deg., (D) $\delta = 37.8$ deg., and (E) $\delta = 44.8$ deg. The foil is at $\alpha = -8.8$ deg. for all cases. [9]	112
Figure 4.3:	Surfaces of minimum wall pressure coefficient vs. foil angle-of-attack and flap angle showing the optimal configuration [9].....	113
Figure 4.4:	Photograph of FPIInnovation's Hooper PSV 2100 Pilot Screen and the prototype adjustable MEF rotor showing the slot between main foil and flap.	115
Figure 4.5:	Plugging envelopes for the two best MEF rotors and the EP rotor.	116

Figure 4.6:	Plugging envelopes for the MEF rotor, the EP rotor and the Hooper XT rotor. Note: the full length XT rotor was trialed and shown here.....	117
Figure 4.7:	Effect of tip speed on rotor power consumption at $V_s=1.0$ m/s.....	117
Figure 4.8:	Effect of tip speed on thickening factor at a slot velocity, $V_s = 1.0$ m/s.	118
Figure 4.9:	Effect of varying flap angle on maximum slot velocity for constant angle-of-attack, $\alpha = -8.83$	119
Figure 4.10:	Effect of varying flap angle on a maximum slot velocity for constant rotor speed, $V_t = 14$ m/s.....	120
Figure 4.11:	Maximum capacity – power relation for 2- and 3- foil rotors.	120
Figure 4.12.	A photograph of the installed prototype AFT MEF™ Rotor following 23 days of continuous operation. There is no trace of stringing or wear.....	122
Figure 4.13	Power versus tip speed for the AFT MEF™ Rotor, EP™ Rotor and the Black Clawson 4 foil and 2 foil rotors. The MEF™ rotor provides a 43% energy reduction over the OEM rotor.	123
Figure 5.1:	Single-element foil geometry.....	128
Figure 5.2:	The computed fluid streamlines colored by pressure contours for a single foil (left) and a multi-element foil (right).	130
Figure 5.4:	The optimized MEF design (left) and the mill-scale prototype rotor (right) installed at Catalyst Paper Recycling Division.	131
Figure 5.5:	Catalyst Paper, Paper Recycling Division Flowsheet.	132
Figure 5.6:	Screen power consumption versus rotor tip speed. Power savings of approximately 42% were obtained compared to the parallel OEM screen. Runnability remained excellent and there was no decrease in operating capacity.	133
Figure 5.7:	Thickening factor versus rotor tip speed. The error bars represent 90% confidence intervals.	134
Figure 5.8:	The MEF rotor provided a higher stickies removal efficiency than the OEM rotor. Further increases in efficiency were obtained as rotor speed was decreased. The error bars represent 90% confidence intervals.....	135

Figure 5.9:	Stickies removal efficiency measurements by count and area with equivalent 0.15 mm (0.006”) wedgewire cylinders and a reject rate of 22.5% by mass.	136
Figure 5.10:	Stickies Distribution (mm ²).	137
Figure 5.11:	MEF rotor at the end of the trial period. The pulp shown in this photo was deposited during drainage of the pulp screen and was easily washed away. There was no accumulation or plugging between the foil and flap.	137
Figure 6.1:	The inner workings of a small pressure screen with a two foiled rotor. .	141
Figure 6.2:	The MEF rotor profile with angle-of-attack (α), flap angle (δ), and chord length defined.....	143
Figure 6.3:	Computational domain and a typical mesh. The model shown is for a four foil rotor.	144
Figure 6.4:	Contours of velocity relative to the foil and streamlines for a rotor with (a) two foils, (b) three foils, (c) four foils, and (d) six foils. The cylinder is 0.508 m in diameter.	148
Figure 6.5:	Relative velocity one chord length upstream of the foil (normalized by tip speed) vs. radius (normalized by the cylinder radius r_0) for a rotor with varying number of foils. The cylinder is 0.508 m in diameter.	149
Figure 6.6:	Pressure contours and streamlines for a rotor with (a) two foils, (b) three foils, (c) four foils, and (d) six foils. The cylinder is 0.508 m in diameter.	150
Figure 6.7:	Traces of pressure coefficient along the cylinder wall for a rotor with varying number of foils. The cylinder is 0.508 m in diameter.	151
Figure 6.8:	Minimum pressure coefficient on the cylinder wall for varying foil geometries. The effect of varying the pulse frequency (i.e. the number of foils) is much larger than the effect of varying the foil geometry. The cylinder is 0.508 m in diameter.....	151
Figure 6.9:	Surface of minimum pressure coefficient at the cylinder wall as a function of pulse frequency and flap angle for a 0.508 m diameter cylinder.	152
Figure 6.10:	Surface of minimum pressure coefficient at the cylinder wall as a function of pulse frequency and flap angle for a 0.80 m diameter cylinder.	152

Figure 6.11:	Effect of foil flap angle on minimum pressure coefficient for varying cylinder diameters. All results are at a constant pulse frequency of $f = 45.41$ Hz. The 0.30 m diameter data is from direct CFD results for a two foil rotor, while the 0.508 m and .080 m diameter data is interpolated from the surfaces in Figures 6.7 and 6.8, respectively.	153
Figure 6.12:	The two foil MEF rotor used in the pilot plant trials.	155
Figure 6.13:	Traces of pressure coefficient along the screen cylinder wall for two and three foil MEF rotors in a PSV2100 screen. The cylinder is 0.30 m in diameter.....	157
Figure 6.14:	Maximum capacity envelopes for the two and three foil MEF rotors in the PSV2100 screen.	157
Figure 6.15:	Numerically predicted minimum pressure on the cylinder vs. experimental maximum slot velocity for the two and three foil MEF rotors.	158
Figure 6.16:	Effect of rotor tip speed on reject thickening factor for the two and three foil MEF rotors in the PSV2100 screen.....	158
Figure 7.1:	A schematic illustrating (a) out-flow screens and (b) in-flow screens. ..	163
Figure 7.2:	The multi-element foil (MEF) with angle-of-attack (α) and flap angle (δ) defined.....	165
Figure 7.3:	Computational domain, boundary conditions, and a typical mesh.	167
Figure 7.4:	Pressure contours and streamlines for a NACA 8312 at an angle-of-attack of (a) $\alpha = 1$ deg., (b) $\alpha = 3$ deg., and (c) $\alpha = 5$ deg.	169
Figure 7.5:	Pressure traces and streamlines for varying flap angles and a constant angle-of-attack of $\alpha = 1$ deg. The flap is at (a) $\delta = 0$ deg., (b) $\delta = 7$ deg., (c) $\delta = 15$ deg., and (d) $\delta = 22$ deg.....	170
Figure 7.6:	Pressure traces and streamlines for varying angle-of-attack at a constant flap angle of $\delta = 0$ deg. The angle-of-attack is (a) $\alpha = 1$ deg., (b) $\alpha = 3$ deg., (c) $\alpha = 5$ deg., and (d) $\alpha = 7$ deg.....	171
Figure 7.7:	Traces of pressure coefficient on the cylinder wall for the MEF at varying angles-of-attack and a constant flap angle.	172

Figure 7.8:	The effect of varying flap angle on the minimum C_P on the cylinder. The dashed line represents the best result for the NACA 8312 single-element foil.	174
Figure 7.9:	The effect of varying flap angle on the maximum C_P on the cylinder. The dashed line represents the best result for the NACA 8312 single-element foil.	174
Figure 7.10:	The effect of vary flap angle on the force coefficient on the cylinder. The dashed line represents the best result for the NACA 8312 single-element foil.	175
Figure 7.11:	Pressure contours and streamlines for the MEF at $(\alpha, \delta) = (3, 7)$ deg., the optimum configuration.....	176
Figure 8.1:	A typical contoured slot design with key dimensions identified [9].	182
Figure 8.2:	Top view (a) and side view (b) of the volume used for the analysis.	183
Figure 8.3:	Experimental rotor power as a function of tip speed for the EP rotor in air with a linear least squares fit.....	186
Figure 8.4:	The UBC GL&V MR8 pilot pressure screen. The rotor and cylinder installation can be seen in the inset.....	187
Figure 8.5:	Schematic showing how cylinder D (left) varies compared to the other geometries.	188
Figure 8.6:	Slot velocity as a function of rotor power for cylinder A, showing a typical plugging envelope. Note the reduction in power as flow rates are increased for a constant rotor speed.....	190
Figure 8.7:	Maximum capacity envelopes for all cylinders studied.....	190
Figure 8.8:	Experimental and theoretical rotor power as a function of feed flow rate for cylinder A at various rotor tip speeds. The curves represent results from equation 5.	192
Figure 8.9:	Experimental and theoretical rotor power as a function rotor tip speed for cylinder A at various feed flow rates. The curves represent results from equation 5.....	192

Figure 9.1:	A single averaged pressure pulse measured at the cylinder wall representative of the pressure pulse data. The pulse shown is an ensemble average of 500 individual pulses.....	200
Figure 9.2:	Minimum C_P at the cylinder wall as a function of foil configuration. The surface was constructed using 12 separate measurements.....	200
Figure 9.3:	Maximum C_P at the cylinder wall as a function of foil configuration. The surface was constructed using 12 separate measurements.....	201
Figure 9.4:	Integrated C_F at the cylinder wall as a function of foil configuration. The surface was constructed using 12 separate measurements.....	201
Figure 9.5:	Maximum slot velocity as a function of foil configuration at $V_t = 16$ m/s. The surface was constructed using 9 separate measurements.	202
Figure 9.6:	Maximum slot velocity as a function of minimum pressure at all tip speeds.....	203
Figure 9.8:	Maximum slot velocity as a function of maximum pressure at all tip speeds.....	206
Figure 9.9:	Maximum slot velocity as a function of maximum pressure at (a) $V_t = 10$ m/s, (b) $V_t = 12$ m/s, (c) $V_t = 14$ m/s, and (d) $V_t = 16$ m/s.	207
Figure 9.10:	Maximum slot velocity as a function of integrated force at all tip speeds. ..	209
Figure A1:	Computational domain and a typical mesh.....	222
Figure A2:	Details of key areas of the mesh: (a) the C-meshes around the foils and, (b) the mesh in the slot between the two foils.	223

List of Symbols

a_1	Emperical constant, dimensionless
a_2	Emperical constant, m/s
A_C	Cylinder open area, m ²
A_f	Feed inlet cross-sectional area, m ²
b	Friction coefficient
C	Consistency, %
c	Chord length, m
C_A	Accept stream consistency, %
C_D	Drag coefficient, dimensionless
C_F	Feed stream consistency, %
C_P	Pressure coefficient, dimensionless
C_{Power}	Power coefficient, dimensionless
C_q	Capacity coefficient, dimensionless
C_R	Reject stream consistency, %
C_V	Volumetric concentration, %
d	Fibre diameter, m
D	Cylinder diameter, m
D_P	Pressure drop coefficient
E	Contaminant or fractionation efficiency
f	Frequency, s ⁻¹
F	Integrated force (Chapters 7 and 9), N; Torque due to friction (Chapter 8), N·m
g	Clearance between foil and cylinder, m
h	Ride height, m
k	Turbulent kinetic energy, J/kg
K_H	Hydraulic resistance, dimensionless
l	Fibre length (Chapter 1), m; Main foil trailing edge length (Chapter 2), m
m	Experimental constant, dimensionless
N	Crowding number (Chapter 1), dimensionless; Number of foils (Chapter 6)

P	Pressure, Pa
P_{et}	Penetration number, dimensionless
P_i	Passage ratio of substance i , fraction
$Power$	Power, W
Q	Screening quotient, dimensionless
Q_A	Accept stream volumetric flow rate, m ³ /s
Q_F	Feed stream volumetric flow rate, m ³ /s
Q_{max}	Maximum volumetric flow rate through cylinder, m ³ /s
Q_R	Reject stream volumetric flow rate, m ³ /s
r	Radius, m
Re	Reynolds number, dimensionless
R_M	Mass reject rate, dimensionless
R_V	Volumetric reject rate, dimensionless
S	Cross-sectional area, m
T	Thickening factor (Chapters 1, 4, and 5), dimensionless; Torque (Chapter 8), N·m
t	Foil thickness, m
u	x-direction velocity component, m/s
v	y-direction velocity component, m/s
V_{avg}	Average flow velocity, m/s
V_S	Slot velocity, m/s
V_t	Rotor tip speed, m/s
V_{tan}	Tangential velocity component, m/s
W	Slot width, m
X_i	Mass fraction of substance i , fraction
y^+	Inner-law wall unit, dimensionless

Greek Letters

α	Angle-of-attack, degrees
β	Empirical constant (Chapter 1), dimensionless; Inlet angle (Chapter 8), degrees
γ	Slip factor, dimensionless

δ	Flap angle, degrees
ε	Turbulent dissipation rate, J/kg/s
λ	Empirical constant, dimensionless
μ	Dynamic viscosity, Pa·s
ν	Kinematic viscosity, m ² /s
ρ	Density, kg/m ³
σ	Compressive stress, N/m ²
φ	Fractionation index, dimensionless
ω	Specific turbulent dissipation rate, 1/s

Acknowledgements

I would like to thank my family and friends for their love and support. I would also like to express my appreciation to my supervisors Dr. James Olson and Dr. Carl Ollivier-Gooch for their guidance. Finally, I would like to thank my colleagues and the staff at the Pulp and Paper Centre for their support and friendship, especially Jens Heymer and Tim Patterson.

Co-Authorship Statement

For the work presented in Chapter 2, the design of the research program was a collaborative effort between me and the co-authors, Dr. James Olson and Dr. Carl Ollivier-Gooch. I conducted all of the simulations and analysis of the data presented. The written work was also done by me, with the co-authors acting in an advisory role.

For the work in Chapter 3, the design of the research program was a collaborative effort between me and Dr. Olson. The experiments in the study were carried out by me with assistance from Phil Wallace. The data analysis was conducted by me. The simulations were conducted by me. The manuscript preparation was conducted by me with Dr. James Olson and Dr. Carl Ollivier-Gooch acting in an advisory role.

For Chapter 4, the design of the research program was conducted by me. The experiments in the study were conducted by Mathieu Hamelin, Dr. James Olson, and me. The data analysis was performed by me. The written work was a collaborative effort between all of the co-authors.

For Chapter 5, the trial plan was assembled by me and Cameron Pflueger. The mill trial was carried out by Cameron Pflueger. The data analysis was performed by me, Cameron Pflueger, and Dr. James Olson. The manuscript preparation was a collaboration effort between Dr. Olson, Cameron Pflueger, and me.

For Chapter 6, the research plan was developed by me. I carried out all simulations in the study. The pilot plant data was collected by Mathieu Hamelin, Dr. Olson, and me. Analysis of the data was carried out by me. The manuscript was prepared by me, with the co-authors acting in an advisory role.

For the work presented in Chapter 7, the trial plan was developed by me in collaboration with the other co-authors, Dr. James Olson, Dr. Carl Ollivier-Gooch, and Dr. Robert Gooding. I conducted all of the simulations in the paper and performed the analysis of

the data. The manuscript was prepared by me with advisement from Dr. Olson and Dr. Ollivier-Gooch.

In Chapter 8, the trial plan for this study was developed by me and Dr. Olson, with advisement from the other co-authors. The experiments in the paper were conducted by Alexandra Regairaz and me. The analysis in the paper was conducted by me. The manuscript was prepared by me with Dr. James Olson and Dr. Ollivier-Gooch acting in an advisory role.

Chapter 1

Introduction

1.1 Background

Pressure screens are the most effective way to remove contaminants from a pulp stream and are used in all pulp and paper mills world wide. These contaminants include unpulped pieces of wood (shives), bark, rack, plastic, adhesives, and other oversized particles. Pressure screens are also used to fractionate pulp, or separate the pulp by fibre length, for targeted processing and the production of high value products. The use of pressure screens greatly improves the strength, optical properties and smoothness of the resulting paper.

A pressure screen splits the feed stream into an accept stream and a contaminated reject stream. The performance of a pressure screen is typically measured by its capacity, contaminant removal or fractionation efficiency, and power consumption. Capacity is the amount of pulp passed through to the accept stream, typically measured in tons per day. Efficiency is the mass flow of unwanted debris in the reject stream compared to the mass flow in the feed, or

$$E = \frac{Q_R}{Q_F} \frac{C_{R,X}}{C_{F,X}} = R_V \frac{C_{R,X}}{C_{F,X}} \quad (1.1)$$

where E is the screening efficiency, Q_R is the volumetric flow rate of the rejects, Q_F is the volumetric flow rate of the feed, $C_{R,X}$ is the consistency of a given material X in the rejects, $C_{F,X}$ is the consistency of a given material X in the feed, and R_V is the volumetric reject ratio [1]. An ideal pressure screen will maximize efficiency and capacity, while at the same time minimizing power consumption.

Figure 1.1 shows an illustration of a typical pressure screen. There are two main components in a pressure screen: a rotor and a screen cylinder with slots or holes, which are on the order of 0.1 mm in size. The unscreened pulp enters the screening chamber tangentially via the feed stream and passes into the screening chamber. Fibres and particles that are small enough will pass through the apertures in the screen cylinder and into the accept flow. Oversized debris will pass down the axial length of the cylinder and exit via the reject stream.

During normal operation, the small apertures in the cylinder will become plugged with fibres, flocs, and other oversized debris. The rotor therefore serves to prevent the apertures in the cylinder from plugging, allowing for an increase in performance of the screen. The rotation of the rotor has the effect of adding tangential velocity and turbulence to the flow, which helps fluidize the pulp, and of generating pressure pulses at the surface of the cylinder, backflushing the flow through the apertures and clearing them of debris [2-5]. The design of the rotor and the speed at which it is operated directly affect the maximum capacity of the pressure screen [6].

There are two types of screens in use in the industry – in-flow and out-flow screens. With an out-flow screen, the feed passes into the center of the cylinder and the accepts pass radially through the apertures outside the cylinder. An in-flow screen functions in the opposite manner, with the feed passing along the outside of the cylinder and the accepts passing through the apertures into the center. The rotor for an out-flow screen is therefore placed inside the cylinder, and it is placed on the outside of the cylinder for in-flow screens. The differences between in-flow and out-flow screens are illustrated in Figure 1.2. Foil rotors in out-flow screens have been the subject of numerous studies [1-16], but in-flow rotors have not been well studied. One study, however, suggested that in-flow screens have greater efficiency due to the use of centrifugal forces for the removal of high density particles in addition to the barrier removal of the screen cylinder [17].

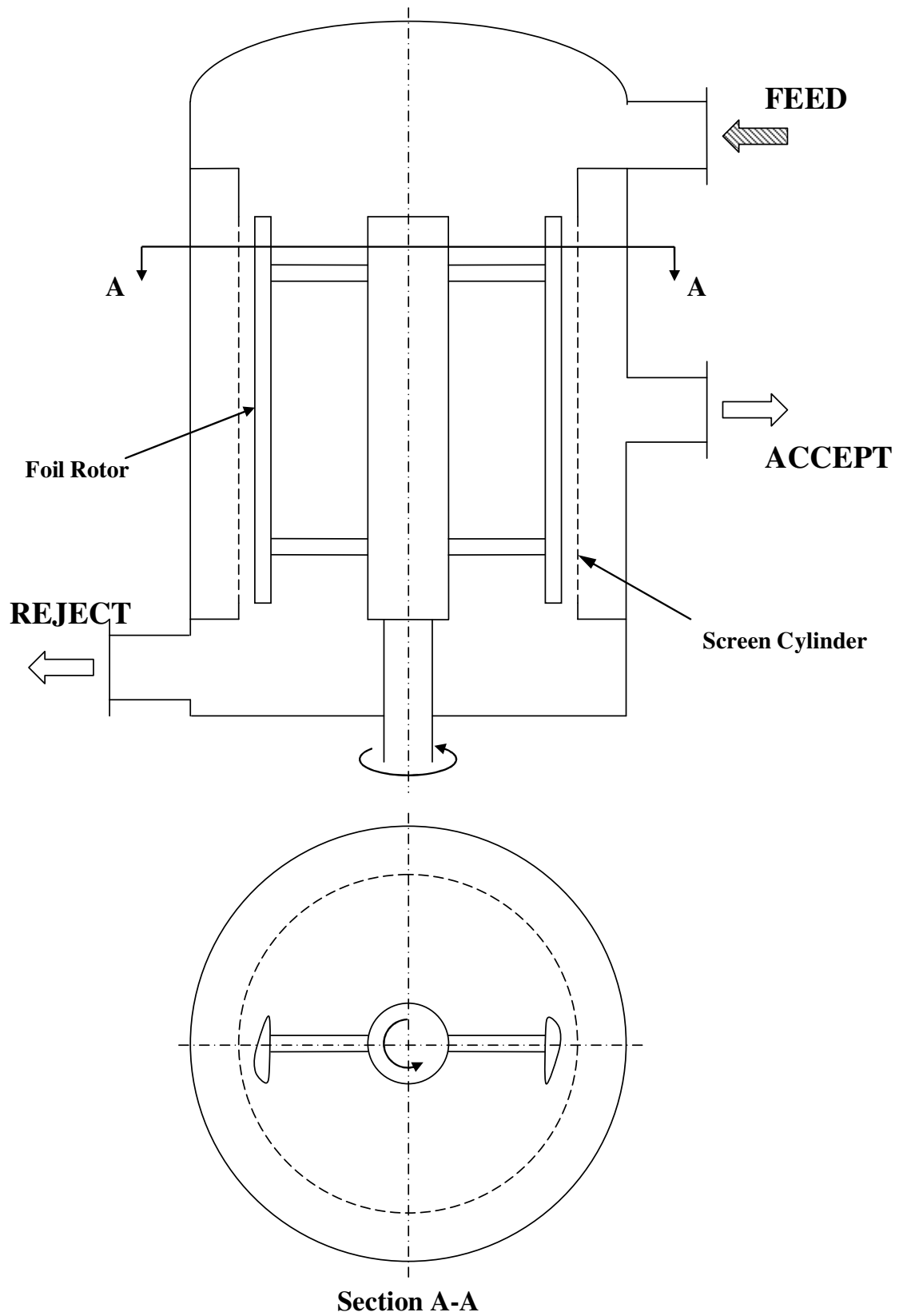


Figure 1.1: An illustration of a modern pressure screen.

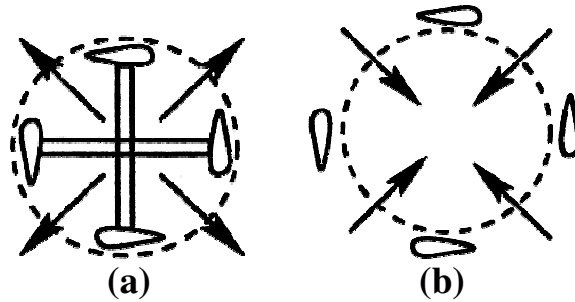


Figure 1.2: A schematic illustrating (a) out-flow screens and (b) in-flow screens.

There are two general types of rotors: solid core and foil rotors. Solid core rotors consist of hydrodynamic elements attached to the outer surface of an inner drum core and allow for the flow to pass over only one side of the elements. Foil rotors are similar in concept to the airfoils used on wings of aircraft and allow the flow to pass over both the upper and lower surface of the foil. Solid core rotors are more structurally resilient and are usually used earlier in the pulping process for higher consistency screening. Foil rotors offer greater control over the shape of the pressure pulse generated by the rotor and are used later in the process for fine screening applications. This thesis focuses on the performance of foil rotors.

This thesis investigates the hydrodynamics and the effects of the rotor design on pressure screen performance, which are not well understood. A series of seven experimental and numerical studies were conducted to investigate the effects of rotor design and operating parameters on pressure screen hydrodynamics, on the pressure pulses generated by the rotors, and on the overall pressure screen performance. First, however, a complete review of the literature relating to pressure screening will be conducted, followed by a detailed statement of this thesis's objectives.

1.2 Literature Survey

1.2.1 Rheology of Pulp Fiber Suspensions

Pulp fiber suspensions are complicated two-phase flows that are an active research topic. Pulp suspensions are found at a wide range of mass concentrations, or consistencies, within the papermaking process, from 0.01% up to 15%, and the fluid properties of the pulp vary greatly across this range. The rheology of pulp suspensions is controlled by fiber-fiber interactions and the forces involved in the contact of the fibers with each other.

Pulp suspensions are never truly homogeneous and as fibres contact each other they tend to form into flocs, or concentrated bundles of fibres. The presence of flocs affects the quality of the end result paper and, with respect to screening, can limit the capacity of a pressure screen by causing the cylinder to prematurely plug because the flocs will be retained by the screen cylinder. Also, the presence of flocs in a pulp suspension adds additional complexity and has a strong influence on pulp rheology. The formation and behavior of flocs is therefore an important subject when studying pulp flows. The presence of flocs in pulp suspensions and the strength of the flocs have been found to increase with consistency and fibre length, although they have also been shown to form at very low consistencies [18-23].

The most common parameter used in describing the fluid properties of a pulp suspension and the level of interaction between the fibres is the crowding number N , defined by Kerekes *et al.* as

$$N = \frac{2}{3} C_V \left(\frac{l}{d}\right)^2, \quad (1.2)$$

where C_V is the volumetric concentration, l is the fibre length, and d is the fibre diameter [20]. The crowding number is the number of fibres in the volume swept out by a single

fibre. Three regimes for pulp solutions were defined Soszynski (and expanded upon by Kerekes and Schell) based upon crowding number: dilute for $N < 1$, semi-concentrated for $1 < N < 60$, and concentrated for $N > 60$ [21, 24]. General types of fibre interactions were assigned to each regime. In the dilute regime the fibres have chance collisions, in the semi-concentrated regime the fibres have forced collisions, and in the concentrated regime there is continuous contact between the fibres [24]. It should be noted that in screening applications, typical crowding number values in the feed are in the range of $1.76 < N < 44$, placing the flows within the semi-dilute regime. Local crowding numbers may be significantly higher within the pressure screen, however, especially in and around the apertures.

Kerekes *et al.* defined the four distinct forces involved in fiber contacts as electrochemical, surface tension, bending, and hooking forces [20]. These forces require energy, varying the rheology of the suspension, and are the mechanisms by which flocs are formed.

The mechanical forces, hooking and bending, are caused by physical contact between fibres. Hooking forces are the result of two or more fibres literally becoming hooked or entangled with each other, normally due to curls, surface fibrillation, or kinks in the fibres. Hooking forces are most influential in dilute flows ($N < 1$). Bending forces, in concert with friction forces, result in flocs and the formation of a fibre mat in the concentrated regime ($N > 60$). As fibres slide past each other, the bending of the fibres causes a normal force, amplifying the friction forces and inhibiting the motion of the fibres [20, 25]. The level of friction forces therefore depends upon the coefficient of friction of the fibres and the magnitude of the bending forces. The coefficient of friction is largely dependent on the surface roughness of the fibres, and the bending forces depend upon the wood type and consistency of the suspension [26-31].

The final two forces, surface tension and electrochemical forces, are generally less influential than the mechanical forces [20]. Surface tension forces were found to be caused largely by air bubbles trapped in the fiber networks, particularly for consistencies

above 8%, leading to flocculation and the need for de-aeration of the pulp before certain processes. Electrochemical forces have been shown to be of secondary importance, although certain additives can increase their influence [32].

The flow conditions in which flocs form and disperse have also been studied in some detail. In early work, Mason defined flow characteristics that led to the formation of flocs in a dilute suspension ($N < 1$). He found that a dynamic equilibrium is established of floc formation and floc dispersion. Fibres are brought together through their relative translation and rotation within the flow and the forces described above lead to flocculation. Weak flocs are dispersed by hydrodynamic forces in the flow, however, and increasing the levels of shear in the flow leads to a reduction in the size of the flocs that are formed [33]. It has been shown in later studies that the shape and stiffness of the fibres is also important in the level of fibre flocculation [34].

A number of studies have investigated floc formulation in decelerating-turning flows and in decaying turbulence, both of which are of particular interest to screening applications. It was found that coherent flocs formed when the flow decelerated and turned [25, 35]. Based on these results, it was postulated by Kerekes that the flocculation in these circumstances was due to local crowding of the fibres caused by an inability of the fibres to turn with the flow [36]. Turbulence is commonly used in papermaking as a method to disperse flocs and to fluidize the pulp (a process discussed later in this chapter). However flocs have been found to form rapidly as the turbulence decays and the shear in the flow decreases [18, 20]. Flows with decaying turbulence have been found to be the most common sources of floc formation in papermaking, and the flocs can form rapidly in decaying turbulence, even at low consistencies [36].

Flocs are dispersed in shear flows. Various studies have investigated the effectiveness of different types of shear flows in reducing the size and dispersing flocs. It has been found that extensional flows disrupt large flocs more quickly than a simple shear flow, but the flocs are not entirely dispersed and small fragments remain, whereas the flocs are eventually entirely eliminated in a simple shear flow [37, 38]. This effect has been seen

for extensional flows in contracting channels, where weak softwood pulp flocs were seen to sometimes rupture, but stronger kraft flocs would remain intact [39, 40].

The flow properties of a pulp suspension vary significantly from a Newtonian fluid. Fibre suspensions require a yield stress before the fluid reacts with continuous strain at constant stress. Unlike other non-Newtonian fluids, the yield stress for a pulp suspension is difficult to measure because of non-uniformities in the fibre network due to flocs and because of the tendency of the fibres to slide along a wall. This effect causes the measured yield stress at a wall to be influenced by friction forces [41, 42].

Various techniques have been developed to measure the yield stress of a fibre suspension. The most common is the application of stress to the suspension with a rotary shear device [43-47]. It has been found that the yield stress of a suspension is approximately proportional to the consistency of the suspension to the third power [47, 48].

The viscosity of a pulp suspension is as complex as the yield stress. In situations where the fibre lengths are not much smaller than the reference length or channel size the flow can not necessarily be considered a continuum. This is of concern in screening since slot widths can be smaller than the average fibre length in the suspension. Also, fibres and flocs can migrate away from walls in shear flows, causing the local consistency near the wall to be much less than that away from the wall. For these reasons, modeling pulp flows simply as a non-Newtonian fluid is not valid in certain circumstances [42].

Illustrating the complexity of the subject, the shear viscosity of pulp at low consistencies was found by Chen et al. to have Newtonian behavior at low levels of shear, unstable behavior at moderate levels of shear, and Newtonian behavior again at high levels of shear [49]. This is likely due to the formation of flocs at moderate levels of shear that are broken up by the shear at higher levels. Milliken used falling ball rheometry to measure the viscosity of suspensions at varying consistencies. A critical crowding number of $N = 33$ was found, below which viscosity varied linearly with consistency and above which viscosity varied cubically with consistency [50]. Bennington and Kerekes also found that

viscosity varied with consistency to the third power for consistencies of $C > 1\%$ by measuring the viscous dissipation in turbulent pulp flows [51].

Due to these complexities, it is desirable for the pulp to achieve a fluidized state, both for design and operation purposes. Fluidization occurs when the pulp suspension acts as a fluid, with continuous strain under a constant stress. Turbulence is required to achieve the necessary strain rates to exceed the yield stress of the pulp and achieve fluidization [43, 51, 52]. Other properties of fluidized pulp suspensions include that they obey the power law in mixing, that the power number is independent of Reynolds number in mixing, and that pressure energy can be recovered from kinetic energy for pumping purposes [51, 53]. Achieving and maintaining fluidization of the pulp is referred to as a concern in both pressure screen rotor and cylinder design often, but without much clarification. It may be that turbulence, and the higher strain rates associated with it, is in fact the goal in order to diminish the formation of flocs.

The rheology of pulp suspensions in specific applications relating to paper making has been studied in varying levels of detail. These include pipe flows, headbox flows (contracting channels), and impinging jets. The most commonly studied of these, and the most influential to screening applications, are pipe flows. The behavior of pulp suspensions in pipe flows effects the condition of the pulp as it enters and exits a pressure screen. Three separate flow regimes have been identified for pulp suspensions in pipe flow: plug flow, mixed flow, and turbulent flow [54]. Each flow regime has also been found to have a corresponding friction loss behavior. In the plug flow regime, the flow is dominated by interactions between the plug and the wall and the friction between the two boundaries. As velocity is increased, a water annulus is formed between the plug and the wall and hydrodynamic shear begins to influence the flow, and eventually the plug and the wall cease to interact. As the annulus becomes turbulent, the mixed flow phase begins, which is analogous to the transition to turbulence. Finally, the flow becomes fully turbulent and the plug is disrupted. In the turbulent regime, a phenomenon called turbulent drag reduction occurs, where the friction losses of the pulp suspension are less than those found for water at the same flow velocity. The exact mechanisms of this

phenomenon are still a topic of research, but it is believed that it occurs because of dampening of turbulent fluctuations by small flocs and fibres and because large flocs aid in momentum transfer [55-63].

1.2.2 Screening Theory

The physics involved in fractionating and removing contaminants from pulp using a pressure screen are very complex and there are still significant gaps in the literature. There are two general methods by which the pulp is filtered: barrier screening and probability screening. In barrier screening, solid-solid separation occurs when particles are too large in all dimensions to pass through the apertures in the cylinder. In probability screening, the apertures are smaller than one of the dimensions of the particles being accepted by the cylinder. There are barrier screening concepts involved in the removal of large contaminants such as shives and flocs, but pressure screens typically function using probability screening concepts due to the large length to diameter ratios of wood fibres. Additionally, the visco-elastic properties of ink and plastic in the pulp (so called “stickies”) make barrier screening difficult [64, 65].

The mechanics of probability screening are quite complex and not wholly understood. In order to pass through the apertures in the cylinder the fibres must be aligned properly. The motion of fibres in a pulp suspension is very difficult to predict due to interactions of the fibres with the fluid, boundaries and other fibres.

Several researchers have investigated the motion of fibres in flow through a narrow aperture with a cross flow, which is a simplified model of a pressure screen. Gooding and Kerekes used high speed video to make general observations about fibre behavior and found that there is a layer of lower fibre concentration near the wall, similar to the annulus found in pipe flows and referred to as the “wall effect” [66, 67]. It was also observed that long, stiff fibres would rotate in order to enter the slot (referred to as the “turning effect”), while long flexible fibres would bend when entering the slot. These results were expanded upon by Kumar et al., who found that the passage of fibres through

the slot increased with slot width and fibre flexibility, and decreased with increased fibre length and upstream flow velocity. It was also found that lower slot velocities led to greater fractionation efficiency [68]. Yu and Defoe supported these findings by studying fibres passing through a slot in a cross-flow using high speed video. They also found that orientation of the approaching fibre and its position with respect to the wall affected the probability of its passage [69]. Finally, Olson studied the behavior of fibres flowing through a single slot in a turbulent cross-flow and found the fibre concentration near the wall was a function of fibre length. This was determined to be due to interactions between the fibres and the wall. As the fibres rotated in the boundary layer, long stiff fibres would bounce or “pole vault” away from the wall [70]. These studies have offered insight into the fundamental mechanisms involved in screening, but there are still considerable gaps in the literature, especially with the added complexity of pulsed flow caused by the rotor.

In an effort to better understand the relative importance of the variables involved, Martinez et al. developed a model for the capacity of a pressure screen based on a force balance of a floc passing through a slot in a screen cylinder, where the floc experiences frictional and compressive stresses from the slot walls as well as hydrodynamic forces [71]. They found that the maximum flow through the cylinder Q_{max} is related to the cylinder slot geometry and flow conditions by

$$Q_{max} = A_C \left(\frac{2}{\rho K_H} \right)^{1/2} [P - 2\mu\sigma \left(\frac{T}{W} \right)]^{1/2}, \quad (1.3)$$

where A_C is the open area of the cylinder, ρ is the fluid density, K_H is the hydraulic resistance, P is the magnitude of the suction pressure of the rotor pulse, μ is the static coefficient of friction between the floc and the walls of the slot, σ is the compressive stress in the floc, T is the throat length of the slot, and W is the slot width. The hydraulic resistance is used to describe the pressure drop across the slot:

$$\Delta P = K_H \left(\frac{1}{2} \rho V_s^2 \right), \quad (1.4)$$

where ΔP is the pressure drop across the slot and V_s is the average velocity of the flow through the slot [72]. It was found that K_H is dependent on the slot velocity with the following form:

$$K_H = a_1 + \frac{a_2}{V_s}, \quad (1.5)$$

where a_1 and a_2 are empirically determined constants [ibid.] The values of μ and σ are dependent on the properties of the pulp and, along with the magnitude of the suction pressure P_P , are difficult to measure and were therefore found through linear regression from experimental results. Based on equation 1.3, the maximum capacity of the screen therefore increases with increasing slot width, cylinder open area, and pressure pulse strength, and decreases with increasing slot throat length, hydraulic resistance, fluid density, and the pulp-dependent static friction coefficient and floc compressive stress.

Researches have also worked to model the efficiency of pressure screens. Nelson developed the screening quotient Q to relate the mass reject ratio of a pressure screen to the contaminant removal efficiency, and to provide a single value to relate pressure screen performance. Take care not to confuse the screening quotient Q with volumetric flow rates, which will have a subscript (such as Q_F , which is the volumetric flow rate of the feed stream). Efficiency was shown to be related to the screening quotient and mass reject ratio as follows:

$$E = \frac{R_M}{1 - Q + QR_M}, \quad (1.6)$$

where E is the contaminant removal efficiency and R_M is the mass reject rate [73]. The mass reject rate R_M is defined as

$$R_M = \frac{Q_R C_R}{Q_F C_F}, \quad (1.7)$$

where Q_R is the volumetric flow rate of the reject, Q_F is the volumetric flow rate of the feed, C_R is the consistency of the reject, and C_F is the consistency of the feed [67].

Work was done by other researchers to further develop the screening quotient, and it was found that the screening quotient could also be calculated as

$$Q_i = 1 - \frac{X_{Ai}}{X_{Ri}}, \quad (1.8)$$

where X_{Ai} and X_{Ri} are the mass fractions of the component i in the accepts and rejects, respectively [74]. When applied to fractionation efficiency, the screening quotient is related to long and short fibre removal efficiencies by

$$E_L = \frac{E_S}{1 - Q + QE_S}, \quad (1.9)$$

where E_L is the long fibre removal efficiency and E_S is the short fibre removal efficiency. The long fibre removal efficiency E_L is the portion of the long fibres directed to the reject stream, which it is desirable to maximize, and the short fibre removal efficiency E_S is the amount of short fibres directed to the reject stream, which it is desirable to minimize [75].

It was found in analysis conducted by Gooding and Kerekes that Nelson's screening quotient is based upon a mixed flow model of the flow through the screen, where the screening zone is assumed to be well mixed in all directions [67, 73, 76]. Gooding and Kerekes also derived pressure screen performance equations based upon a plug flow model, where there is perfect radial mixing but no axial mixing in the screening zone. A key concept to the plug flow model is the passage ratio P_p , defined as

$$P_p = \frac{C_s}{C_U}, \quad (1.10)$$

where C_s is the pulp concentration in the slot and C_U is the concentration upstream of the slot. Passage ratio essentially describes the extent to which fibres or debris pass through an individual slot. It is common to specify the passage ratio of specific contaminants or, in the case of fractionation, specific fibre lengths. Based upon the plug flow model, it was found for probability screening that

$$E = R_M^{\frac{P_C}{P_P}}, \quad (1.11)$$

where P_C and P_P are the passage ratio for contaminants and pulp, respectively [67]. It was also found that

$$\frac{C_R}{C_F} = \left[\frac{Q_R}{Q_F} \right]^{P-1}, \quad (1.12)$$

where C_R is the consistency in the rejects, C_F is the consistency in the feed, Q_R is the volumetric flow rate of the rejects, and Q_F is the volumetric flow rate of the feed.

Introducing the common screening parameters thickening factor T , which describes the increase in consistency of the rejects, and volumetric reject ratio R_V , equation 1.11 can be further simplified:

$$T = \frac{C_R}{C_F}, \quad (1.13)$$

$$R_V = \frac{Q_R}{Q_F}, \quad (1.14)$$

and therefore

$$T = R_V^{P-1}. \quad (1.15)$$

The normalized consistency drop D_P , which reflects the consistency drop of the accepts, was expressed with the plug flow model as

$$D_P = \frac{C_F - C_A}{C_F} = \frac{R_V^P - R_V}{1 - R_V}, \quad (1.16)$$

where C_A is the consistency of the accepts [76]. The plug flow model was shown in a series of pilot plant trials to perform better at predicting pressure screen performance than the mixed flow model [ibid.].

Due to its importance in the performance of a pressure screen, a number of researchers have investigated the factors effecting passage ratio [66, 70, 77]. The dimensionless penetration number Pe_t was introduced by Kumar to describe screen operational and geometric parameters, defined as

$$Pe_t = \frac{WV_s}{lV_t}, \quad (1.17)$$

where W is the slot width, V_s is the average slot velocity, l is the fibre length, and V_t is the rotor tip speed [77]. Passage ratio was modeled as a function of the penetration number by Olson and Werhrett:

$$P = \begin{cases} \frac{Pe_t}{2mk} & \text{if } P < \frac{1}{2} \\ 1 - \frac{mk}{2Pe_t} & \text{if } P \geq \frac{1}{2} \end{cases}, \quad (1.18)$$

where m and k are experimentally determined constants of proportionality [1, 78].

The plug flow performance equations above have also been expanded to describe the performance of pressure screens when used for fractionation. Fractionation is generally described by changes to the fibre length distribution of the pulp [1]. Fractionation efficiency $E(l)$ has been represented as the mass flow of fibres of length l in the reject stream divided by the mass flow of the fibres of length l in the feed. Fractionation efficiency $E(l)$ is therefore

$$E(l) = \frac{Q_R C_R(l)}{Q_F C_F(l)} = R_v \frac{C_R(l)}{C_F(l)} = R_v T(l). \quad (1.19)$$

where $C_R(l)$ and $C_F(l)$ are the concentrations of fibres of length l in the feed and reject streams, respectively, and $T(l)$ is the thickening factor for fibres of length l [1, 79]. From the plug flow model, fractionation efficiency $E(l)$ is therefore related to passage ratio $P(l)$ by

$$E(l) = R_v^{P(l)}. \quad (1.20)$$

It was found experimentally in pilot screening trials that, for cylinders with smooth hole apertures, the passage ratio $P(l)$ is related to fibre length by

$$P(l) = e^{-l/\lambda}, \quad (1.21)$$

where λ is an empirically determined constant [79]. The constant λ was found to increase with increasing slot velocity and with aperture diameter [ibid.]. Other screening trials

found that passage ratio behaved slightly differently for slotted cylinders and that, for slotted cylinders, $P(l)$ is related to fibre length by

$$P(l) = e^{(-l/\lambda)^\beta}, \quad (1.22)$$

where, again, λ and β are empirically determined constants [1]. Olson found that a value of $\beta = 0.5$ provided the best fit for slotted screen cylinders, and as seen in equation 1.21, smooth hole apertures have a value of $\beta = 1.0$ [ibid]. These models imply that smooth holed cylinders would have better fractionation efficiency than slotted cylinders because of the fact that the passage ratio of the long fibre fractions would decrease more slowly for the slotted cylinders. Ideal fractionation would occur when there is a passage ratio of $P = 1.0$ for short fibre fractions and a passage ratio of $P = 0.0$ for long fibre fractions. In the same studies, passage ratio was also found to be independent of volumetric reject ratio R_V [1, 79].

Finally, an additional parameter, the index of fractionation φ , was introduced by Olson et al. to better describe the performance of a pressure screen [79]. The index of fractionation φ is defined as

$$\varphi = E_L - E_S, \quad (1.23)$$

where E_L is the removal efficiency of fibres above a given length, and E_S is the removal efficiency of fibres below a given length. E_L and E_S are the portions of long and short fibres, respectively, in the reject stream. The index of fractionation varies from $\varphi = 0$ in the case of no fractionation to $\varphi = 1$ in the case of perfect fractionation. Perfect fractionation is achieved if $E_L = 1$, where all the long fibres are passed to the rejects, and $E_S = 0$, where all the short fibres are passed to the accepts.

1.2.3 Cylinder Geometry and Hydrodynamics

The hydrodynamics of the flow in and around the apertures in the cylinder have been studied by a number of researchers, and cylinder design has evolved as more is understood about the phenomena involved. The apertures in pressure screen cylinders are either holes or slots of varying widths/diameters, and can have a smooth or contoured profile. An example of a typical contoured slot geometry with key dimensions identified is shown in Figure 1.3 [80]. Modern slotted cylinders nearly always have a contour of some sort, however. Each design has specific advantages and disadvantages and is therefore fitted to a given screening task.

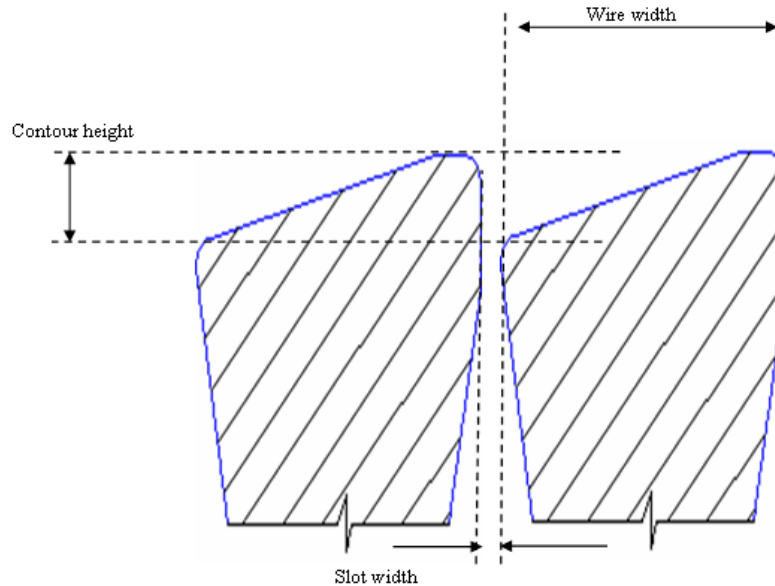


Figure 1.3: A typical contoured slot design with key dimensions identified [80].

Holed cylinders are typically used in coarse screening applications, such as knot removal (with aperture diameters of 6 to 20 mm), and for pulp fractionation (with hole diameters of 0.8 to 3 mm) [14]. As shown previously in equations 1.21 and 1.22, it has been found that smooth hole cylinders have greater fractionation efficiency [1, 79]. Other studies have found that comparable fractionation efficiencies can be obtained with slotted cylinders, however, as long as the proper slot geometry and operating conditions are used

[81]. In the past, holed cylinders were considered to have a higher capacity than slotted cylinders due to a higher cylinder open area [82], but this is changing due to advances in slot contour design and manufacturing techniques, especially the introduction of wedge-wire slotted cylinders. Wedge-wire slotted cylinders can provide up to a 100% increase in the open area of the cylinder compared to machined slots [83]. Additionally, it has been shown that if the distance between the apertures in holed cylinders is too small relative to the fibre length, fibres can become stapled between holes, reducing capacity [84].

The introduction of contoured slots has greatly increased the capacity of slotted screen cylinders by allowing for control of the flow conditions around the slot. This has also allowed for the use of slots down to 0.1 mm in width, which in turn increases the efficiency of slotted cylinders [8]. Gooding studied a smooth and a contoured aperture in a cross-flow experimentally and using computational fluid dynamics (CFD) [72]. It was found that contoured apertures generally have a lower hydraulic resistance across the aperture, as described in equations 1.4 and 1.5, which implies a higher slot velocity at a given pressure drop across the cylinder. It was also found that the effect of a given contour shape was dependent on the flow conditions, specifically the upstream cross-flow velocity and the slot velocity, and that simply having a contour is not sufficient to improve performance. It was also shown that the contour created two vortices in the flow – one at the entrance of the slot caused by the trailing edge of the contour and a second inside the slot. The vortex inside the slot was reduced in size as the slot velocity was increased, and was completely eliminated above slot velocities of 1.3 m/s. A single large vortex was seen in the slot for smooth slots, which also decreased in size with increasing slot velocity. The vortex still occupied 30% of the slot at a slot velocity of 9.3 m/s, however [ibid.].

Similar results were seen by Halonen et al., who studied the flow in and around smooth and contoured slots in a cross-flow using CFD and laser Doppler velocimetry (LDV), a laser velocity measurement technique [85]. It was again found that a large vortex existed in the slot for smooth slots. For contoured slots, a single vortex was observed outside of

the slot on the trailing edge of the contour. A vortex inside the slot may not have been observed for the contoured slots, as seen by Gooding, because of differences in the slot velocities studied [72, 85]. Halonen et al. found the use of contoured slots significantly reduced hydraulic resistance across the slot, and significantly increased the turbulent kinetic energy and velocity fluctuations at the entrance to the slot [85]. The increase in turbulent kinetic energy caused by the contours allows for a higher maximum screen capacity by keeping the pulp fluidized at the inlet to the apertures [86, 87].

A number of researchers have studied the effect of varying modern slot contours on the flow conditions at the cylinder wall [80, 88]. It was shown by Mokamati that increasing the height of the contour increased both the size of the vortex at the entrance of the slot and the distance downstream between the slot and the point of flow re-attachment. Increasing slot velocity was found to reduce the size of the vortices at the slot entrance [ibid.]. Also, turbulence intensity at the cylinder wall was found to increase with increasing contour height and to decrease with increasing wire width [80].

Contoured slotted cylinders have been shown to have increased contaminant removal efficiency compared to smooth hole cylinders, most likely because of the hydrodynamic effects described above which allow for the use of smaller slots [89, 90]. They also have greater operational flexibility than smooth hole cylinders [11]. Contoured slotted cylinders have been found to have lower fractionation efficiency, however, because long fibres are passed through the apertures more easily. It has also been found that increasing the contour height increases the maximum capacity of the screen and reduces the efficiency [91].

1.2.4 Pressure Screen Rotor Studies

The purpose of the rotor in a pressure screen is to prevent the screen apertures from becoming plugged with fibres and debris and, in doing so, increase the maximum capacity of the screen. It is generally believed that the rotor effects screen performance in two ways: it provides a tangential velocity to the flow on the feed side of the screen

plate, and, more importantly, it generates a negative pressure pulse on the screen. The negative pressure pulse generated by the rotor backflushes the apertures, clearing any fibre or debris accumulations [4]. Increasing the tip speed of the rotor increases the magnitude of the pressure pulses generated by the rotor, the frequency of the pulses, and the tangential velocity of the flow in the screen, and has been shown to increase the maximum capacity of the screen [6, 17, 71, 84]. The induced tangential velocity generates turbulence in the flow near the screen wall through any turbulence in the wake of the rotor and through interaction of the flow with the cylinder wall and slot contours. It is speculated that this mixes the flow and keeps the pulp fluidized, preventing the formation of a fibre mat at the inlet of the apertures [86, 87]. The precise mechanisms by which the rotor affects screen performance are not well understood, however.

Most investigations of rotor performance have studied the overall screen performance of various rotor types and made inferences about the hydrodynamics based on those results. Julien Saint Amand and Perrin [8] compared a blade rotor with an extended negative pressure pulse to a foil rotor and concluded that the foil rotor provides a lower passage ratio (and therefore, presumably, improved fractionation but lower screen capacity). Olson *et al.* compared a Centrisorter bump rotor to a Hooper PSV blade type rotor and found only slight differences in passage ratio between the rotors, depending on aperture size. For 1.8 mm diameter holes, the rotors performed identically, and for 1.0 mm diameter holes, there was only a slight increase in fibre passage ratio for the blade-type rotors. It was speculated that the fact that rotor type did not play a significant role in this study was due to the relatively gentle pulse [79]. Gooding *et al.* inferred from these results that subtleties in the rotor design, such as the exact dimensions and geometry of the foil and the operating parameters (tip speed, clearance, etc.), are more important to screen performance than the generic type of rotor [92].

Increasing the tip speed of the rotor increases the tangential speed of the flow in the cylinder [66, 93-96]. Gooding introduced the slip factor γ to describe the tangential flow velocity as a function of rotor tip speed:

$$V_{tan} = (1 - \gamma)V_t, \quad (1.24)$$

where V_{tan} is the tangential flow velocity [66]. Gooding estimated the slip factor to be approximately 0.85, but the value of the slip factor is likely dependent upon the rotor geometry (particularly the drag coefficient) and the flow conditions. Researchers have also found that the slip factor decreases down the axial length of the screen (i.e. the tangential velocity of the fluid increases) [94-96], likely because of the flow being accelerated by drag from the rotor.

Increasing the rotor tip speed has also been found to increase the power consumption of the rotor significantly [97]. Olson et al. found that the power coefficient C_{Power} to be Reynolds number independent, where

$$C_{Power} = \frac{Power}{\rho V_t^3 D^2}, \quad (1.25)$$

where $Power$ is the power consumption of the rotor and D is the rotor diameter.

Reynolds number Re (based on diameter) is defined as

$$Re = \frac{\rho V_t D}{\mu}, \quad (1.26)$$

where μ is the dynamic viscosity of the fluid. This implies that the power consumption of the rotor increases cubically with rotor tip speed. It was also found that the value of the power coefficient was highly dependent upon the rotor geometry. They also determined that flow rates in the screen affected rotor power consumption, and that the power coefficient was approximately linearly dependent upon the capacity coefficient, with capacity coefficient C_q defined as

$$C_q = \frac{Q_F}{V_t D^2}. \quad (1.27)$$

The effect of varying rotor tip speed on passage ratio has been investigated by several researchers, but the exact effect of the rotor on passage ratio is still not well understood. Julien Saint Amand and Perrin found that, for a constant volumetric reject ratio, passage ratio increased with increasing tip speed in some cases, but decreased in others [8, 9]. Wakelin and Corson also studied the effect of varying rotor tip speed on reject thickening and passage ratio, and their results support the findings of Julien Saint Amand and Perrin [8-12]. They found that passage ratio increased with increasing rotor tip speed for contoured holes and slots, but that the opposite was true for small, smooth holes. They also observed that a “critical rotor speed” existed, beyond which passage ratio approached a constant value and was not generally affected by rotor speed [10, 12].

The pressure pulse generated by the rotor is key to the backflushing action which clears the apertures of debris and increases screen capacity. There have been a number of studies experimentally investigating the pressure pulses generated by a pressure screen rotor. Yu studied the pressure pulses from a single S-type solid core rotor for a range of tip speeds and flow rates [13]. It was observed that the pressure pulses were not affected by increasing flow rates, although the tip speeds studied were all fairly high (15 m/s to 25 m/s). Atkins studied the effects of flow rate, tip speed, and consistency on the pressure pulses generated by a foil rotor and a solid core step rotor [14]. It was found that, with water, increasing reject rate at a constant feed flow rate (i.e. increasing accept flow while reducing reject flow) had no effect on the pressure pulse below a reject ratio of $R_V = 0.3$ for either the step rotor or foil rotor. Increasing the feed flow caused the magnitude of the pressure pulse generated by the foil rotor to increase, however. No explanation was offered for this phenomenon. Atkins also found that varying consistency between 0.0% and 2.8% had little effect on the pressure pulse for both rotors, while other researchers found that increasing consistency caused a reduction in the pulse magnitude [5, 98]. Atkins and Yu also both observed a reduction in the strength of the pressure pulses generated by the rotor as the flow moves axially down the cylinder [13, 14]. This is likely due to a reduction in the relative velocity of the flow relative to the rotor as the flow is accelerated by drag caused by the rotor, as discussed previously. While

insightful, neither study thoroughly investigated the combined effects of rotor geometry and slot velocity on the pressure pulses generated by the rotor.

The magnitude of the pressure pulse has been shown by researchers to increase with increasing rotor tip speed, however the shape of the pulse does not change [2-5, 98]. The pressure coefficient of a given rotor has been found to be Reynolds number independent in various laboratory experiments and CFD studies, where pressure coefficient C_p is defined as

$$C_p = \frac{P}{(1/2)\rho V_t^2}, \quad (1.28)$$

where P is pressure. The pressure pulses generated by the rotor are therefore proportional to the rotor tip speed squared [ibid.]. It is a key hypothesis of this thesis that if the C_p of a rotor can be increased, the rotor can then be slowed and still generate the same magnitude pressure pulse, reducing power consumption without effecting the screen capacity.

The pressure pulses generated by pressure screen rotors have been shown to have a positive portion at the leading edge followed by a stronger negative portion [2-5, 13, 14, 98]. Solid core rotors have typically been found to have a stronger positive pulse than foil rotors. Researchers have debated what the ideal shape of the pressure pulse is for maximum screen performance. Feng *et al.* proposed that it is desirable to maximize the magnitude of the minimum C_p generated by the rotor in order to maximize the backflushing of the slots, allowing the rotor to be slowed to save power without reducing screen capacity [4]. They also hypothesized that it is desirable to minimize the magnitude of the positive pulse: a positive pressure could cause oversized debris to become lodged in the apertures or, in the case of deformable debris such as stickies, to pass through the apertures, reducing efficiency. This theory will be examined in this thesis.

Feng and Gonzales also studied the effect of varying the geometry of foil rotor elements on the pressure pulse generated by the rotor using CFD and a laboratory screen, respectively [ibid.]. They found that increasing the camber, or curvature, of the foil greatly increased both the width and magnitude of the pressure pulse. They also showed that increasing the angle-of-attack α of the foil, defined as the angle of the foil with the tangent line, increased the magnitude of the negative portion of the pressure pulse while at the same time reducing the undesirable positive portion of the pressure pulse. Beyond a certain angle-of-attack, however, it was found the foil would begin to stall and the magnitude of the pressure pulse would diminish. This was especially true for highly cambered foils, which would stall at very low angles-of-attack. Similar observations were made by Niinimäki, who showed that increasing the foil angle-of-attack improves the maximum capacity of the screen [7].

Other factors affecting the magnitude of the pressure pulse at the cylinder wall are the gap between the foil and the cylinder and the pulp consistency. Reducing the gap between the foil and the cylinder wall was shown in a laboratory screen and using CFD to increase the magnitude of the pressure pulse [2-5, 98]. There are mixed results in the literature about the effect of consistency on the pressure pulse magnitude, however. Gonzales and Pinon found that increasing feed consistency reduced the magnitude of the pressure pulse using a laboratory screen. Other researchers have found that varying feed consistency has no effect on the pressure pulse, however [13, 14, 99]. Atkins measured the pressure pulses from a step rotor and a foil rotor over a wide range of feed consistencies ($C_F = 0.0\%$ to over 2.5%) and found little variation in the positive or negative portions of the pressure pulse for either rotor [14].

CFD is increasingly being used as a tool to study pressure screen rotors [2, 4, 14, 99, 100]. Key difficulties exist in modeling the problem, however, especially the complicated rheology of pulp and the unsteady nature of the problem. Karvinen and Halonen made an early attempt at validating CFD for modeling pressure screen foil rotors in 1984 and obtained good numerical results for the time [99]. They assumed the fluid to be water ($C_F = 0$) and used the standard $k-\varepsilon$ turbulence model with a finite difference

scheme to solve the flow field. The results they obtained showed that the shape of the foil has a significant effect on the shape of the pressure pulse.

Wikström and Fredriksson used a commercial CFD package (finite volume) to study two different rotors in a screen [100]. The general behavior of the pressure pulse for a foil rotor in water was captured well, but the CFD overestimated the magnitude of the pressure pulse.

While the previous two studies discussed provided cursory investigations into the quality of CFD results, they did not provide a detailed validation of the tool. Feng *et al.* therefore used the experimental results obtained by Gonzales to investigate the usefulness of CFD as a design tool [2, 4, 5]. A foil rotor was modeled using a commercial CFD package (finite volume) for a wide range of tip speeds, gap heights, foil camber, and angles-of-attack. A variation in experimental and numerical C_p magnitudes was once again observed, but it was concluded that, in general, the CFD captured the pressure pulse signatures well, especially in terms of trends.

1.2.5 Airfoil Development

Airfoils have been extensively studied for over a century. Descriptions of key features can be found in any aerodynamics text: recommended readings include Anderson [101] and Abbott and von Doenhoff [102] for in depth discussions of airfoil geometries. To summarize, however, a typical airfoil is defined in terms of its chord length, camber, and thickness, as shown in Figure 1.4. The chord length is defined by a line connecting the leading and trailing edges. The camber line represents the curvature of the airfoil and is defined as the average distance between the upper and lower surfaces. The camber of the foil gives the maximum distance between the chord line and the camber line. The thickness of the foil is the distance between the upper and lower surfaces and, finally, the angle-of-attack of the foil, α , is defined as the angle between the freestream velocity, u_∞ , and the chord line. A variety of airfoil naming conventions have been established, with the NACA systems being the most common [102].

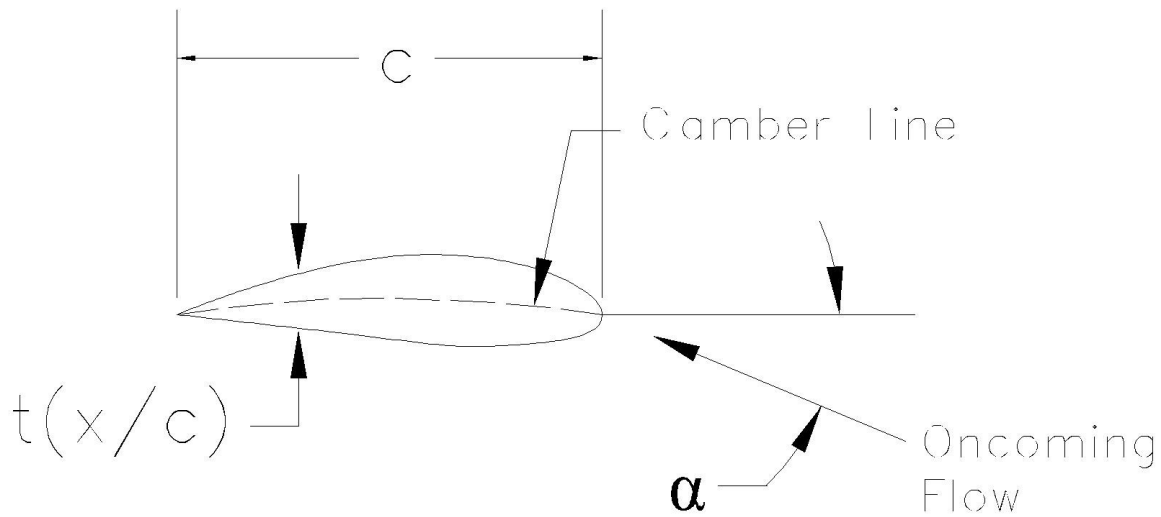


Figure 1.4: Airfoil nomenclature for a single-element foil.

A thick airfoil ($t/c > 0.16$) experiences trailing edge flow separation, while a thinner airfoil ($0.10 < t/c < 0.16$) will experience leading edge separation [101]. This is mostly due to the change in the radius of the leading edge of the foil as thickness is varied. Trailing edge separation occurs more gradually and leads to “softer” stall characteristics. However, thinner foils that experience leading edge separation have a higher maximum lift, or the integrated pressure acting on the foil [ibid.].

Increasing the camber of a foil increases the lift generated by a foil. It also has the effect of moving the stagnation point at the leading edge of the foil towards the lower surface of the foil [ibid.]. This effect was shown by Feng *et al.* to also reduce the positive pulse on the wall of the cylinder [4]. Increasing the camber of the foil also causes the foil to stall at a slightly lower angle-of-attack, however [101].

This work will also investigate the use of multi-element rotor foils for pressure screen applications. The most common example of multi-element foils is the leading and trailing edge flaps seen on fixed wing aircraft. A deployed flap has the effect of

increasing the effective camber of a foil, which leads to higher lift and, therefore, an increased pressure acting on the screen basket in a pressure screen. Also, and more importantly, a slotted multi-element foil will be able to reach significantly higher angles-of-attack before stall at a given Reynolds number than a single element foil. Once again, this leads to greatly increased lift on the foil.

1.2.6 Inverted Foils in Ground Effect

The inverted foils in ground effect used as the front wings of Formula One (F1) cars have many similarities to a pressure screen rotor foil, and insight can be gained from the work done on that topic. In addition to having geometric similarities, the front wings on F1 cars operate at comparable Reynolds number (on the order of $Re = 10^5$, based on chord length) [103-106]. There are obvious differences, however, namely the fluid (air versus pulp), the absence of slots and curvature in the wall boundary, and the fact that pressure screen rotors act in their own wake.

It is well known in aerodynamics that a ground effect exists and that an airfoil has an increase in lift as it approaches the ground [101]. Researchers have found that the same effect occurs for an inverted foil as well. Zerihan and Zhang found in wind tunnel studies that the down force provided by an inverted cambered foil at a constant angle-of-attack increases as the distance between the ground and the foil decreases [104]. Reducing the height of the foil was found to cause the foil to stall from the trailing edge, however, and at a critical point (approximately $h/c = 0.1$, where h is the height of the foil from the ground) the downward lift dropped off suddenly. The same effects were seen for multi-element wings, as well [105].

Katz and Garcia studied the effect of varying the flap angle of the front wing in a wind tunnel study [107]. They found that downward lift increased approximately linearly with increasing flap angle. The same study also found that increasing the angle-of-attack of the front foil diverted the flow from the undercarriage of the car, causing unfavorable flow conditions for components downstream of the wing and a net loss in down force for

the entire car. These results may explain why the wings of F1 cars tend to be at low angles-of-attack and why the bulk of the literature focuses on variation of the flap angle.

Researchers have also used CFD in inverted foils in ground effect. Mahon and Zhang investigated the predictive capabilities of several turbulence models for solving the Reynolds averaged Navier-Stokes equations (RANS) for the flow around single- and double-element inverted foils in ground effect [106, 108]. All of the models had good agreement with wind tunnel data for the surface pressure on the foils and the velocity profile of the wake well, but they all slightly over-predicted surface pressure. For the single element foil, the $k-\omega$ SST model was found to be the best for predicting the surface pressure on the foil and the realizable $k-\varepsilon$ model was best at predicting the wake velocity profile. For the double-element foil, the realizable $k-\varepsilon$ model had the best performance for both surface pressures and wake velocity profile.

1.3 Research Objectives

It has been shown in the literature that the use of a rotor clearly increases the capacity of a pressure screen by preventing plugging of the apertures in the cylinder. The exact mechanisms by which this occurs are not well understood, however. It was also found the power consumption of the screen is dependent on the tip speed of the rotor cubed and that significant power savings could be achieved by slowing the rotor [97]. Additionally, researchers have demonstrated that the magnitude of the pressure pulse generated by a rotor is proportional to the tip speed of the rotor squared and that varying the geometry of the rotor element can increase magnitude of the non-dimensional pressure coefficient for the rotor [2-5, 98]. It has been theorized that by maximizing the magnitude of the pressure coefficient, the rotor can be slowed and power consumption can be reduced without affecting the capacity of the screen.

The general goals of this thesis are to provide a better understanding of the hydrodynamics of pressure screen foil rotors, how the rotor design affects the overall pressure screen performance, and to apply this knowledge and other existing theories to

develop a high-performance pressure screen rotor. The application of multi-element foil technology to pressure screen rotors was also investigated, in order to better achieve these objectives. The specific objectives of this thesis are to:

1. Use CFD to determine the optimal design of a multi-element foil (MEF) pressure screen rotor and compare its performance to a single-element foil rotor.
2. Experimentally confirm the CFD results using a laboratory pressure screen.
3. Experimentally determine the effect of slot velocity on the performance of the rotor.
4. Experimentally determine the effect of varying rotor foil geometry on overall pressure screen performance.
5. Determine the industrial performance of the MEF pressure screen rotor.
6. Use CFD and pilot plant experiments to determine the effects of pressure pulse frequency and cylinder diameter on the performance of pressure screen rotors.
7. Numerically investigate the hydrodynamics of in-flow pressure screen rotors and determine the optimal MEF configuration for in-flow screens.
8. Analytically and experimentally determine factors other than rotor tip speed that govern the power consumption of a pressure screen rotor.

These objectives were addressed through seven individual studies. These seven studies and their goals are as follows:

1.3.1 A Numerical Investigation into the Effectiveness of Multi-Element Pressure Screen Rotor Foils

Previous studies found that increasing the camber and angle-of-attack increased the magnitude of the negative pressure pulse and lowered the magnitude of the positive pressure pulse generated by the rotor. Beyond a certain angle-of-attack, the foil would stall, however, and the pressure pulse would diminish in strength. Additionally, heavily cambered foils would stall at much lower angles-of-attack. This study investigates, using computational fluid dynamics, the use of multi-element foils (MEFs) to pressure to delay

stall and increase the performance of pressure screen foil rotors. The effects of varying the angle-of-attack, flap angle, trailing edge geometry of the main foil, and the positioning of the flap with respect to the main foil are studied in order to optimize the shape of the pressure pulse generated by the rotor at the cylinder wall. Additional details of the numerical model used in this study are included in Appendix A.

1.3.2 Experimental Measurement of Pressure Pulses from a Pulp Screen Rotor

The pressure pulses generated by the multi-element foil developed in Chapter 2 and a single-element foil are measured experimentally in a laboratory pressure screen. The effect of varying the MEF angle-of-attack, flap angle, and slot velocity on the pressure pulses are investigated in order to determine the effect of flow rates on the pressure pulses and the optimal foil configuration. Additionally, the experimental results are compared to the CFD results in order to determine the validity of the numerical model.

1.3.3 High Performance Multi-Element Foil (MEF) Pulp Screen Rotor - Pilot and Mill Trials

The effect of varying the geometry of the MEF rotor on pressure screen performance is evaluated in a pilot plant study using a PSV 2100 pressure screen. The effects of varying the MEF angle-of-attack and flap angle on the screen capacity, power consumption and thickening are studied. Preliminary power consumption data from a full scale MEF mill trial is also presented, which is discussed in detail in Chapter 5, and preliminary findings on the effects of pulse frequency are shown, which are discussed in detail in Chapter 6.

1.3.4 High Performance Foil Rotor Improves De-Ink Pulp Screening

In this study, the performance of the MEF is evaluated in a full scale de-ink mill trial. This is the final study in the development of the MEF rotor: a numerical optimization study, laboratory trials, pilot plant trials, and now a full scale mill trial. The MEF was run in parallel and compared to a single-element foil rotor representing the current state of the art. In the study, the power consumption, thickening, sticky removal efficiency,

and the overall runnability of the screen running the MEF is compared to that running the OEM rotor.

1.3.5 Effect of Pulse Frequency and Cylinder Diameter on Pressure Screen Rotor Performance

Researchers have implied that increasing the frequency of the pressure pulses by the rotor increases the capacity of the screen, but there have not been any significant studies on the topic. Also, industrial pressure screens vary greatly in diameter, but the foil size is not scaled with diameter and the effect of varying diameter on foil performance is not well understood. This study uses CFD to investigate the effects of varying the frequency of the pressure pulses on foil performance by changing the number of foils on the rotor. By isolating the effect of diameter on the pressure pulse frequency, the effect of varying the diameter of the screen cylinder on foil performance was also studied. Finally, the numerical results for varying pulse frequency are compared to pilot plant results for a two-foil and three-foil rotor.

1.3.6 A Numerical Study of Multi-Element Pressure Screen Rotor Foils with In-Flow Cylinders

There are no substantial studies of in-flow pressure screen rotors, with the bulk of the literature focusing solely on out-flow screens. This study therefore investigates, using computational fluid dynamics, the hydrodynamics of foil rotors in in-flow pressure screens. An optimization of the MEF with an in-flow cylinder was also conducted, allowing for comparisons to be made to the results found in Chapter 2.

1.3.7 Influence of Cylinder Design and Other Factors on Capacity and Power Consumption in a Pressure Screen

In this study, factors effecting pressure screen power consumption other than rotor design are investigated analytically and experimentally. The effect of varying the contour

designs of slotted cylinders on power consumption and capacity is investigated experimentally using a laboratory pressure screen. Additionally, a power equation is developed using an angular momentum balance in order to determine the effects of flow rate, feed chamber design, and other factors on the screen power consumption. Finally, the power equation developed is compared to experimental results. Additional details of the analysis in this chapter are included in Appendix B.

1.4 References

1. Olson, J.A., "Fibre length fractionation caused by pulp screening, slotted screen plates", *J. Pulp Paper Sci.*, 27(8): 255-261, 2001.
2. Feng, M., "Numerical Simulation of the pressure pulses generated by a pressure screen foil rotor", M.A.Sc. Thesis, Dept. Mech. Eng., Univ. British Columbia, 2003.
3. Feng, M., Olson, J.A., Ollivier-Gooch, C.F., Xia, J., and Gooding, R.W., A computational fluid dynamic (CFD) tool for advanced pulp screen foil rotor design", ABTCP Conf., Sau Paulo, Brazil, Oct. 2003.
4. Feng, M., Gonzalez, J., Olson, J.A., Ollivier-Gooch, C., Gooding, R.W., "Numerical simulation and experimental measurement of pressure pulses produced by a pulp screen foil rotor", *J. Fluids Eng.*, 127(3): 347-357, 2005.
5. Gonzales, J., "Characterization of design parameters for a free foil rotor in a pressure screen", M.A.Sc. Thesis, Dept. Mech. Eng., Univ. British Columbia, 2002.
6. Pflueger, C.D., Olson, J.A., and Gooding, R.W., "The performance of the EP Rotor in de-ink pulp screening", Preprints 2007 Appita Conf.
7. Niinimaki, J., "Phenomena affecting the efficiency of a pressure screen", 1999 Tappi Pulping Conf., 957-966.
8. Julien Saint Amand, F., and Perrin, B., "Fundamentals of screening: Effect of rotor design and fibre properties", 1999 Tappi Pulping Conf., 941-955.
9. Julien Saint Amand, F., and Perrin, B., "Basic parameters affecting screening efficiency and fibre loss", 2000 PTS-CTP Deinking Symposium, 26.1–26.22.
10. Wakelin, R.F., Blackwell, B.G., and Corson, S.R., "The influence of equipment and process variables on mechanical pulp fractionation in pressure screens", 1994 Appita Conf., 611-621.
11. Wakelin, R.F., and Corson, S.R., "TMP long fractionation with pressure screens", 1995 Int. Mech. Pulping Conf., 257-265.
12. Wakelin, R.F., and Corson, S.R., "Reject thickening behavior of TMP screening", *Pulp Paper Can.*, 99(1): 27-30, 1998.
13. Yu, C.J., "Pulsation measurement in a screen. Part I: Pulse signature and magnitude of S-shape rotor", 1994 Tappi Engineering Conf., 767-782.

14. Atkins, M., "Axial variations and entry effects in a pressure screen", Ph. D. Thesis, Dept. of Eng., Univ. of Waikato, 2007.
15. Delfel, S., Ollivier-Gooch, C., and Olson, J., "A numerical investigation into the effectiveness of multi-element pressure screen rotor foils", *J. Fluid Eng.*, 131(1): 011101-1, 2009.
16. Hamelin, M., Delfel, S., Olson, J., and Ollivier-Gooch, C., "High performance multi-element foil (MEF) pulp screen rotor – pilot and mill trials", 2009 Paptac Conf. preprints.
17. Levis, S., "Screening of secondary fibers", *Progress in Paper Recycling*, 1(1): 31-45, 1991.
18. Kerekes, R.J., "Pulp flocculation in decaying turbulence: A literature review", *J. Pulp and Paper Sci.*, 9(3): TR86-91, 1983.
19. Jokinen, O., and Edeling, K., "Flocculation tendency of papermaking fibres", *Paperi ja Puu*, 67(5): 317-325, 1985.
20. Kerekes, R.J., Soszynski, R.M., and Tam Doo, P.A., "The flocculation of pulp fibres", *Trans. 8th Fund. Res. Symp.*, Oxford, 265-310, 1985.
21. Kerekes, R.J., and Schell, C.J., "Characterization of fibre flocculation regimes by a crowding factor", *J. Pulp paper Sci.*, 18(1): J32-J38, 1992.
22. Kerekes, R.J., and Schell, C.J., "Effects of fiber length and coarseness on pulp flocculation", *Tappi J.*, 78(2): 133-139, 1995.
23. Dodson, C.T.J., "Fiber crowding, fiber contacts, and fiber flocculation", *Tappi J.*, 79(9): 211-216, 1996.
24. Soszynski, R.M., "The formation and properties of coherent flocs in fibre suspensions", Ph. D. Thesis, Univ. of British Columbia, 1987.
25. Soszynski, R.M., and Kerekes, R.J., "Elastic interlocking of nylon fibers suspended in liquid, part 1: Nature of cohesion among fibers", *Nord. Pulp Paper Res. J.*, 3(4): 172-179, 1988.
26. Wahren, D., "Fiber network structures in papermaking operations", *Proc. Cutting Edge Conf.*, Inst. Paper Chem., Appleton, WI, USA, p. 112, 1979.
27. Farnood, R.R., Loewen, S.R., and Dodson, C.T.J., "Estimation of intra-floc forces", *Appita J.*, 47(5): 391-395, 1994.

28. Ringner, J., and Rasmuson, A., "Finite element analysis of contact forces in three dimensional, non-bonded fibre networks", *Nord. Pulp Paper Res. J.*, 16(2): 118-124, 2001.
29. Hansson, M.T., and Rasmuson, A., "Finite element analysis of three dimensional fibre networks", *Nord. Pulp Paper Res. J.*, 19(1): 105-111, 2004.
30. Andersson, S.R., and Rasmuson, A., "Dry and wet friction of single pulp and synthetic fibres", *J. Pulp Paper Sci.*, 23(1): J5-10, 1997.
31. Andersson, S.R., Ringner, J., and Rasmuson, A., "The influence of some fibre and solution properties on pulp fibre friction", *J. Pulp Paper Sci.*, 26(2): 67-71, 2000.
32. Mason, S.G., "How I became interested in colloid science", *J. Colloid Interface Sci.*, 71(1): 8-10, 1979.
33. Mason, S.G., "The flocculation of cellulose fibre suspensions", *Pulp Paper Mag. Can.*, 99-104, 1948.
34. Schmid, C., Switzer, L., and Kingenberg, D., "Simulations of fiber flocculation effects of fiber properties and interfiber friction", *J. Rheol.*, 44(4): 781-809, 2000.
35. Jacquelin, G., Prepared contribution, *Trans. 3rd Fund. Res. Symp.*, Cambridge, 299-304, 1966.
36. Kerekes, R.J., "Perspectives on fibre flocculation in papermaking", *Int. Paper Physics Conf., Niagara-on-the-Lake*, p. 23-31, 1995.
37. Kao, S.V., and Mason, S.G., "Dispersion of particles by shear", *Nature*, 253(5493): 619-621, 1975.
38. Switzer, L.H., and Klingenberg, D.J., "Simulations of fiber floc dispersion in linear flow fields", *Nord. Pulp Paper Res. J.*, 18(2): 141-144, 2003.
39. Duffy, G.G., and Norman, B.G., "Fibre flocculation in conical contractions simulating the papermachine flowbox slice", *Int. Symp. Papermachine Headboxes*, Dept. of Chem. Eng., McGill Univ., Montreal, June 3-5, 1979.
40. Kerekes, R.J., "Pulp floc behavior in entry flow to constrictions", *Tappi J.*, (1): 88-91, 1983.
41. Andersson, S.R., Ringner, J., and Rasmuson, A., "The network strength of non-flocculated fibre suspensions", *Nord. Pulp Paper Res. J.*, 14(1): 61-70, 1999.
42. Duffy, G.G., "The importance of mechanistic-based models in fibre suspension flow", *54th Appita Conf., Melbourne*, Vol. 1, p. 337-342, 2000.

43. Gullichsen, J., and Harkonen, E., "Medium consistency technology, 1: Fundamental data", *Tappi J.*, 64(6): 69-116, 1981.
44. Bennington, C.P.J., Kerekes, R.J., and Grace, J.R., "The yield stress of fibre suspensions", *Can. J. Chem Eng.*, 68(5): 748-757, 1990.
45. Bennington, C.P.J., Azevedo, G., John, D.A., Birt, S.M., and Wolgast, B.H., "The yield stress of medium- and high- consistency mechanical pulp fibre suspensions at high gas contents", *J. Pulp Paper Sci.*, 21(4): J111-118, 1995
46. Wikstrom, T., and Rasmuson, A., "Yield stress of pulp suspensions: the influence of fibre properties and processing conditions", *Nord. Pulp Paper Res. J.*, 13(3): 243-250, 1998.
47. Dalpke, B., and Kerekes, R.J., "The influence of fibre properties on the apparent yield stress of flocculated fibre suspensions", *J. Pulp Paper Sci.*, 31(1): 39-43, 2005.
48. Switzer, L.H., and Klingenberg, D.J., "Rheology of sheared flexible fiber suspensions via fiber-level simulations", *J. Rheol.*, 47(3): 759-778, 2003.
49. Chen, B., Tatsumi, D., and Matsumoto, T., "Floc structure and flow properties of pulp fiber suspensions", *J. Rheol.* 30(1): 19-25, 2002.
50. Milliken, W.J., Gottlieb, M., Graham, A.L., Mondy, L.A., and Powell, R.L., "The viscosity-volume fraction relation for suspensions of rod-like particles by falling-ball rheometry", *J. Fluid Mech.*, 202: 217-232, 1989.
51. Bennington, C.P.J., and Kerekes, R.J., "Power requirements for pulp suspension fluidization", *Tappi J.*, 79(2): 253-258, 1996.
52. Kerekes, R.J., "Rheology of fibre suspensions in papermaking: An overview of recent research", *Nord. Pulp Paper Res. J.*, 21(5): 598-612, 2006.
53. Wikstrom, T., Ronnmark, Y., and Rasmuson, A., "A new correlation for the onset of fluidization in pulp suspensions", *Nord. Pulp Paper Res. J.*, 17(4): 374-381, 2002.
54. Robertson, A.A, and Mason, S.G., "The flow characteristics of dilute fibre suspensions", *Tappi J.*, 40(50): 326-335, 1957.
55. Duffy, G.G., Moller, K., Lee, P.F.W., and Milne, S.W.A., "Design correlations for groundwood pulps and the effects of minor variables on pulp suspension flow", 27th Appita Conf., Rotorua, 327-333, 1974.

56. Duffy, G.G., Titchener, A.L., Lee, P.F.W., and Moller, K., "The mechanisms of flow of pulp suspensions in pipes", *Appita J.*, 29(5): 363-370, 1976.
57. Duffy, G.G., "High-consistency flow of pulp suspensions in pipes", *Tappi J.*, 61(8): 85-88, 1976.
58. Duffy, G.G., "A review and evaluation of design methods for calculating friction loss in stock piping systems", *Tappi J.*, 59(8): 124-127, 1976.
59. Duffy, G.G., "Flow models and pipeline design equations for fibre suspension flow", 1st Nat. Conf. on Rheology, Melbourne, 61-65, 1979.
60. Duffy, G.G., "Flow of medium consistency wood pulp fibre suspensions", *Appita J.*, 48(1): 51-55, 1995.
61. Duffy, G.G., and Lee, P.F.W., "Drag reduction in the turbulent flow of wood pulp suspensions", *Appita J.*, 31(4): 280-286, 1978.
62. Duffy, G.G., and Abdullah, L., "Flow of fibre suspensions in small diameter pipes", 56th Appita Conf., Rotorua, 127-133, 2002.
63. Duffy, G.G., and Abdullah, L., "Fibre suspension flow in small diameter pipes", *Appita J.*, 56(4): 290-295, 2003.
64. Rienecker, R., "Screening of recovered paper stock for the production of graphic papers", *Voith Paper Twogether*, 10: 12-16, 2000
65. Julien Saint Amand, F., and Perrin, B., "Screening: Experimental approach and modeling", *Tappi Pulping Conf. Proc.*, Montreal, 1019-1031, 1998.
66. Gooding, R.W., "The passage of fibres through slots in pulp screening", M.A.Sc. thesis, University of British Columbia, Canada, 1986.
67. Gooding, R.W., and Kerekes, R.J., "Derivation of performance equations for solid-solid screens", *Can. J. of Chem. Eng.*, 67(5): 801-805, 1989.
68. Kumar, A., Gooding, R.W., and Kerekes, R.J., "Factors controlling the passage of fibres through slots", *Tappi J.*, 81(5): 247-254, 1998.
69. Yu, C.J., and Defoe, R.J., "Fundamental study of screening hydraulics Part 1: Flow patterns at the feed-side surface of screen baskets; mechanisms of fiber-mat formation and remixing", *Tappi J.*, 77(8): 219-226, 1994.
70. Olson, J.A., "The effect of fibre length on passage through narrow apertures", Ph.D. thesis, University of British Columbia, Canada, 1996.

71. Martinez, D.M., Gooding, R.W., and Roberts, N., "A force balance model of pulp screen capacity", *Tappi J.*, 82(4): 181-187, 1999.
72. Gooding, R.W., "Flow resistance of screen plate apertures", Ph.D. thesis, University of British Columbia, Canada, 1996.
73. Nelson, G.L., "The screening quotient: A better index for screening performance", *Tappi J.*, 64(5): 133-134, 1981.
74. Sloane, M.C., "Kraft pulp processing – pressure screen fractionation", *Appita*, 53(3): 220-226, 2000.
75. Olson, J.A., Roberts, N., Allison, B., and Gooding, R.W., "Fibre length fractionation caused by pulp screening", *J. of Pulp and Paper Sci.*, 24(12): 393-397, 1998.
76. Gooding, R.W., and Kerekes, R.J., "Consistency changes caused by pulp screening", *Tappi J.*, 75(11): 109-118, 1992.
77. Kumar, A., "Passage of fibres through screen apertures", Ph.D. thesis, University of British Columbia, Canada, 1991.
78. Olson, J.A., and Wherrett, G., "A model of fractionation by slotted screen apertures", *J. of Pulp and Paper Sci.*, 24(12): 398-403, 1998.
79. Olson, J.A., Allison, B.J., and Roberts, N., "Fibre length fractionation caused by pulp screening, smooth-hole screen plates", *J. of Pulp and Paper Sci.*, 26(1): 12-16, 2000.
80. Mokamati, S., "Effect of aperture geometry on the steady flow through the narrow apertures in a pulp screen: Numerical and experimental study", Ph.D. thesis, University of British Columbia, 2007.
81. Wakelin, R.F., and Corson, S.R., "TMP long fibre fractionation with pressure screens", *Pulp and Paper Can.*, 98(12): 179-182, 1997.
82. Hooper, A.W., "Screening of mechanical pulp – effect of control parameters and screen operation on pulp quality", *Pulp and Paper Manufacture Vol. 2 Mechanical Pulping*, Tappi, Atlanta, 1987.
83. Ahnger, A., and Hautala, J., "Stock fractionation and purity control on processing of recycled-fiber-based stock", 48th Appita General Conf. Proc., Carlton, 387-394, 1994.
84. Gooding, R.W., and Craig, D.F., "The effect of slot spacing on pulp screen capacity", *Tappi J.*, 75(2): 12-16, 1992.

85. Halonen, L., Ljokkoi, R., and Peltonen, K., "Improved screening concepts", Tappi Pulping Conf. Proc., Seattle, 61-66, 1989.
86. Frejborg, F., "Profiled screens remove stickies, cut rejects, plugs, fractionation, wear", Pulp and Paper, 60(3): 83-85, 1986.
87. Frejborg, F., "Profiled screens improve TMP system efficiency and increase pulp quality", Pulp and Paper, 61(6): 90-101, 1987.
88. Dong, S., "Modeling fiber motion in pulp and paper equipment", Ph.D. thesis, University of British Columbia, Canada, 2002.
89. Frejborg, F., and Giambrone, J., "Improvement of new and old screens in cleaning efficiency at maintained or increased capacity", Tappi Pulping Conf. Proc., 529-532, 1989.
90. Halonen, L., Ljokkoi, R., and Peltonen, K., "Improved screening concepts", Tappi Conf. Proc., 207-212, 1990.
91. Niinimäki, J., Dahl, O., Kuopanportti, H., and Ammala, A., "The effect of screen surface properties on pressure screening – the selection of expedient screen basket for GW application", Papeeri ja Puu, 80(8): 601-605, 1998.
92. Gooding, R.W., Olson, J.A., and Roberts, N., "Parameters for assessing fibre fractionation and their application to screen rotor effects", Int. Mech. Pulping Conf. Proc., Helsinki, 2001.
93. Bennington, C.P.J., Kerekes, R.J., and Grace, J.R., "Motion of pulp fibre suspensions in rotary devices", Can. J. of Chem. Eng., 69(1): 251-258, 1991.
94. Rienecker, R., "Spectro screen D – A new concept for effective screening within the stock consistency range of approx. 3%", Voith Paper Together, 1992.
95. Niinimäki, J., "On the fundamentals of pressure screening", Ph.D. thesis, University of Oulu, Finland, 1998.
96. Weeds, Z., "Pressure screening studies with wood pulp", Ph.D. thesis, University of Waikato, New Zealand, 2006.
97. Olson, J.A., Turcotte, S., Gooding, R.W., "Determination of power requirements for solid core pulp screen rotors", Nordic Pulp Paper Res. J., 19(2): 213-217, 2004.
98. Pinon, V., Gooding, R.W., Olson, J.A., "Measurements of pressure pulses from a solid core screen rotor", Tappi J., 2(10): 9-12, 2003.

99. Karvinen, R., and Halonen, L., "The effect of various factors on pressure pulsation of a screen", *Paperi ja Puu*, 2: 80-83, 1984.
100. Wikstrom, T., and Fredriksson, B., "Hydrodynamics in a pressure screen – consequences on the separation process", 5th Research Forum on Recycling, 197-202, 1999.
101. Anderson, J.D., "Fundamentals of Aerodynamics", 2nd ed., McGraw-Hill, Inc., 1991.
102. Abbot, I.H., and Von Doenhoff, A.E., "Theory of Wing Sections", McGraw-Hill Book Company, 1949.
103. Katz, J., "Aerodynamics of race cars", *Annu. Rev. Fluid Mech.*, 38: 27-63, 2006.
104. Zerihan, J., and Zhang, X., "Aerodynamics of a single element wing in ground effect", *J. Aircraft*, 37(6): 1058-1064, 2000.
105. Zhang, X., and Zerihan, J., "Aerodynamics of a double element wing in ground effect", *AIAA J.*, 41(6): 1007-1016, 2003.
106. Mahon, S., and Zhang, X., "Computational analysis of pressure and wake characteristics of an aerofoil in ground effect", *J. Fluids Eng.*, 127(3): 290-298, 2005.
107. Katz, J., and Garcia, D., "Aerodynamics effects of Indy car components" *SAE J. Passenger Cars: Mech. Syst.*, SAE 2001-01-3311, 2322-2330, 2002.
108. Mahon, S., and Zhang, X., "Computation analysis of a inverted double-element airfoil in ground effect", *J. Fluids Eng.*, 128(6): 1172-1181, 2006.

Chapter 2

A Numerical Investigation into the Effectiveness of Multi-Element Pressure Screen Rotor Foils¹

2.1 Introduction

As the most industrial efficient and effective way to remove shives and contaminants from a pulp stream, pressure screens are used in paper making worldwide. Screening has a positive effect on the overall quality of the paper, including its strength, appearance and optical qualities. Additionally, modern screens are used to separate the fibres in the pulp by length and flexibility (known as “fractionating” the pulp), allowing for long and short fibres to be processed separately and for the production of high value paper. The ability to efficiently filter and fractionate pulp is making pressure screens increasingly important to both mechanical and chemical pulping processes.

A pressure screen is comprised of two major elements, the rotor and the screen cylinder, and it splits a contaminated feed stream into accept and reject streams. The feed stream typically enters the screen tangentially and is passed between the rotor and the screen cylinder. A pressure drop across the screen cylinder allows for sufficiently small particles to pass through small apertures (either slots or holes) in the screen cylinder and on into the accept stream. Oversized particles and the fraction of long fibres that are retained by the screen cylinder continue down the length of the screen and leave via the reject stream.

This work is focused upon the performance of the rotor, which has two main functions within the screen. First, it provides a high tangential velocity to the flow, inducing turbulence at the screen plate that helps keep the pulp fluidized. Second, and more

¹ A version of this chapter has been published. Delfel, S., Ollvier-Gooch, C., Olson, J., “A numerical investigation into the effectiveness of multi-element pressure screen rotor foils”, J. of Fluids Eng., 131(1), 011101-1, 2009.

importantly, as the foil passes along the feed side of the screen cylinder it generates a negative pressure pulse that backflushes the apertures, clearing any debris from the apertures that would cause them to plug. This action has a dramatic affect on screen performance, typically measured by three parameters -- the fractionation or contamination removal efficiency of the screen; the capacity of the screen, defined as the amount of pulp in the accept stream; and the power consumption of the screen. An ideal screen would maximize efficiency and capacity, and at the same time minimize power consumption.

There are two general types of rotors used in screens: solid core and foil rotors. Foil rotors are similar to the airfoils used on the wings of aircraft and allow the flow to circulate around the foil and are typically used in low consistency, fine screening. Solid core rotors, on the other hand, consist of elements attached to the outer surface of an inner drum core, and allow the flow to only pass over the outer surface of the element. Solid core rotors are usually used earlier in the screening process for higher consistency screening, while foil rotors are used later in the process for fine screening and fractionation. This work will focus on the performance of foil rotors.

In a previous study, Olson, Turcotte and Gooding found experimentally that the non-dimensional power coefficient is independent of Reynolds number, with power coefficient defined as

$$C_{Power} = \frac{Power}{\rho \cdot V_t^3 \cdot D^2}, \quad (2.1)$$

where *Power* is the power consumption of the rotor, ρ is the fluid density, V_t is the rotor tip speed, and D is the diameter of the rotor [1]. Reynolds number is based on foil chord length and is defined as

$$Re = \frac{\rho V_t c}{\mu}, \quad (2.2)$$

where c is the chord length of the foil and μ is the fluid viscosity. The power consumption of the rotor is therefore proportional to the tip speed of the rotor cubed and a reduction in the rotor velocity would lead to a large reduction in the power required.

Additional studies have shown that increasing the magnitude of the negative pressure pulse generated by the rotor will increase the capacity of the screen, particularly for slotted screen cylinders [2, 3, 4, 5, 6, 7]. Pinon, Gooding and Olson and Gonzales, found that the non-dimensional pressure pulse generated by the rotor is also independent of Reynolds Number, with the non-dimensional pressure defined by the pressure coefficient

$$C_p = \frac{P}{0.5 \cdot \rho \cdot V_t^2}, \quad (2.3)$$

where P is the pressure [8, 9], implying that the magnitude of the pressure pulse generated by the rotor varies quadratically with the rotor velocity. It is desirable to slow the rotor tip speed in order to reduce power consumption, but this will also reduce the magnitude of the pressure pulse. We therefore want to maximize the pulse generated by the foil at a given tip speed. This is the primary goal in pressure screen rotor design.

Gonzales and Feng *et al.* both studied the effect of a wide range of foil variables on the pressure pulse generated by a foil rotor. They observed that the magnitude of the negative pressure pulse for a given foil increased with angle-of-attack to a maximum value, and then decreased at higher angles-of-attack (the exception being the NACA 8312 foil, which had a maximum peak magnitude at 0 deg. angle-of-attack) [9, 10]. Niinimäki made similar observations, showing that increasing foil angle-of-attack improves the capacity of the screen [2]. Additionally, Gonzales and Feng *et al.*, found that the undesirable positive pressure pulse decreased with increasing foil angle-of-attack. They also showed that pressure pulse width and magnitude both increase with increasing foil camber [9, 10].

In order to achieve higher angles-of-attack at lower Reynolds numbers, it is common practice in the aerospace field to use multi-element airfoils. Multi-element foils delay stall on the foil by allowing high energy flow on the lower surface of the foil to pass through the slot between the main foil and the flap, reenergizing the boundary layer on the upper surface of the foil. They also have the added effect of increasing the effective camber of the foil as the flap deflection is increased [11].

Therefore, in an effort to reduce the rotor velocity while maintaining screen performance, the goal of this study is to determine the effectiveness of multi-element pressure screen rotor foils in controlling the magnitude and shape of the negative pressure pulse generated. The effects of varying the major foil geometry parameters was studied using computational fluid dynamics (CFD). Specifically, the effects of the flap angle, the foil angle-of-attack, the main foil trailing edge geometry, and the positioning of the leading edge of the flap were studied. The numerical model is validated using existing experimental data for single-element rotor foils.

2.2 Numerical Method

The FLUENT 6.1 commercial solver was used to numerically solve the discretized Navier-Stokes equations for this study. The problem is assumed to be isothermal, two dimensional, and steady state, allowing the Navier-Stokes equations to be reduced to the continuity and x - and y -momentum equations. The FLUENT solver is a second-order accurate finite volume solver: control volume averages are found for each flow variable and the fluxes at the control volume faces are then found through second-order spatial interpolation from the control volume center. All cases included in this study were solved at steady-state with the SIMPLEC algorithm for pressure-velocity coupling.

Turbulence was modeled using the standard k - ε turbulence model with enhanced wall treatment. The k - ε model solves additional transport equations for turbulent kinetic energy, k , and turbulent dissipation rate, ε , along with the continuity and momentum

equations in order to find closure for the Reynolds stresses. The $k-\varepsilon$ model was selected over other available turbulence models as an adequate balance between accuracy and computational cost and because of a history of its use in screening type problems [10, 12]. Following the results of Mahon and Zhang [12], the enhanced wall treatment for the $k-\varepsilon$ model was included in the simulations. In essence, with the enhanced wall treatment the turbulent quantities are computed directly all the way into the viscous sublayer, with the laminar and turbulent laws-of-the-wall being blended in the near-wall region. While being considerably more expensive computationally, the enhanced wall treatments allowed for substantial improvement in the accuracy of the solution, especially for the pressure field, which is the main focus of this study [13, 14].

2.3 Computational Domain and Mesh Generation

The cross-section of a PSV 2100 pressure screen was modeled as shown in Figure 2.1. In all cases 2-D hybrid structured/unstructured multi-block meshes were used, in Cartesian coordinates. A very fine C-mesh was used around the foils in order to obtain acceptable boundary layer and wake resolution. As required by the $k-\varepsilon$ turbulence model with enhanced wall treatment, the first mesh cell at the foil surface lies at a non-dimensional distance of $y^+ \approx 1$. In order to minimize CPU time, a much coarser structured mesh was used in the far field and an unstructured block was added to smoothly blend the fine C-mesh and the coarse far field meshes. All meshes were generated using Gambit, the commercial pre-processing package for Fluent.

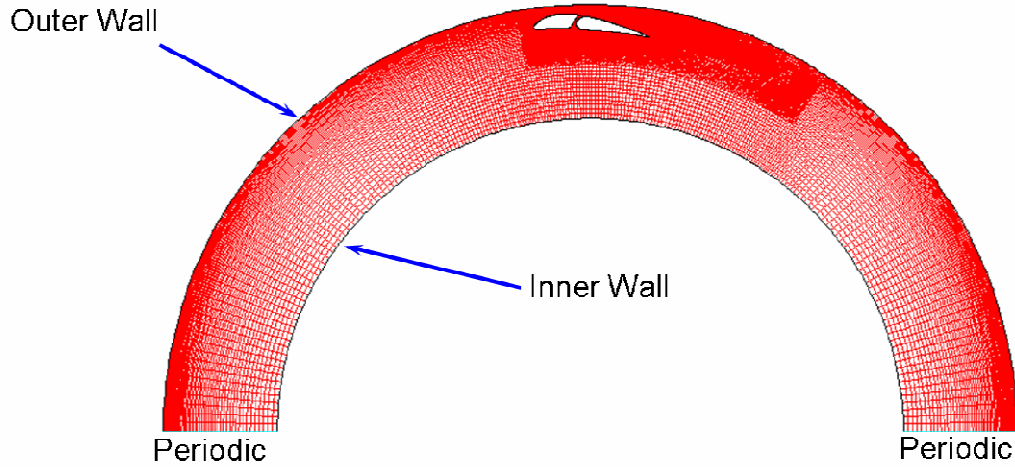


Figure 2.1: Computational domain and a typical mesh.

2.4 Boundary Conditions

The domain is rotationally periodic in order to simulate a two-bladed rotor. The periodicity of the flow ensures that it is turbulent, even though typical Reynolds numbers are on the order of $Re = 10^5$ based on foil chord length, as each foil is operating in the wake of the preceding foil. A rotating computational coordinate system moving at the same speed as the foil is assigned to the center of the cylinder, because the flow is steady when viewed in this frame. The inner and outer cylinder walls and the foil walls are all set with no-slip boundary conditions. The inner cylinder wall and the foil walls are set with zero angular velocity relative to the spinning computational coordinate system. The outer wall, which represents the screen cylinder, is stationary and is therefore set to zero angular velocity in the absolute coordinate system.

The inner cylinder wall has a radius of $r_{inner} = 0.73 * r_{outer}$ and is representative of the core of fluid at the center of the screen moving at the rotor's angular velocity. It is a simplification that greatly reduces computational time by allowing us to remove grid

points outside the area of interest. Feng studied the effect of the inner wall diameter in a simulation of a PSV 2100 and found that below an inner wall radius of $r_{inner} < 0.867 * r_{outer}$, the effect on measured pressure pulse is negligible [15]. The complex flow through the screen cylinder is not considered here (ie. $V_{slot} = 0.0$ m/s), which is equivalent to the critical design case of a plugged screen.

There are a number of other assumptions and simplifications that have been made in the study that should be noted: water at 20°C, rather than pulp, is used in the simulations (consistency is 0.0%), and the flow in the simulations is two-dimensional. Gonzales studied the effect of pulp consistency on the pulse, and found that increasing consistency reduced the magnitude of the pulse, but the shape and trends remained unchanged [9]. Also, pulp consistency during screening is generally very low, on the order of 1-2%, and turbulent pulp suspensions in this range have been found to behave as a Newtonian fluid with the same density and viscosity as water [ibid.]. Using water rather than pulp is therefore reasonable for this design problem. Finally, screen rotor foils typically have aspect ratios of 8 or more with a low relative axial, or spanwise, flow velocity, making the two-dimensional assumption a valid representation of a slice of the foil near mid-span.

2.5 Grid Independence and Model Validation

The experimental data collected by Gonzales [9] and Feng *et al.* [10] for a NACA 8312 foil rotor was used to validate the model. As mentioned previously, in the those studies pressure traces on the screen cylinder were measured for a variety of single-element foils under different operating conditions using the Cross-Sectional Screen (CSS), a laboratory screen which was designed to represent a section of a PSV 2100 pressure screen. For this study, the magnitude of the negative pressure pulse, measured in terms of non-dimensional pressure coefficient, C_P , as defined in equation 2.2, was used to determine both the independence of the solution from the computational grid resolution and the accuracy of the converged solution.

Grid independence studies were conducted for both the single- and multi-element foils used in the study. For the single-element model, five geometrically similar meshes were generated with grid resolutions of 65,000 to 400,000 volumes. The solution was found to be grid independent for meshes larger than 190,000 volumes. For the multi-element model, three geometrically similar grids were studied with grid resolutions between 80,000 volumes and 300,000 volumes. The solution was found to be grid independent for grids larger than 160,000 volumes. By removing excess volumes in the far-field, the grid count for the multi-element model was reduced around 80,000 volumes without effecting grid independence. For the optimized meshes, 58% of the control volumes lie within the foil boundary layer and wake regions of the mesh.

The NACA 8312 was modeled in the PSV 2100 using the numerical model described previously at a Reynolds number of $Re = 5 \times 10^5$, an angle-of-attack of $\alpha = 0$ deg., a chord length of $c = 4$ cm, and a minimum gap between the foil and the screen cylinder of $g = 3$ mm. These numerical results were compared to experimental results for the same foil, in the same configuration, operating in water with no accept flow [9, 10]. Figure 2.2 shows the experimental and numerical pressure traces along the screen cylinder plotted together. The minimum C_p on the screen cylinder for the foil in these operating conditions was found to be $C_p = -0.708$, which matches the experimental data within 5%.

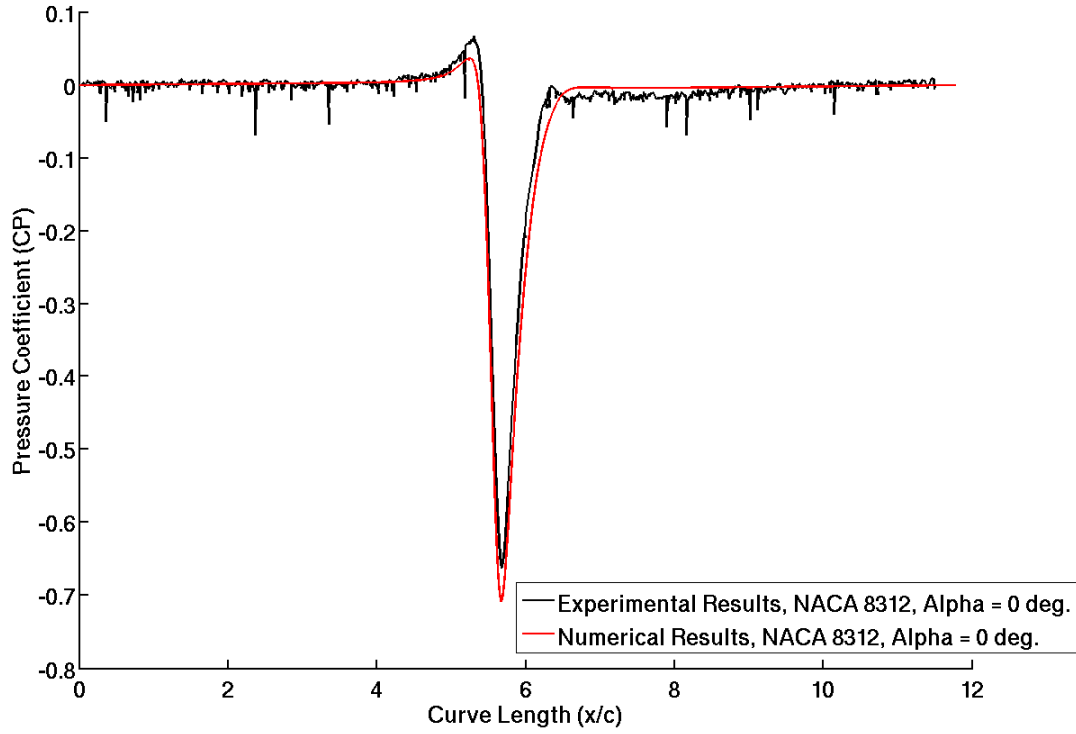


Figure 2.2: Experimental and numerical results for pressure traces on the screen cylinder for a NACA 8312 rotor foil at $Re = 5 \times 10^5$, an angle-of-attack of $\alpha = 0$ deg, a chord of $c = 4$ cm, and a gap of $g = 3$ mm.

2.5 Results and Discussion

A multi-element rotor foil based upon a NACA 8312 foil was studied using the aforementioned numerical techniques. The effect of a number of foil parameters on the pressure pulse generated by the foil was studied, including foil angle-of-attack, main foil trailing edge geometry, flap deflection, and the positioning of the flap relative the main foil. The multi-element foil with these parameters defined is shown in Figure 2.3.

The NACA 8312 was used as the starting point for our multi-element foil since it generated the strongest negative pressure pulse of the foils studied by Feng *et al.* [10]. A

smooth-splined slot was placed in the NACA 8312 to create the multi-element foil, so that the flap chord was 35% of the total foil chord ($c_{flap} = 0.35*c$), as can be seen in Figure 2.3. The upper surface was unchanged from the original NACA 8312's profile, and the length of the spline at the trailing edge of the main foil was defined as the trailing edge lip length, l . The angle between the chord line of the foil with no flap deflection and the horizontal is referred to as the angle-of-attack (α) of the foil, and the angle of between the flap chord line and the undeflected chord is referred to as the flap deflection angle (δ).

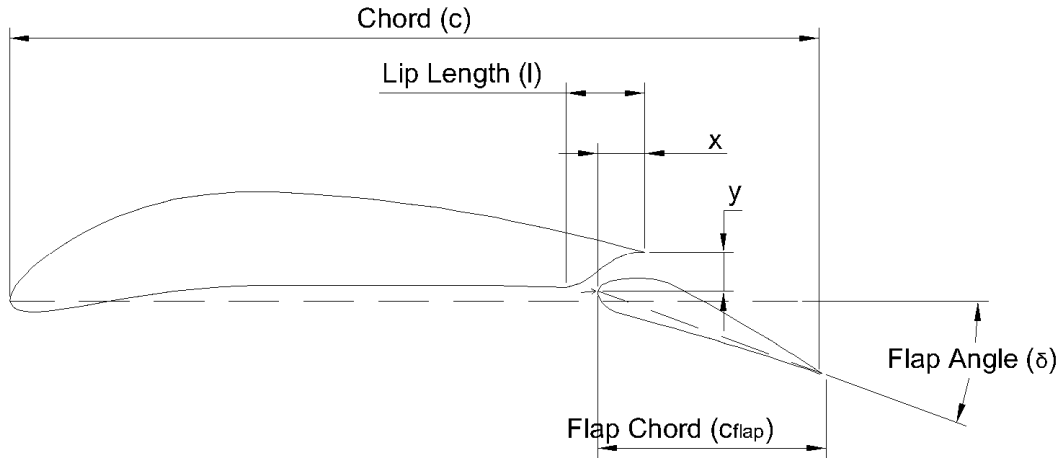


Figure 2.3: Multi-element rotor foil with specific foil parameters defined.

2.5.1 Lip Length

The effect of the main foil trailing edge design is shown in Figure 2.4, which shows pressure contours and streamlines for a multi-element foil with varying lip lengths. There is a small separation bubble at the trailing edge of the main foil for the lip length of $l = 0.25*c$, which is a source of unwanted pressure drag. As can be seen in Figure 2.5, which shows the pressure trace along the screen cylinder for each trailing edge geometry, the lip length has a slight effect on the pressure pulse, with the $l = 0.50*c$ foil having a slightly

wider and stronger negative pulse. Because the $l = 0.50*c$ foil has a slightly stronger pulse and no separation at the lip, this lip length was used for the rest of the study.

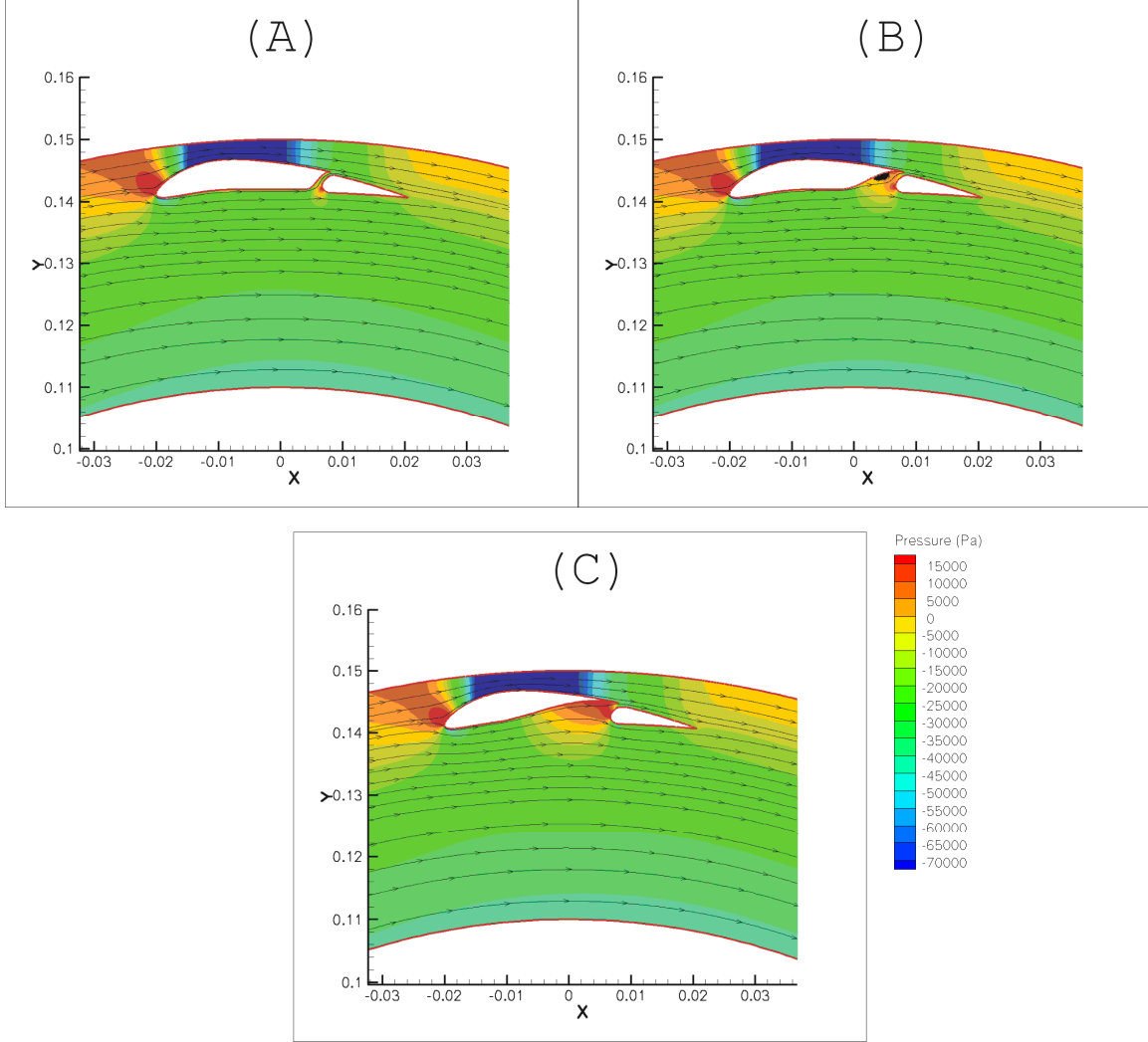


Figure 2.4: Pressure contours and streamlines for a multi-element foil with varying main foil trailing edge lip length: (A) $l = 0.10*c$, (B) $l = 0.25*c$, and (C) $l = 0.50*c$. The foil is at $\alpha = 0$ deg. and the flap is at $\delta = 7$ deg. for all cases. The Reynolds number is $Re = 5 \times 10^5$.

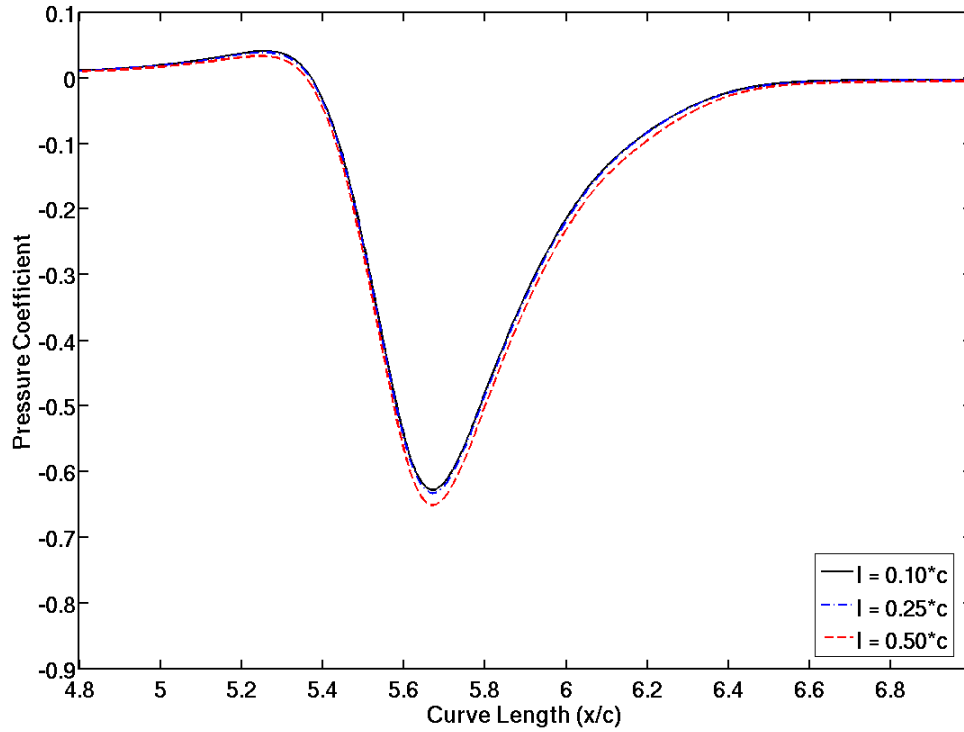


Figure 2.5: Pressure traces on the screen cylinder for a multi-element foil with varying main foil trailing edge lip length l . The foil is at $\alpha = 0$ deg. and the flap is at $\delta = 7$ deg. for all cases. The Reynolds number is $Re = 5 \times 10^5$.

2.5.2 Angle-of-Attack

Figure 2.6 shows pressure contours and streamlines as angle-of-attack is varied for a multi-element foil with no flap deflection. The negative pressure pulse between the upper surface of the foil and the screen cylinder widens until an angle-of-attack of $\alpha = 4$ deg., an improvement over the single-element NACA 8312 which was shown to lose suction strength at any angle-of-attack greater than $\alpha = 0$ deg. for these operating conditions. The multi-element foil is able to delay stall relative to the NACA 8312 by allowing the flow from the lower surface of the foil to pass through the slot and reenergize the boundary layer on the upper surface of the foil. Additionally, as the stagnation point at the leading edge of the foil rotates more towards the lower surface of

the foil with increasing angle-of-attack, the positive pressure pulse emanating from the stagnation point to the screen cylinder dissipates. After $\alpha = 4$ deg., the boundary layer begins to thicken and the negative pressure region starts to shrink. At $\alpha = 10$ deg., the main foil has started to stall and the beginnings of a separation bubble can be seen. The results of this flow separation are a reduction in suction and an increase in pressure drag on the foil, as mentioned previously.

A clearer picture of how angle-of-attack affects the pressure on the screen cylinder due to the foil can be seen in Figures 2.7 and 2.8. Figure 2.7 shows the wall pressure traces for a multi-element foil with constant flap angle at various angles-of-attack, and Figure 8 shows the peak positive and negative pressures on the wall at each angle-of-attack. The peak negative pressure can be seen at $\alpha = 4$ deg. with a value of $C_P = -0.78$. Beyond $\alpha = 4$ deg. the effect of the flow separation can be seen in an increasing loss in peak suction magnitude and pulse width. The reduction in the positive pressure pulse on the wall due to the stagnation point as the angle-of-attack is increased, as mentioned previously, can also be seen. This phenomenon was also observed by Feng *et al.* [10] and is believed to be favorable, as a positive pulse would have the affect of pushing unwanted debris through the screen cylinder and reduce the efficiency of the screen.

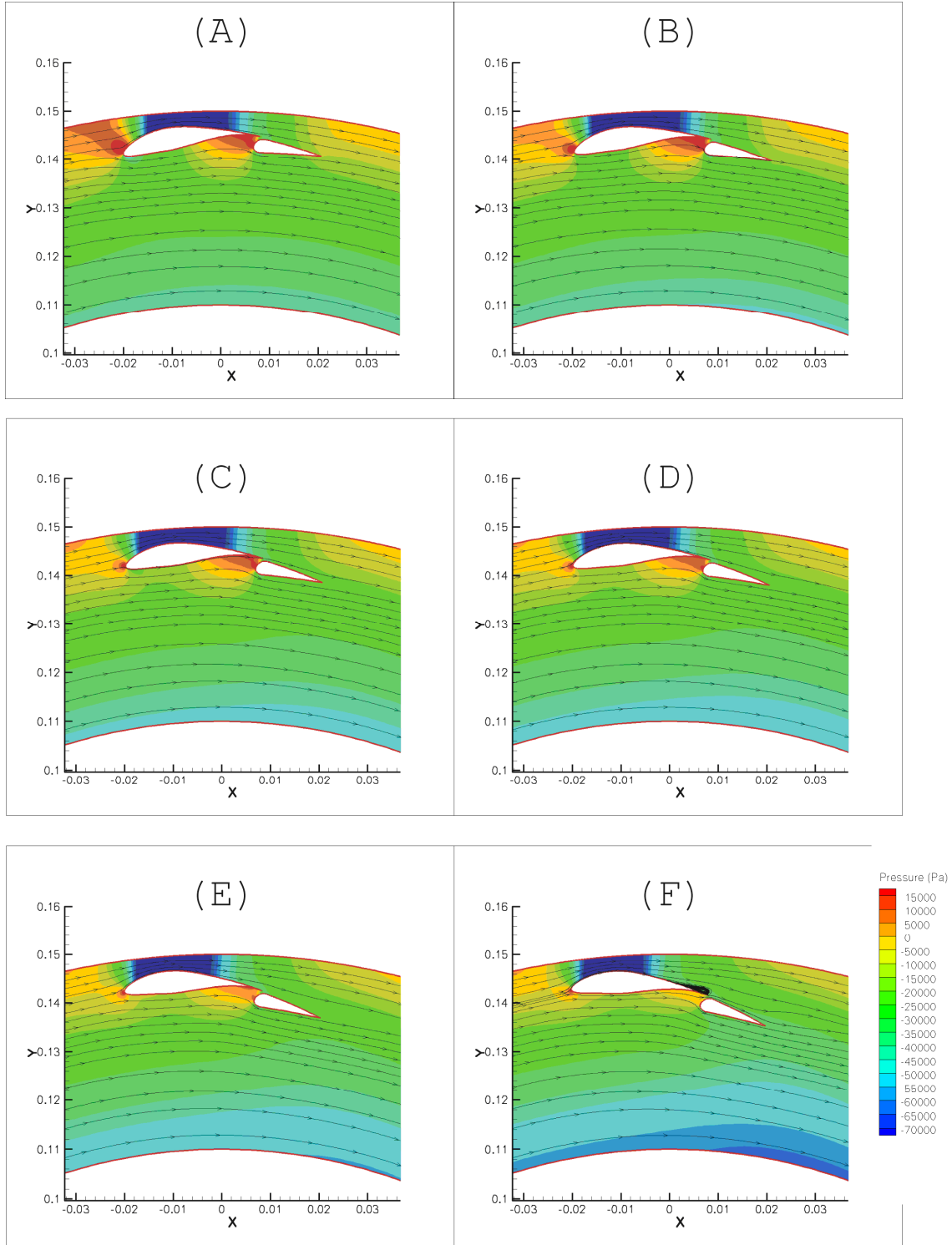


Figure 2.6: Pressure contours and streamlines for a multi-element foil at (A) $\alpha = 0^\circ$, (B) $\alpha = 2^\circ$, (C) $\alpha = 4^\circ$, (D) $\alpha = 5^\circ$, (E) $\alpha = 7^\circ$, and (F) $\alpha = 10^\circ$. The flap is at $\delta = 7^\circ$ and $l = 0.5 \cdot c$ for all cases. The Reynolds number is $Re = 5 \times 10^5$.

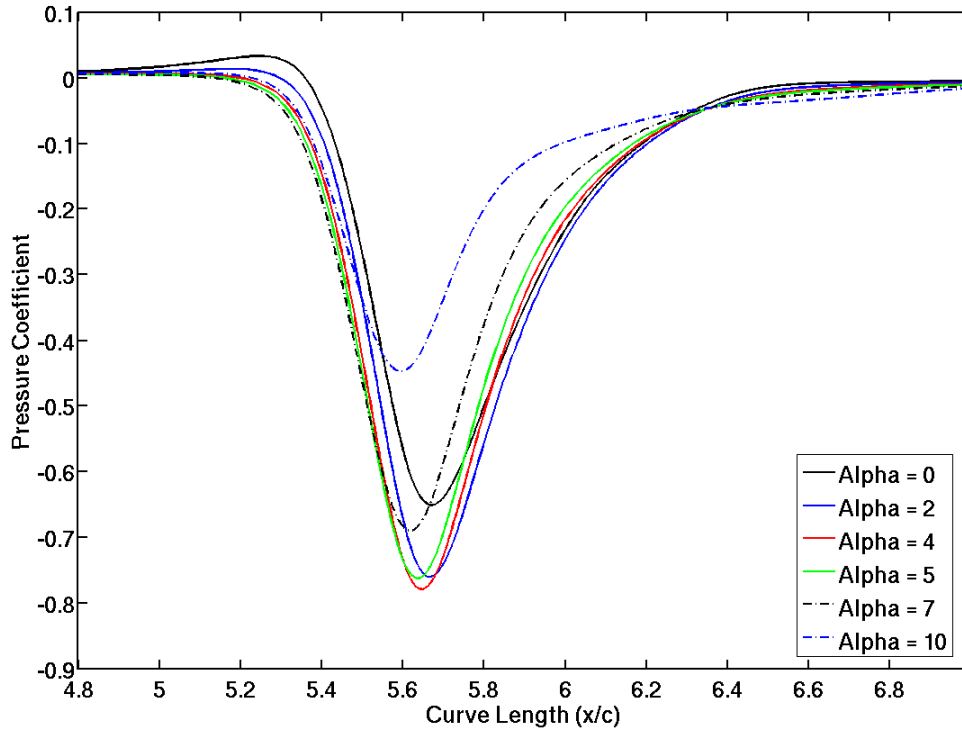


Figure 2.7: Pressure traces on the screen cylinder for a multi-element foil at varying angles-of-attack. The flap is at $\delta = 7$ deg. and $l = 0.5*c$ for all cases. The Reynolds number is $Re = 5 \times 10^5$.

2.5.3 Flap Angle

Figure 2.9 shows pressure contours and streamlines and Figure 2.10 shows the pressure traces on the screen cylinder for a multi-element foil at varying flap angles with a constant angle-of-attack of $\alpha = 0$ deg. As can be seen, deflecting the flap, which is effectively an increase in the camber of the foil, causes the pressure pulse to widen and strengthen until $\delta = 19$ deg., after which the flow over the flap begins to separate and suction at the screen cylinder diminishes. At $\delta = 36$ deg., the flap has stalled fully and the beginnings of vortex shedding can be seen. Interestingly, increasing flap angle also has the affect of forcing the stagnation point towards the lower surface of the leading edge of the foil, diminishing the positive pulse on the screen cylinder.

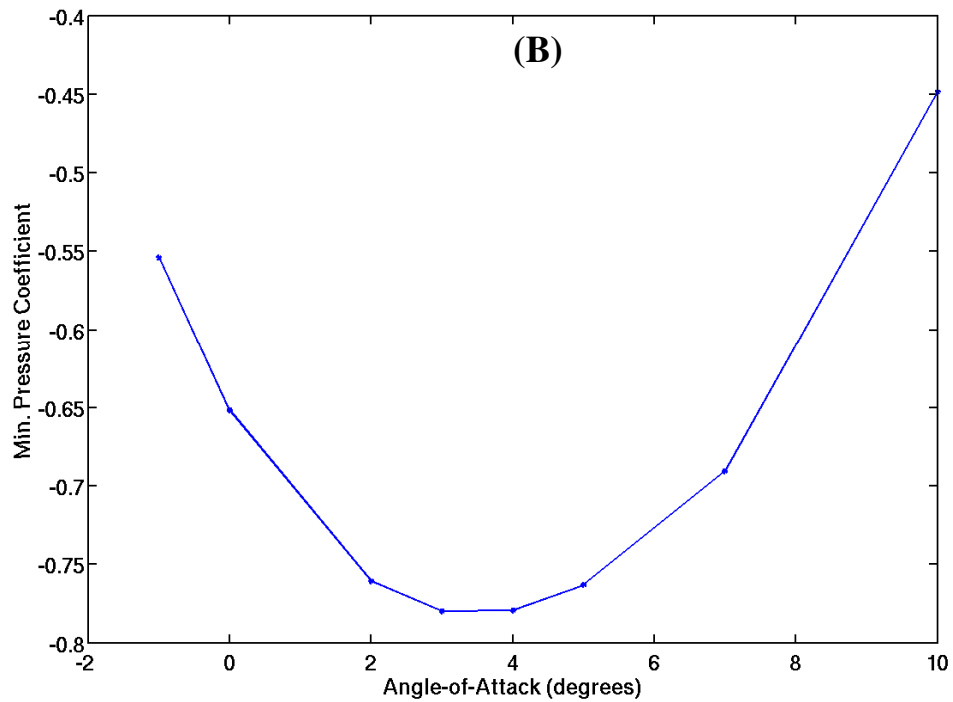
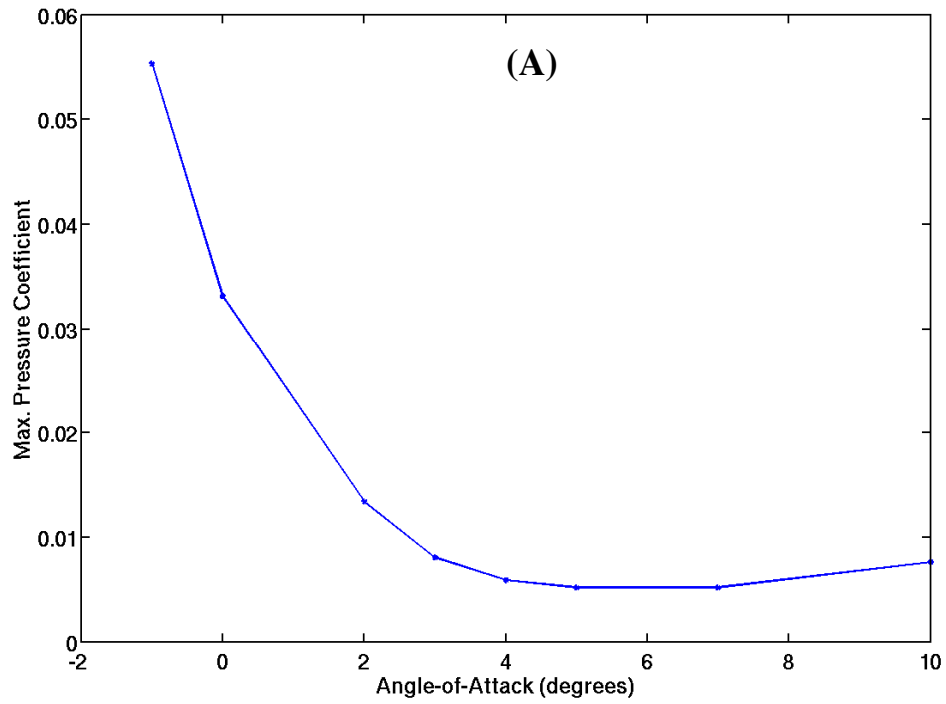


Figure 2.8: (A) Maximum wall pressure coefficient on the screen cylinder and (B) minimum wall pressure coefficient on the screen cylinder vs. foil angle-of-attack. The flap is at $\delta = 7$ deg. and $l = 0.5 \cdot c$ for all cases. The Reynolds number is $Re = 5 \times 10^5$.

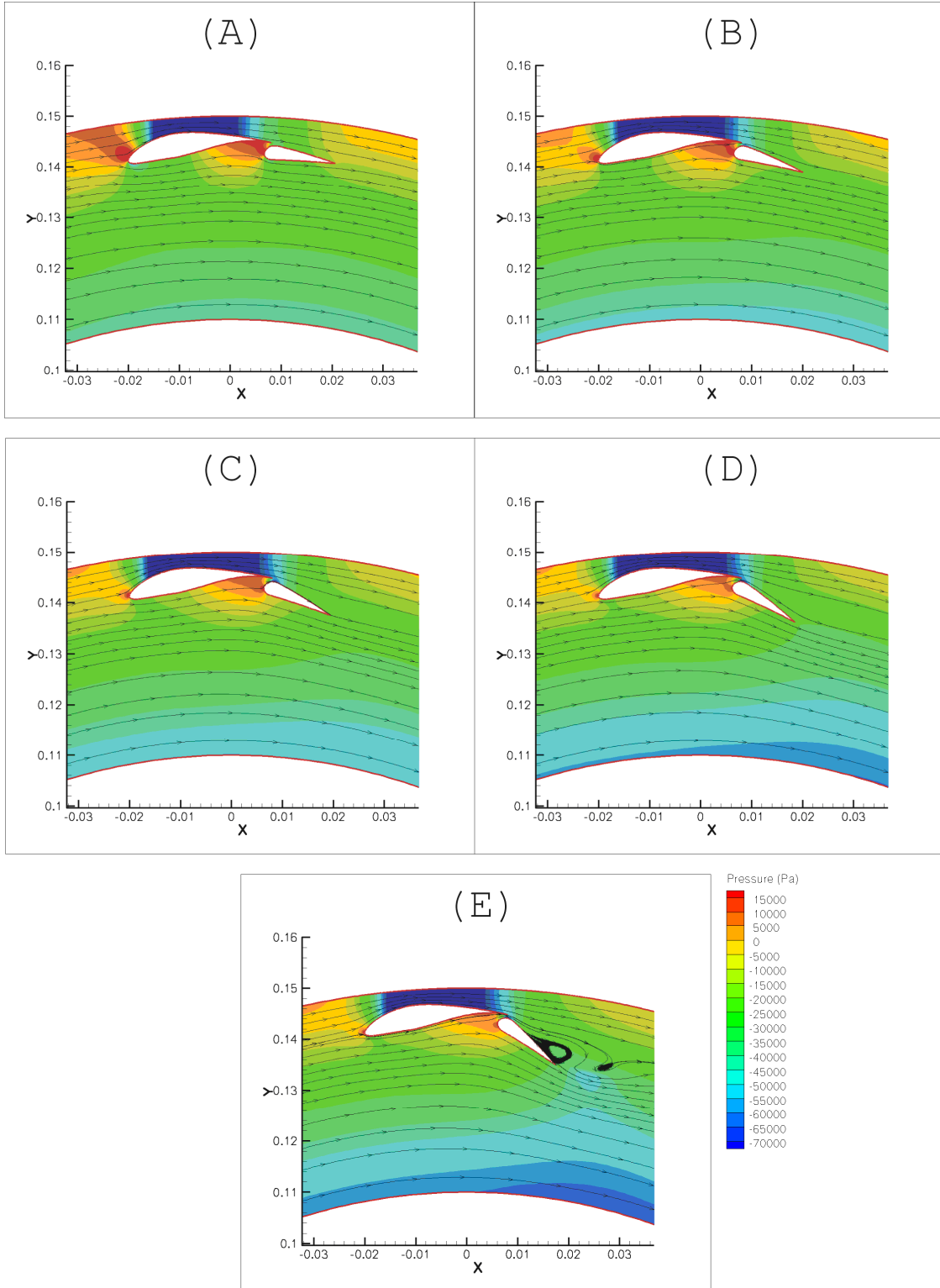


Figure 2.9: Pressure contours and streamlines for a multi-element foil at (A) $\delta = 7$ deg., (B) $\delta = 15$ deg., (C) $\delta = 22$ deg., (D) $\delta = 29$ deg., and (E) $\delta = 36$ deg. The foil is at $\alpha = 7$ deg. and $l = 0.5 \cdot c$ for all cases. The Reynolds number is $Re = 5 \times 10^5$.

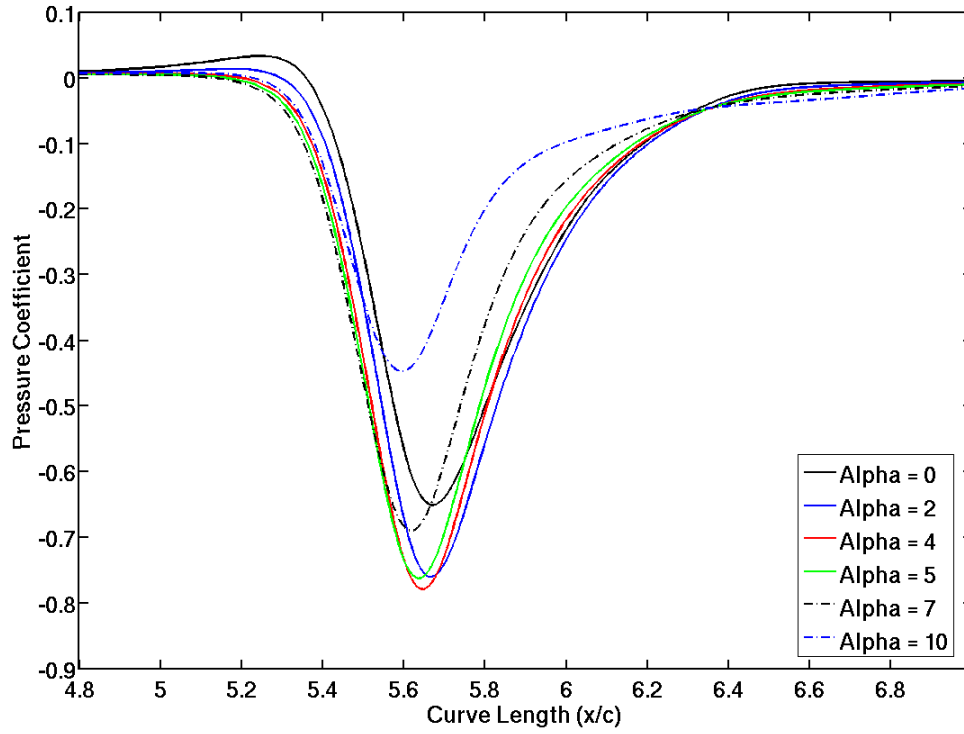


Figure 2.10: Pressure traces on the screen cylinder for a multi-element foil at varying flap angles. The foil is at $\alpha = 0$ deg. and $l = 0.5*c$ for all cases. The Reynolds number is $Re = 5 \times 10^5$.

Figure 2.11 shows the peak positive and negative C_p values on the screen cylinder versus δ for a series of angles-of-attack between $\alpha = -1$ deg. and $\alpha = 3$ deg. Varying the flap angle has a similar effect at each of the angles, with a clear optimum existing for minimum C_p and with maximum C_p approaching a negligible value. At lower angles-of-attack, however, the foil is more resistant to stall and the optimal minimum C_p value occurs at higher values of δ .

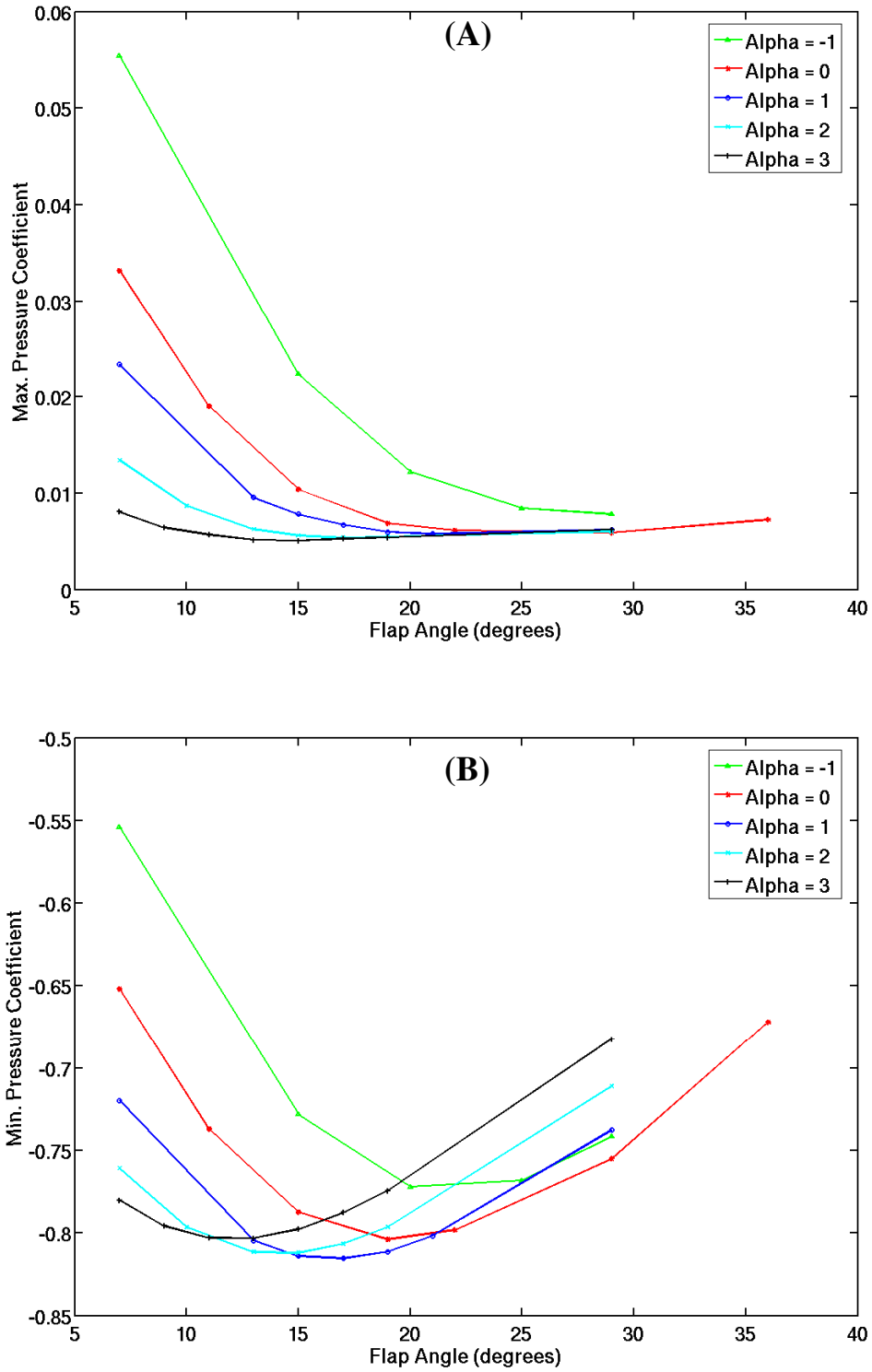


Figure 2.11: (A) Maximum wall pressure coefficient at the screen cylinder and (B) minimum wall pressure coefficient at the screen cylinder vs. flap angle for various angles-of-attack. $l = 0.5 \cdot c$ for all cases. The Reynolds number is $Re = 5 \times 10^5$.

The α - and δ -sweep data was combined to make surfaces of minimum and maximum C_P values versus both α and δ , as shown in Figure 2.12. The surfaces were created from 37 cases using the two dimensional cubic interpolation functions contained in MATLAB [16]. Minimum C_P is shown to have a strong dependence on flap angle for angles-of-attack at which the flow is fully attached, creating a “trough”-like shape with a clear minimum of $C_P = -0.82$ at $(\alpha, \delta) = (1.2, 16)$. The gradients close to the optimum are relatively low, however, allowing for flexibility in the foil design. Beyond $\alpha = 7$ deg., any deflection of the flap causes the foil to stall and the pressure is not dependent on flap angle. Maximum C_P behaves differently and approaches $C_P = 0$ everywhere except at small angles of both α and δ .

2.5.4 Flap Positioning

The effect of the positioning of the flap foil with respect to the main foil was also studied. There is special interest in the effect of flap positioning due to concerns that if the gap between the flap and the main foil is too small, it will become plugged with pulp, shives, or contaminants in the pulp stream. Figures 2.13 and 2.14 show the effect of varying the x - and y -position of the leading edge of the flap, respectively, at an angle-of-attack of $\alpha = 1$ deg. and a flap angle of $\delta = 15$ deg. In both cases the flap leading edge position is measured from the trailing edge of the main foil in percent chord.

As can be seen in Figure 2.13, the x -positioning of the flap has little effect on both the negative and positive pulses except for at $x = 0.0 * c$, where the negative pulse diminishes and the positive pulse increases. Figure 2.14 shows a stronger correlation between the y -position of the flap and both the positive and negative pressure pulses, however. At $y = -0.04 * c$, the gap between the flap and the main foil is too small and not enough fluid is able to pass through the slot, causing the flap to lose its effect. As the gap is increased to too large of a value, the flap and the main foil lose the ability to interact with each other, causing an increase in positive pulse and a loss of suction.

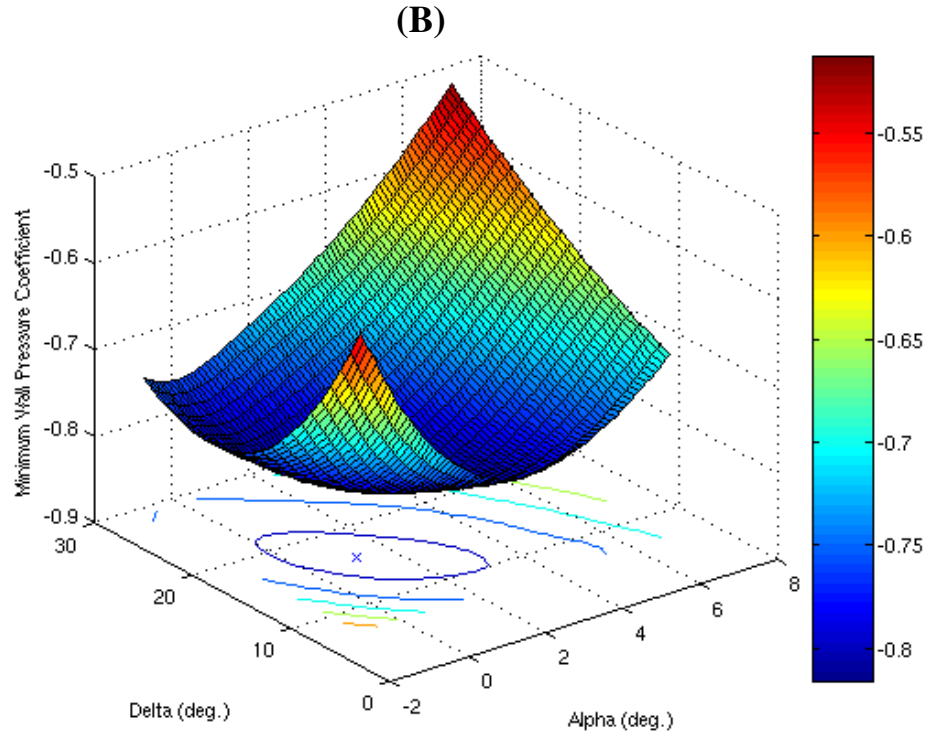
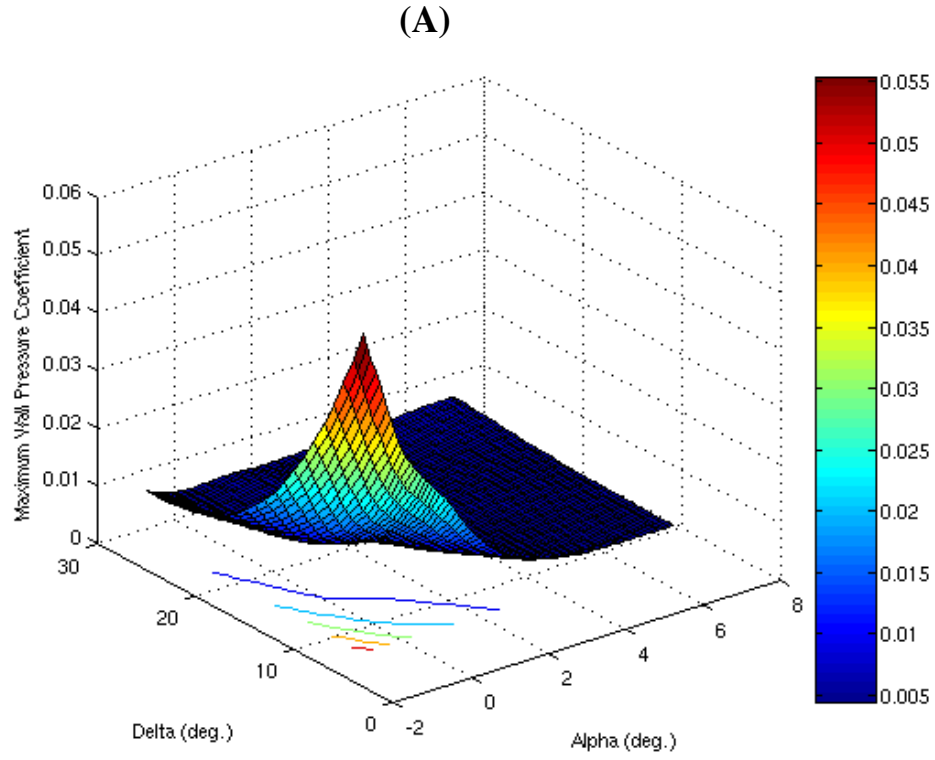


Figure 2.12: Surfaces of (A) maximum wall pressure coefficient and (B) minimum wall pressure coefficient vs. foil angle-of-attack and flap angle. $l = 0.5 \cdot c$ for all cases. The Reynolds number is $Re = 5 \times 10^5$.

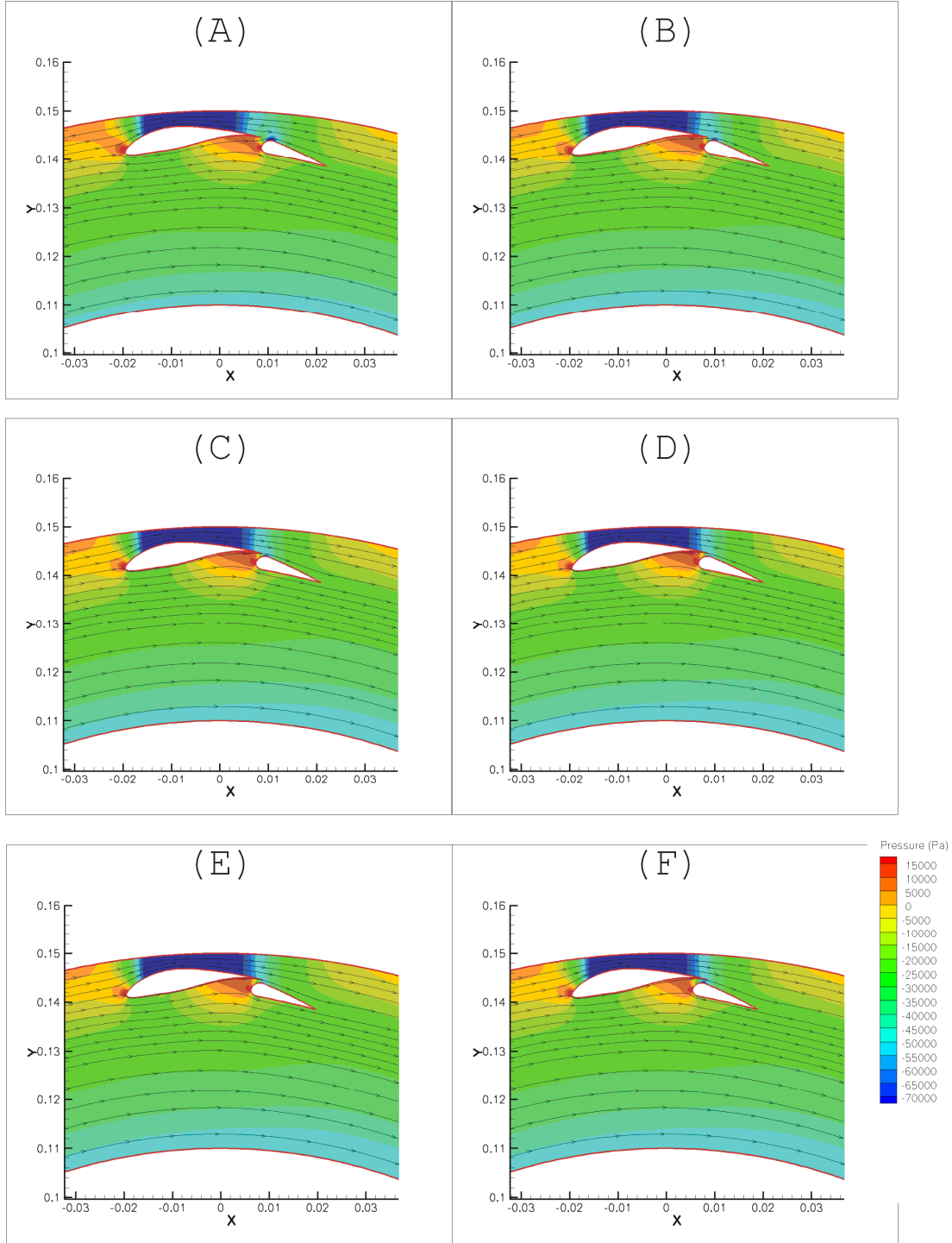


Figure 2.13: Pressure contours and streamlines for a multi-element foil with varying x -positions for the flap leading edge. The flap leading edge is at (A) $x = 0.00 * c$, (B) $x = -0.02 * c$, (C) $x = -0.03 * c$, (D) $x = -0.05 * c$, (E) $x = -0.06 * c$, and (F) $x = -0.08 * c$. In all cases the flap leading edge is at $y = -0.05 * c$, $\alpha = 1 \text{ deg.}$, $\delta = 15 \text{ deg.}$, and $l = 0.5 * c$.

The Reynolds number is $Re = 5 \times 10^5$.

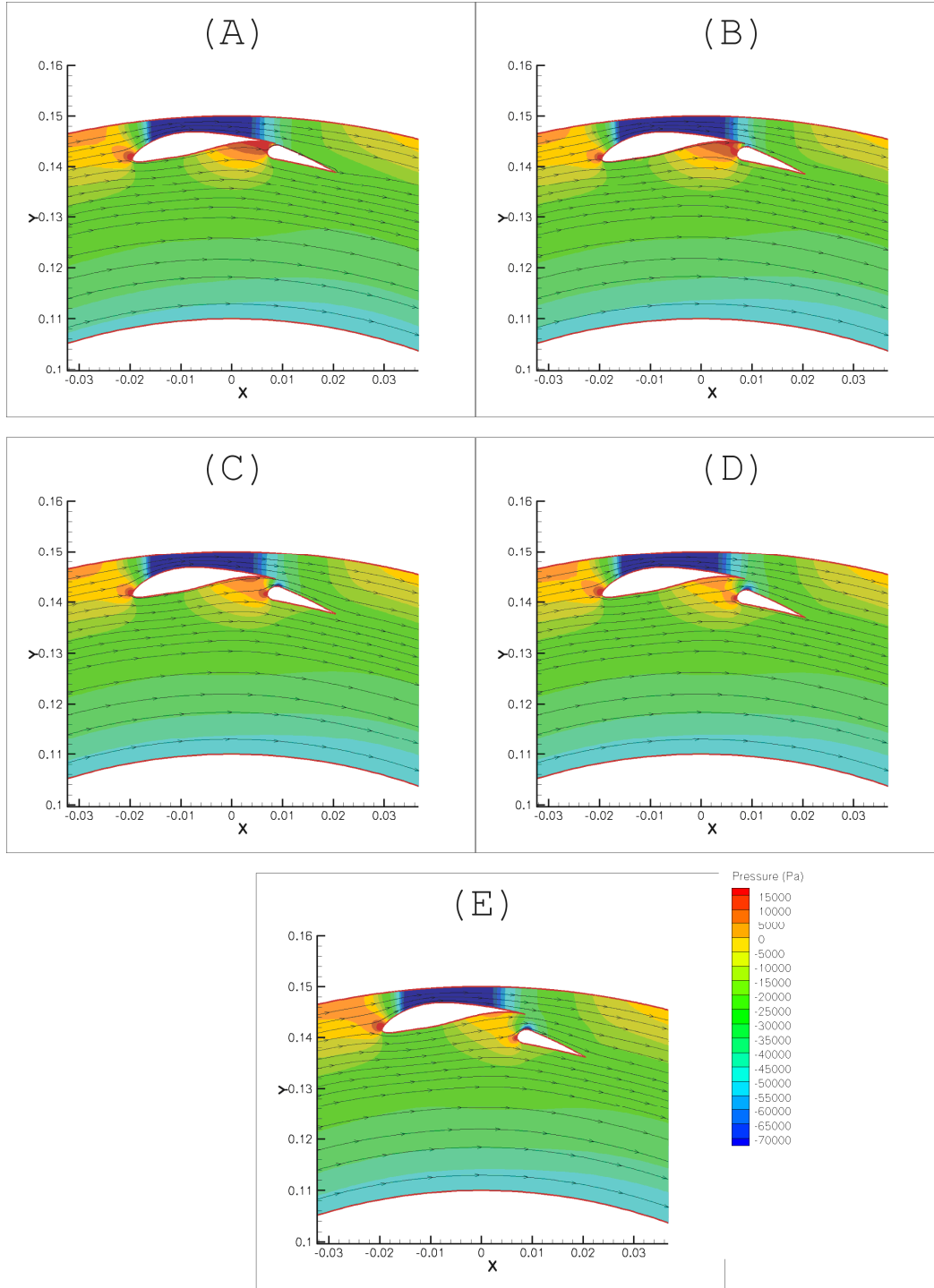


Figure 2.14: Pressure contours and streamlines for a multi-element foil with varying y -positions for the flap leading edge. The flap leading edge is at (A) $y = -0.04 * c$, (B) $y = -0.05 * c$, (C) $y = -0.07 * c$, (D) $y = -0.09 * c$, and (E) $y = -0.11 * c$. In all cases the flap leading edge is at $x = 0.04 * c$, $\alpha = 1 \text{ deg.}$, $\delta = 15 \text{ deg.}$, and $l = 0.5 * c$. The Reynolds number is $Re = 5 \times 10^5$.

Once again, surfaces of maximum and minimum C_P were created, this time versus flap foil x - and y -positioning, as shown in Figure 2.15. Note that, as previously mentioned, minimum C_P was shown to have a strong dependence on y -position, while the gradients in the x -direction were much smaller. A peak minimum C_P value of $C_P = -0.81$ was found to be at $(x,y) = (-0.050, -0.052)*c$. On a typical industrial screen with a chord length on the order of 100 mm , this would correspond to a gap of 2 mm , which, being an order of magnitude larger than the slots in the screen cylinder is not likely to clog with the debris and fibers being filtered by the screen. Since all maximum C_P are between $C_P = 7 \times 10^{-3}$ and $C_P = 1.2 \times 10^{-2}$, maximum C_P is determined to be close to zero and independent of the flap positioning for this foil configuration.

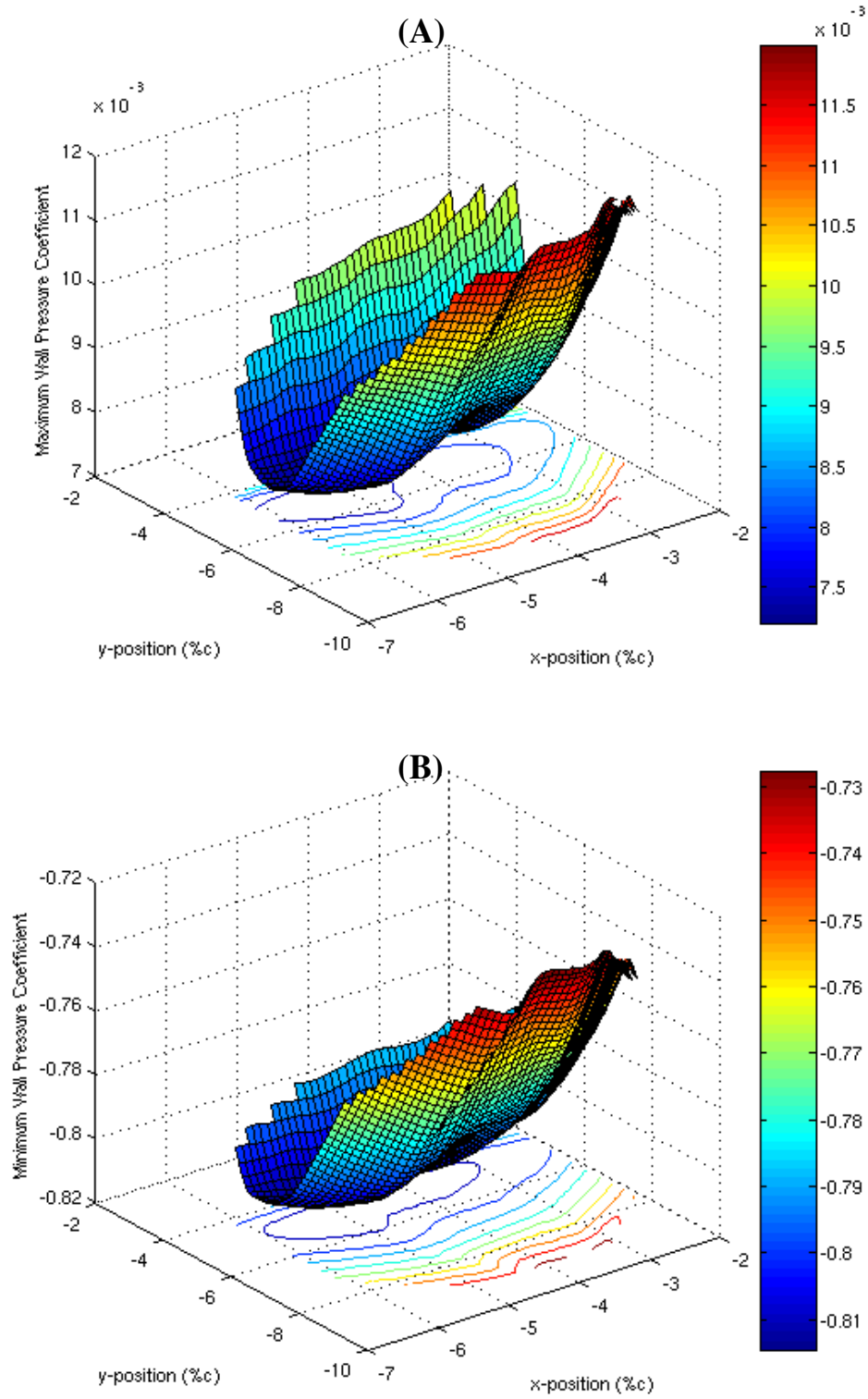


Figure 2.15: Surfaces of (A) maximum wall pressure coefficient and (B) minimum wall pressure coefficient vs. flap leading edge x- and y-position. The foil is at $\alpha = 1$ deg., $\delta = 15$ deg., and $l = 0.5*c$ for all cases. The Reynolds number is $Re = 5 \times 10^5$.

2.6 Conclusions

We have studied the ability of multi-element pressure screen rotor foils to provide greater control over the shape and magnitude of the pressure pulses generated by the rotor. Both the negative and positive pressure peak was shown to have a strong dependence on both angle-of-attack and flap angle. Maximum C_p approached values close to a negligibly small value with increasing α and/or δ . Minimum C_p reached an optimum value with both increasing α and δ before the flow began to separate from the foil and suction was lost. The x -positioning of the flap was shown to have little effect on foil performance, while the y -positioning had a large affect on both maximum and minimum C_p values.

In general, the multi-element foil outperformed the single-element NACA 8312 on which it was based. It was able to reach a positive angle-of-attack without stalling, allowing for the positive pressure pulse to be eliminated. Also, the deflection of the flap allowed for a significant increase in the effective camber of the foil, which provided a stronger and wider negative pulse. The minimum negative C_p for the multi-element foil was 15% stronger than that of the single-element NACA 8312. Additionally, the gradients in minimum negative C_p were low near the optimum for the multi-element foil, allowing for flexibility in the design of the foil.

2.7 References

1. Olson, J.A., Turcotte, S., Gooding, R.W., “Determination of power requirements for solid core pulp screen rotors”, *Nordic Pulp Paper Res. J.*, 19(2): 213-217, 2004.
2. Niinimäki, J., “Phenomena affecting the efficiency of a pressure screen”, 1999 Tappi Pulping Conf., Orlando, October 31-November 4, 1999, 957-966.
3. Julien Saint Amand, F., and Perrin, B., “Fundamentals of screening: Effect of rotor design and fibre properties”, 1999 Tappi Pulping Conf., Orlando, October 31-November 4, 1999, 941-955.
4. Julien Saint Amand, F., and Perrin, B., “Basic parameters affecting screening efficiency and fibre loss”, 2000 PTS-CTP Deinking Symposium, Munich, Germany, May 9-12, 2000, 26.1–26.22.
5. Wakelin, R.F., and Corson, S.R., “Reject thickening behavior of TMP screening”, *Pulp and Paper Canada*, 99(1): 27-30, 1998.
6. Wakelin, R.F., and Corson, S.R., “TMP long fibre fractionation with pressure screens”, 1995 Int. Mech. Pulping Conf., Ottawa, Canada, June 12-15, 1995, 257-265.
7. Wakelin, R.F., Blackwell, B.G., Corson, S.R., “The influence of equipment and process variables on mechanical pulp fractionation in pressure screens”, 1994 Appita Conf., Melbourne, Australia, May 2-6, 1994, 611-621.
8. Pinon, V., Gooding, R.W., Olson, J.A., “Measurements of pressure pulses from a solid core screen rotor”, *Tappi J.*, 2(10): 9-12, 2003.
9. Gonzales, J., “Characterization of design parameters for a free foil rotor in a pressure screen”, M.A.Sc. Thesis, Dept. of Mech. Eng., University of British Columbia, 2002.
10. Feng, M., Gonzalez, J., Olson, J.A., Ollivier-Gooch, C., Gooding, R.W., “Numerical simulation and experimental measurement of pressure pulses produced by a pulp screen foil rotor”, *J. Fluids Eng.*, 127(2): 347-357, 2005.
11. Abbott, I.H., and Von Doenhoff, A.E., “Theory of Wing Sections”, McGraw-Hill, 1949.
12. Mahon, S., and Zhang, X., “Computational analysis of pressure and wake characteristics of an aerofoil in ground effect”, *J. Fluids Eng.*, 127(2): 290-298, 2005.

13. Pope, S.B., “Turbulent Flows”, Cambridge Press, 2000.
14. Fluent, Inc., “Fluent user’s guide”, 2003.
15. Feng, M., “Numerical simulation of the pressure pulses produced by a pressure screen foil rotor”, M.A.Sc. Thesis, Dept. of Mech. Eng., University of British Columbia, 2003.
16. The Mathworks, Inc., “MATLAB Users Guide”, 2002.

Chapter 3

Experimental Measurement of Pressure Pulses from a Pulp Screen Rotor²

3.1 Introduction

Pressure screens are the most industrially effective way to remove contaminants from a pulp stream, improving the strength, smoothness, and optical qualities of the paper.

Pressure screens are also used to fractionate the pulp stream, separating the fibers by length for differing processing and the development of high value pulp products.

Pressure screens are comprised of two main components: a screen cylinder with narrow slots or small holes and a rotor. The unscreened pulp enters the screen tangentially via a feed stream and passes into the center of the cylinder. Fibres pass through the apertures in the cylinder into the accept stream while oversized debris does not pass through the apertures and instead passes down the length of the screen and exits through the reject port. In order to prevent the small apertures in the cylinder from plugging, the rotor generates pressure pulses at the cylinder surface, backflushing the flow through the apertures and clearing them of debris [1-4].

Previous studies have shown that the magnitude of the pressure pulses generated by the rotor directly affects the capacity of the screen [5-11]. It has also been shown that the non-dimensional pressure coefficient is Reynolds number independent, where the pressure coefficient C_P is defined as

$$C_P = \frac{P}{(1/2)\rho V_t^2}, \quad (3.1)$$

² A version of this chapter will be submitted for publication. Delfel, S., Olson, J., Ollivier-Gooch, C., and Wallace, P., "Experimental measurement of pressure pulses from a pulp screen rotor".

P is the static pressure, ρ is the fluid density, and V_t is the tip speed of the rotor [4, 12]. Reynolds number Re is defined as

$$Re = \frac{\rho V_t c}{\mu}, \quad (3.2)$$

where c is the foil chord length and μ is the dynamic viscosity of the fluid. This means that for fully turbulent flow we expect that the magnitude of the pressure pulses generated by the rotor is proportional to the tip speed squared.

Previous studies also found that the power consumption of the rotor is proportional to the tip speed of the rotor cubed, and that the non-dimensional power coefficient is also Reynolds number independent [13]. The power coefficient C_{Power} is defined as

$$C_{Power} = \frac{Power}{\rho V_t^3 D^2}, \quad (3.3)$$

where $Power$ is the power consumption of the rotor and D is the diameter of the rotor. By maximizing the magnitude of the C_P generated by the rotor, the rotor can be slowed, reducing power consumption without reducing the maximum capacity of the screen. This is the primary goal in pressure screen rotor design.

There have been a number of studies experimentally investigating the pressure pulses generated by a pressure screen rotor. Yu studied the pressure pulses from a single S-type solid core rotor for a range of tip speeds and flow rates [14]. It was observed that the pressure pulses were not affected by increasing flow rates, although the tip speeds studied were all fairly high (15 m/s to 25 m/s). Recently, Atkins studied the effects of flow rate, tip speed, and consistency on the pressure pulses generated by a foil rotor and a solid core step rotor [15]. It was found that, with water, increasing reject rate R_V at a constant feed flow rate (i.e. increasing accept flow while reducing reject flow) had no effect on the

pressure pulse below $R_V = 0.3$ for either the step rotor or foil rotor. Increasing the feed flow caused the magnitude of the pressure pulse generated by the foil rotor to increase, however. No explanation was offered for this phenomenon. Atkins also found that varying consistency between 0.0% and 2.8% had little effect on the pressure pulse for both rotors. While insightful, neither study thoroughly investigated the combined effects of rotor geometry and slot velocity on the pressure pulses generated.

Previous works have also established computational fluid dynamics (CFD) as a useful tool in the study of pressure screen rotors. Karvinen and Halonen made early attempts at validating CFD for use with pressure screen rotors, and achieved good results for the time [16]. Wikstrom studied numerically the pressure pulses generated by two separate rotor shapes [17]. Atkins used a 3-D CFD model to study the pulses from a single solid-core rotor and found very good agreement with experimental results [15]. Recent studies have also used CFD to optimize the shape of the rotor elements [3, 18, 19].

The effect of varying the geometry of the element shape on the pressure pulse from a foil rotor was investigated by Gonzales experimentally and Feng *et al.* numerically, using CFD [3, 4]. The apparatus used by Gonzales was a small, laboratory “cross-sectional screen”, which represented a thin, 2 in. slice of a pressure screen and had no accept flow near the sensor. They found that increasing the camber, or curvature, of the foil greatly increased both the width and magnitude of the pressure pulse. They also showed that increasing the angle-of-attack α of the foil, defined as the angle of the foil with the tangent line, increased the magnitude of the negative portion of the pressure pulse while at the same time reducing the undesirable positive portion of the pressure pulse. Similar observations were made by Niinimäki, who showed that increasing the foil angle-of-attack improves the maximum capacity of the screen [6]. Beyond a certain angle-of-attack, however, Gonzales and Feng *et al.* found the foil would begin to stall and the magnitude of the pressure pulse would diminish. This was especially true for highly cambered foils, which would stall at very low angles-of-attack [3, 4].

In order to achieve higher angles-of-attack with highly cambered foils without flow separation, a multi-element foil (MEF) rotor was designed using CFD [19]. The multi-element foil, similar in concept to flaps on an airplane, was shown to delay the foil from stalling by allowing high energy flow on the lower surface of the foil to pass through the slot between the main foil and flap, reenergizing the boundary layer over the upper surface of the foil. The MEF, shown in Figure 3.1, was also shown to have the added benefit of effectively increasing the camber of the foil by deflecting the flap. This led to a significant increase in the magnitude of the negative pressure pulse generated by the foil compared to a typical single-element rotor foil. The MEF was tested in pilot plant and mill trials, and was shown to be capable of lowering the rotor power consumption significantly, by operating at lower tip speeds, without affecting screen capacity [20, 21]. In addition to increased industrial performance, the MEF has been shown to be useful in research applications due to the ability to easily study the effects of foil geometry by changing the angle-of-attack and flap angle.

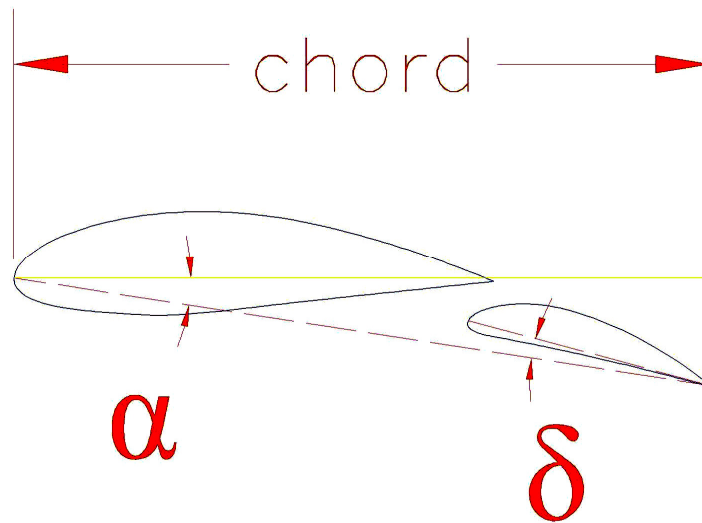


Figure 3.1: Cross section of the MEF with angle-of-attack (α), flap angle (δ), and chord length defined.

In an effort to provide insight for and improve upon pressure screen rotor design, this study directly measures the pressure pulses generated by foil rotors in a true screening environment, using a laboratory pressure screen. The effect of varying foil geometry on the pressure pulses is studied using 12 different MEF configurations and a single-element foil rotor, representing the current state of the art. Additionally, the effects of rotor tip speed and slot velocity on the pressure pulses are also studied. Finally, CFD predictions of pressure are compared with experimental measurements for the MEF rotor.

3.2 Experimental Setup

A Belloit MR-8 laboratory pressure screen was used in the study, shown in Figure 3.2. The MR-8 is 8 in. (20.32 cm) in diameter and is equipped with a variable frequency drive (VFD) that allows for control of the rotor speed and power measurements. The screen is also equipped with magnetic flow meters on the accept and reject lines, and pressure sensors on the feed, accept, and reject pipes. The screen is fed from a 1,000 L stock tank, with the accept and reject streams recirculating back into the feed tank. Water (0.0% consistency) was used in the experiment for a number of reasons.

The pressure pulses generated by the rotor were measured using an Entran EPX micro-sensor. The sensor diaphragm has a diameter of 0.15 in. and was installed with the diaphragm flush with the feed side of the cylinder wires, as shown in Figure 3.3. The sensor was installed so that only a portion of a single wire and two slots are affected. The sensor was installed half way down the axial distance of the cylinder in order to avoid any unsteadiness in the flow as it enters and exits the cylinder. Atkins and Yu both observed a reduction in the strength of the pressure pulses generated by the rotor as the flow moves axially down the cylinder [14, 15]. This is likely due to a reduction in the velocity of the flow relative to the rotor as the flow is accelerated by drag from the rotor. By placing the sensor at the axial midpoint, it is the intention to capture the median magnitude pressure pulse.

The pressure sensor signal was captured at 100k samples per second. At the highest tip speed studied ($V_t = 15$ m/s), this amounts to 3,937 samples per revolution. The samples were collected continuously and then split into individual pulses for each foil in post-processing, as shown in Figure 3.4. This was done to account for any physical differences between the two foils on the rotor, including differences in gap or manufacturing defects. Additionally, as done in previous studies [1-4, 14, 15, 18, 19], the data was zeroed to a “freestream” value to isolate the pressure pulses from the rotor from any pressure variations caused by changing flow rates. The average pressure half way between each of the two pulses was used for this value. Because the flow in the screen is turbulent, it was necessary to generate an ensemble average of the pulses. In building the ensemble average a minimum of 500 pulses from each foil was collected. When averaged, the minimum values for each pulse were aligned to prevent any loss in the magnitude of the pulse due to small errors or fluctuations in rotor speed during the sampling period.

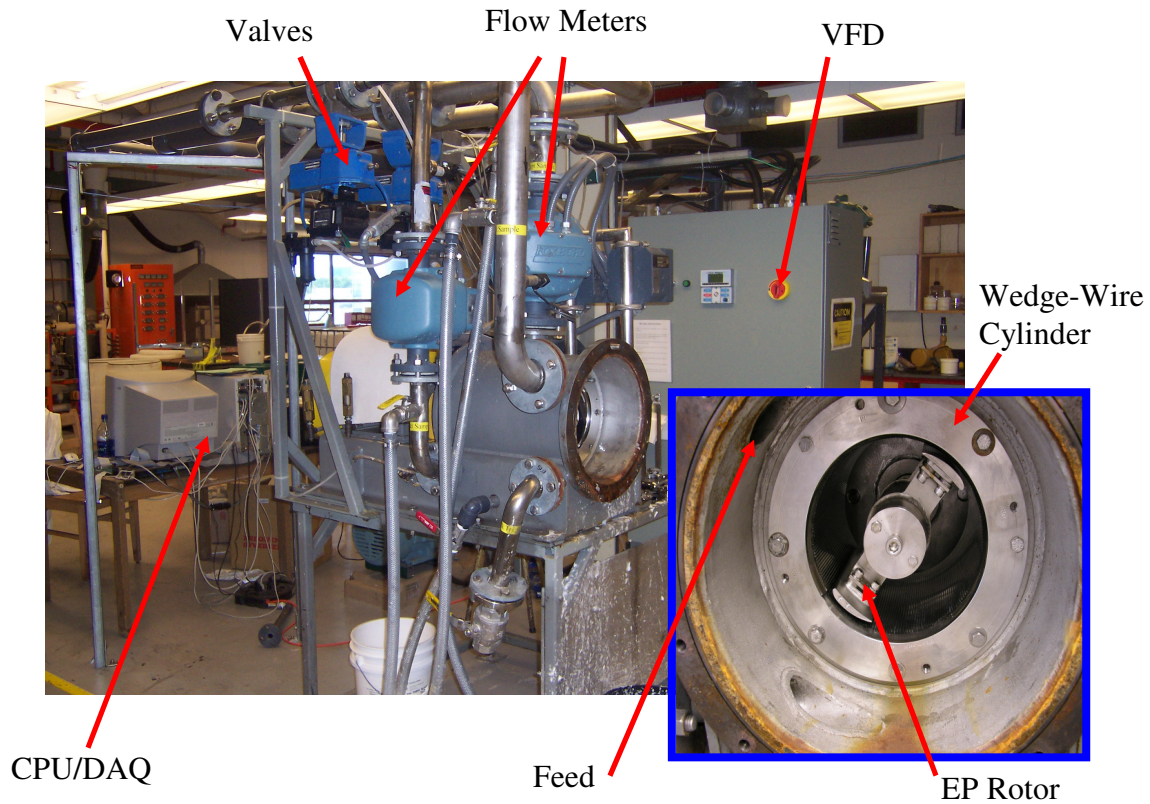


Figure 3.2: The MR-8 laboratory pressure screen with key components called out.

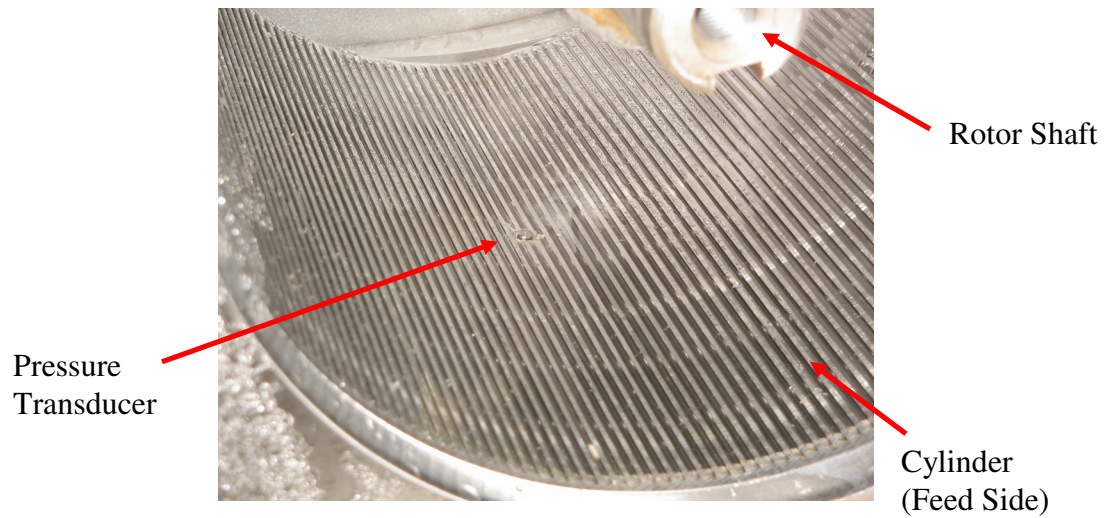


Figure 3.3: Installation of the pressure sensor in the wedge wire cylinder.

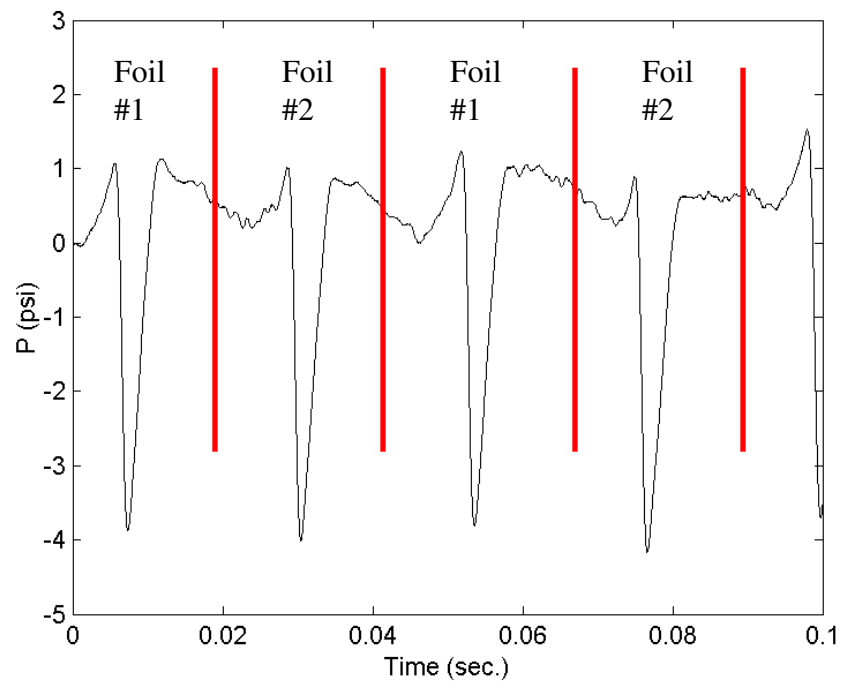


Figure 3.4: A sample of the raw pressure pulse data collected. The red lines illustrate how the data was split between the two foils for averaging.

Thirteen separate rotors were tested in the study: twelve MEF configurations and a single-element foil (AFT EP) rotor. Table 3.1 shows the specific MEF geometries studied and the test parameters. The angle-of-attack (α) of the MEF was varied between zero and six deg., and the flap angle (δ) was varied between 12 and 22 deg. The angles of the foils are set by CNC milled end plates in order to reduce errors in the geometry. The MEF and the EP used both have chord lengths of 60 mm.

A gap of 5 mm between the foils and the cylinder was used. The tip speed of the rotor was varied, in 2 m/s increments, between 5 m/s and 15 m/s for each rotor tested. The slot velocity was varied at a constant volumetric reject rate of $R_V = 0.25$ between zero and three meters per second, which was the maximum slot velocity obtainable without increasing the feed pressure. Slot velocity V_S is defined as

$$V_S = \frac{Q_A}{A_C}, \quad (3.4)$$

where Q_A is the volumetric flow rate of the accept stream and A_C is the open area of the cylinder. It is important to note that the slot velocity is the time averaged velocity through the slots, not the instantaneous flow velocity. For instance, a slot velocity of $V_S = 0$ m/s does not mean that there is no instantaneous flow through the slot.

Table 3.1: Test parameters and foil configurations studied experimentally.

Foil Parameters:	
EP and MEF Chord:	60 mm
MEF Angles-of-attack:	0, 2, 4, 6 deg.
MEF Flap Angles:	12, 17, 22 deg.
Clearance Gap:	5 mm
Cylinder Parameters:	
Cylinder Diameter:	20.32 cm
Cylinder Height:	22.70 cm
Contour Height/Contour Width/Slot Width	0.9/3.2/0.15 mm
Test Parameters:	
Tip Speeds:	5, 7, 9, 11, 13, 15 m/s
Slot Velocities:	0, 1, 2, 3 m/s
Volumetric Reject Rate:	0.25
Feed Pressure:	172.4 kPa
Consistency:	0.0%
Temperature:	20-25 °C

3.3 Experimental Results and Discussion

3.3.1 Error Analysis

An averaged pressure pulse for the EP rotor at three different tip speeds at $V_S = 0$ m/s is shown in Figure 3.5 with 99% confidence intervals. The plots show pressure plotted versus the length along the cylinder wall, where the curve length x is found by

$$x = V_t \cdot t, \quad (3.5)$$

where t is sample time. These confidence intervals are representative for those seen throughout the study. Even at the lowest tip speeds, where the pressures are in the lower quarter of the rated interval for the sensor, there is a very high level of confidence in the results.

3.3.2 Effect of Tip Speed

The effect of varying tip speed on the pressure pulses generated by the rotor at $V_S = 0$ m/s is shown in Figure 3.6 for the EP rotor and in Figure 3.7 for one of the MEF configurations. Increasing the tip speed increases the magnitude of the pressure pulses generated while maintaining the pulse shape.

The non-dimensional pressure coefficient, equation 1, is plotted along the cylinder wall for varying tip speeds in Figures 3.8 and 3.9 for the EP and the MEF configuration, respectively. The traces of pressure coefficient for both rotors collapse onto a single curve, showing that, as seen in previous studies [4, 12], the magnitude of the non-dimensional pressure pulse is independent of Reynolds number. Below a tip speed of $V_t = 11$ m/s, the magnitude of the pressure pulse generated by the EP begins to diminish and the dimensionless pressure C_P no longer collapses to a single curve. This is an indication that the flow is beginning to separate from the foil. The same can be seen for the MEF configuration below $V_t = 9$ m/s.

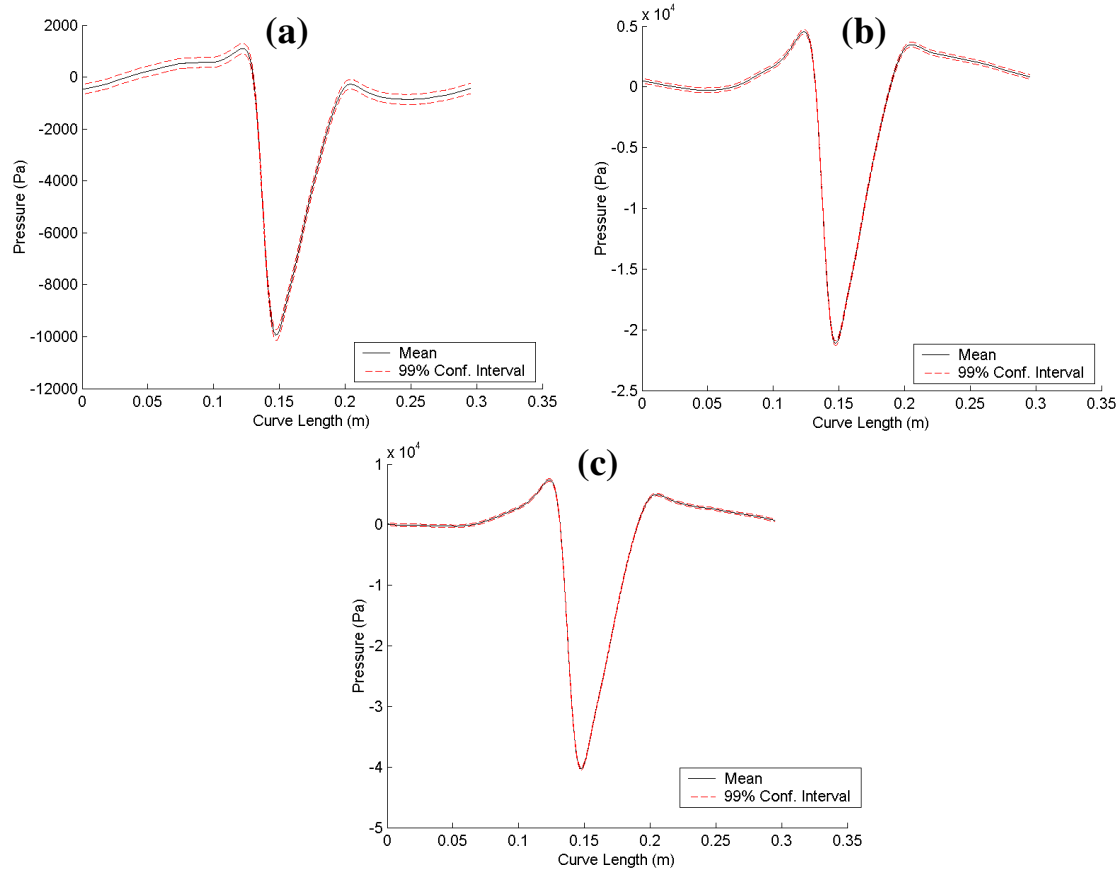


Figure 3.5: The ensemble average pressure pulse and 99% confidence intervals for the EP rotor at $V_S = 0$ m/s and (a) $V_t = 7$ m/s, (b) $V_t = 11$ m/s, and (c) $V_t = 15$ m/s. The 99% confidence intervals shown are representative of those found throughout the study.

To more clearly illustrate this effect, Figure 3.10 shows the minimum and maximum C_P values plotted versus Reynolds number for the EP rotor. The solid line in the plots represents the average of the minimum and maximum C_P values for tip speeds over $V_t = 11$ m/s ($Re = 66,000$), where the flow around the foil is likely to be fully attached. Above $Re = 60,000$, the minimum and maximum C_P values are clearly independent of Reynolds number. At the lower tip speeds, however, the C_P values begin to fluctuate.

Similar results can be seen for the MEF in Figures 3.11 and 3.12, which show minimum and maximum C_P versus Reynolds number, respectively, for three different MEF configurations with increasing flap angles. The three different configurations shown

have the same angle-of-attack, but are at increasing flap angles. For the first two configurations, the magnitude of the minimum and maximum C_p is constant at and above a tip speed of $V_t = 9$ m/s ($Re = 54,000$). The last configuration shown, which has the highest flap angle, shows signs of instability below $V_t = 11$ m/s ($Re = 66,000$). While it is not entirely conclusive, the increase in flap angle may be causing the foil to begin stalling earlier than the configurations with lower flap angles.

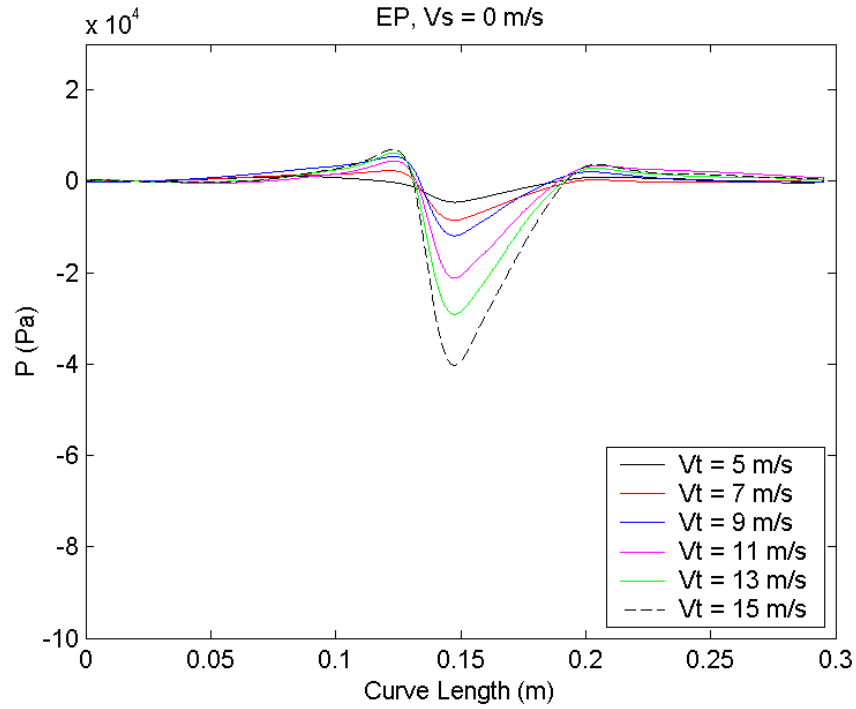


Figure 3.6: Pressure traces for EP rotor at various tip speeds and $V_s = 0$ m/s.

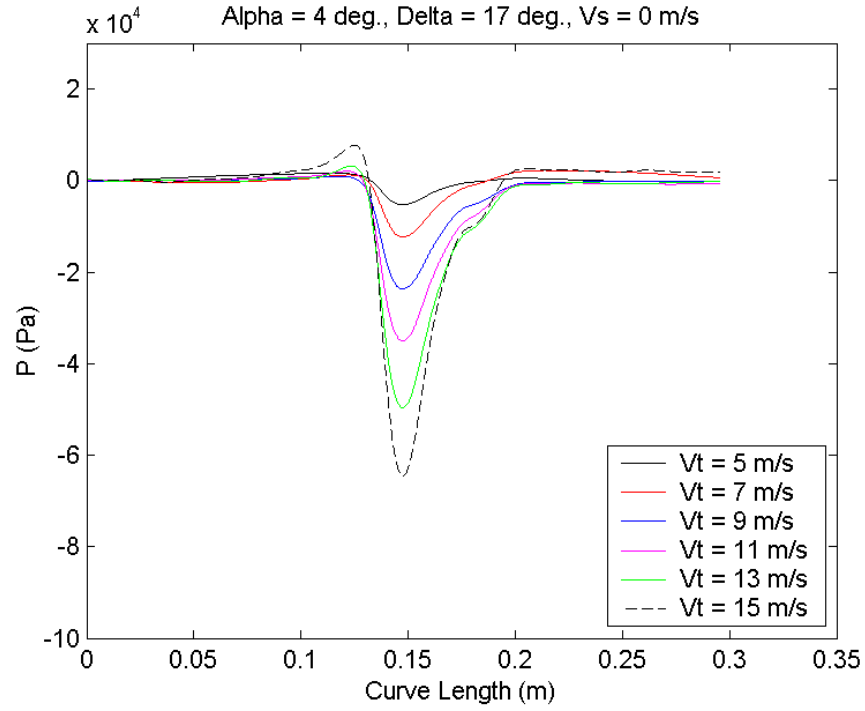


Figure 3.7: Pressure traces for the MEF rotor at $(\alpha, \delta) = (4, 17)$ deg., at various tip speeds, and at $V_s = 0$ m/s.

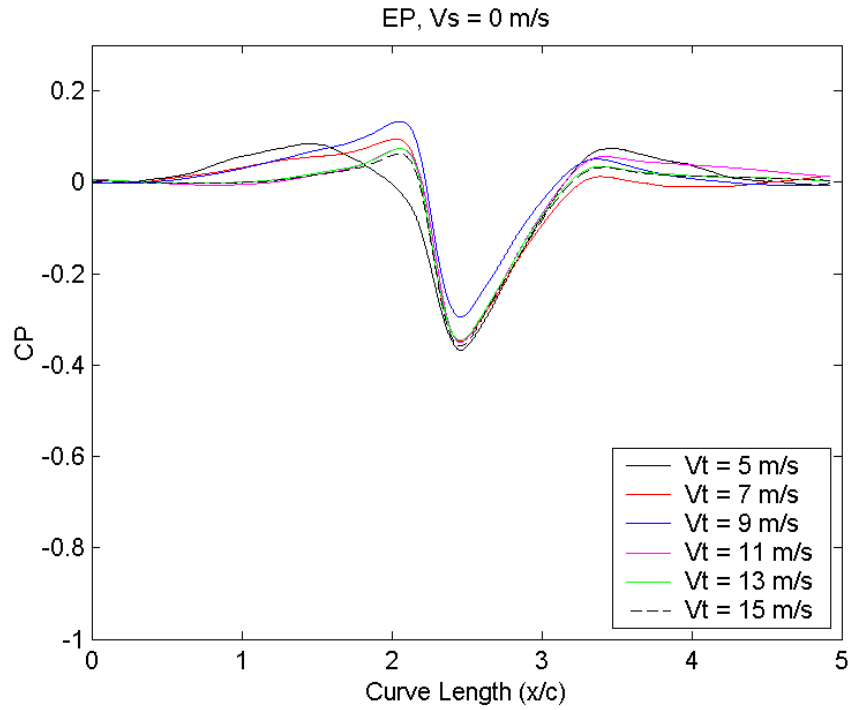


Figure 3.8: Traces of non-dimensional pressure coefficient for the EP rotor at various tip speeds and $V_s = 0$ m/s.

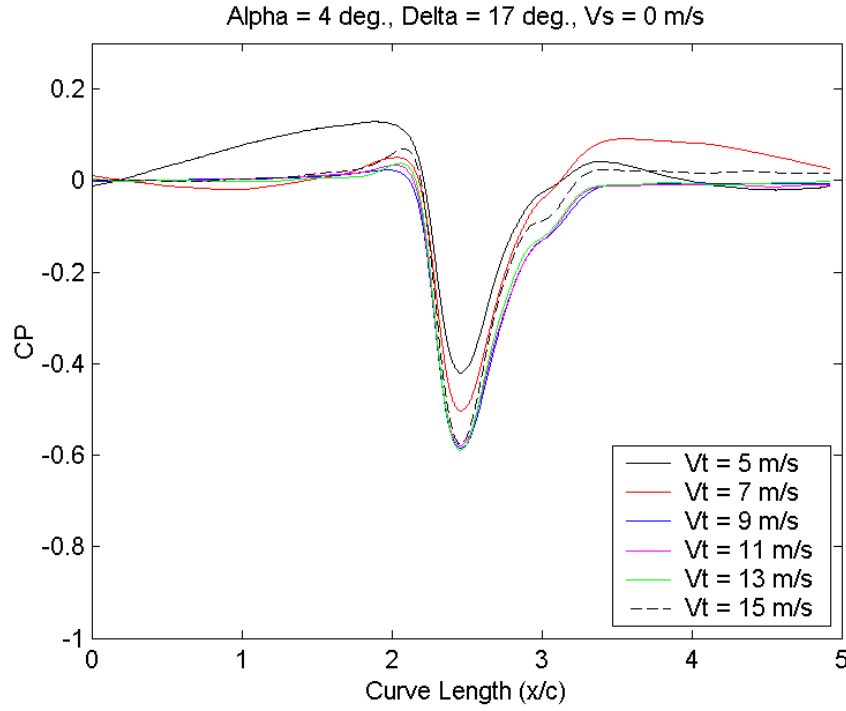


Figure 3.9: Traces of non-dimensional pressure coefficient for the MEF rotor at $(\alpha, \delta) = (4, 17)$ deg., at various tip speeds, and at $V_s = 0$ m/s.

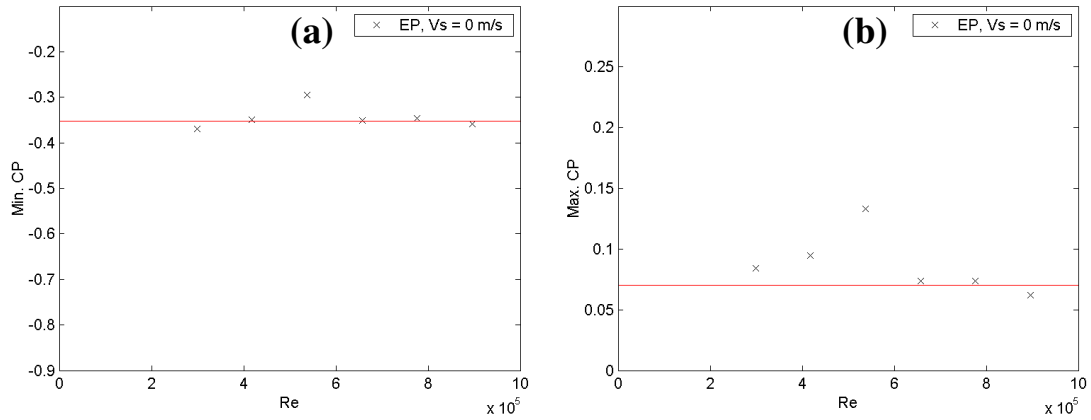


Figure 3.10: (a) Minimum pressure coefficient and (b) maximum pressure coefficient plotted as a function of Reynolds number for the EP rotor at $V_s = 0$ m/s. The solid line represents the average of values above $Re = 60,000$.

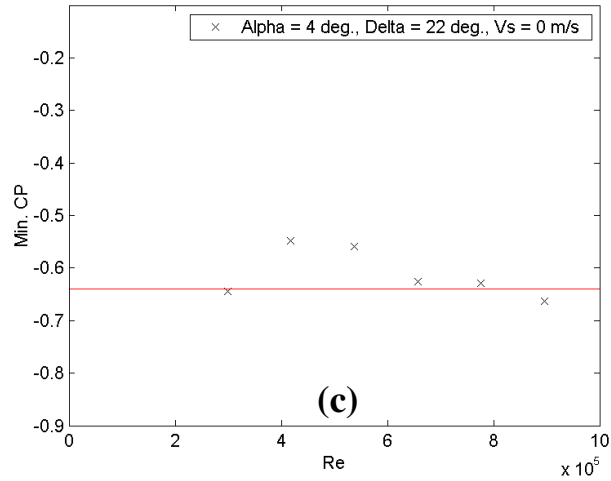
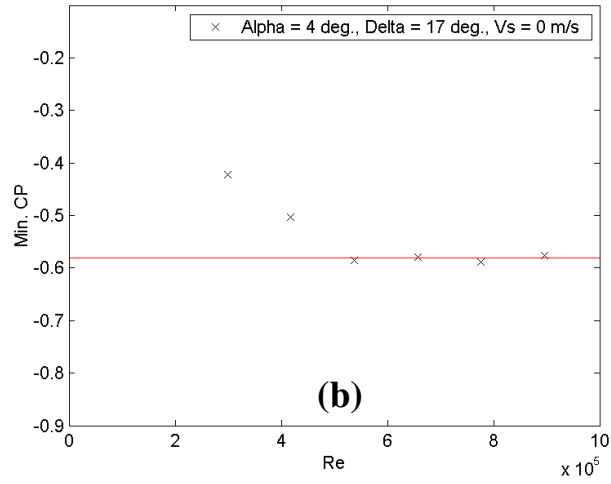
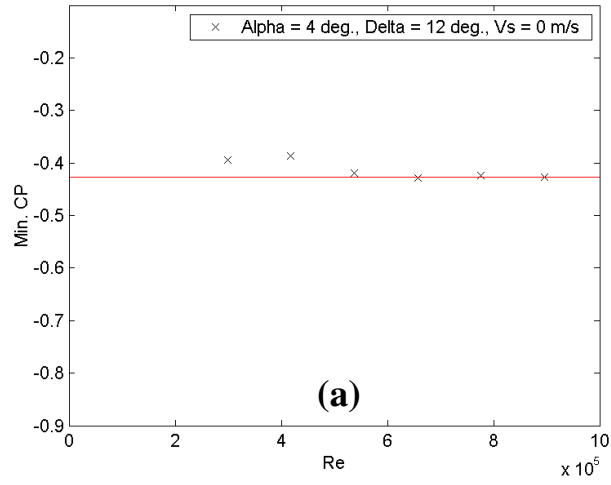


Figure 3.11: Minimum pressure coefficient plotted as a function of Reynolds number for the MEF rotor at (a) $(\alpha, \delta) = (4, 12)^\circ$, (b) $(\alpha, \delta) = (4, 17)^\circ$, and (c) $(\alpha, \delta) = (4, 22)^\circ$ at $V_s = 0$ m/s. The solid line represents the average of values above $Re = 60,000$.

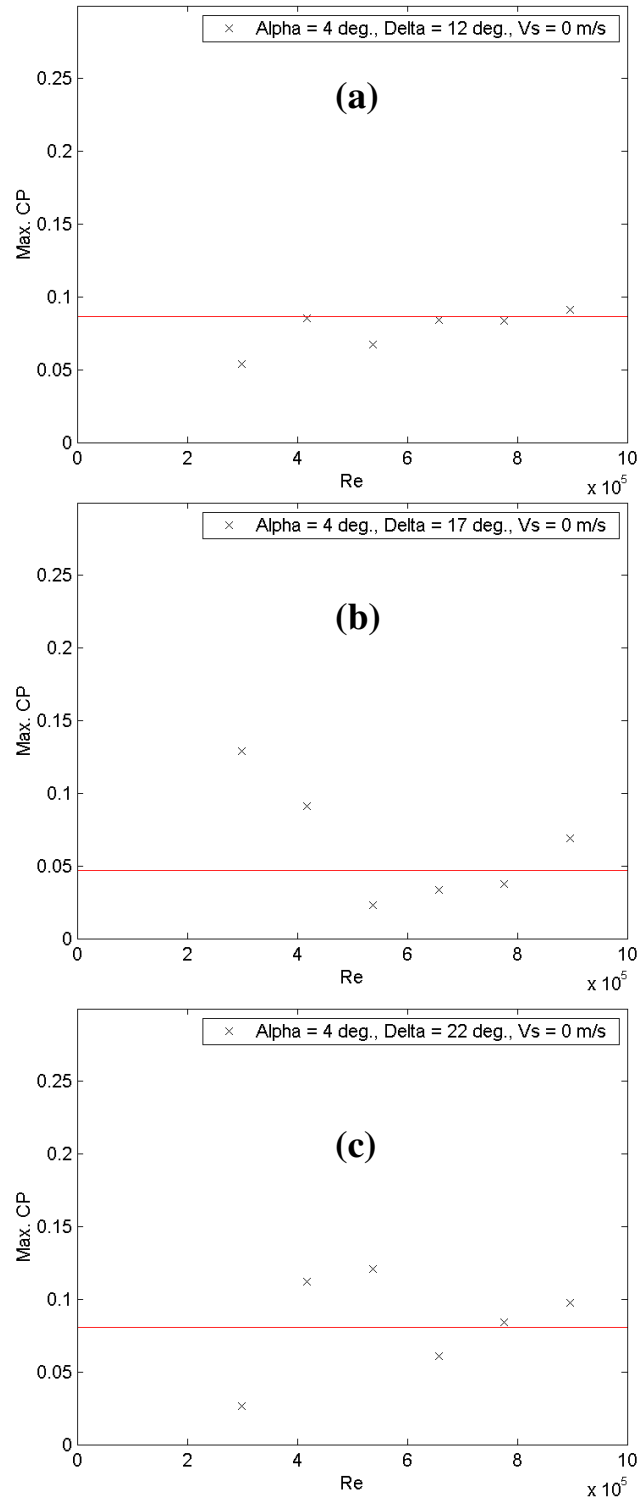


Figure 3.12: Maximum pressure coefficient plotted as a function of Reynolds number for the MEF rotor at (a) $(\alpha, \delta) = (4, 12)$ deg., (b) $(\alpha, \delta) = (4, 17)$ deg., and (c) $(\alpha, \delta) = (4, 22)$ deg. at $V_s = 0$ m/s. The solid line represents the average of values above $Re = 60,000$.

3.3.3 Effect of Varying MEF Geometry

The effect of varying the angle-of-attack of the MEF at a constant flap angle on the non-dimensional pressure pulse generated by the foils is shown in Figure 3.13. Increasing the angle-of-attack of the foil increases the magnitude of the negative pressure pulse and reduces the magnitude of the positive pressure pulse. Similarly, the effect of varying the flap angle of the MEF at a constant angle-of-attack on the pressure pulse is shown in Figure 3.14. Increasing the flap angle increases the magnitude of the negative pressure pulse.

The effects of varying the MEF geometry are more clearly seen in Figure 3.15, which shows minimum C_p plotted versus flap angle, with lines of constant angle-of-attack, at different tip speeds. The angle-of-attack is varied from $\alpha = 0$ deg. to $\alpha = 6$ deg., and the flap angle is varied from $\delta = 12$ deg. to $\delta = 22$ deg. There are clear trends of increasing magnitude of the minimum C_p when increasing both the angle-of-attack and the flap angle, and there is not an optimum for either variable within the range of geometries tested, indicating that lower C_p designs may be possible. Also, the trends do not vary with tip speed. The highest magnitude minimum C_p measured at $V_t = 13$ m/s was at $(\alpha, \delta) = (6, 22)$, at $C_p = -0.81$, which is 126% higher in magnitude than measured for the EP rotor. Additionally, it is interesting to note that although the magnitude of the non-dimensional pressure pulses was shown previously in Figures 3.9 and 3.11 to reduce at tip speeds below $V_t = 9$ m/s, the trends remain unchanged even at $V_t = 7$ m/s. This implies that the flow has only partially separated from the foil at this point and the foil is not fully stalled.

The effect of varying the MEF geometry on the maximum pressure coefficient is shown in Figure 3.16. At $V_t = 7$ m/s, the maximum pressure pulse is unresponsive to changes in the geometry. As mentioned previously, the flow is likely separating from the foil at this point. At the higher tip speeds, clear trends can be seen, both for varying angle-of-attack and flap angle. As shown in previous studies [1, 3, 4, 19], increasing the angle-of-attack and flap angle reduces the magnitude of the positive pressure pulse. Unlike what was seen in past studies, however, there is an optimal configuration at $(\alpha, \delta) = (4, 17)$ deg.,

beyond which increasing the angle-of-attack and flap angle increases the magnitude of pressure pulse. At the optimal configuration at $V_t = 13$ m/s, the maximum pressure coefficient is $C_p = 0.038$, which is 39% lower than measured for the EP rotor.

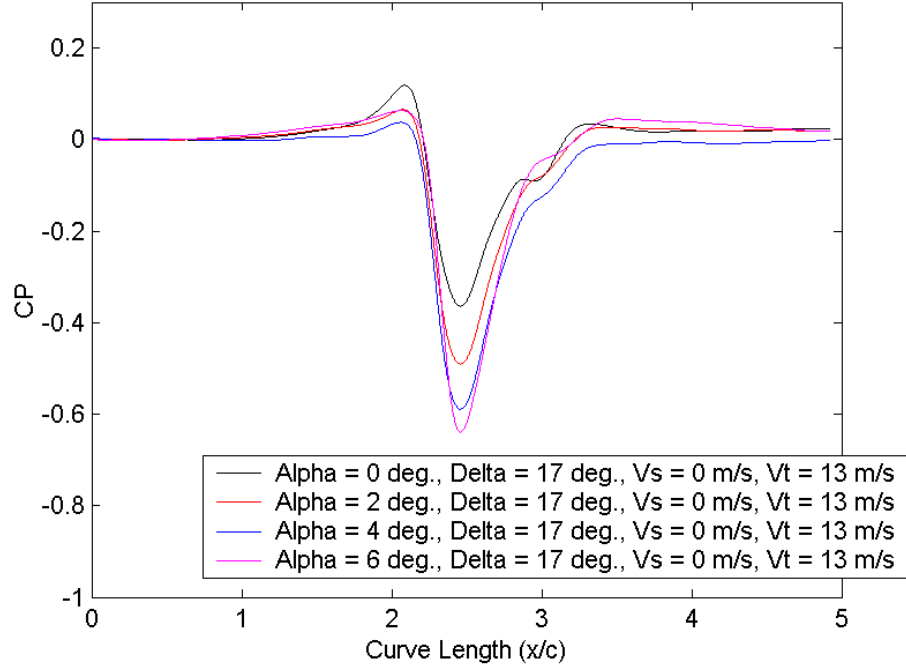


Figure 3.13: Effect of varying angle-of-attack on the non-dimensional pressure trace for the MEF at a constant flap angle ($\delta = 17$ deg.). The tip speed is $V_t = 13$ m/s and the slot velocity is $V_s = 0$ m/s.

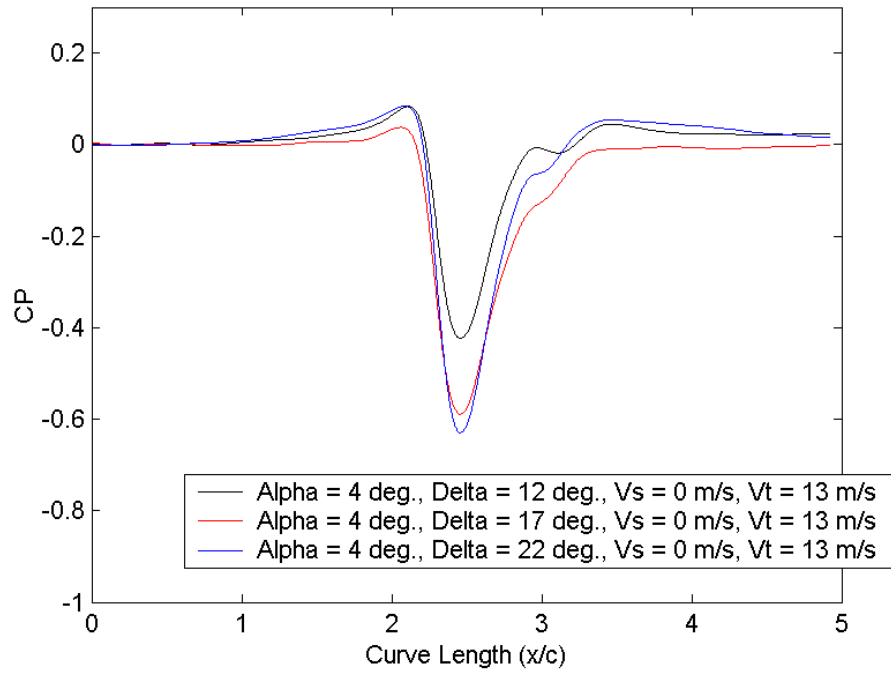


Figure 3.14: Effect of varying flap angle on the non-dimensional pressure trace for the MEF at a constant angle-of-attack ($\alpha = 4$ deg.). The tip speed is $V_t = 13$ m/s and the slot velocity is $V_s = 0$ m/s.

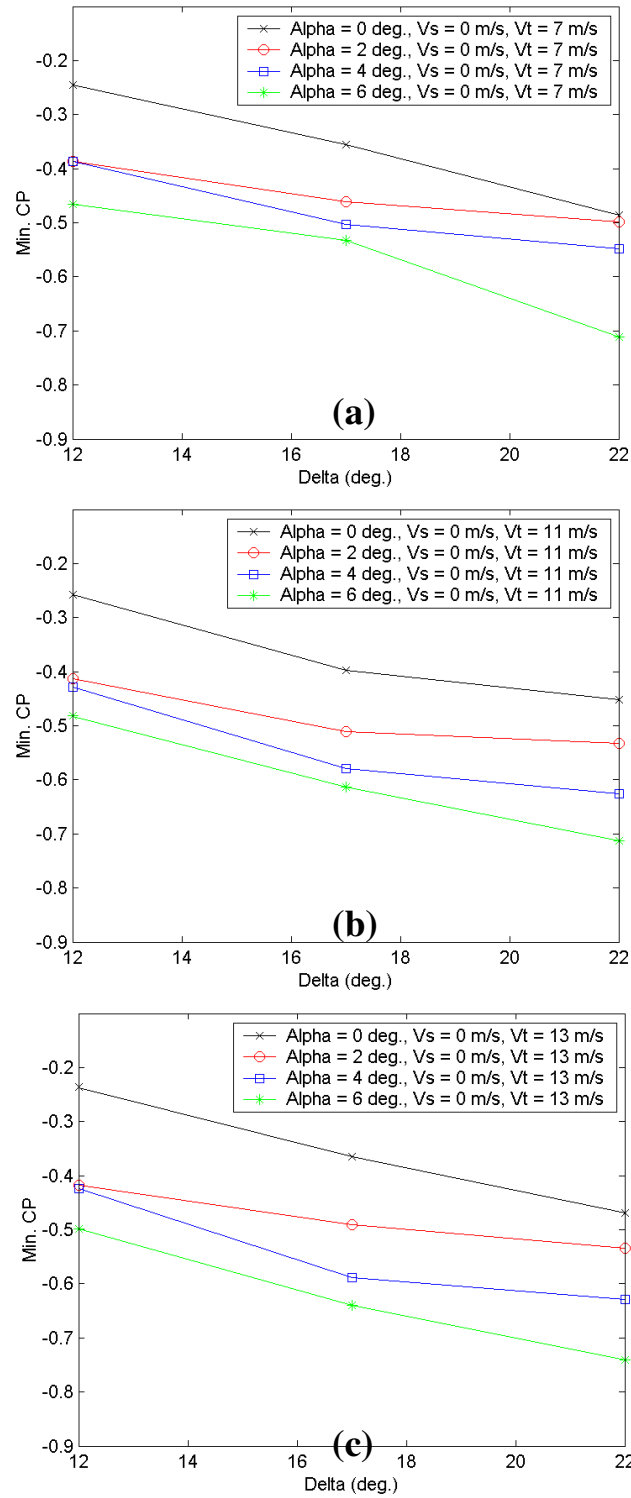


Figure 3.15: Effect of varying the MEF flap angle on the minimum pressure coefficient, with lines of constant angle-of-attack, at $V_s = 0$ m/s and (a) $V_t = 7$ m/s, (b) $V_t = 11$ m/s, and (c) $V_t = 13$ m/s.

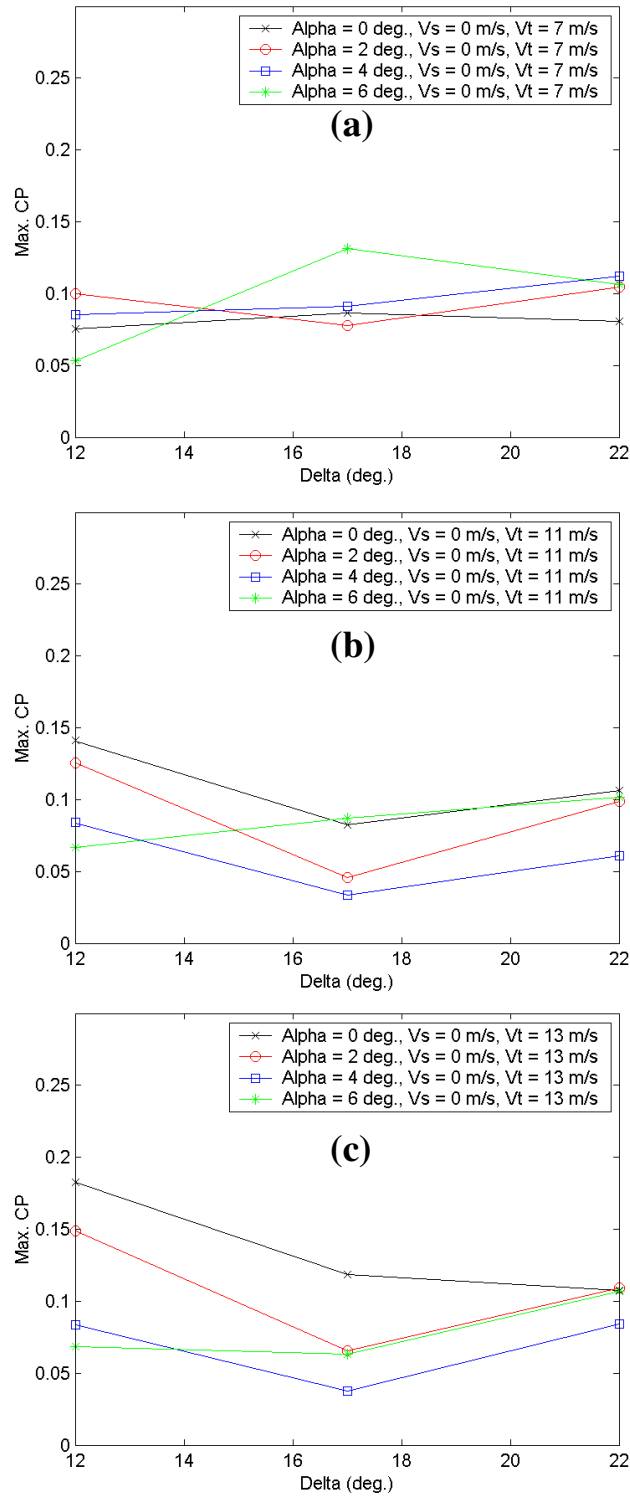


Figure 3.16: Effect of varying the MEF flap angle on the maximum pressure coefficient, with lines of constant angle-of-attack, at $V_s = 0$ m/s and (a) $V_t = 7$ m/s, (b) $V_t = 11$ m/s, and (c) $V_t = 13$ m/s.

3.3.4 Effect of Slot Velocity

The effect of increasing the slot velocity on the non-dimensional pressure pulse for the EP rotor at various tip speeds is shown in Figure 3.17. At high tip speeds, where the flow around the foil is fully attached, increasing the slot velocity has no effect on the magnitude or shape of the pressure pulse. Increasing slot velocity appears to increase the tip speed at which stall occurs, however. At $V_t = 9$ m/s, for instance, the pressure pulses for $V_s = 0$ m/s and $V_s = 1$ m/s are largely unaffected, but the pressure pulses for slot velocities above $V_s = 1$ m/s diminish in strength as slot velocity is increased. At $V_t = 7$ m/s and below, only the pressure pulse at $V_s = 0$ m/s has retained its shape and magnitude, while the pressure pulses at higher slot velocities have diminished in strength. The large amount of noise in the pressure trace at the higher slot velocities indicates that the flow is likely separated from the foil. Increasing slot velocity likely causes flow separation from the foil at higher tip speeds because of the increasing adverse pressure gradient associated with it.

Similar results can be seen for the MEF in Figure 3.18, which shows the effect of varying slot velocity on the non-dimensional pressure pulse for an MEF configuration at different tip speeds. At $V_t = 11$ m/s and above, varying slot velocity has little or no effect on the pressure pulse. Below $V_t = 11$ m/s, however, increasing slot velocity causes the foil to stall and a reduction in the magnitude of the minimum pulse.

This is also seen clearly in Figure 3.19, which shows the minimum pressure coefficient plotted as a function of slot velocity for the EP rotor. Increasing slot velocity can be seen to have little effect on the minimum pressure coefficient at higher tip speeds, where the flow is fully attached to the foil. Increasing V_s can again be seen to reduce the tip speed at which flow separation begins, however. This is indicated by the curve for $V_t = 9$ m/s, which shows a reduction in the magnitude of minimum C_p at $V_s = 3$ m/s, even though it had been unaffected at the lower slot velocities.

The effect of slot velocity on the minimum pressure coefficient for three different MEF configurations with constant angle-of-attack ($\alpha = 6$ deg.) is shown in Figure 3.20. The same effects that were seen for the EP are shown for the MEF, as well: Increasing slot velocity has little effect on the magnitude of the minimum pressure coefficient at higher tip speeds, but increases the tip speed at which flow separation begins. It also appears that increasing the flap angle causes the foil to stall earlier as slot velocity is increased. This is indicated by the curve for $V_t = 11$ m/s, which is unaffected by slot velocity at $(\alpha, \delta) = (6, 12)$ deg. As the flap angle is increased, however, the minimum pressure coefficient at $V_t = 11$ m/s is increasingly effected by slot velocity. This is likely due to the increase in effective camber as the flap angle is increased, which has been shown in previous studies to make the foil more susceptible to flow separation [3, 4].

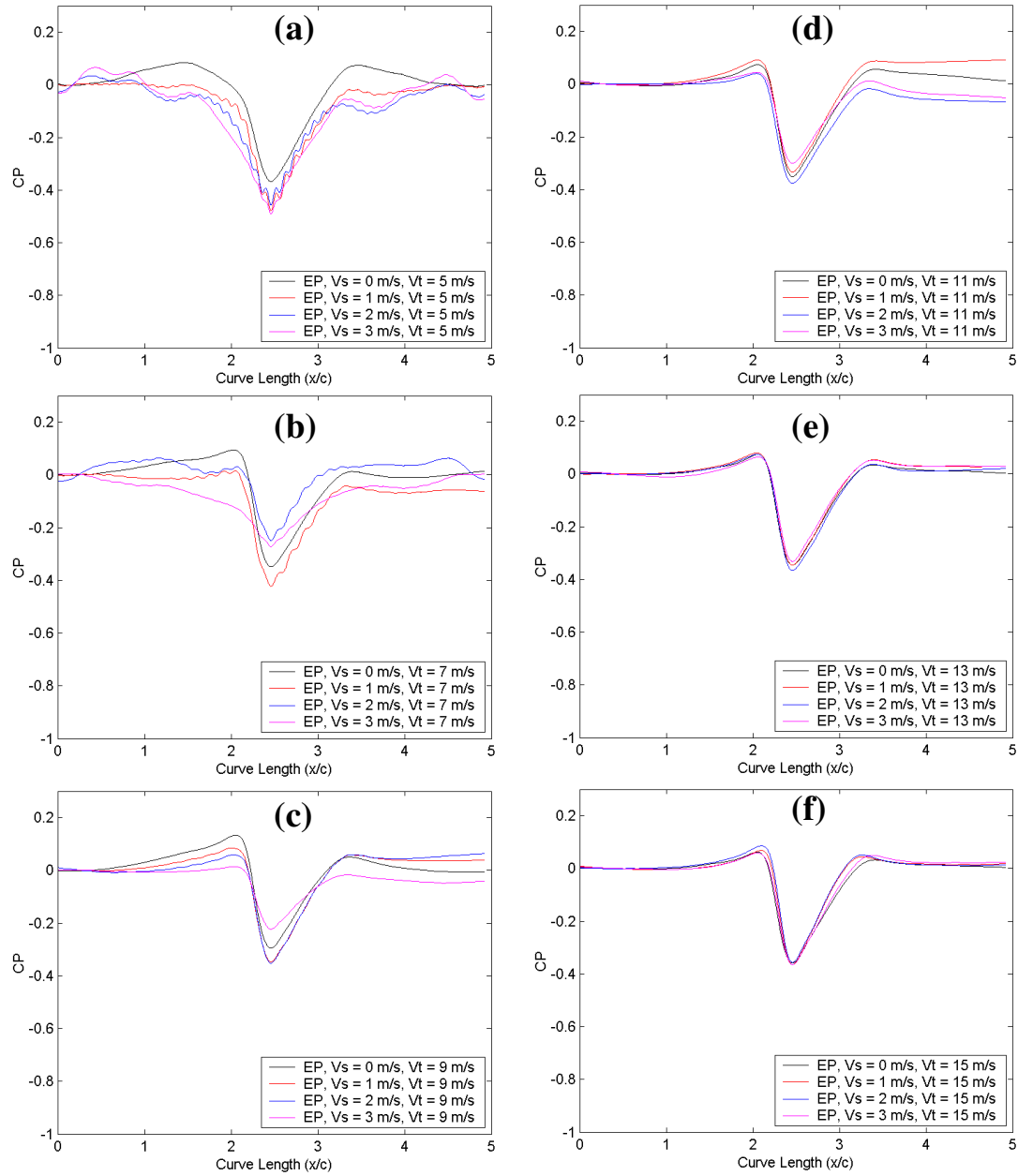


Figure 3.17: Effect of varying slot velocity on the non-dimensional pressure trace for the EP rotor at (a) $V_t = 5$ m/s, (b) $V_t = 7$ m/s, (c) $V_t = 9$ m/s, (d) $V_t = 11$ m/s, (e) $V_t = 13$ m/s, and (f) $V_t = 15$ m/s.

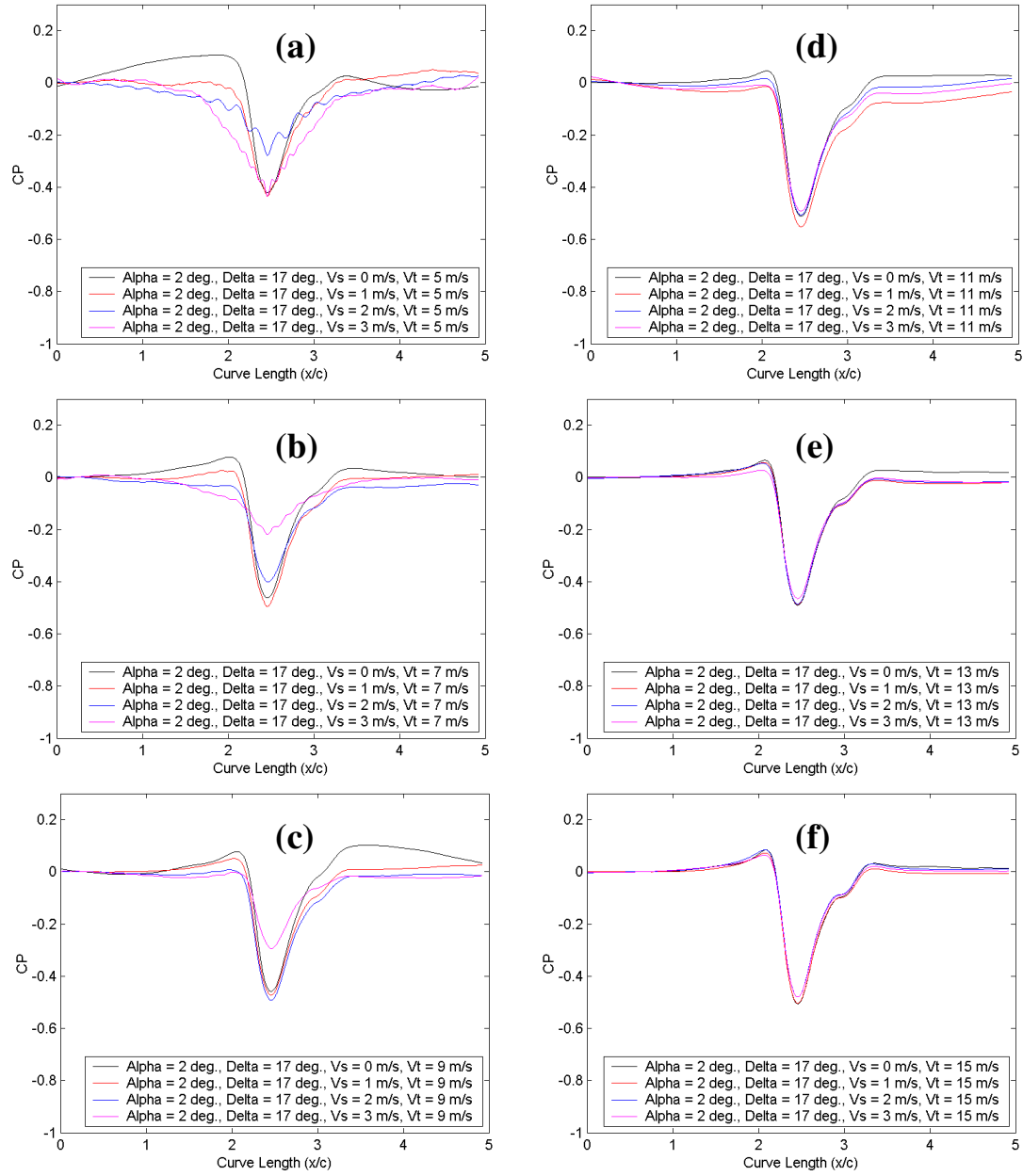


Figure 3.18: Effect of varying slot velocity on the non-dimensional pressure trace for the MEF rotor at $(\alpha, \delta) = (2, 17)$ deg. at (a) $V_t = 5$ m/s, (b) $V_t = 7$ m/s, (c) $V_t = 9$ m/s, (d) $V_t = 11$ m/s, (e) $V_t = 13$ m/s, and (f) $V_t = 15$ m/s.

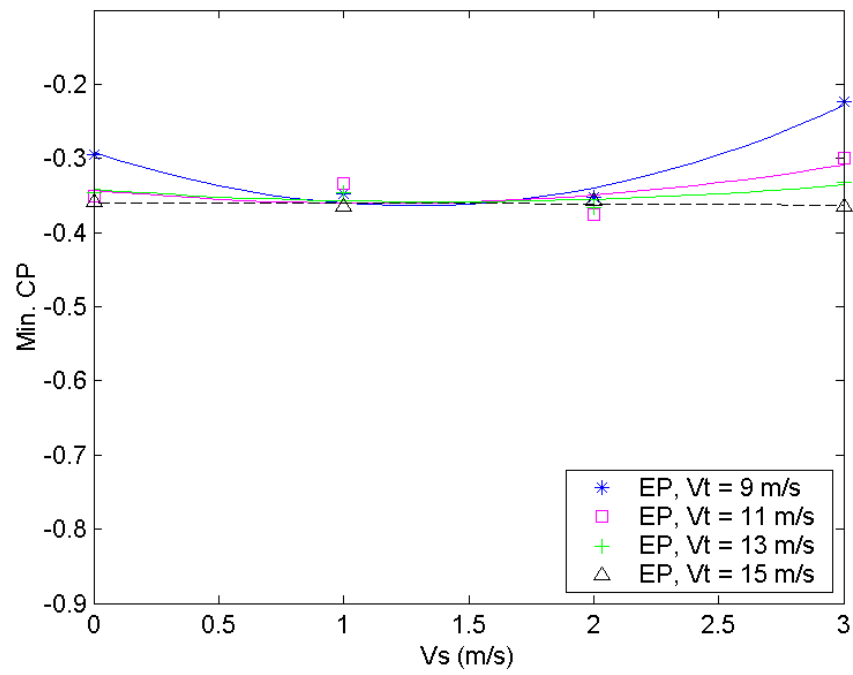


Figure 3.19: Minimum pressure coefficient as a function of slot velocity for the EP rotor at various tip speeds.

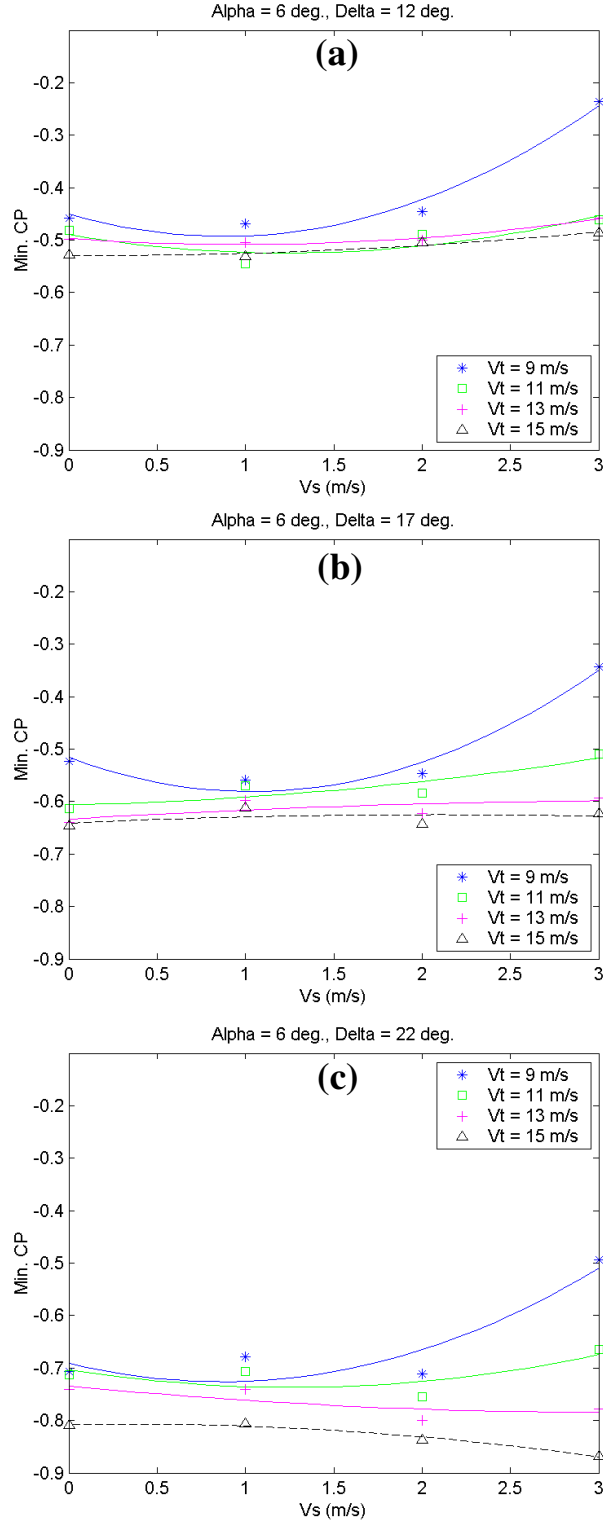


Figure 3.20: Minimum pressure coefficient as a function of slot velocity for the MEF rotor at (a) $(\alpha, \delta) = (6, 12)^\circ$, (b) $(\alpha, \delta) = (6, 17)^\circ$, and (c) $(\alpha, \delta) = (6, 22)^\circ$, at various tip speeds.

Minimum pressure coefficient plotted as a function of MEF flap angle at $V_t = 7$ m/s, with lines of constant angle-of-attack, is shown in Figure 3.21 for four different slot velocities. At $V_s = 0, 1$ and 2 m/s, increasing slot velocity does not change the trends for varying geometry, even at the low tip speed of $V_t = 7$ m/s where the magnitude of the minimum pressure coefficient is reduced. This again implies that the foil is not fully stalled at this tip speed and that the flow still responds to changes in geometry. At $V_s = 3$ m/s, however, the foil appears to be fully stalled at $V_t = 7$ m/s and the minimum C_P is unresponsive to changes in geometry. At higher tip speeds, the trends for varying geometry on minimum C_P were unaffected by increasing slot velocity, even at $V_s = 3$ m/s. These same results were found for the effect of varying slot velocity on the trends for varying geometry on the maximum C_P .

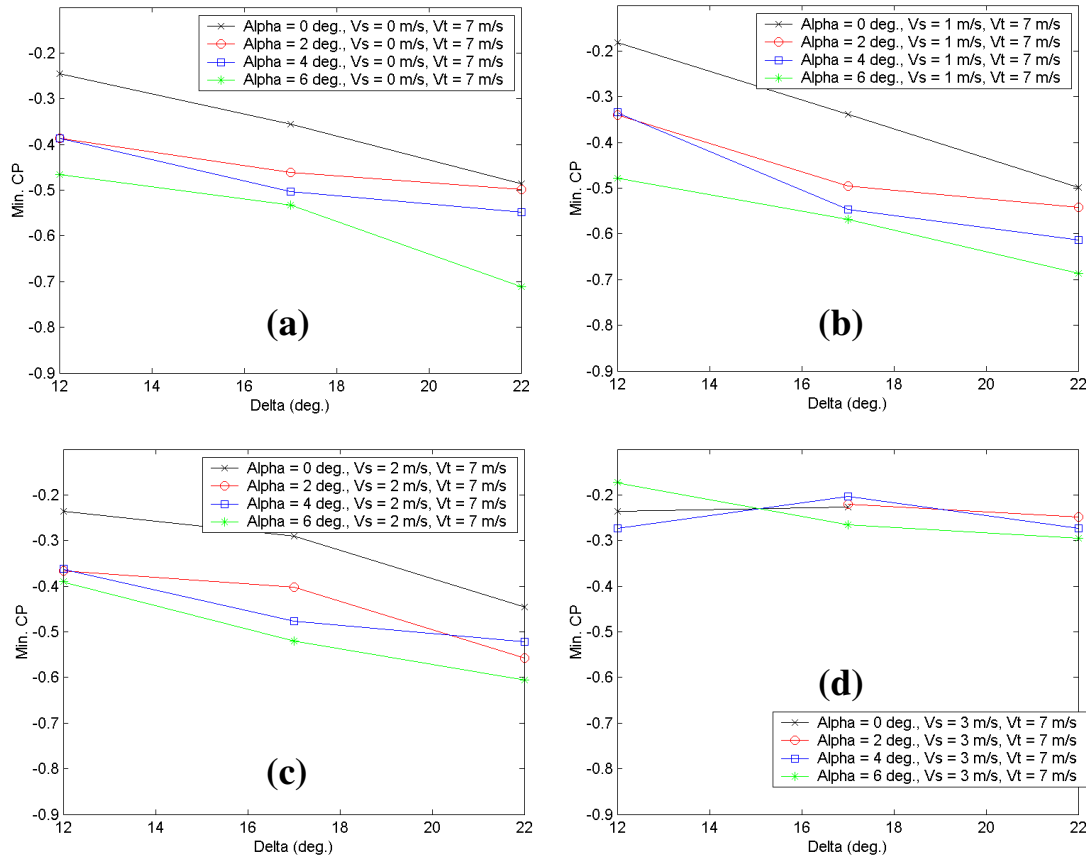


Figure 3.21: Effect of varying the MEF flap angle on the minimum pressure coefficient, with lines of constant angle-of-attack, at $V_t = 7$ m/s and (a) $V_s = 0$ m/s, (b) $V_s = 1$ m/s, (c) $V_s = 2$ m/s, and (d) $V_s = 3$ m/s.

3.4 Numerical Methods

The MEF rotor in the MR8 pressure screen was numerically modeled using the methods described in Delfel *et al.* [19]. Figure 3.31 shows how the domain was modeled, as well as a typical mesh and boundary conditions used in the problem. The discretized Navier-Stokes equations were solved using the FLUENT 6.1 commercial solver, a second order finite volume solver. The problem is assumed to be two-dimensional, isothermal, and steady state. All meshes were generated using GAMBIT, the pre-processing package for FLUENT.

The domain is rotationally periodic, simulating a two-bladed rotor. A rotating coordinate system spinning at the same speed as the rotor is set at the center of the cylinder, since the flow is steady from this frame of reference. Eliminating the time dependence and solving the problem as steady state reduces the computational costs of the problem significantly. The inner wall and the foil were set to have zero velocity relative to the spinning computational coordinate system. The outer wall, which represents the cylinder wall, is set to have zero velocity in the absolute coordinate system.

There are a number of assumptions made in the CFD model, including that the problem is two-dimensional and that there is no flow through the cylinder wall. Typical pressure screen rotors have high aspect ratios and the axial flow velocity is a very low, making the two-dimensional assumption valid. Modeling the cylinder as a solid wall is meant to represent the critical case of a plugged cylinder. It also significantly reduces computational costs by eliminating the need to model the complicated flow through the slots.

Turbulence in the flow was modeled using the standard k - ε model with enhanced wall treatment and the k - ω SST model, and the effectiveness of each was compared. The standard k - ε model finds closure for the Reynolds Stresses by solving additional transport equations for the turbulent kinetic energy k and the turbulent dissipation rate ε . The k - ω SST model is similar to the standard k - ε model, but it instead solves transport equations for k and ω , the ratio of dissipation rate to turbulent kinetic energy, in the near-wall

region. Far from the wall, however, it blends the $k-\omega$ model into the standard $k-\varepsilon$ model. In some cases, the $k-\omega$ SST model has been shown to outperform the $k-\varepsilon$ model, especially in cases with swirling flows, significant streamline curvature, and adverse pressure gradients [22-25]. Additional details of the turbulence models are beyond the scope of this work and are left to the references [23, 26].

Both turbulence models studied require the first mesh point from the foil surface to be at a wall unit of $y^+ = 1$. This required a very fine C-mesh to be used around the foil and in the wake region, as shown in Figure 3.22. A much coarser mesh was used in the far field in order to reduce computational costs, and the two meshes were blended using an unstructured block. A full grid independence study was conducted with geometrically similar meshes spanning 32,000 volumes to 300,000 volumes. The solution was found to be grid independent for meshes over 75,000 volumes.

The operating conditions used for the simulations are shown in Table 3.2. The foil chord length, gap, angles-of-attack and flap angles studied are the same as those used in the experiments. The simulations were run at a tip speed of $V_t = 20$ m/s.

Table 3.2: Test conditions used in the simulations.

Foil Parameters:	
MEF Chord:	60 mm.
Angles-of-attack:	0, 2, 4, 6 deg.
Flap Angles:	12, 17, 22 deg.
Clearance Gap:	5 mm.
Cylinder Parameters:	
Cylinder Diameter:	20.32 cm.
Test Parameters:	
Tip Speed:	20 m/s
Fluid:	Water, 20 °C

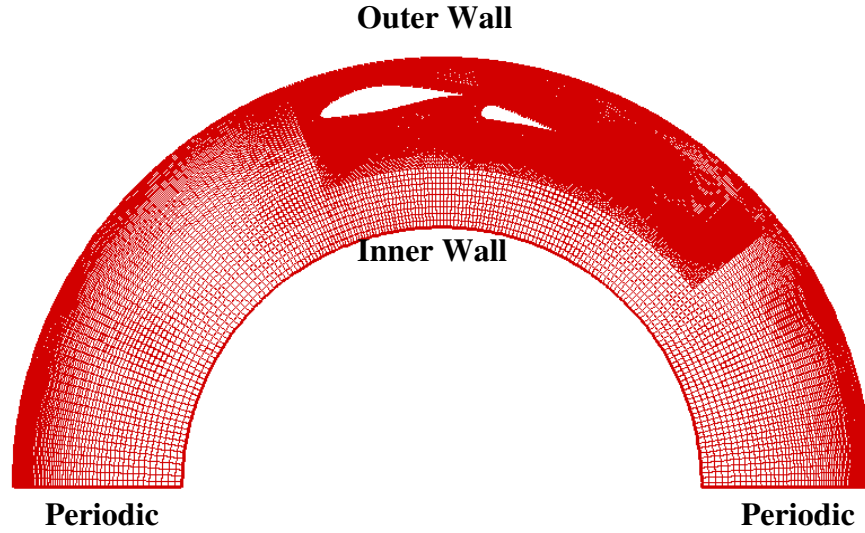


Figure 3.22: Computational domain used in the study and a typical mesh with boundary conditions labeled.

3.5 Numerical Results and Discussion

Figure 3.23 shows the experimental and numerical non-dimensional pressure traces for the MEF at $(\alpha, \delta) = (0, 22)$ deg. Changing the turbulence model can be seen to have little effect on the numerical results. Also, for the configuration shown, the numerical results capture the negative portion of the pressure pulse well, but severely under predict the magnitude of the positive pressure pulse. The numerical results for the $k-\epsilon$ model over predict the magnitude of the negative pressure pulse by 5.8%, while the results for the $k-\omega$ SST model over predict the magnitude of the negative pressure pulse by 7.3%. Because the $k-\epsilon$ model was shown to have slightly better performance, all numerical results shown and discussed from here on were generated using that turbulence model.

Figure 3.24 shows minimum pressure coefficient plotted as a function of flap angle with lines of constant angle-of-attack from the CFD results. The results for $\alpha = 0$ deg. and $(\alpha, \delta) = (2, 12)$ deg. match well with the experimentally measured values. Increasing either angle-of-attack or flap angle beyond $(\alpha, \delta) = (2, 12)$ deg. causes a reduction in the

magnitude of the minimum pressure coefficient, with an optimum value at $(\alpha, \delta) = (0, 22)$ deg. This is significantly different than what was shown experimentally, where the magnitude of the minimum pressure coefficient continued to increase as angle-of-attack and flap angle were increased.

The reduction of the magnitude of the negative pressure pulse as the angle-of-attack and flap angle are increased beyond an optimum value is likely due the flow separating from the foil. This was described in Delfel *et al.* [19] and is also shown in Figure 3.25, which shows pressure contours and streamlines for the MEF at varying angle-of-attack and a constant flap angle. As the angle-of-attack is increased beyond $\alpha = 2$ deg., the main foil begins to stall, reducing the magnitude of the negative pressure pulse. The reason that the simulations predict flow separation well before what was found experimentally is likely due to use of a solid wall boundary condition rather than the actual slotted screen cylinder. If the flow through the slots had been simulated, momentum would have been transferred through the slots as they were backflushed, preventing flow separation over the foil.

The use of the solid wall rather than modeling the flow through the slots therefore makes the simulations overly conservative in the predicting the angles for the optimum MEF configuration – the experimental results show that the MEF can be operated at higher angles without stalling the foil. While this limits the effectiveness of the model used, it is still been shown to be a useful tool, since the MEF was designed using this model and has been shown to perform well in pilot plant and full scale mill trials [20, 21]. The results from the numerical model may also provide insight into how the optimum configuration of the rotor changes as the cylinder blinds. As the cylinder blinds, the numerical results suggest that the MEF at higher angles-of-attack would stall and cause the screen to fail suddenly, but the MEF at lower angles-of-attack would not be as strongly affected. Further analysis, both experimentally and numerically, is needed to fully understand these phenomena, however.

The CFD results for the effect of varying the MEF geometry on the maximum pressure coefficient are shown in Figure 3.26. As mentioned previously, the model under predicts the magnitude of the maximum pressure coefficient by an order of magnitude compared to the experimental results. The trends for the unstalled cases match the experimental results well in that increasing both the flap angle and the angle-of-attack reduce the magnitude of the maximum pressure pulse. Beyond $(\alpha, \delta) = (2, 17)$ deg., however, increasing flap angle causes the magnitude of the maximum pressure coefficient to increase. Also, beyond $\alpha = 2$ deg., where there is heavy flow separation, increasing both the flap angle and the angle-of-attack causes the maximum pressure coefficient to increase slightly. The reason that the CFD under predicts the magnitude of the maximum pressure coefficient is again likely due to the use of a solid wall boundary rather than a slotted cylinder. With a slotted cylinder, the adverse pressure gradient across the slots would likely cause the stagnation point at the leading edge of the foil to be further towards the upper surface of the foil (closer to the cylinder) than in the case of a solid cylinder wall. As discussed in other studies, this would cause the positive pressure pulse transmitted from the foil to screen wall to be stronger [1, 3, 4, 19].

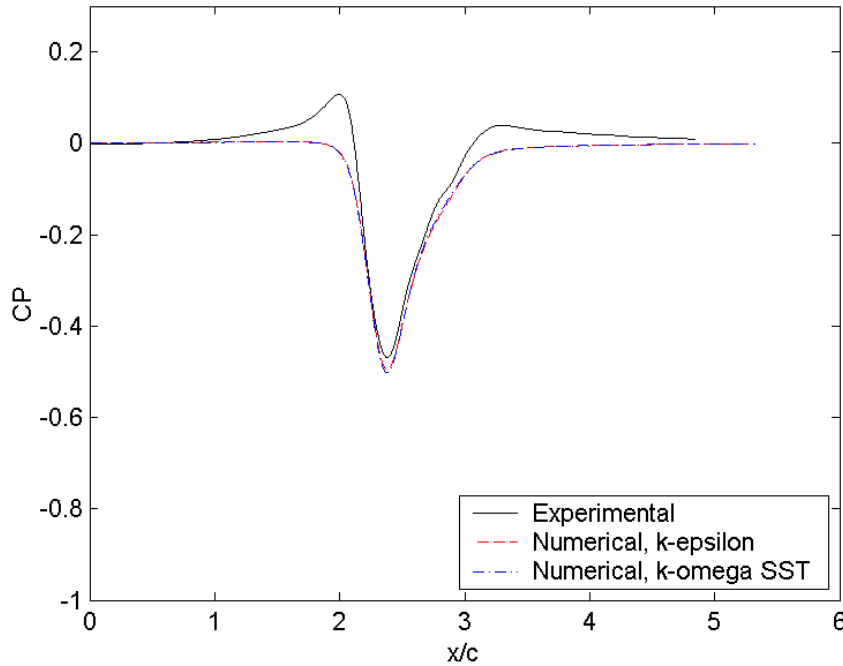


Figure 3.23: Experimental and numerical non-dimensional pressure traces for the MEF at $(\alpha, \delta) = (0, 22)$ deg.

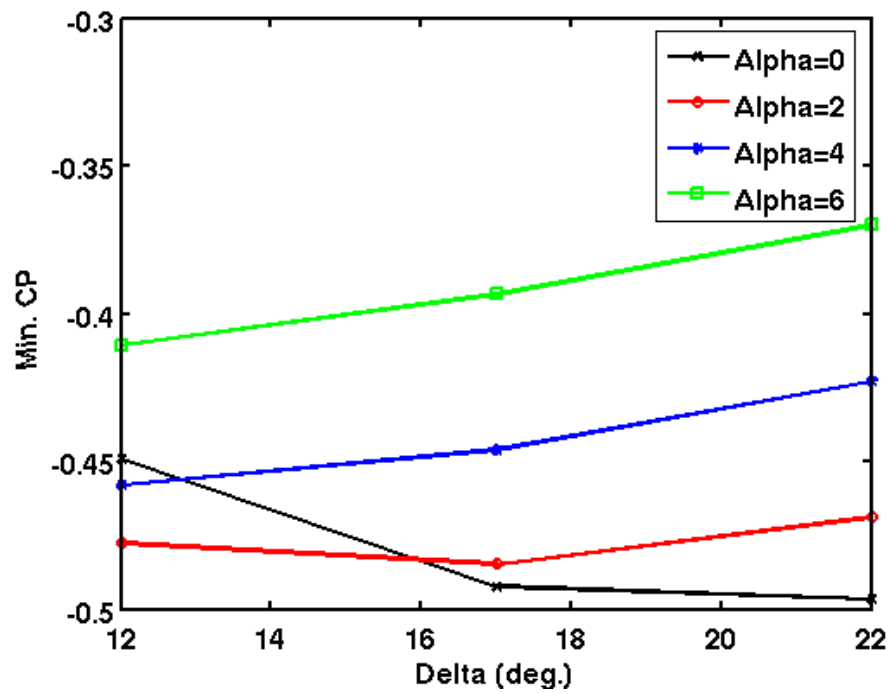


Figure 3.24: Numerically predicted minimum pressure coefficient on the cylinder wall for varying MEF geometry. The results were obtained using the $k-\epsilon$ turbulence model.

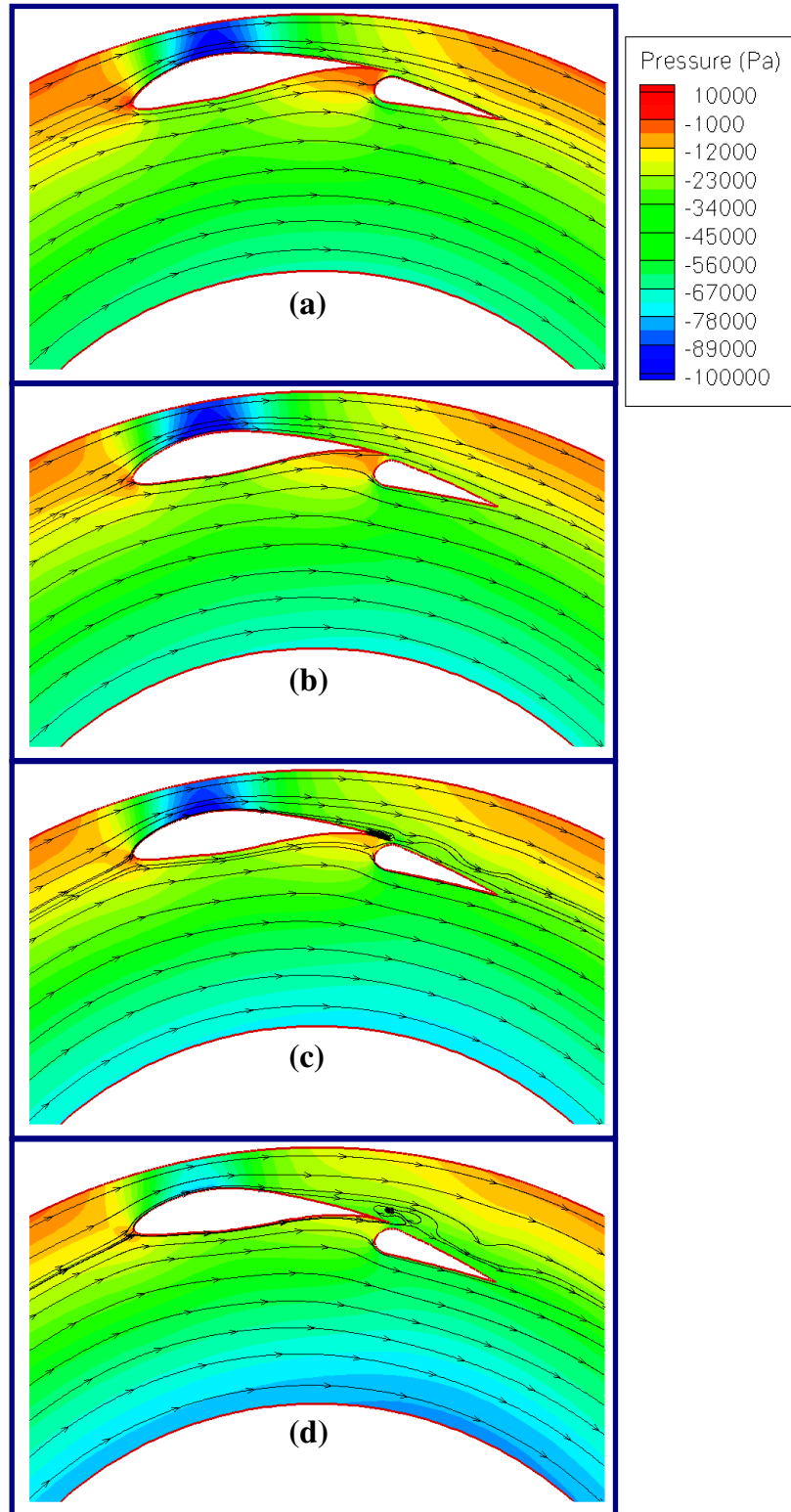


Figure 3.25: Numerically generated pressure contours and streamlines for the MEF at (a) $\alpha = 0$ deg., (b) $\alpha = 2$ deg., (c) $\alpha = 4$ deg., and (d) $\alpha = 6$ deg., and a flap angle of $\delta = 12$ deg.

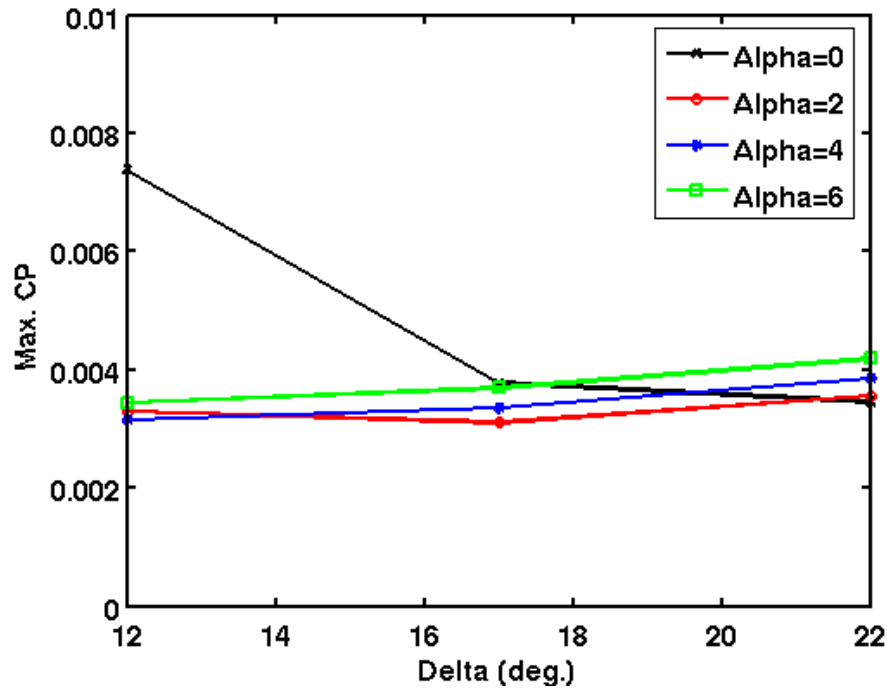


Figure 3.26: Numerically predicted maximum pressure coefficient on the cylinder wall for varying MEF geometry. The results were obtained using the $k-\epsilon$ turbulence model.

3.6 Conclusions

The pressure pulses produced by a multi-element foil rotor and a single-element foil rotor were studied experimentally in a laboratory pressure screen. The effects of foil angle-of-attack, flap angle, rotor tip speed and flow rates on pressure pulse magnitude and shape were determined.

It was shown that at high enough tip speeds, the non-dimensional pressure pulse is Reynolds number independent, and that the magnitude of the pressure pulse varies with rotor tip speed squared. At low tip speeds the magnitude of the non-dimensional pressure pulse begins to fluctuate and diminish, most likely due to the onset of separation of the flow over the foils.

It was also shown that increasing both the angle-of-attack and the flap angle of the MEF increases the magnitude of the negative pressure pulse. The best MEF configuration in terms of the magnitude of the negative pressure pulse was at $(\alpha, \delta) = (6, 22)$ deg., generating a peak negative pressure coefficient of $C_p = -0.81$, which was a 126% increase in magnitude compared to the single-element foil. Increasing the angle-of-attack and the flap angle also reduced the magnitude of the positive portion of the pressure pulse until an optimal angle, beyond which the magnitude of the positive pulse increased. The best performing MEF configuration with respect to the positive pulse reduced the magnitude of the maximum C_p by 39% compared to the single-element foil rotor.

Increasing the slot velocity was shown to have no effect on the magnitude of the pressure pulses or the trends for varying geometry above a critical tip speed. The critical tip speed at which the pressure pulse caused by the foil becomes Reynolds number independent was found to increase with increasing slot velocity. This is most likely due to the increase in adverse pressure gradient associated, which leads to flow separation at lower Reynolds numbers.

Finally, the results of a CFD model of the MEF rotor in a pressure screen were compared to the experimental results. For low angles-of-attack, the simulations predicted the negative portion of the pressure pulse well, but significantly under predicted the magnitude of the positive pulse. The CFD model also predicted the foil would begin to stall above an angle-of-attack of $\alpha = 2$ deg., causing the magnitude of the negative pressure pulse to diminish. This caused the simulations to under predict the magnitude of the negative pressure pulse at higher angles of attack. It is likely that the simulations over predicted flow separation due to the use of a solid wall as the screen cylinder, which was meant to represent a plugged cylinder. In reality, low momentum fluid is transferred to the foils as the slots are backflushed, preventing stall. In spite of these limitations, the CFD model has been shown to provide insight into the flow physics and to be a useful design tool for pressure screen rotors.

3.7 References

1. Feng, M., “Numerical Simulation of the pressure pulses generated by a pressure screen foil rotor”, M.A.Sc. Thesis, Dept. Mech. Eng., Univ. British Columbia, 2003.
2. Feng, M., Olson, J.A., Ollivier-Gooch, C.F., Xia, J., and Gooding, R.W., A computational fluid dynamic (CFD) tool for advanced pulp screen foil rotor design”, 2003 ABTCP Conf.
3. Feng, M., Gonzales, J., Olson, J.A., Ollivier-Gooch, C., and Gooding, R.W., “Numerical simulation of the pressure pulses produced by a pressure screen foil rotor”, J. Fluid Eng., 127(2):347-357 (2005).
4. Gonzales, J., “Characterization of design parameters for a free foil rotor in a pressure screen”, M.A.Sc. Thesis, Dept. Mech. Eng., Univ. British Columbia, 2002.
5. Pflueger, C.D., Olson, J.A., and Gooding, R.W., “The performance of the EP Rotor in de-ink pulp screening”, 2007 Appita Conf., 165-169.
6. Niinimäki, J., “Phenomena affecting the efficiency of a pressure screen”, 1999 Tappi Pulping Conf., 957-966.
7. Julien Saint Amand, F., and Perrin, B., “Fundamentals of screening: Effect of rotor design and fibre properties”, 1999 Tappi Pulping Conf., 941-955.
8. Julien Saint Amand, F., and Perrin, B., “Basic parameters affecting screening efficiency and fibre loss”, 2000 PTS-CTP Deinking Symposium, 26.1–26.22.
9. Wakelin, R.F., Blackwell, B.G., and Corson, S.R., “The influence of equipment and process variables on mechanical pulp fractionation in pressure screens”, 1994 Appita Conf., 611-621.
10. Wakelin, R.F., and Corson, S.R., “TMP long fractionation with pressure screens”, 1995 Int. Mech. Pulping Conf., 257-265.
11. Wakelin, R.F., and Corson, S.R., “Reject thickening behavior of TMP screening”, Pulp Paper Can., 99(1): 27-30, 1998.
12. Pinon, V., Gooding, R.W., Olson, J.A., “Measurement of pressure pulses from a solid core rotor”, Tappi J., 2(10): 9-12, 2003.
13. Olson, J.A., Turcotte, S., Gooding, R.W., “Determination of power requirements for solid core pulp screen rotors”, Nordic Pulp Paper Res. J., 19(2):213-217, 2004.

14. Yu, C.J., "Pulsation measurement in a screen. Part I: Pulse signature and magnitude of S-shape rotor", 1994 Tappi Engineering Conf., 767-782.
15. Atkins, M., "Axial variations and entry effects in a pressure screen", Ph. D. Thesis, Dept. of Eng., Univ. of Waikato, 2007.
16. Karvinen, R., and Halonen, L., "The effect of various factors on pressure pulsation of a screen", Paperi ja Puu, 2: 80-83, 1984.
17. Wikstrom, T., and Fredriksson, B., "Hydrodynamics in a pressure screen – consequences on the separation process", 5th Research Forum on Recycling Preprints, 1999, 197-202.
18. Luukonen, A., Delfel, S., Olson, J., Pflueger, P., and Ollivier-Gooch, C., "Numerical simulations of pressure pulses produced by a solid core pressure screen rotor", 2007 Appita Conf., 265-271.
19. Delfel, S., Ollivier-Gooch, C., and Olson, J., "A numerical investigation into the effectiveness of multi-element pressure screen rotor foils", J. Fluid Eng., 131(1): 011101-1, 2009.
20. Olson, J.A., Pflueger, C., Delfel, S., Ollivier-Gooch, C.F., Martin, P., Vaultot, F., and Gooding, R., "High Performance Foil Rotor Improves De-Ink Pulp Screening", Progress in Paper Recycling, 2009 (?).
21. Hamelin, M., Delfel, S., Olson, J., and Ollivier-Gooch, C., "High performance multi-element foil (MEF) pulp screen rotor – pilot and mill trials", 2009 Paptac Conf. preprints.
22. Naser, J.A., "Prediction of Newtonian and non-Newtonian flow through concentric annulus with centerbody rotation", Int. Conf. on CFD in Mineral and Metal Proc. and Power Generation Proc., CSIRO, Melbourne, 273-278, 1997.
23. Wilcox, D.C., "Turbulence modeling for CFD", California, USA, DWC Industries, Inc., 1998.
24. Menter, F.R., "Performance of popular turbulence models for attached and separated adverse pressure gradient flows", AIAA J., 30(8): 2066-2072, 1992.
25. Menter, F.R., "2-Equation eddy-viscosity turbulence models for engineering applications", AIAA J., 32(8): 1598-1605, 1994.
26. Pope, S.B., "Turbulent Flows", Cambridge Press, 2000.

Chapter 4

High Performance Multi-Element Foil (MEF) Pulp Screen Rotor – Pilot and Mill Trials³

4.1 Introduction

Pressure screens are the most industrially effective method of removing oversize contaminants, such as, stickies and shives that reduce the strength, smoothness and optical properties of paper. Pressure screens are also used to fractionate the long and coarse fibres for targeted processing and enable the development of high-value specialty pulp products. In TMP screening, pressure screens are used to separate the long and coarse fibres for separate reject refining that improves quality and saves energy. For these reasons, pressure screens are an increasingly important unit operation in pulping, recycling and papermaking.

The two performance determining components of a pressure screen are the screen cylinder and rotor. Once the unscreened pulp enters the screen via the feed stream, the accept fibres pass through small slots or holes in the screen cylinder to the accept stream, while oversized particles continue down the length of the cylinder to the reject stream. The rotor uses a foil which generates pressure pulses at the screen surface to backflush the narrow slotted apertures, clearing them of accumulations that could lead to plugging [1-4]. The rotor design and speed thus directly affect the maximum capacity of the screen [5].

³ A version of this chapter has been accepted for publication. Hamelin, M., Delfel, S., Olson, J., and Ollivier-Gooch, C., “High performance multi-element foil (MEF) pulp screen rotor – pilot and mill trials”, Pulp and Paper Canada, 2009.

Previous experimental and computational studies have examined the effect of rotor design on screen performance. These studies showed that the pressure pulse generated by the foil has two components: a positive pressure component created by the stagnation point on the leading edge of the foil and a negative pressure component generated over the top surface of the foil that performs the backflusing action. The positive pressure component that forces deformable debris through the screen cylinder and lowers efficiency was shown to be nearly eliminated when the foil was oriented to have a positive angle-of-attack with the screen cylinder. Angle-of-attack is defined as the angle of the foil chord relative to a line tangential to the cylinder. The magnitude of the negative pressure component is directly related to the capacity of the screen [2].

The magnitude of the negative pressure pulse is proportional to the square of the rotor tip speed, V_t [1-4]. Pilot studies have shown that the maximum capacity of the screen increases approximately linearly with rotor tip speed [5]. The power consumed by the rotor, however, increases with the cube of tip speed [7]. Therefore, small increases in rotor tip speed can significantly increase power consumption and screen operating costs. Increasing the camber (i.e. the curvature) of the foil was also shown to increase the strength and width of the negative pressure pulse generated by the rotor. The high camber foils were found, however, to stall almost immediately at a very small angle-of-attack. In order to obtain the effect of a highly cambered foil at a high angle-of-attack, multi-element foil (MEF) technology was developed for a pulp screen [8]. Similar to the flaps on an aircraft deployed during landing, multi-element airfoils generate high lift (negative pressure) at low speeds enabling high camber foils to operate at positive angle-of-attacks without stalling. Stall is prevented by allowing higher energy fluid from the lower surface of the foil to pass through the slot between the main foil and the flap in order to re-energize the boundary layer on the upper surface of the foil.

To determine the optimal design configuration of a multi-element foil rotor, a systematic computational fluid dynamic simulation studies was completed [9]. The angle-of-attack, flap angle and position were optimized for our multi-element foil rotor. In this study,

FLUENT 6.1 was used to numerically solve the discretized Navier-Stokes equations. The problem was assumed to be two dimensional, and steady state, allowing the Navier-Stokes equations can be reduced to the continuity and x - and y -momentum equations. Turbulence was modeled using the standard k - ϵ turbulence model with enhanced wall treatment. The solver is a second-order finite volume solver: control volume averages are found for each flow variable and the fluxes at the control volume faces are then found through a second-order spatial interpolation from the control volume center.

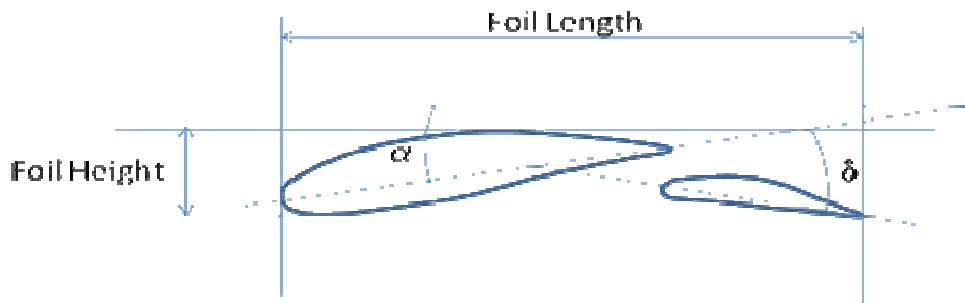


Figure 4.1: MEF showing angle-of-attack, α , and flap angle, δ .

The effect of varying flap angle, α , can be seen in Figure 4.2. Figure 4.2 shows pressure contours and streamlines for a multi-element foil at varying flap angles with a constant angle-of-attack of $\alpha = -8.8 \text{ deg}$. As can be seen, deflecting the flap, which is effectively an increase in the camber of the foil, causes the pressure pulse to widen and strengthen until $\delta = 27.8 \text{ deg}$, after which the flow over the flap begins to separate and suction at the wall diminishes. At $\delta = 44.8 \text{ deg}$, the flap has stalled fully and the beginnings of vortex shedding can be seen. Interestingly, increasing flap angle also has the affect of forcing the stagnation point towards the lower surface of the leading edge of the foil, diminishing the positive pulse on the screen.

Similarly the effect of angle-of-attack, α , was determined [9]. From the α - and δ -sweep data was combined to make surfaces of the minimum pressure on the cylinder (Suction pulse magnitude) given in terms of non-dimension pressure, C_p , where

$$C_P = \frac{P}{0.5 \cdot \rho \cdot V_i^2} \quad (4.1)$$

The C_P values, versus both α and δ , are shown in Figure 4.3. Minimum C_P is shown to have a strong dependence on flap angle for angles-of-attack at which the flow is fully attached, creating a “trough”-like shape with a clear minimum of $C_P = -0.82$ at $(\alpha, \delta) = (-7.6, 24.8)$. The gradients close to the optimum are relatively low, however, allowing for flexibility in the foil design. Beyond $\alpha = -1.8$ deg., any deflection of the flap causes the foil to stall and the pressure becomes independent of flap angle.

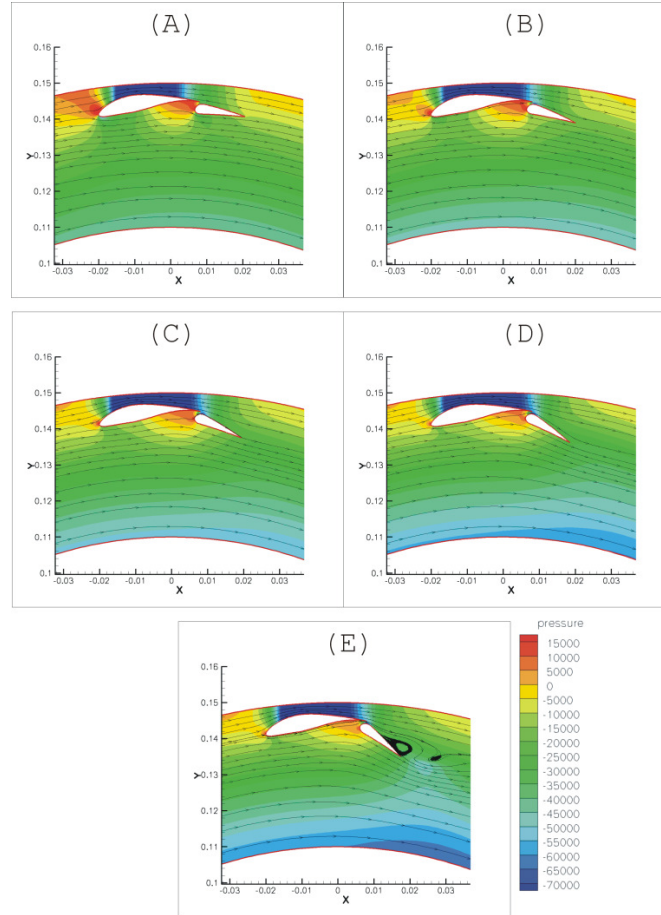


Figure 4.2: Pressure contours and streamlines for a multi-element foil at (A) $\delta = 15.8$ deg., (B) $\delta = 23.8$ deg., (C) $\delta = 30.8$ deg., (D) $\delta = 37.8$ deg., and (E) $\delta = 44.8$ deg. The foil is at $\alpha = -8.8$ deg. for all cases. [9]

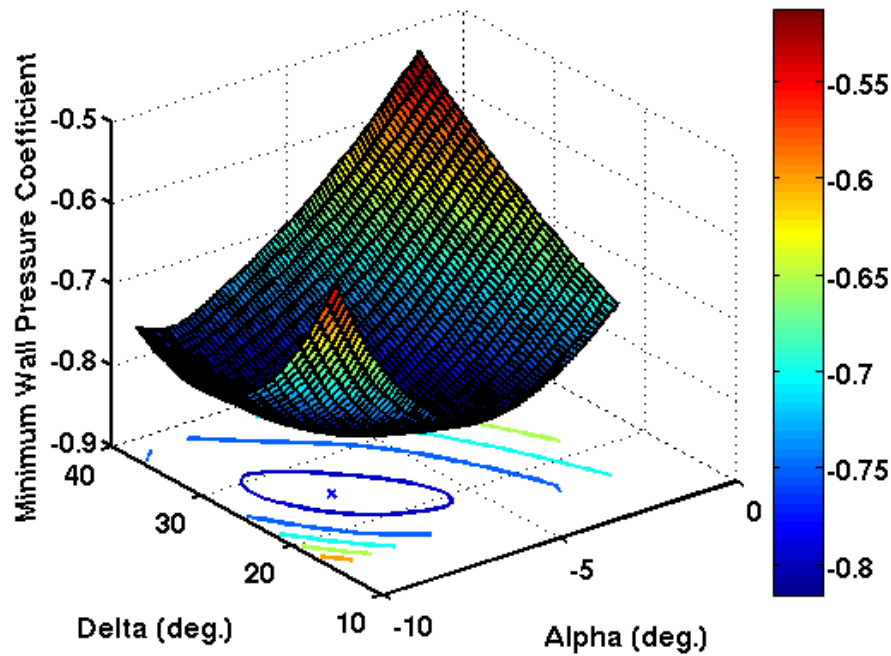


Figure 4.3: Surfaces of minimum wall pressure coefficient vs. foil angle-of-attack and flap angle showing the optimal configuration [9].

4.2 Pilot Screening Trials

To experimentally validate the fluid and pressure simulations and to determine the performance of the optimal multi-element foil rotor a series of pilot screening trials were conducted for a range of angle-of-attack and flap angle configurations.

The study was conducted at the FPIInnovations – Paprican Division, Vancouver screening pilot plant using a fully instrumented Hooper PSV 2100 pressure screen. The screen was equipped with a variable frequency drive (VFD), allowing for rotor tip speeds of up to 20 m/s. A wedge-wire cylinder with a 3.2 mm wire width, 0.9 mm contour height, and a 0.2 mm slot width was used in the trial. The cylinder has a diameter of 0.286 m and an open area of 5.98%. Due to the large diameter bearing column on the lower half of the screen, the cylinder was modified by covering the lower 9 out of 15 rings with metal strips, reducing the active screening area and allowing the use of a shorter foil length,

appropriate for the bearing housing. The effective open area of the screen after the modifications was $8.7 \times 10^{-3} \text{ m}^2$.

The pulp used was a 1.5% consistency 50% hardwood, 50% softwood (by mass) kraft pulp which represents a model deink pulp. The feed was supplied from a 10,000 L stock tank kept at a nominal temperature of 49° C. The feed concentration varied significantly over the course of the test from a starting concentration of 1.524% to a low of 1.227% due to the leaking of seal water into the stock. Feed samples were collected at least once for each rotor configuration, while reject and accept samples were collected at a slot velocity of 1.0 m/s for every rotor speed.

For each rotor configuration tested the maximum slot velocity-power curve was determined by setting the rotor speed to a constant value and increasing the slot velocity until the onset of plugging. The point of maximum slot velocity versus rotor power, creates a failure envelope (or maximum slot velocity envelope) for each rotor and is used to compare the performance of each configuration.



Figure 4.4: Photograph of FPInnovation's Hooper PSV 2100 Pilot Screen and the prototype adjustable MEF rotor showing the slot between main foil and flap.

The angle-of-attack, α , is the angle of the main foil chord with respect to the horizontal, and the flap angle δ is the angle between the flap chord and the main foil chord. Three different angles-of-attack were tested, varying from -8.8 deg. to -3.3 deg., and at each angle-of-attack three separate flap angles were tested, varying from 18.8 deg. to 28.8 deg. In addition to the MEF foil rotor, a single foil rotor EP and a OEM Hooper XT rotor was tested for comparison.

4.3 Results and Discussion

The maximum capacity envelopes for the two best MEF and EP rotors are shown in Figure 4.5, with the XT rotor omitted for clarity (the XT rotor is shown in Figure 4.6). The key gains in performance for the MEF come from its ability to run reliably below a tip speed of 10 m/s. Several of the MEF configurations ran reliably at 8 m/s, and the suboptimal MEF configurations performed similarly to the EP. Configuration 6, corresponding to $\alpha = -3.3$ deg and $\delta = 23.8$ deg, had the lowest minimum power consumption measured: 2.0 kW at $V_t = 8.0$ m/s, $V_s = 2.68$ m/s, a 26% reduction in minimum power versus the single foil EP rotor. Configuration 3, corresponding to $\alpha = -3.3$ deg and $\delta = 18.8$ deg, had the highest capacity at a given rotor power, with an improvement of 31% in maximum slot velocity versus the single foil (EP) at $V_t = 12$ m/s and a constant power of approximately 3 kW.

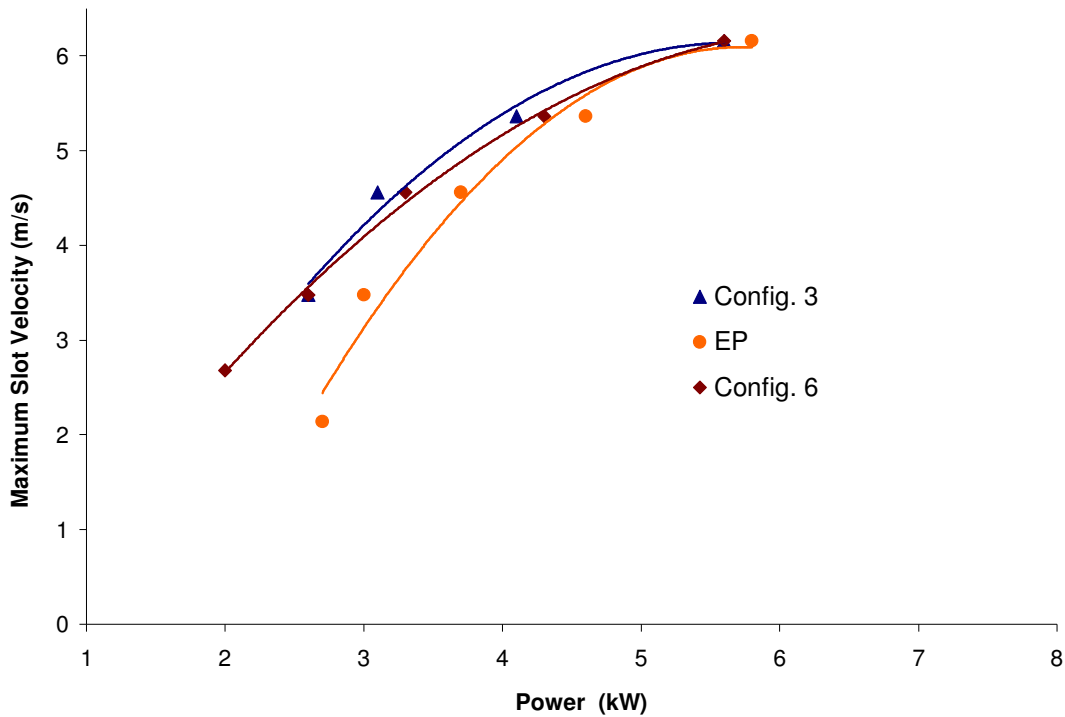


Figure 4.5: Plugging envelopes for the two best MEF rotors and the EP rotor.

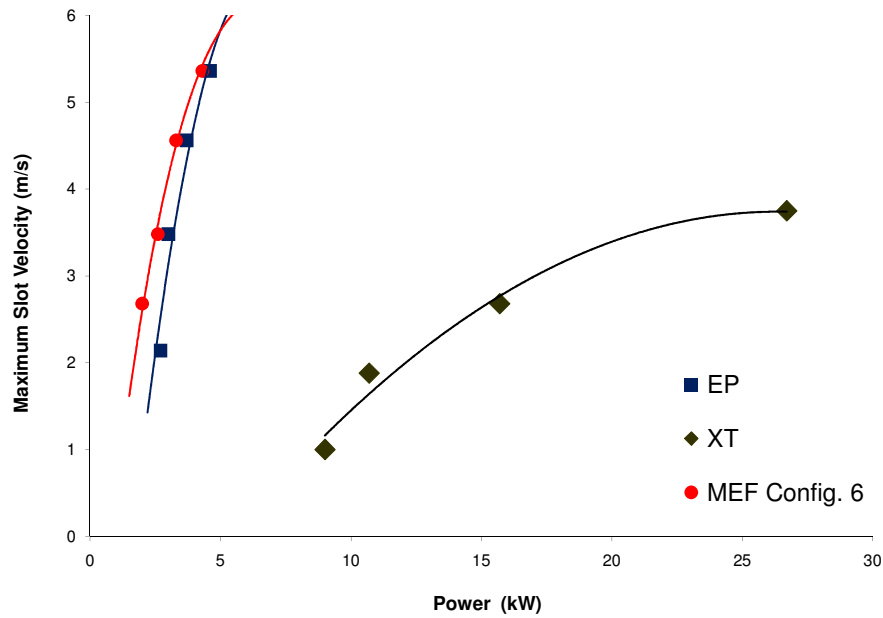


Figure 4.6: Plugging envelopes for the MEF rotor, the EP rotor and the Hooper XT rotor. Note: the full length XT rotor was trialed and shown here.

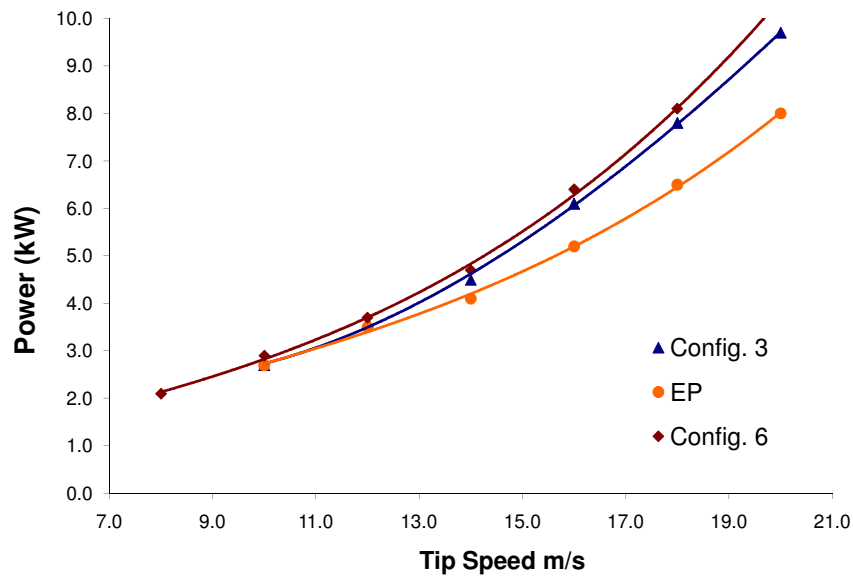


Figure 4.7: Effect of tip speed on rotor power consumption at $V_s=1.0$ m/s.

Figure 4.7 shows power consumption as a function of rotor tip speed. As expected, since single-element foils typically have lower drag coefficients, the EP rotor uses less power at a given tip speed than the MEF. The power savings for the MEF come from its ability to operate at lower tip speeds.

Figure 4.8 shows the effect of tip speed on thickening factor for each rotor at a constant slot velocity, $V_s = 1.0$ m/s. Both MEF configurations thickened less than the EP at low tip speeds. MEF configuration 6 had the best performance with respect to thickening, operating at a constant reject thickening factor (Reject consistency divided by accept consistency), $T = 1.1$. The XT rotor had significantly higher thickening than all other rotors tested.

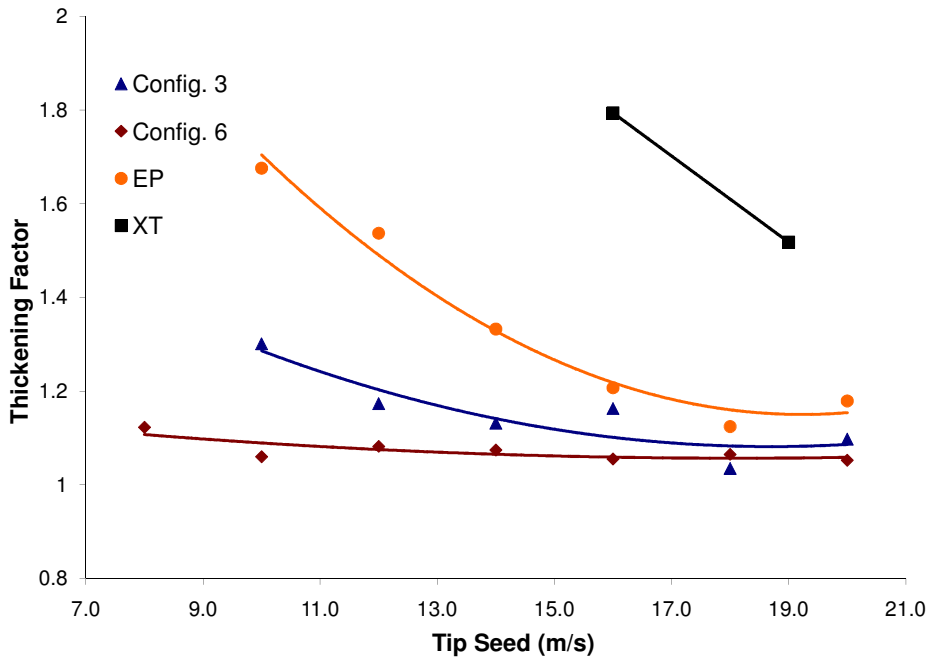


Figure 4.8: Effect of tip speed on thickening factor at a slot velocity, $V_s = 1.0$ m/s.

The effect of varying flap angle at constant angle-of-attack on maximum slot velocity and power is shown in Figure 4.9. The higher flap angles were able to achieve lower tip speeds, allowing for a larger reduction in power. However, at the higher tip speeds there isn't a significant improvement in capacity at a given power. Similarly, Figure 4.10 shows lines of maximum slot velocity for varying flap angle at constant angle-of-attack and a constant rotor speed. There is a clear trend of improved performance with increasing angle-of-attack and increasing flap angle. In the case of both flap angle and angle-of-attack, the optimal angles were higher than predicted numerically and the optimum angles are likely higher than those tested. This difference is expected performance is attributed to the differences in rheology between water and pulp suspensions and the use of a solid, rather than slotted, wall for the screen cylinder in the simulations. We hypothesize that turbulent pulp suspensions delay separation in comparison to water and that this phenomenon may be similar to turbulent drag reduction of pulp suspensions in pipe flow. The presence of slots in the cylinder, as discussed in Chapter 3, allows low momentum flow to enter the domain and prevent the foil from stalling.

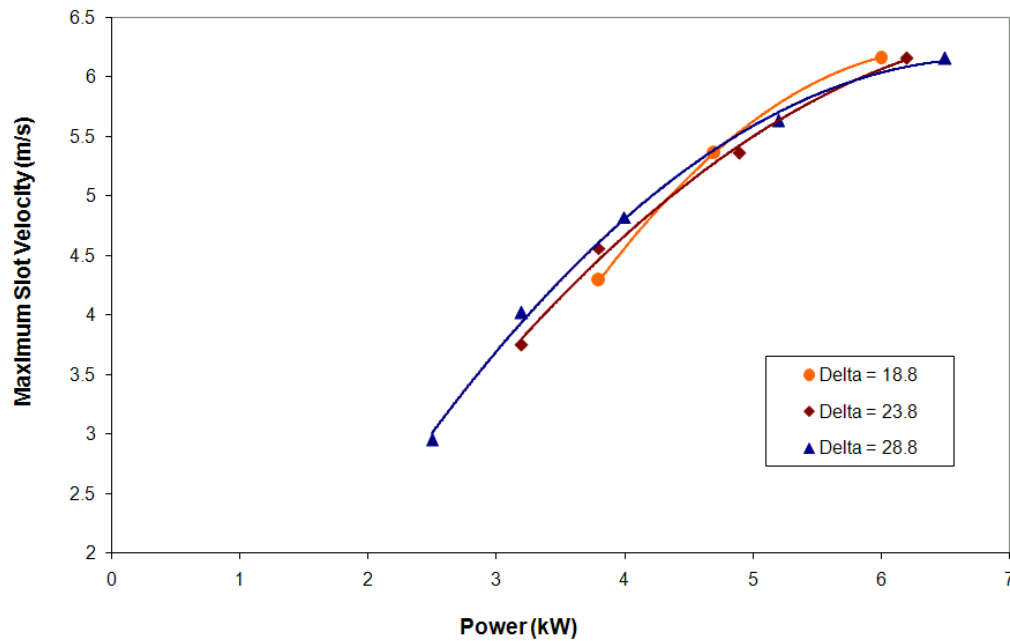


Figure 4.9: Effect of varying flap angle on maximum slot velocity for constant angle-of-attack, $\alpha = -8.8$.

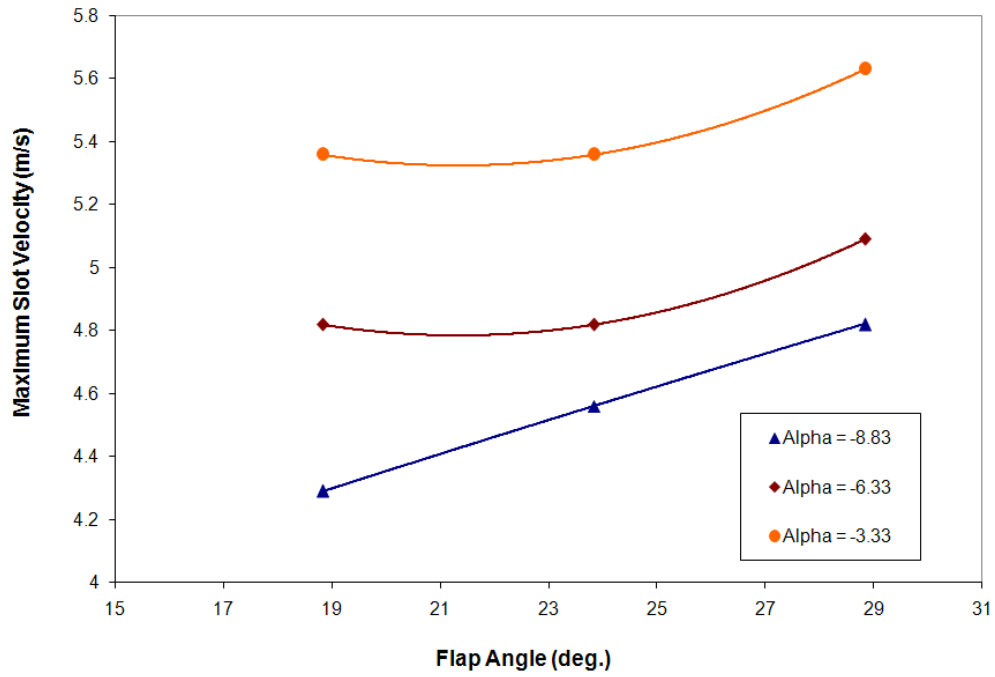


Figure 4.10: Effect of varying flap angle on a maximum slot velocity for constant rotor speed, $V_t = 14\text{m/s}$.

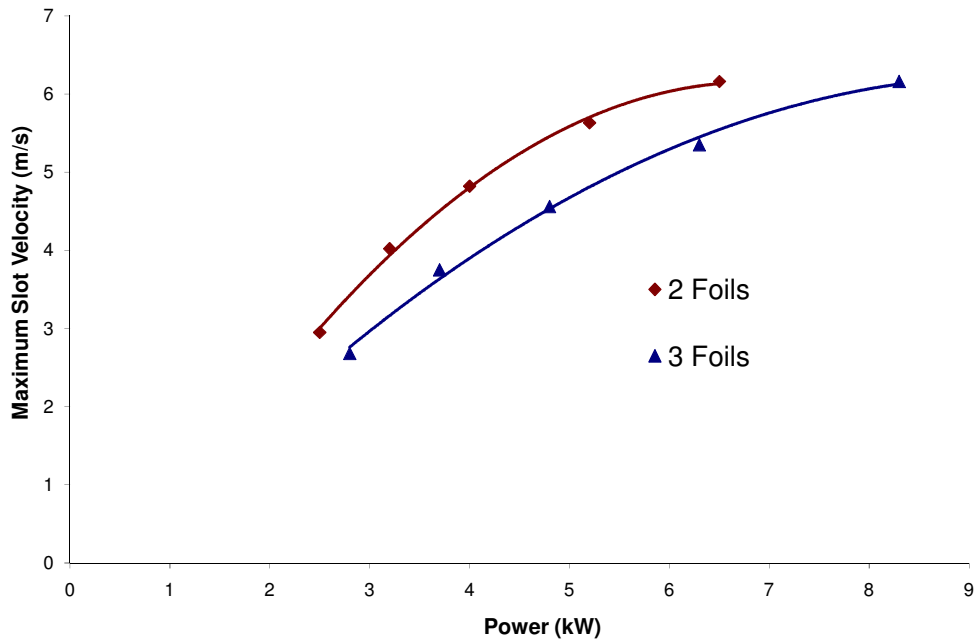


Figure 4.11: Maximum capacity – power relation for 2- and 3- foil rotors.

Finally, the effect of pulse frequency was studied by running one rotor with 2 foils and another with 3 foils, both with the same foil configurations. Figure 4.11 shows the plugging envelopes for the two rotors. As can be seen, the rotor with 2 foils clearly outperforms the 3 foil rotor, obtaining higher slot velocities at a given power. The 3 foil rotor not only used more power at a given tip speed, as would be expected, but also had lower capacity. The decrease in capacity was expected from the numerical simulations and is likely due to the foils following too close to the wake of the foil ahead of it. When the foils are closely spaced, the relative velocity of the foil and water is decreased which reduces the magnitude of the negative pressure pulse and decreases capacity. This phenomenon is examined in detail in Chapter 6.

4.4 Mill Application

The first mill prototype of the new AFT MEF™ rotor was tested in a GR20 primary fine screen at the Catalyst Paper mill in Coquitlam, British Columbia [10]. The MEF rotor was able to maintain the full required capacity of the screen even when operated at a tip speed of 13.3 m/s -- relative to the usual operating speed of 16 m/s. An energy saving of 42% and a significant stickies removal efficiency increase was achieved by operating the screen at this lower speed. This MEF mill trial is discussed in greater detail in Chapter 5.

The second, prototype MEF rotor was installed in a Black Clawson UV 300 at a recycle de-ink mill in the Southern USA (see Figure 4.12). The screen was equipped with a 0.12 mm (0.005") narrow slotted MacroFlow™ MF0623 screen cylinder. A parallel screen was originally equipped with a Black Clawson 4-foil and 2-foil rotor and a 0.15mm (0.006") slotted screen cylinder. The rotor and cylinder were later replaced with an AFT EP™ rotor and 0.12 mm (0.005") slotted screen cylinder. This enabled the performance of the four rotor-cylinder combinations to be compared.

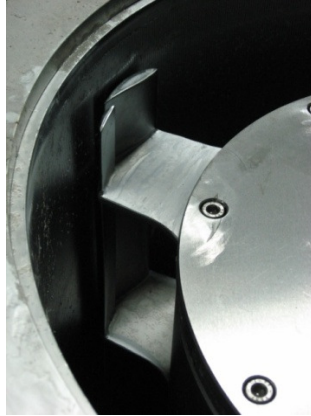


Figure 4.12. A photograph of the installed prototype AFT MEF™ Rotor following 23 days of continuous operation. There is no trace of stringing or wear.

The rotor tip speed was varied using AFT's variable frequency drive (VFD) which was brought to the mill and installed on the MEF trial screen. Figure 4.13 shows the power versus tip speed for the AFT MEF™ rotor and the other rotors at 20.8 m/s. The MEF™ rotor was initially installed and ran at 20.8 m/s. At this speed it consumed less power than the Black Clawson 4 foil rotor (66.3HP) and the EP™ rotor (73.3 HP). The Black Clawson 2 foil rotor consumed 57.4HP at a tip speed of 20.8 m/s.

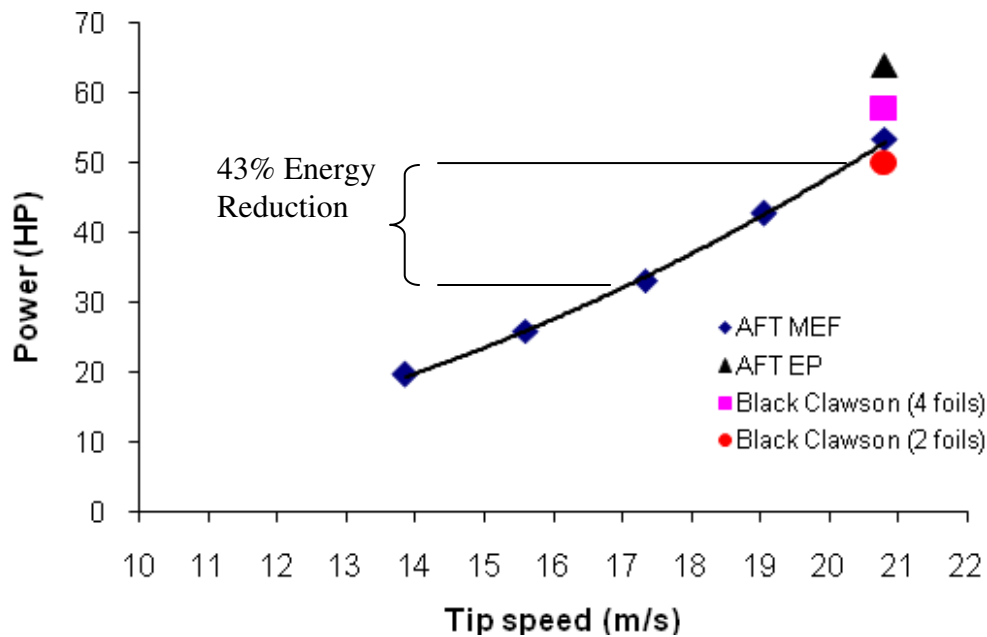


Figure 4.13 Power versus tip speed for the AFT MEF™ Rotor, EP™ Rotor and the Black Clawson 4 foil and 2 foil rotors. The MEF™ rotor provides a 43% energy reduction over the OEM rotor.

To determine the minimum power required to maintain capacity using the AFT MEF™ rotor the VFD was used to decrease rotor speed in 1.7 m/s increments. When the rotor was reduced to 13.9 m/s it began to plug over time. The rotor speed was then increased to 17.3 m/s to ensure adequate capacity. At this conservative rotor speed, the resulting energy savings over the OEM rotor is approximately 43%. The rotor speed could have most likely been reduced to 15.6 m/s which would have resulted in an energy savings of 61%. The minimum rotor speed was higher for the mill trials than pilot trials. This can be due to many factors that include differences in feed furnish, encompassing fibre length, fibre flexibility, fines content and debris content, as well as, differences in cylinder slot width: 0.12 mm used in the mill trial and 0.2 mm used in the pilot trials.

4.5 Conclusions

A new patented rotor technology has been developed to increase the strength and duration of rotor pulsations at low speeds without producing undesirable, positive pulse components. The improved pulse strength at low speeds results in higher capacity at significantly reduced energy consumption. The reduction of the positive pressure pulse along with the ability to run smaller slotted screen cylinders results in improved contaminant removal efficiencies. In this study, we determined the performance of several MEF configurations in pilot screening trials and demonstrated the advanced power savings in mill trials.

The pilot screening trials showed that the best MEF configuration was configuration 6 which has an angle-of-attack of -3.3 degrees and a flap angle of 23.8.

1. The optimal MEF had a 26% reduction in power and a 31% improvement in slot velocity in comparison with the state-of-the-art AFT EP™ Rotor.
2. Varying the foil configuration had a clear effect on performance -- higher angles-of-attack and flap angles led to improved power savings.
3. Pulse frequency was shown to have a considerable effect on screen performance. The 2 foil rotor performed better than the 3 foil rotor.
4. Both the EP and optimal MEF far outperformed the XT rotor in terms of power and capacity.

A prototype MEF™ rotor was installed in a Black Clawson UV 300 pressure screen at a recycle de-ink mill in Southern USA . The screen was equipped with a 0.12 mm (0.005”) slotted MacroFlow™ MF0623 screen cylinder. The mill trial demonstrated that:

5. The MEF™ rotor was capable of reliably operating at high capacity with narrow (0.12mm) slotted screen cylinder.
6. The MEF™ rotor was shown to provide a conservative 43% energy savings over the OEM rotor.

7. The rotor showed no signs of wear, stringing or plugging of the slot between the rotor and flap after 23 days of operation.

The excellent results of this trial follow on the fundamental benefits of the MEF™ rotor design. The MEF™ rotor uses its unique design to avoid boundary layer separation. Lower tip speeds and power are thus possible without compromising the action of the rotor or capacity of the screen.

4.6 References

1. Feng, M., “Numerical simulation of the pressure pulses produced by a pressure screen foil rotor”, M. A. Sc. Thesis, Dept. Mech. Eng., Univ. British Columbia, 2003.
2. Feng, M., Olson J.A., Ollivier-Gooch, C.F., Xia J., and Gooding, R.W., “A computational fluid dynamic (CFD) tool for advanced pulp screen foil rotor design” ABTCP Conf., San Paulo, Brazil, Oct. 2003.
3. Feng, M., Gonzalez J., Olson, J.A., Ollivier-Gooch, C., and Gooding, R.W., “Numerical simulation of the pressure pulses produced by a pressure screen foil rotor”, J. Fluid Eng. 127(2):347-357, 2005.
4. Gonzalez, J.A., “Characterization of design parameters for a free foil rotor in a pressure screen”, M. A. Sc. Thesis, Dept. Mech. Eng., Univ. British Columbia, 2002.
5. Pflueger, C.D., Olson, J.A., and Gooding, R.W., “The performance of the EP Rotor in de-ink pulp screening”, Preprints 2007 Appita Conf.
6. Julien Saint Amand, F., Perrin, B., Gooding, R., Huovinen, A., Asendrych, D., and Favre-Marinet, M., “Optimisation of screen plate design for the removal of stickies from deinking pulps”, PTS-Deinking Symposium, 2004.
7. Olson, J.A., Turcotte, S., and Gooding, R.W., “Determination of power requirements for solid core pulp screen rotors”, Nordic Pulp and Paper Res. J. 19(2):213-217, 2004.
8. Olson, J.A., and Ko, J., “Multi-Element Airfoil for Pulp Screens”, U.S. Patent No. 6,883,669, Apr. 26, 2005.
9. Delfel, S., Ollivier-Gooch, C., and Olson, J., “A numerical investigation into the effectiveness of multi-element pressure screen rotor foils”, J. Fluid Eng., 131(1): 011101-1, 2009.
10. Olson, J.A., Pflueger, C., Delfel, S., Ollivier-Gooch, C.F., Martin. P., Vaultot, F. and Gooding, R. “High Performance Foil Rotor Improves De-Ink Pulp Screening”, Progress in Paper Recycling, 17(4), 2008.

Chapter 5

High Performance Foil Rotor Improves De-Ink Pulp Screening⁴

5.1 Introduction

Pressure screens are the most effective means of removing oversize contaminants, such as stickies and shives, which reduce the strength, smoothness and optical properties of paper. Pressure screens are also used to fractionate the pulp by fibre length allowing for the production of high-value products. For these reasons, pressure screens are an increasingly important unit operation in pulping, recycling and papermaking.

A pressure screen contains two main components: the screen cylinder and rotor. Once the unscreened pulp enters the screen via the feed stream, the accept fibres pass through small slots or holes in the screen cylinder to the accept stream, while oversized particles continue down the length of the cylinder to the reject stream. The rotor uses a foil which generates pressure pulses at the screen surface to backflush the narrow slotted apertures clearing them of accumulations that could lead to plugging [1-4]. The rotor design and speed thus directly affect the maximum capacity of the screen [5].

The pressure pulsations typically contain two components. There is a negative (or suction) component which performs the backflushing action. One seeks to maximize this. There is also a positive component which could cause stickies to be extruded and forced through the slot and into the accept stream [6]. One seeks to minimize, or eliminate, the positive pressure pulse component.

⁴ A version of this chapter has been published. Olson, J., Pflueger, C., Delfel, S., Ollivier-Gooch, C., Martin, P., Vaultot, F., and Gooding, R., “High performance foil rotor improves de-ink pulp screening”, *Progress in Paper Recycling*, 17(4), 2008.

Previous investigations into screen rotor design have shown that increasing the magnitude of the negative pressure pulse generated by the rotor will increase the capacity of the screen [2]. The magnitude of the negative pressure pulse is proportional to the square of the rotor tip speed [1-4]. Pilot studies have shown that the maximum capacity of the screen increases approximately linearly with rotor tip speed [5]. The power consumed by the rotor, however, increases with the cube of tip speed [7]. Therefore, small increases in rotor tip speed can significantly increase power consumption and screen operating costs.

To improve the power-capacity relation of a screen rotor, several studies have examined the effect of rotor foil design on the magnitude of the negative pressure pulse [1-3]. The "angle of attack" was identified as a key parameter in rotor foil performance, and it is the angle formed between the chord of the foil and the direction of the fluid, as shown in Figure 5.1. In a pulp screen, the general fluid flow is circumferential. Thus the angle-of-attack is the angle of the foil chord relative to a line tangential to the cylinder.

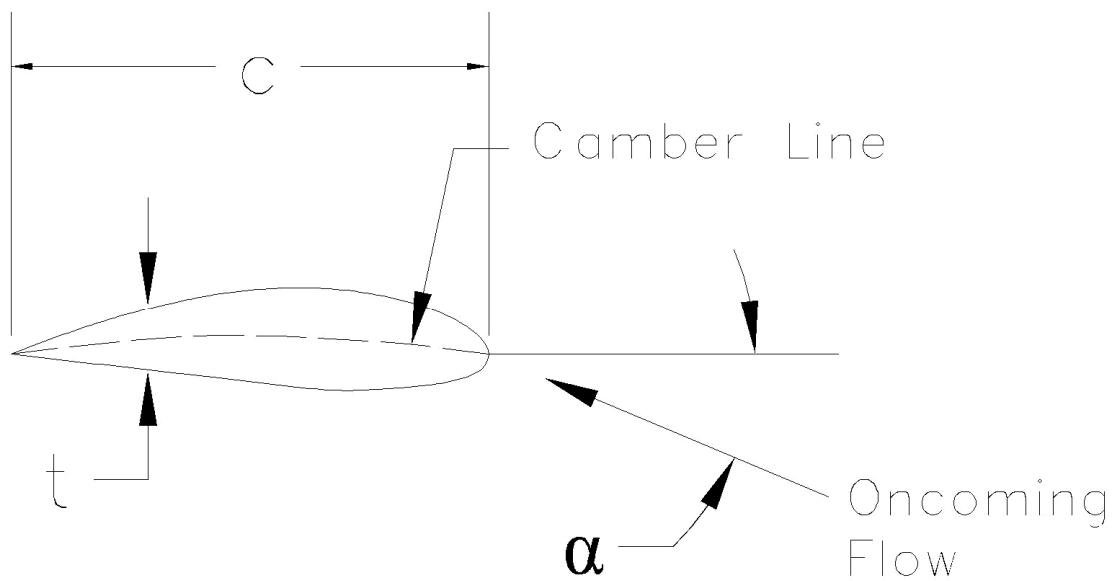


Figure 5.1: Single-element foil geometry.

These fundamental studies showed that increasing the angle-of-attack of the foil would do two things: First, it increases the magnitude of the negative pressure pulse generated by the foil prior to the point of flow separation. Second, the undesirable positive pulse at the leading edge of the foil was eliminated. At higher angles-of-attack, however, the foil would stall and the strength of the suction pulse would diminish.

Increasing the camber (i.e. the curvature) of the foil was also shown to increase the strength and width of the negative pressure pulse generated by the rotor. The high camber foils were found, however, to stall almost immediately at a very small angle-of-attack. In order to obtain the effect of a highly cambered foil at a high angle-of-attack, multi-element foil (MEF) technology was developed for a pulp screen [8]. Similar to the flaps on an aircraft, multi-element airfoils allow higher energy flow from the lower surface of the foil to pass through the slot between the main foil and the flap in order to re-energize the boundary layer on the upper surface of the foil. This has the effect of preventing stall on the foil, allowing for higher magnitude negative pulses at a given rotor tip speed, while at the same time eliminating the positive pulse component. Figure 5.2 shows the pressure contours for single and multi-element foils and how a stronger and wider pressure pulse is generated by the MEF configuration.

The main parameters of pulp screen performance are: capacity, debris removal efficiency and power consumption. Capacity is the mass flow of pulp in the accept stream of the screen. Debris removal efficiency reflects the ability of the screen to direct oversize debris from the feed to the reject stream. Power is best expressed as the net power to the screen (excluding winding losses), but is most commonly given as the total power, as shown on the Distributed Control System (DCS) in a pulp mill. The goal in designing high-performance rotors is to improve on one of the performance parameters without compromising the others. This study examines the results from a prototype MEF rotor in a mill study which meets this goal.

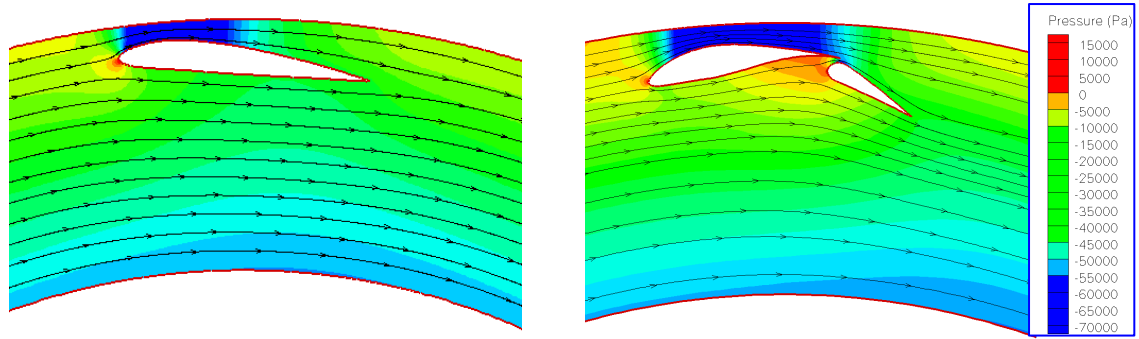


Figure 5.2: The computed fluid streamlines colored by pressure contours for a single foil (left) and a multi-element foil (right).

5.2 Rotor Design and Experimental Setup

The design of the MEF rotor was evaluated using computational fluid dynamics (CFD). CFD has been validated for use as a tool in pressure screen rotor design in a number of studies. In the case of the MEF rotor, a second-order finite volume solver, FLUENT 6.1, was used to numerically solve the discretized Navier-Stokes equations. Following the results in Mahon and Zhang [9], the $k-\varepsilon$ model with enhanced wall treatments was used to model the turbulence in the flow.

A commercial, high-cambered foil rotor was used as a starting point for the new foil design [4-5]. A wide range of foil parameters were studied, including the foil angle-of-attack, the flap angle, and the positioning of the flap with respect to the main foil. Figure 5.3 shows the effect of varying the angle-of-attack (α) and the flap angle (δ) of the foil on the streamlines and pressure field. Increasing both flap angle and angle-of-attack eliminates the positive pressure pulse at the leading edge and increases the strength of the negative pulse prior to stall. Figure 5.3 also shows that the maximum suction pulse is achieved with an angle-of-attack of 3 degrees, and a flap angle of 19 degrees. As the angles are further increased, the negative pulse begins to decrease as the multi-element foil begins to stall. After a thorough analysis, optimal foil angles were chosen and a mill prototype was built by Advanced Fiber Technologies, as shown in Figure 5.4.

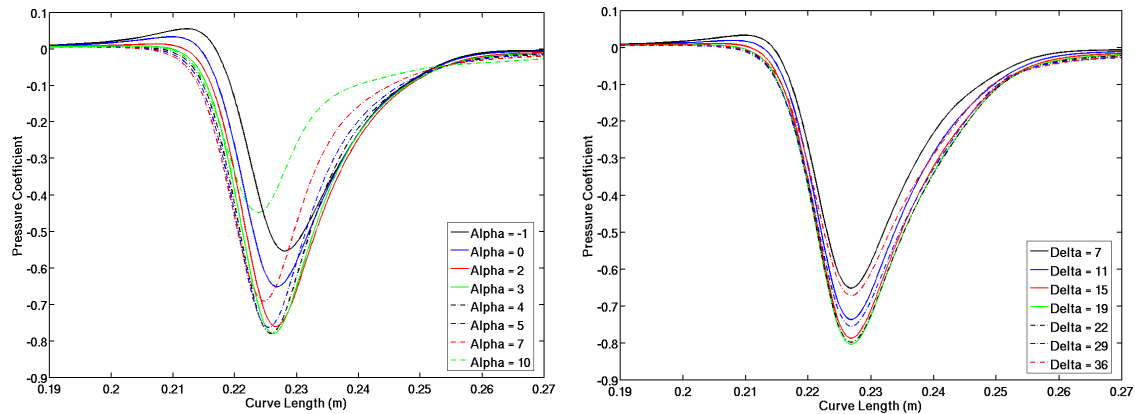


Figure 5.3: Pressure traces and contours for varying degrees of foil angle-of-attack (alpha), and flap angle (delta) of the multi-element foils.

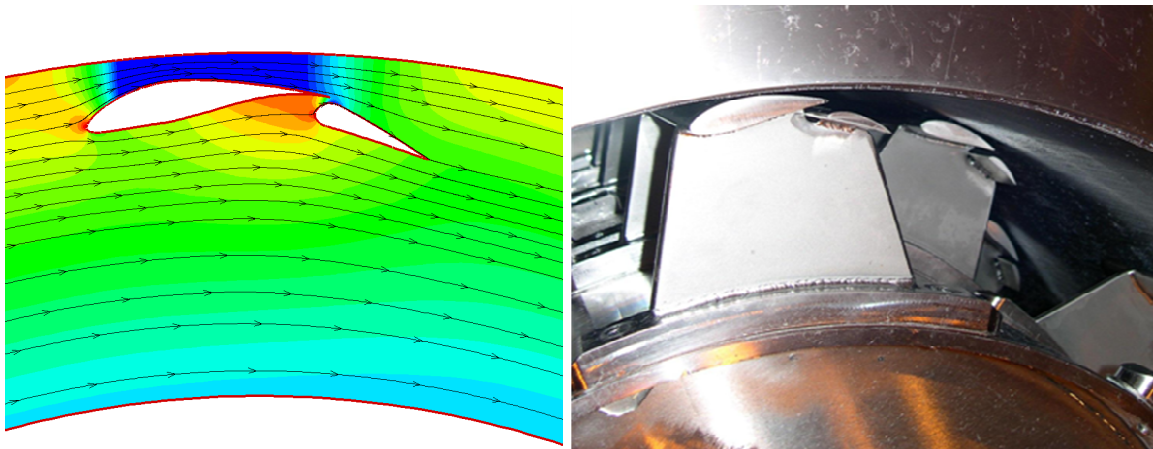


Figure 5.4: The optimized MEF design (left) and the mill-scale prototype rotor (right) installed at Catalyst Paper Recycling Division.

The mill scale prototype rotor was installed in a fully-instrumented GR20 primary fine screen at the Catalyst Paper, Paper Recycling Division, de-ink pulp mill in Coquitlam, British Columbia, Canada. The rotor was evaluated in parallel to a screen with the original equipment manufacturer (OEM) rotor, a standard Voith Multifoil, offering an easy comparison to the current OEM rotor technology. Identical wedgewire cylinders with 0.15 mm (0.006”) slots were installed in both screens. The OEM rotor was operated at a tip speed of 16 m/s (60 Hz). Figure 5.5 shows the flow diagram of the recycle mill.

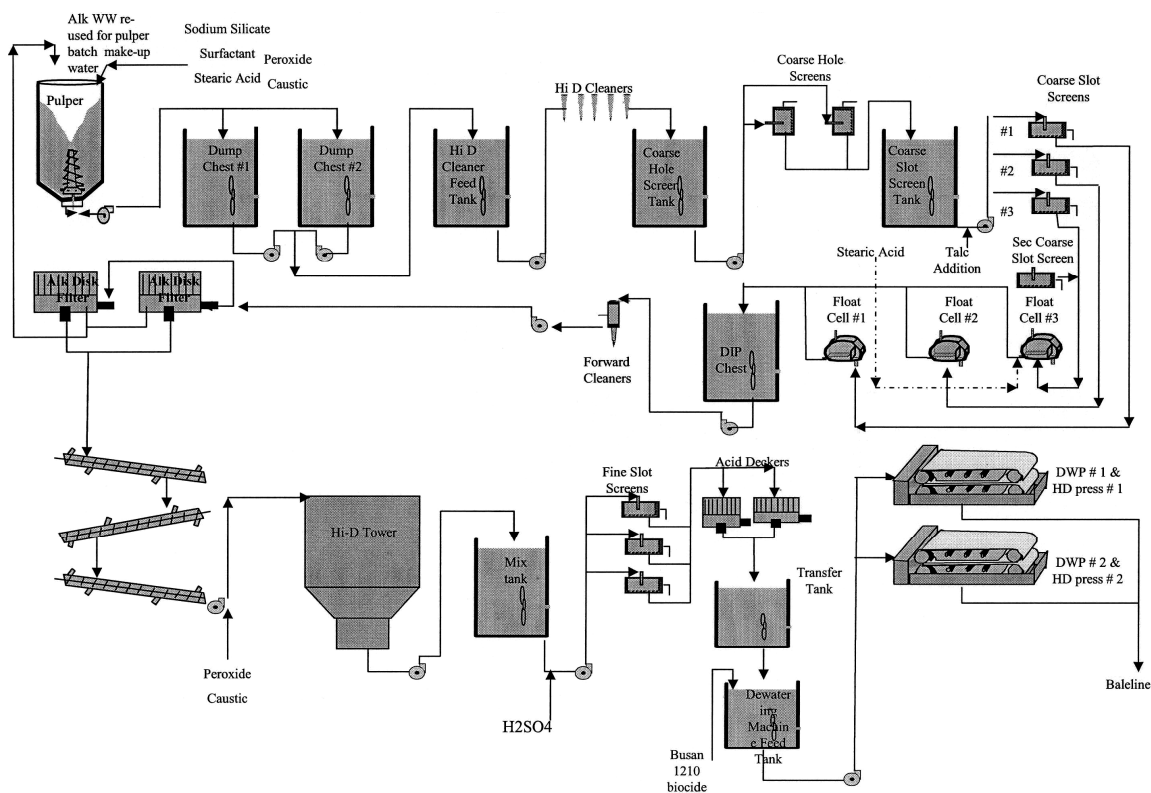


Figure 5.5: Catalyst Paper, Paper Recycling Division Flowsheet.

A variable frequency drive was used to optimize the rotor speed and evaluate the effect of tip speed on performance in terms of power consumption, stickies removal efficiency, and capacity. For the period of the trial, the screens were run at the mill's normal operating conditions: a reject rate of 22.5% (by mass), feed consistency between 1.1 and 1.3%, and slot velocity of 1.3 m/s.

5.3 Mill Application Results

Power consumption for the MEF rotor is shown in Figure 5.6 as a function of rotor tip speed. Rotor speed was decreased from 16 m/s to a minimum operating speed of 11.2 m/s where the screen plugged. Note that the existing speed of the OEM rotor (of 16 m/s) was based on the OEM's own optimization work at this mill and the mill's finding that the OEM screen would plug at a rotor tip speed of 15 m/s. Differential pressure (i.e. the feed minus the accept pressure) was monitored as an indication of the stability of the screen. Pulp samples were taken at various rotor speeds to evaluate reject thickening. Reject

thickening is the reject consistency divided by the feed consistency. High reject thickening can be a precursor of runnability problems. A stable operating set point was determined to be 13.3 m/s while maintaining capacity, which provided power savings of 42% compared to the parallel screen with the OEM rotor

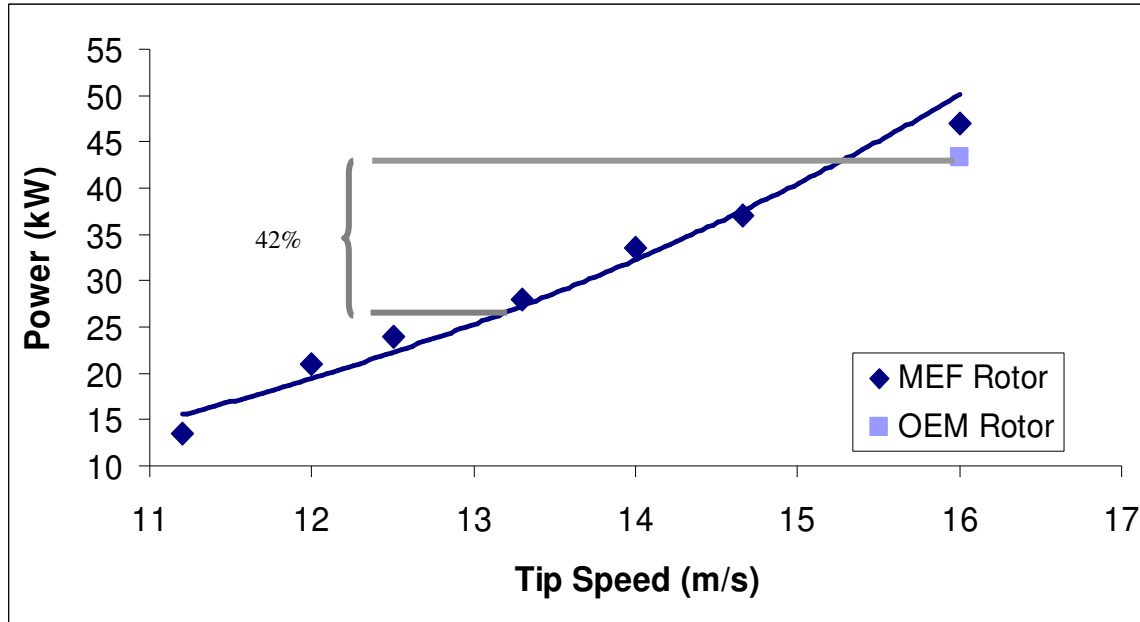


Figure 5.6: Screen power consumption versus rotor tip speed. Power savings of approximately 42% were obtained compared to the parallel OEM screen. Runnability remained excellent and there was no decrease in operating capacity.

Thickening factor is shown in Figure 5.7 as a function of rotor tip speed. The lower thickening factor of the MEF rotor relative to the OEM rotor at equivalent rotor speeds of 16 m/s suggests that the MEF rotor has better runnability and potentially higher capacity. Thickening factor increased as tip speed was reduced. The volumetric reject rate was maintained constant during the trial period (at 14%), thus reject rate (by mass) increased from 19% to 24% as tip speed was reduced. The tip speed of the MEF rotor could be reduced to 13.3 m/s, while maintaining a thickening factor which was approximately equivalent to the existing OEM rotor operating at a speed of 16 m/s. Note that all

consistency measurements have been reconciled, a statistical technique used to minimize error by using redundant data [10].

Stickies removal efficiency was higher with the MEF rotor than the OEM rotor, as shown in Figure 5.8, when operated in the same screen model, same cylinder, same passing velocity, same tip speed and same mass reject rate (of 22.5%). Stickies are deformable debris in the pulp stream made up of inks and plastics. A common mass reject rate was obtained by applying a correction factor based on a plug-flow model of screen performance. The data point for the OEM rotor represents an average of 18 measurements from each of the feed, accept and reject streams taken over time by mill staff, and the data points for the MEF are averaged from 6 measurements from each stream for each tip speed. Further increases in stickies removal efficiency were obtained as the rotor tip speed was reduced. These effects are consistent with the discussion of the fundamental principles of the MEF rotor, which anticipates an increase in stickies removal efficiency due to reduction of a positive component of the pressure – both through rotor design and reduced rotor speed.

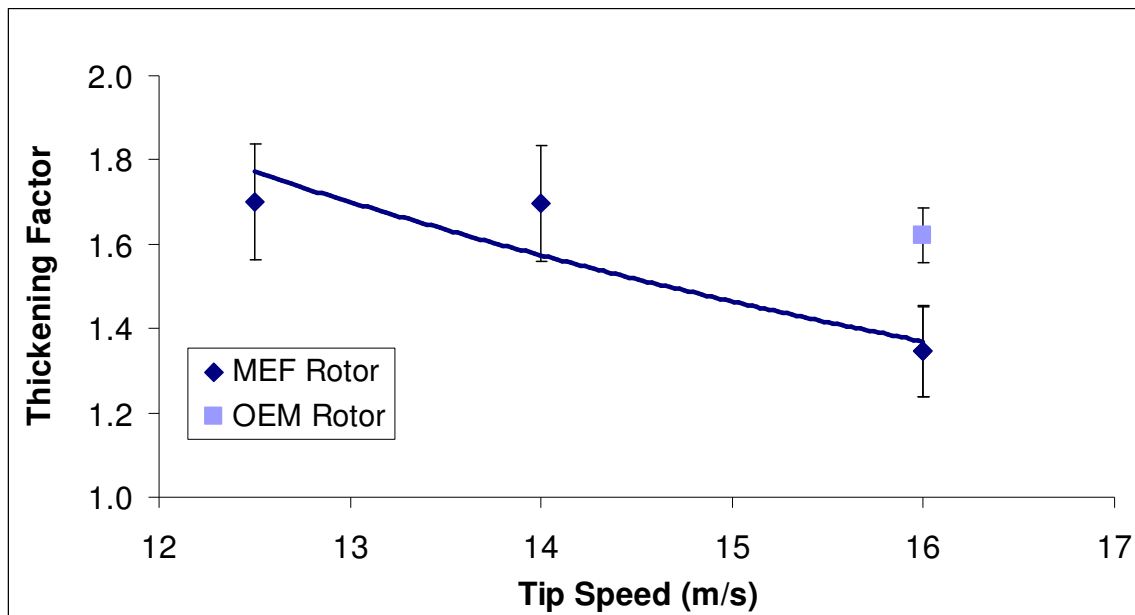


Figure 5.7: Thickening factor versus rotor tip speed. The error bars represent 90% confidence intervals.

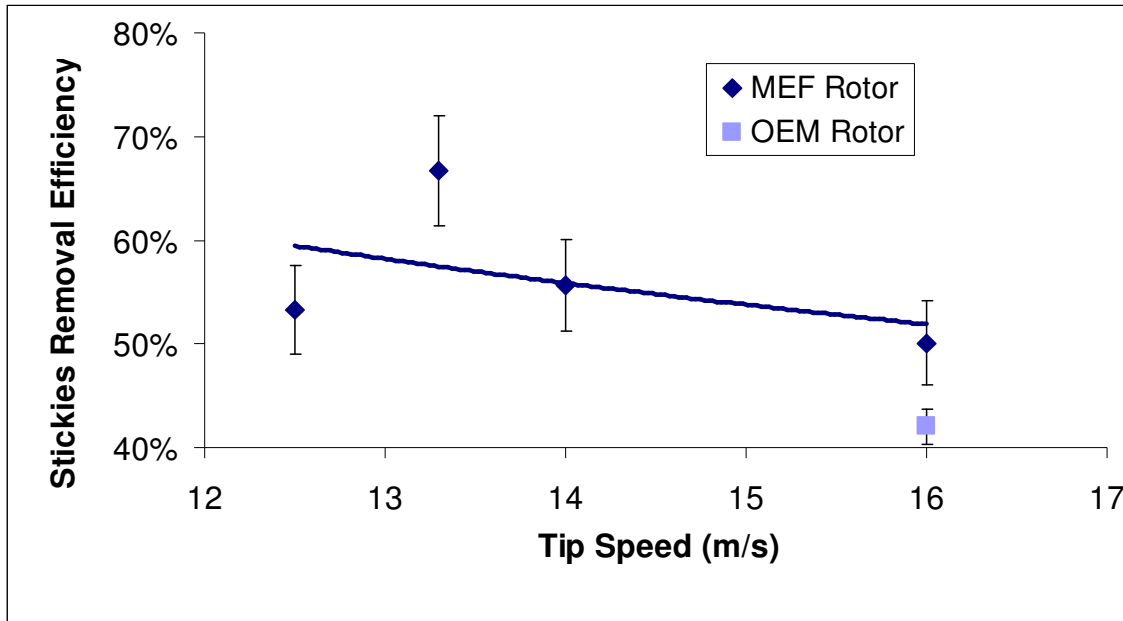


Figure 5.8: The MEF rotor provided a higher stickies removal efficiency than the OEM rotor. Further increases in efficiency were obtained as rotor speed was decreased. The error bars represent 90% confidence intervals.

Stickies removal efficiency was, in fact, determined by using two macro stickies analysis methods. The method used by Catalyst Paper determined the stickies removal efficiency by count. This mill-specific method used a Pulmac screen with 0.15 mm slots to isolate the stickies, followed by a manual count using a microscope. An independent laboratory (CIPP) confirmed the results by measuring the stickies removal efficiency, also using a Pulmac screen with 0.15 mm slots to isolate the specks, but then identifying the stickies through a dying technique, followed by manual verification. Image analysis was used to assess the number and size of the stickies [11].

Samples for the CIPP analysis were taken from both parallel screens while the MEF rotor was operating at the reduced tip speed of 13.3 m/s and the OEM rotor was running at 16 m/s. The results shown in Figure 5.9 confirm the stickies removal efficiency of the MEF rotor is higher than the OEM rotor when measuring efficiency either by count or by area (mm^2/g of oven dried pulp). Efficiencies for both the OEM and MEF rotors are slightly higher in Figure 5.9 than in Figure 5.8, which is a reflection of the day-to-day variability

in the character of the stickies and the efficiency measurements. Figure 5.10 shows the stickies particle distribution from the accept streams of both parallel screens. The substantially higher amount of small stickies in the 0.21 mm² size class suggests that the OEM rotor may have been fragmenting the stickies into smaller particles which would have contributed to the lower efficiency of the OEM screen and a higher stickies count in the accepts. This needs to be confirmed by measuring the stickies size distribution in the feed, accept and reject streams, however.

The good runnability of the MEF rotor should also be noted. The MEF rotor evaluation was made over a 3 week period. The rotor operated reliably throughout this trial period. There was no stringing or any accumulation of pulp or contaminants on the rotor or in the gap between the foil and flap, as shown in Figure 5.11.

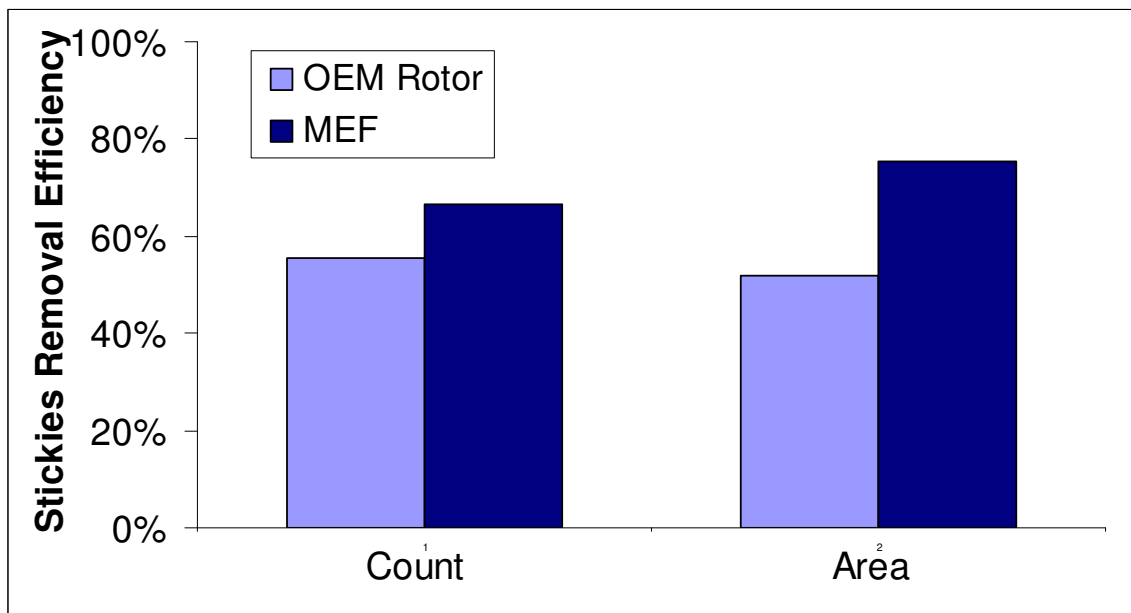


Figure 5.9: Stickies removal efficiency measurements by count and area with equivalent 0.15 mm (0.006") wedgewire cylinders and a reject rate of 22.5% by mass.

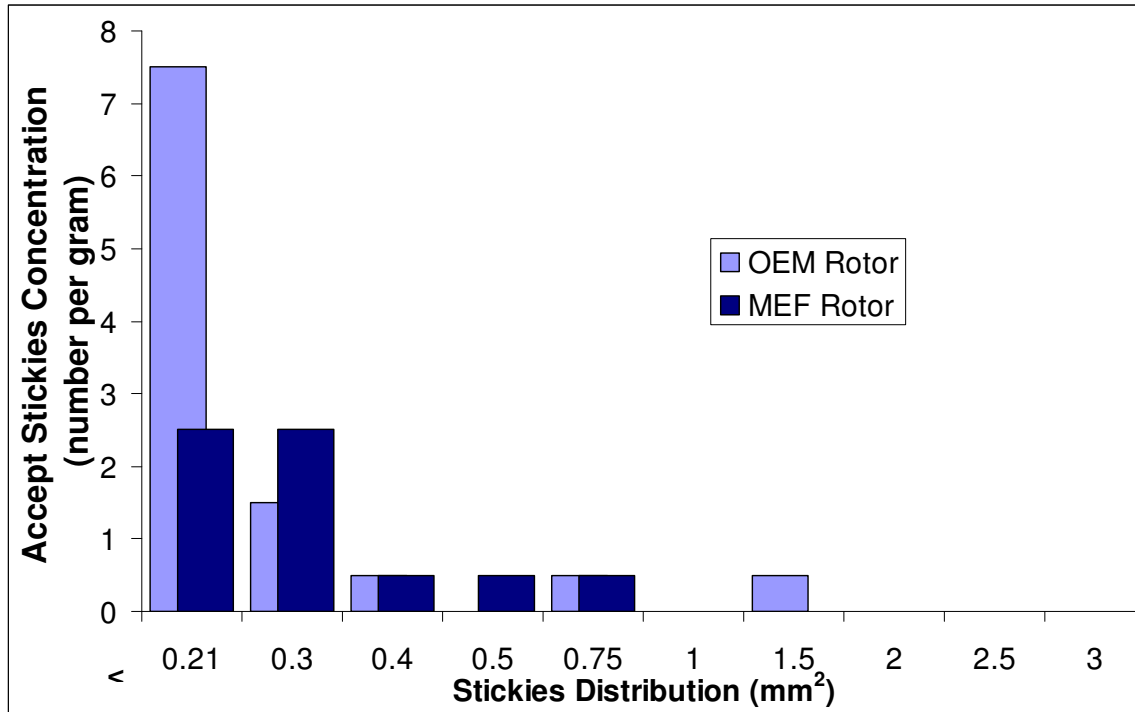


Figure 5.10: Stickies Distribution (mm²).



Figure 5.11: MEF rotor at the end of the trial period. The pulp shown in this photo was deposited during drainage of the pulp screen and was easily washed away. There was no accumulation or plugging between the foil and flap.

5.4 Conclusions

A new patented rotor technology has been developed to increase the strength and duration of rotor pulsations without producing undesirable, positive pulse components. A prototype MEF rotor was tested in the GR20 primary fine screen at the Catalyst Paper mill in Coquitlam, British Columbia. The MEF rotor was able to maintain the full required capacity of the screen even when operated at a top speed of 13.3 m/s -- relative to the usual operating speed of 16 m/s. An energy saving of 42% was achieved by operating the screen at this lower speed.

The thickening factor of the MEF rotor is lower than the OEM rotor at equivalent tip speeds. The stickies removal efficiency of the MEF rotor was higher than the OEM rotor and further increases in efficiency were obtained as the MEF rotor speed was decreased. The MEF rotor was shown to operate reliably and without plugging or stringing during the three week duration of the trial.

The excellent results of this trial follow on the fundamental benefits of the MEF rotor design. While a high degree of foil camber will provide a wider and stronger pulse, traditional, single-piece foils are limited in camber because of the occurrence of phenomenon called "boundary layer separation". The MEF rotor uses its unique design to avoid boundary layer separation. Lower tip speeds are thus possible without compromising the action of the rotor or capacity of the screen. Substantial power savings result. In addition, the MEF has improved stickies removal efficiency. Efficiency is likely increased because the rotor pulse can be optimized to eliminate the positive pressure component, which would tend to force deformable contaminants such as stickies through the screen apertures. This study has thus confirmed the efficacy of the MEF rotor design and demonstrated its practicality in a mill environment.

5.5 References

1. Feng, M., "Numerical simulation of the pressure pulses produced by a pressure screen foil rotor", M. A. Sc. Thesis, Dept. Mech. Eng., Univ. British Columbia, 2003.
2. Feng, M., Olson J.A., Ollivier-Gooch, C.F., Xia J., and Gooding, R.W., "A computational fluid dynamic (CFD) tool for advanced pulp screen foil rotor design" ABTCP Conf. Proc., San Paulo, Brazil, 2003.
3. Feng, M., Gonzalez J., Olson, J.A., Ollivier-Gooch, C., and Gooding, R.W., "Numerical simulation of the pressure pulses produced by a pressure screen foil rotor", J. Fluid Eng. 127(2):347-357, 2005.
4. Gonzalez, J.A., "Characterization of design parameters for a free foil rotor in a pressure screen", M. A. Sc. Thesis, Dept. Mech. Eng., Univ. British Columbia, 2002.
5. Pflueger, C.D., Olson, J.A., and Gooding, R.W., "The performance of the EP Rotor in de-ink pulp screening", Preprints 2007 Appita Conf.
6. Julien Saint Amand, F., Perrin, B., Gooding, R., Huovinen, A., Asendrych, D., and Favre-Marinet, M., "Optimisation of screen plate design for the removal of stickies from deinking pulps", PTS-Deinking Symposium, 2004
7. Olson, J.A., Turcotte, S., and Gooding, R.W., "Determination of power requirements for solid core pulp screen rotors", Nordic Pulp and Paper Res. J. 19(2):213-217, 2004.
8. Olson, J.A., and Ko, J., "Multi-element airfoil for pulp screens", U.S. Patent No. 6,883,669, Apr. 26, 2005.
9. Mahon, S., and Zhang, X., "Computational analysis of pressure and wake characteristics of an aerofoil in ground effect", J. Fluids Eng., 127(3): 290-298, 2005.
10. Ramagnoli and Sanchez, "Data Processing and reconciliation for chemical process operations", Academic Press, 1999.
11. "Macro stickies content in pulp", Laboratory Procedure PL-140, Centre Integre en Pates et Papiers (CIPP), Trois-Rivieres Quebec, April 04, 2002.

Chapter 6

Effect of Pulse Frequency and Cylinder Diameter on Pressure Screen Rotor Performance⁵

6.1 Introduction

Pressure screens are the most industrially effective way to remove contaminants from a pulp stream and are used in pulp mills world wide. Screening improves the quality of the paper, including its strength, appearance and optical qualities. Finally, screening can be used to “fractionate” the pulp, or separate the pulp by fiber length, allowing for different fiber fractions to be processed separately and the production of high value paper.

Pressure screens are composed of two main components: a cylindrical screen with slots or holes, and a rotor which spins inside the cylinder. As shown in Figure 6.1, after the feed flow enters the cylinder tangentially, small enough particles and fibers pass through the apertures in the cylinder wall into the accept stream, while oversized particles pass down the length of the cylinder and out through the reject port. In order to prevent the apertures from plugging, the rotor’s foils pass along the feed side of the cylinder generating a negative pressure pulse and backflushing the apertures. This action has a dramatic effect on the performance of the screen, allowing for higher flow through the cylinder (capacity) or for the use of smaller slots or holes, which improves debris removal or fractionation efficiency.

⁵ A version of this chapter will be submitted for publication. Delfel, S., Ollivier-Gooch, C., Olson, J., and Hamelin, M., “Effect of pulse frequency and cylinder diameter on pressure screen rotor performance”.

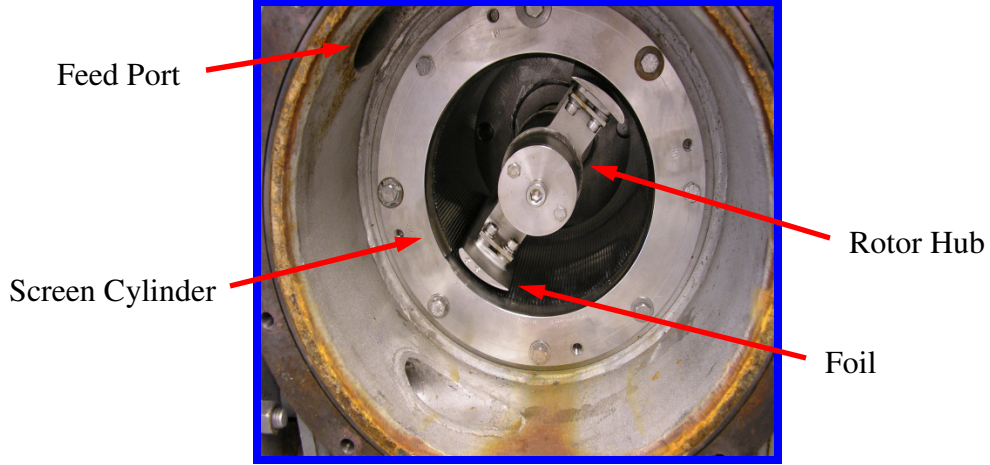


Figure 6.1: The inner workings of a small pressure screen with a two foiled rotor.

In previous studies, the non-dimensional power coefficient has been found to be independent of Reynolds number, where the power coefficient C_{Power} is defined as

$$C_{Power} = \frac{Power}{\rho \cdot V_t^3 \cdot D^2} \quad (6.1)$$

where $Power$ is the power consumption of the rotor, ρ is the fluid density, V_t is the tip speed of the rotor, and D is the cylinder diameter [1]. The power consumption of the rotor is therefore proportional to the rotor tip speed cubed.

It has been shown that increasing the magnitude of the negative pressure pulse generated by the foils allows for greater flow through the screen cylinder (i.e. greater capacity) [2, 3, 4, 5, 6, 7]. The pressure pulse is commonly described by the non-dimensional pressure coefficient C_P , defined as

$$C_P = \frac{P}{0.5 \cdot \rho \cdot V_t^2} \quad (6.2)$$

where P is pressure. The pressure coefficient has also been found to be independent of Reynolds number [8, 9]. Therefore, the magnitude of the pulse generated by a given foil varies proportional to rotor tip speed squared. By maximizing the magnitude of the negative pulse generated by a foil, the tip speed of the rotor can be reduced, reducing the power consumption of the rotor without reducing the maximum capacity of the screen.

While it has been shown that increasing the performance of each individual foil can lead to increased capacity and/or reduced power consumption, the effect of the frequency of the pulses is not well understood. Pulse frequency f is defined as

$$f = N \frac{V_t}{\pi D} \quad (6.3)$$

where N is the number of foils on the rotor. Since it is desirable to operate the rotor at as low a tip speed as possible, this study investigates, using computational fluid dynamics (CFD), the effects of varying the frequency by changing the number of foils on the rotor at a given rotor tip speed.

The rotor used in this study is a novel multi-element foil (MEF) rotor, shown in Figure 6.2. The MEF rotor has been shown to have a stronger pulse, reduced energy consumption, and increased capacity compared to current single-element rotors [10, 11, 12]. In addition to increased industrial performance, the ability to easily change the geometry of the MEF by adjusting the flap angle and angle-of-attack make it useful in research applications.

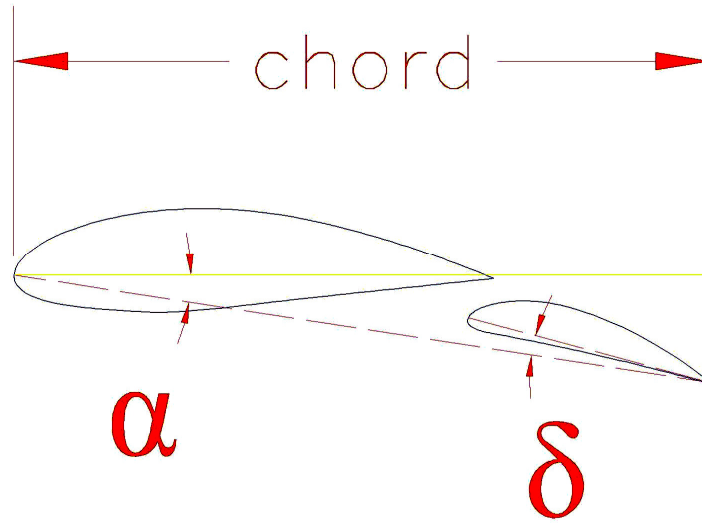


Figure 6.2: The MEF rotor profile with angle-of-attack (α), flap angle (δ), and chord length defined.

This study will also investigate the effect of cylinder diameter on rotor performance. Diameter and pulse frequency are inherently coupled, as increasing the diameter of the cylinder without increasing the number of foils on the rotor will reduce the frequency of the pulses. Screens used in the industry vary in diameter between as small as 0.2 m to as large as 1.7 m. However, the size of the foils, the gap between the foil and the cylinder, and the size of the apertures in the cylinder are typically determined by fiber and debris size and are not scaled with varying cylinder diameter, which adds complexity to the problem.

Finally, the effects of pulse frequency found numerically are verified in a pilot plant study. The power consumption and capacity of a two foil rotor and a three foil rotor with identical foil elements are compared directly.

6.2 Numerical Method

The domain was modeled as shown in Figure 6.3, which also shows a typical mesh and boundary conditions used in solving the problem. The FLUENT 6.1 commercial solver

was used to numerically solve the discretized Navier-Stokes equations. The solver is a second-order finite volume solver and the problem is assumed to be two-dimensional, isothermal, and steady state. Turbulence in the flow was modeled using the standard $k-\epsilon$ turbulence model with enhanced wall treatments, which was found to be a good balance between accuracy and computational cost. The same method has been used successfully in previous foil rotor studies [10, 11, 12, 13]. All mesh generation was done using GAMBIT, the commercial pre-processing package for FLUENT.

The domain is rotationally periodic to simulate the enclosed swirling flow of a pressure screen. The number of foils on the rotor is determined by the location of the periodic boundaries. Periodic boundaries located at 0 and 180 deg. represent a two foiled rotor, for example, while boundaries at 45 and 135 deg. represent a four foiled rotor. A rotating computational coordinate system moving at the same speed as the rotor is set at the center of the cylinder since the flow is steady when viewed from this frame. The foil boundaries as well as the inner and outer walls are set with no slip boundary conditions. The foil and inner wall are set with zero angular velocity relative to the spinning coordinate system, while the outer wall, which represents the screen cylinder, is set with zero velocity in the absolute coordinate system.

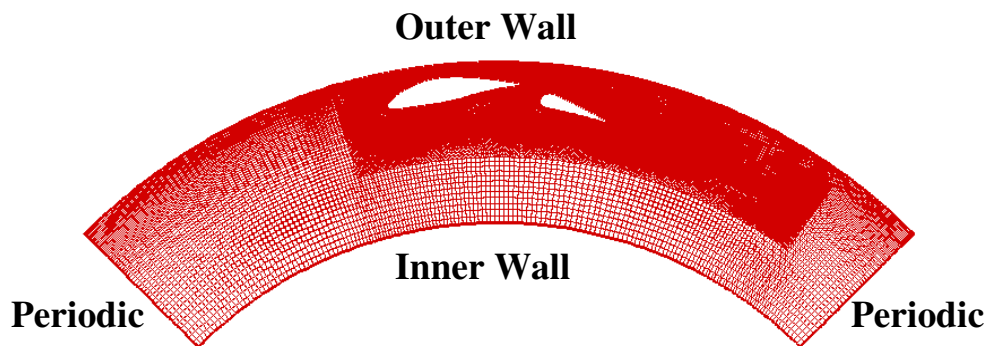


Figure 6.3: Computational domain and a typical mesh. The model shown is for a four foil rotor.

The outer wall, which represents the screen cylinder, is a solid wall in the simulations, which corresponds with a slot velocity of $V_s = 0.0$ m/s. This assumption represents the critical design case of a plugged cylinder and also prevents the need to model the complicated flow through the apertures, significantly reducing computational costs. Other assumptions and simplifications include that water, rather than pulp, is used in the simulations and that the flow is two-dimensional. The consistencies found in screening applications are very low, on the order of 1-2%, and turbulent pulp suspensions in this range have been found to behave as a Newtonian fluid with the same density and viscosity as water [9]. Additionally, previous studies have found that increasing consistency reduces the magnitude of the pressure pulses generated by the rotor, but the shape and trends in the pulses are unchanged [ibid.]. Finally, foil aspect ratios in pressure screens are typically 8 or larger with a relatively low axial flow velocity, making the 2D assumption reasonable.

A clearance of 5 mm between the foil and the cylinder, a foil chord length of 10 cm, and a rotor tip speed of 21 m/s was used in the simulations, unless otherwise noted.

6.3 Numerical Results and Discussion

Using the numerical methods described above, a multi-element foil rotor was studied in a variety of cylinder diameters, configurations, and with a varying number of foils on the rotor, which changes the frequency of the pulses. Figure 6.4 shows contours of velocity relative to the foil for two, three, four, and six foil rotors in a 0.508 m diameter cylinder. As can be seen, adding additional foils to the rotor causes the relative velocity to decrease upstream of the foil, in the gap between the foil and the cylindrical screen, which is critical to screen performance, and in the wake following the foil. This is due to the added drag on the flow from the additional foils, which causes the flow in the cylinder to swirl at a velocity closer to the tip speed of the rotor.

The effects of added foils on the relative velocity is shown more quantitatively in Figure 6.5, which shows the relative velocity profile one chord length upstream of the foil (normalized by the rotor tip speed) as a function of radius (normalized by the cylinder radius r_0). Once again, it can clearly be seen that increasing the number of foils on the rotor reduces the upstream relative velocity. The upstream relative velocity in the region of the foil is 30% less for a four foil rotor compared to a two foil rotor.

Figure 6.6 shows the effects of added foils on the pressure contours. The reduction in relative velocity shown in Figures 6.4 and 6.5 as foils are added to the rotor can be seen to cause a reduction in the strength and width of the negative pressure pulse generated by the foils. This effect is more clearly illustrated in Figure 6.7, which shows the trace of non-dimensionalized pressure along the cylinder wall for rotors with varying number of foils. The magnitude of the negative pressure peak for a six foil rotor is over 54% less than that of a two foil rotor.

Figure 6.8 shows the effect of varying the foil flap angle on the minimum pulse pressure coefficient on the cylinder wall for rotors with different numbers of foils for a 0.508 m diameter cylinder. As can be seen, the effect of varying pulse frequency on the pressure pulse magnitude is much greater than varying the foil geometry. For added clarity, the results in Figure 6.8 were combined to build a surface of minimum pressure coefficient on the screen wall as a function of pulse frequency and foil flap angle. The surface, shown in Figure 6.9, was built from 20 CFD cases using cubic interpolation. The same effects were seen for various cylinder diameters, as shown by Figure 6.10, which shows a surface of minimum wall pressure coefficient vs. pulse frequency and foil flap angle for a 0.80 m diameter cylinder.

It is important to point out that the mechanisms leading to the plugging of the screen cylinder are not well understood. It is theorized that a minimum pulse frequency is required to disrupt flocculation or the formation of a fiber network that would lead to the plugging of the apertures [14, 15]. Therefore, while it has been shown in this study that an individual foil performs significantly better when there are fewer foils on the rotor,

there is likely an optimum number of foils that balances individual foil performance and pulse frequency, leading to maximum screen capacity for a given tip speed.

In order to isolate the effect of the cylinder diameter on foil performance, it is necessary to maintain a constant pulse frequency since, as shown in equation 6.3, varying diameter will change pulse frequency. To accomplish this, lines of constant frequency were interpolated from the surfaces in Figures 6.9 and 6.10 and compared to CFD results for a 0.30 m diameter cylinder. Figure 6.11 shows the effect of varying the foil flap angle on the minimum pressure coefficient at the cylinder wall at a constant frequency for cylinder diameters of 0.30, 0.508, and 0.80 m. As can be seen, increasing cylinder diameter causes a slight reduction in the magnitude of the pressure pulse, with a 5.7% reduction in pulse magnitude for the 0.80 m diameter cylinder compared to the 0.30 m diameter cylinder. Additionally, the optimum flap angle is shown to decrease with increasing cylinder diameter. These effects are likely due to the variation in the curvature of the cylinder wall as the diameter changes, which changes the angle of the incoming and outgoing freestream flows relative to the foil. This effectively changes the angle-of-attack and camber (or curvature) of the foil.

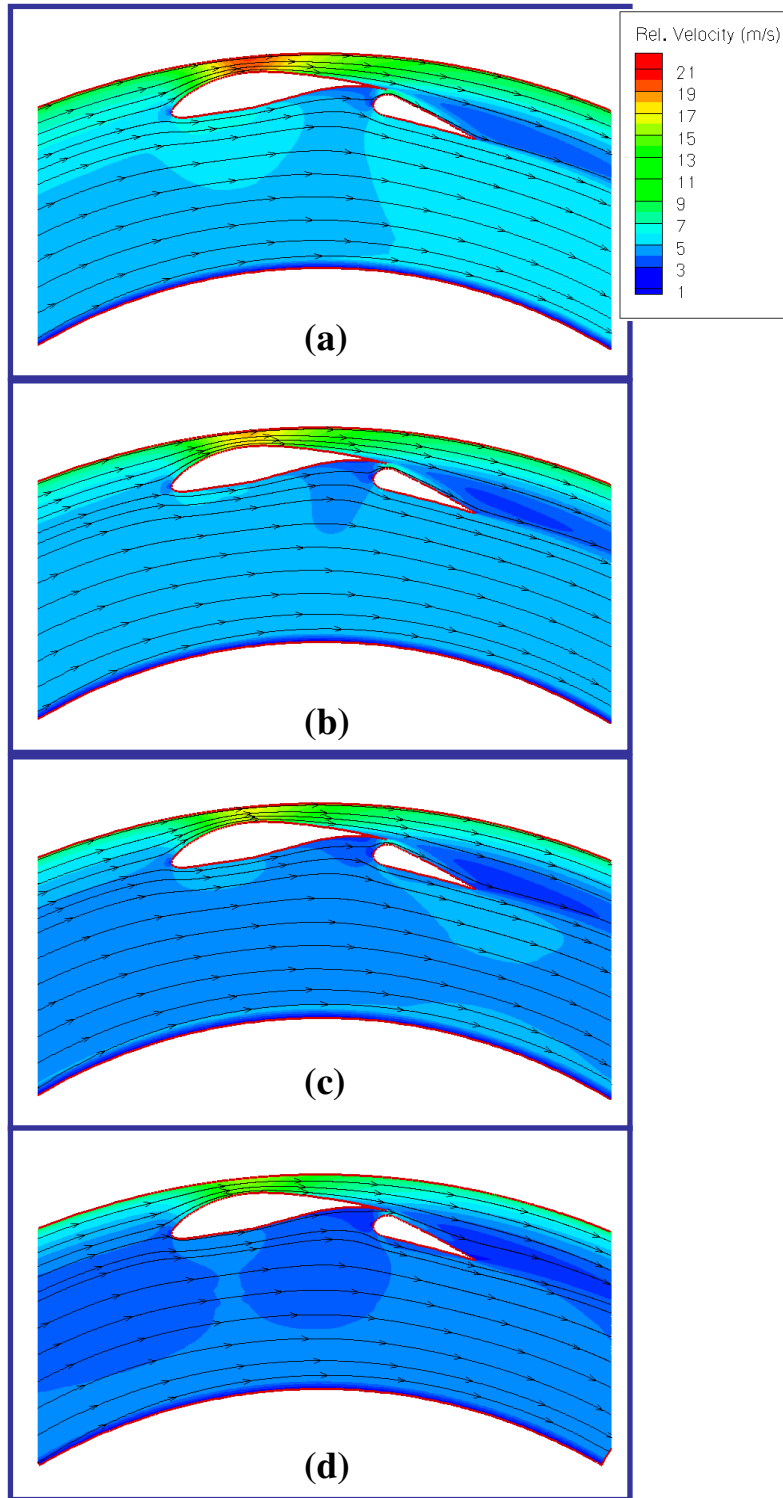


Figure 6.4: Contours of velocity relative to the foil and streamlines for a rotor with (a) two foils, (b) three foils, (c) four foils, and (d) six foils. The cylinder is 0.508 m in diameter.

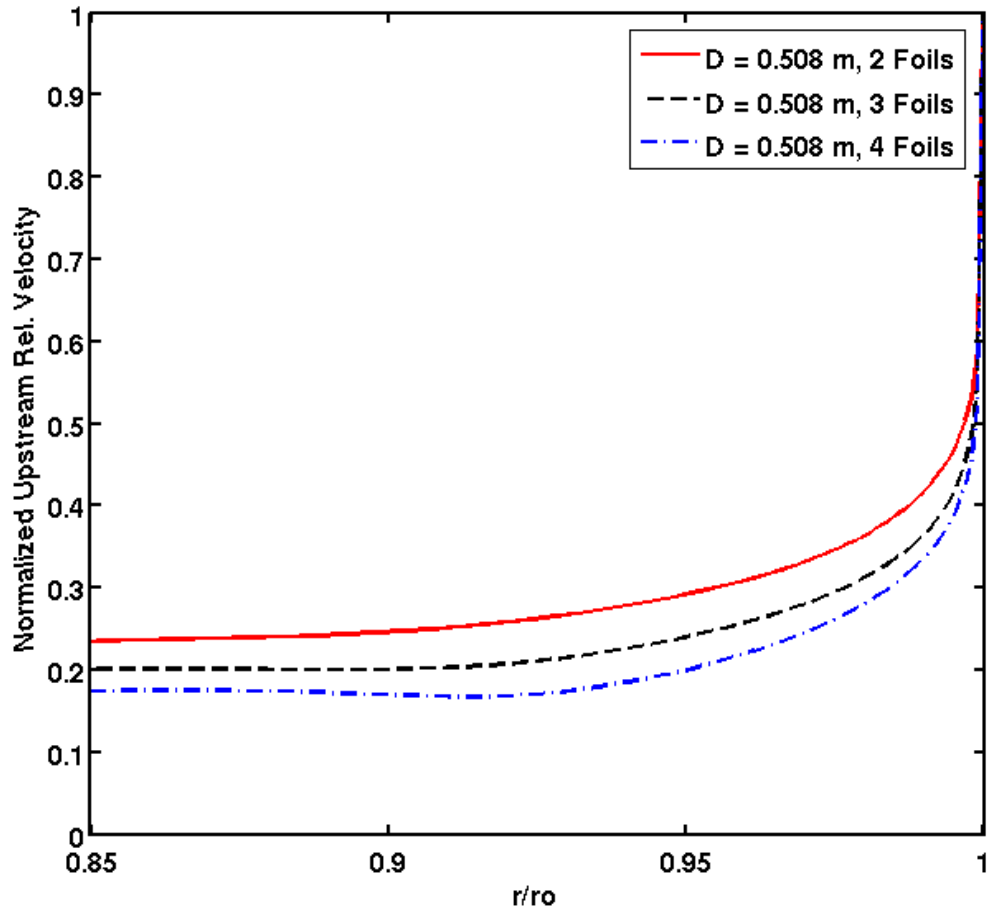


Figure 6.5: Relative velocity one chord length upstream of the foil (normalized by tip speed) vs. radius (normalized by the cylinder radius r_o) for a rotor with varying number of foils. The cylinder is 0.508 m in diameter.

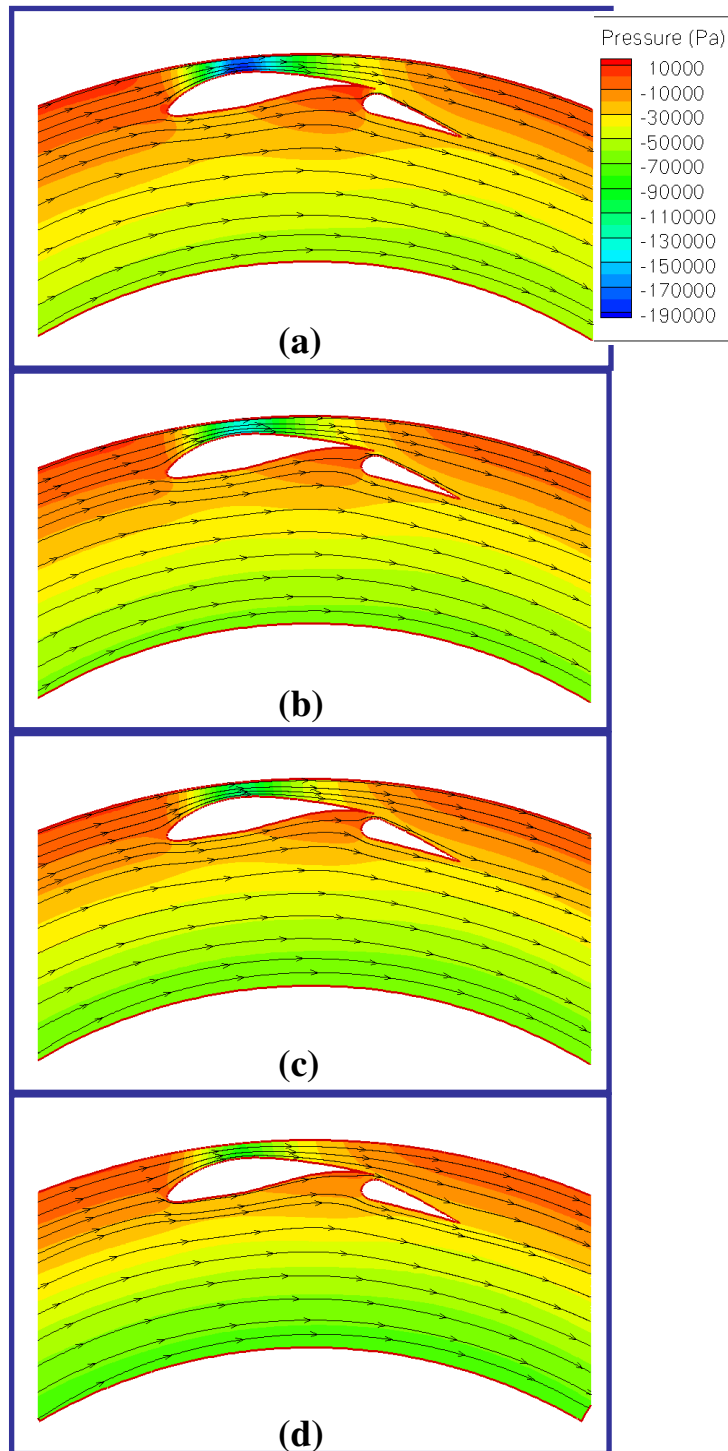


Figure 6.6: Pressure contours and streamlines for a rotor with (a) two foils, (b) three foils, (c) four foils, and (d) six foils. The cylinder is 0.508 m in diameter.

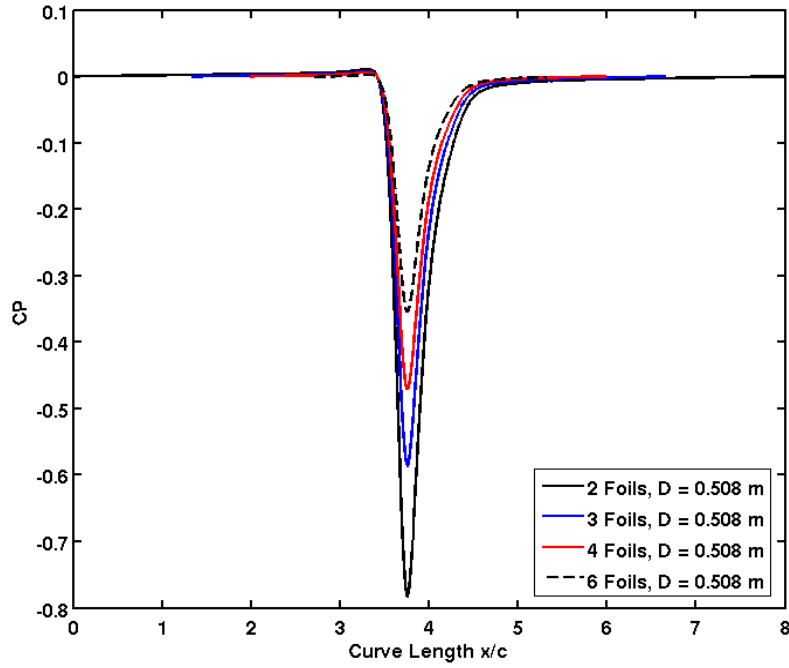


Figure 6.7: Traces of pressure coefficient along the cylinder wall for a rotor with varying number of foils. The cylinder is 0.508 m in diameter.

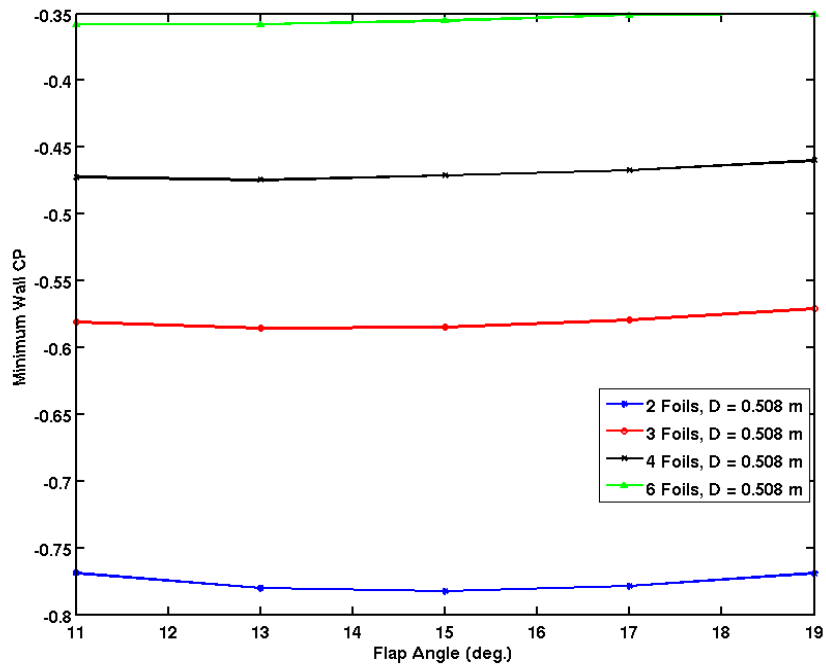


Figure 6.8: Minimum pressure coefficient on the cylinder wall for varying foil geometries. The effect of varying the pulse frequency (i.e. the number of foils) is much larger than the effect of varying the foil geometry. The cylinder is 0.508 m in diameter.

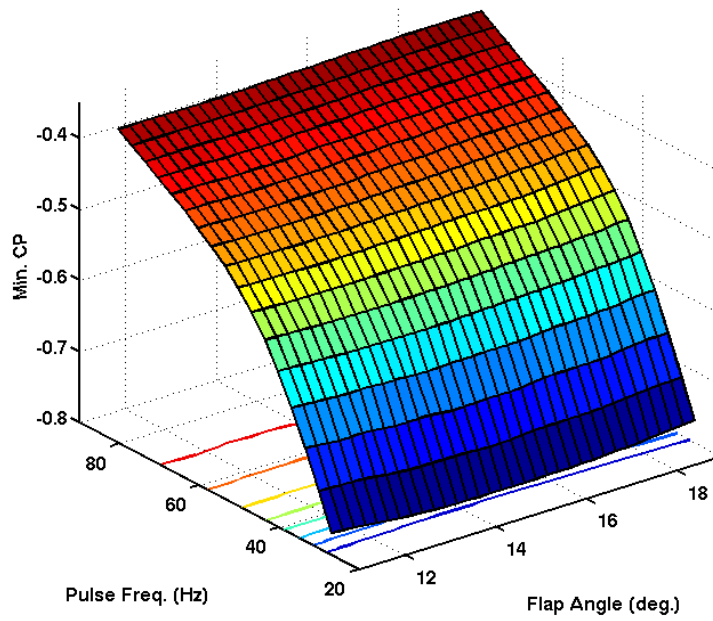


Figure 6.9: Surface of minimum pressure coefficient at the cylinder wall as a function of pulse frequency and flap angle for a 0.508 m diameter cylinder.

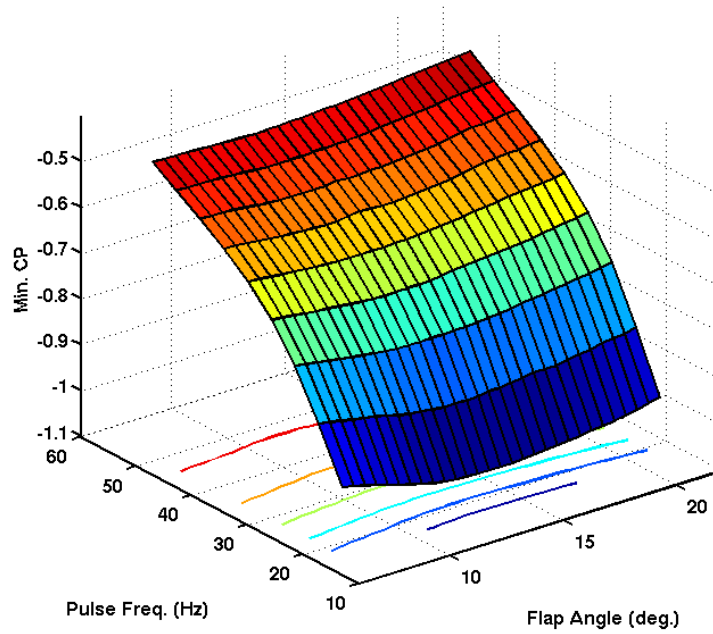


Figure 6.10: Surface of minimum pressure coefficient at the cylinder wall as a function of pulse frequency and flap angle for a 0.80 m diameter cylinder.

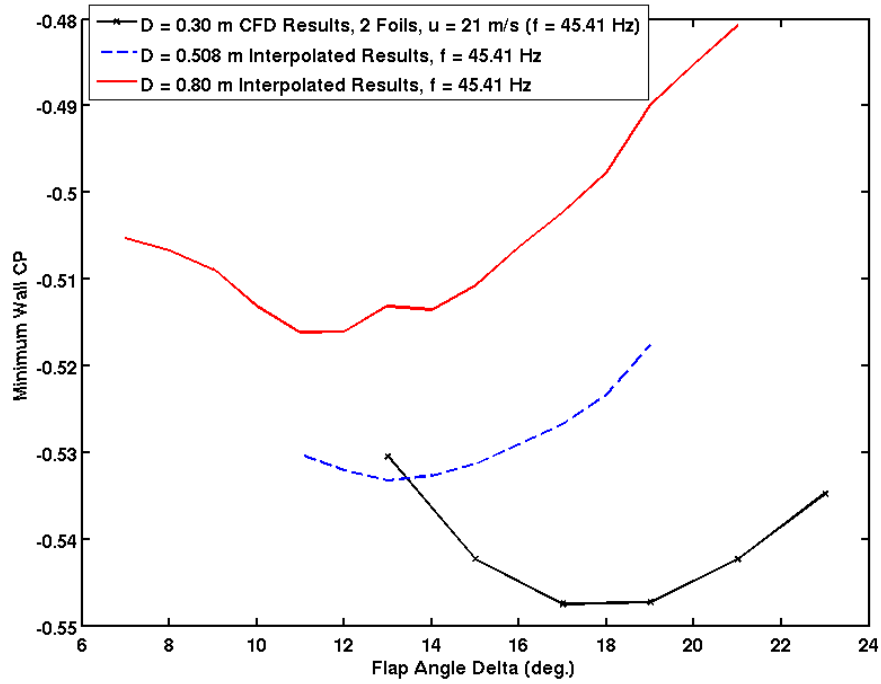


Figure 6.11: Effect of foil flap angle on minimum pressure coefficient for varying cylinder diameters. All results are at a constant pulse frequency of $f = 45.41$ Hz. The 0.30 m diameter data is from direct CFD results for a two foil rotor, while the 0.508 m and .080 m diameter data is interpolated from the surfaces in Figures 6.7 and 6.8, respectively.

6.4 Experimental Setup

To validate the numerical pulse frequency results, a MEF rotor trial was conducted at the FP Innovations – Paprican, Vancouver, pilot plant using a Hooper PSV2100 pressure screen with a 0.30 m diameter cylinder. The results for a two foil and a three foil rotor with identical geometries, as shown in Figure 6.12, were compared. The screen was equipped with a variable frequency drive (VFD), allowing for the speed of the rotor to be adjusted and for the measurement of rotor power consumption. A wedge-wire cylinder with a 3.2 mm wire width, a 0.9 mm contour height, a 0.2 mm slot width, and an open area of 5.98% was used. The flow loop was equipped with pressure sensors, magnetic flow meters, and valve controls on all three streams.

The pulp used in the trial was a 1.5% consistency 50% softwood/50% hardwood kraft pulp, representing a de-ink pulp. The screen was fed from a 10,000 L stock tank. A maximum slot velocity envelope was created for each rotor configuration by setting the rotor tip speed then increasing the flow through the screen at a constant volumetric reject rate until the onset of plugging. The tip speed was then reduced and the procedure was repeated, creating a maximum slot velocity vs. power envelope (or “failure envelope”) for each configuration. Slot velocity V_S is the average speed of the flow through the apertures and is a measure of screen capacity. Failure envelopes are commonly used to measure rotor performance [12].

The thickening factor for the two rotors was also considered as a measurement of performance. The thickening factor T is the consistency of the reject over the consistency of the feed. Excessive thickening can affect the runability of a screen. To generate the thickening curves, feed samples were collected at least once for each rotor configuration and the reject and accept samples were collected at a slot velocity of $V_S = 1.0$ m/s for every tip speed.

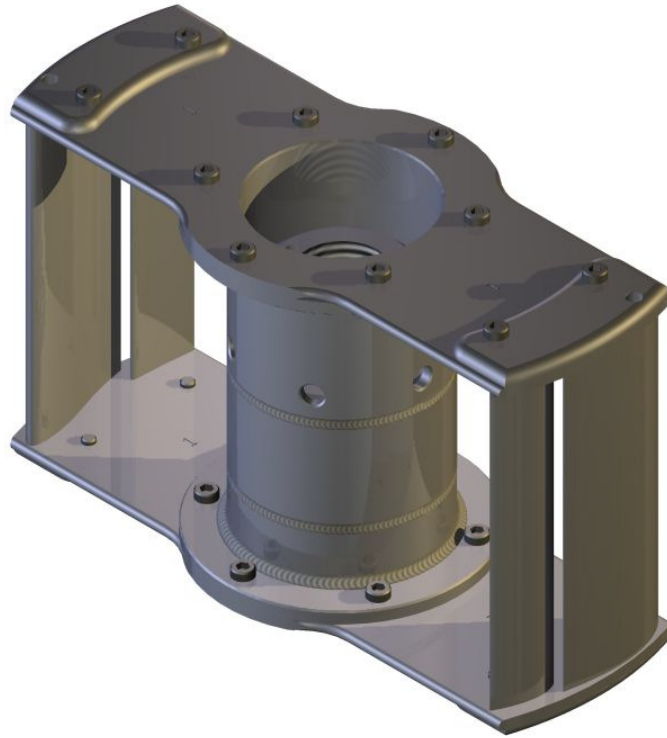


Figure 6.12: The two foil MEF rotor used in the pilot plant trials.

6.5 Experimental Results

Figure 6.13 shows the numerically predicted pressure pulses for two and three foil rotors operating in the PSV2100 screen. The two foil rotor is predicted to have a 33.0% stronger pulse than the three foil rotor. Using equations 6.1 and 6.2, this is predicted to yield a tip speed reduction of 2.8 m/s to generate the same the same pressure pulse. Assuming that the plugging of the cylinder is solely dependent on the magnitude of the pressure pulse, this would result in 34.8% reduction in power.

The plugging envelopes for the two rotors are shown in Figure 6.14. The two foil rotor was able to operate at as much as a 24% higher slot velocity for the same power requirement. Conversely, the two foil rotor consumed between 11% and 24% less power at a given slot velocity than the three foil rotor.

These results match well with the CFD predictions in the sense that a reduced number of foils leads to improved rotor performance. It is interesting to note, however, that the measured power savings are less than predicted using only equations 6.1 and 6.2 and that the power savings are not constant over different flow rates and tip speeds. This may be explained in part by Figure 6.15, which shows the numerically predicted minimum pressure on the cylinder (based on the results in Figure 6.13) vs. the experimental maximum slot velocity. The results for the two foil and three foil rotors do not fall onto the same curve, implying that screen capacity is not entirely determined by the magnitude of the pressure pulse. Additionally, the three foil rotor had a higher maximum slot velocity at a given minimum pressure than the two foil rotor, which suggests that increasing pulse frequency delays the onset of plugging.

Finally, Figure 6.16 shows the effect of rotor tip speed on thickening factor for the two rotors at a constant slot velocity of $V_S = 1.0$ m/s. The three foil rotor had slightly lower thickening at low tip speeds. Overall, however, both rotors performed well with respect to thickening and there was very little difference between the two.

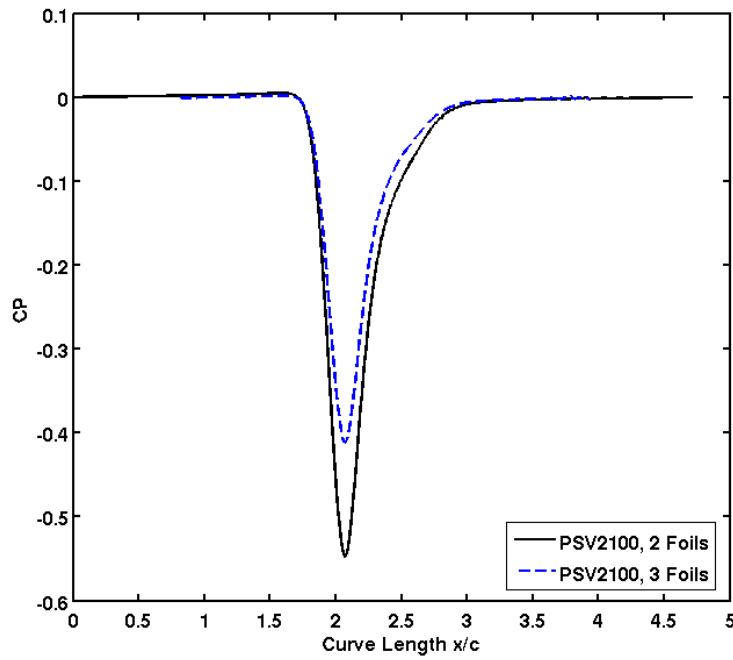


Figure 6.13: Traces of pressure coefficient along the screen cylinder wall for two and three foil MEF rotors in a PSV2100 screen. The cylinder is 0.30 m in diameter.

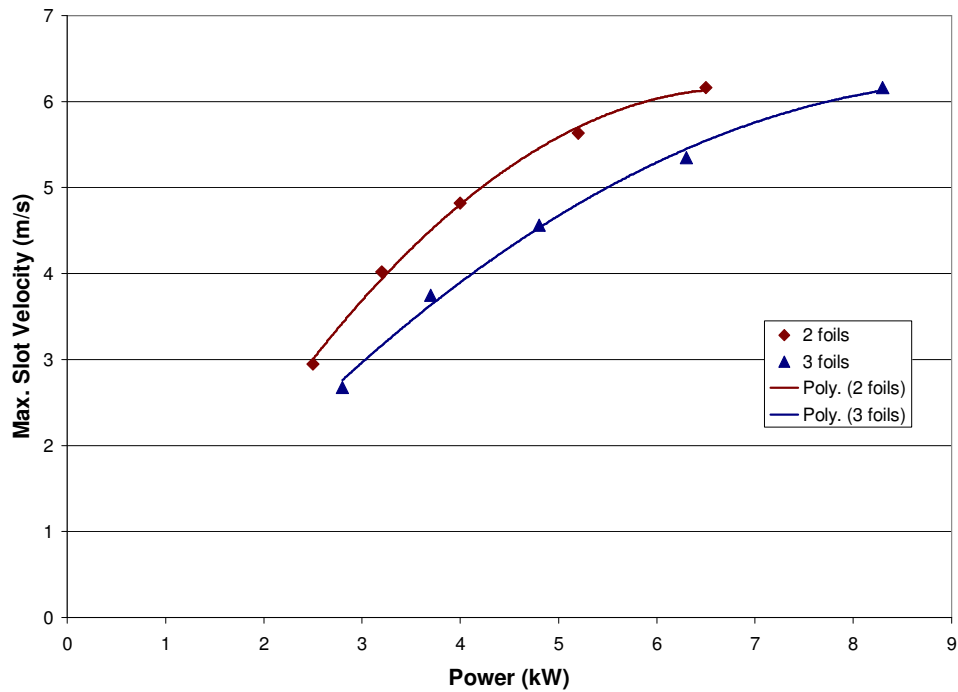


Figure 6.14: Maximum capacity envelopes for the two and three foil MEF rotors in the PSV2100 screen.

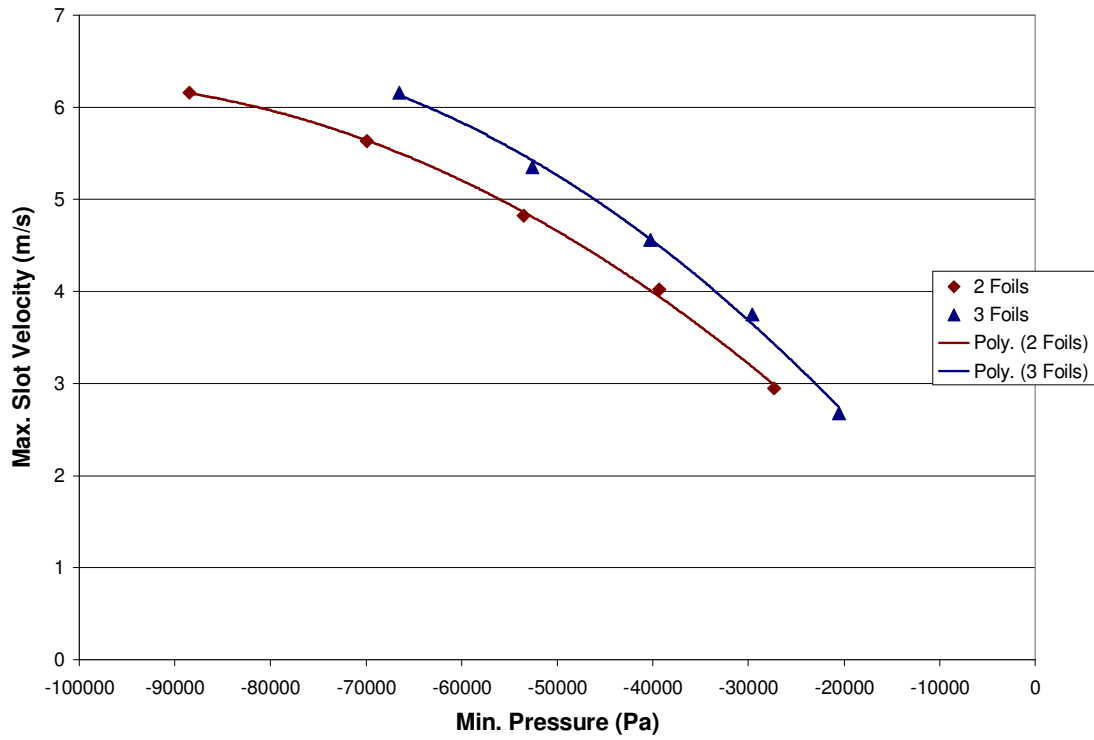


Figure 6.15: Numerically predicted minimum pressure on the cylinder vs. experimental maximum slot velocity for the two and three foil MEF rotors.

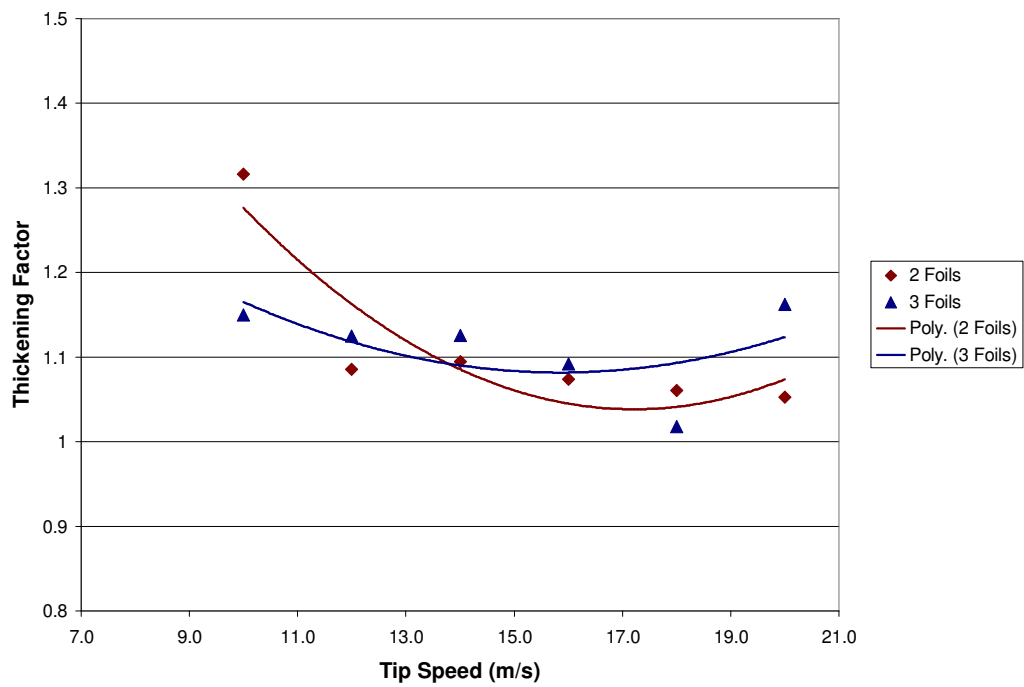


Figure 6.16: Effect of rotor tip speed on reject thickening factor for the two and three foil MEF rotors in the PSV2100 screen.

6.6 Conclusions

The effect of varying pulse frequency on pressure screen rotor performance was studied both numerically, using CFD, and experimentally. It was found that increasing the pulse frequency by adding foils to the rotor significantly decreases the performance of each individual foil. The pressure pulses generated by the foils on a six foil rotor were found to be over 50% weaker than those generated by a two foil rotor. The effect of pulse frequency on pressure pulse magnitude was found to be significantly greater than variations in foil geometry. This was shown to be due to the added drag on the swirling flow in the screen from the additional foils, which lowers the relative velocity of the flow.

These results were verified in pilot screening trials. A two foil and a three foil rotor with identical foil geometries were tested. The two foil rotor was capable of a 24% higher maximum slot velocity at a given power. Conversely, the two foil rotor used up to 24% less power at a given slot velocity. The pilot trials also indicated that, although increasing the performance of the individual foils has been repeatedly shown to improve pressure screen performance, there is likely an unknown dependence on pulse frequency, as well. This dependence on pulse frequency was shown by the fact that the three foil rotor, with a higher pulse frequency than the two foil rotor, had a higher maximum capacity at a given predicted minimum pressure pulse strength.

Finally, the effect of varying cylinder diameter on foil performance was studied, again using CFD. It was found that increasing the diameter of the cylinder slightly reduces the strength of the pressure pulses generated by the foils. There was a 5.7% reduction in the magnitude of the negative pressure pulse for a 0.80 m diameter cylinder compared to a 0.30 m cylinder.

6.7 References

1. Olson, J.A., Turcotte, S., and Gooding, R.W., "Determination of power requirements for solid core pulp screen rotors", *Nordic Pulp and Paper Res. J.* 19(2): 213-217, 2004.
2. Niinimäki, J., "Phenomena affecting the efficiency of a pressure screen", 1999 Tappi Pulping Conf., Orlando, October 31-November 4, 1999, 957-966.
3. Julien Saint Amand, F., and Perrin, B., "Fundamentals of screening: Effect of rotor design and fibre properties", 1999 Tappi Pulping Conf., Orlando, October 31-November 4, 1999, 941-955.
4. Julien Saint Amand, F., and Perrin, B., "Basic parameters affecting screening efficiency and fibre loss", 2000 PTS-CTP Deinking Symposium, Munich, Germany, May 9-12, 2000, 26.1-26.22.
5. Wakelin, R.F., and Corson, S.R., "Reject thickening behavior of TMP screening", *Pulp and Paper Canada*, 99(1): 27-30, 1998.
6. Wakelin, R.F., and Corson, S.R., "TMP long fibre fractionation with pressure screens", 1995 Int. Mech. Pulping Conf., Ottawa, Canada, June 12-15, 1995, 257-265.
7. Wakelin, R.F., Blackwell, B.G., Corson, S.R., "The influence of equipment and process variables on mechanical pulp fractionation in pressure screens", 1994 Appita Conf., Melbourne, Australia, May 2-6, 1994, 611-621.
8. Pinon, V., Gooding, R.W., Olson, J.A., "Measurements of pressure pulses from a solid core screen rotor", *Tappi J.*, 2(10): 9-12, 2003.
9. Gonzales, J., "Characterization of design parameters for a free foil rotor in a pressure screen", M.A.Sc. Thesis, Dept. of Mech. Eng., University of British Columbia, 2002.
10. Delfel, S., Ollivier-Gooch, C., and Olson, J.A., "A numerical investigation into the effectiveness of multi-element pressure screen rotor foils", *ASME J. Fluids Eng.*, 131(1): 1-12, 2009.
11. Olson, J.A., Pflueger, C., Delfel, S., Ollivier-Gooch, C.F., Martin, P., Vaulot, F., and Gooding, R., "High Performance Foil Rotor Improves De-Ink Pulp Screening", *Progress in Paper Recycling*, Accepted August, 2008.

12. Hamelin, M., Delfel, S., Olson, J.A., and Ollivier-Gooch, C.F., "High performance Multi-Element Foil (MEF) pulp screen rotor – pilot and mill trials", Accepted 2009 PAPTAC Ann. Mtg., Montreal, Canada, Feb. 3-4, 2009.
13. Feng, M., Gonzalez, J., Olson, J.A., Ollivier-Gooch, C., and Gooding, R.W., "Numerical simulation of the pressure pulses produced by a pressure screen foil rotor", ASME J. Fluids Eng., 127(2):347-357, 2005.
14. Niinimäki, J., and O. Dahl, "A Comparison of Pressure Screen Baskets with Different Slot Widths and Profile Heights - Selection of the Right Surface for a Groundwood Application", Paperi ja Puu - Paper and Timber, 80(8), 31, 1998.
15. Cox, M., B. Fredriksson, and J. Koikkalainen, "Mill Experience with High-consistency, Screening Technology for Recycled Fibre", Paper Technology, 41(9), 31, 2000.

Chapter 7

A Numerical Study of Multi-Element Pressure Screen Rotor Foils with In-Flow Cylinders⁶

7.1 Introduction and Background

Pressure screens are the most commonly used method for removing contaminants from a pulp stream. Pressure screens can also be used to fractionate the pulp, separating the pulp by fiber length and allowing for the production of higher value papers. These processes improve the strength, optical qualities and appearance of the end product.

Pressure screens operate by splitting a feed flow into a clean accept flow and a contaminated reject flow. The two main components of a pressure screen are the screen cylinder and the rotor. The feed enters the cylinder tangentially and passes down its length. Fibres pass through the small holes or narrow slots in the cylinder into the accept stream, while oversized debris passes down the length of the screen into the reject stream. The rotor serves to prevent the apertures in the cylinder from plugging. As the elements of the rotor pass an aperture, the negative pressure pulses generated by the rotor backflush the aperture and clear it. This action dramatically increases the capacity of the screen and allows for the use of smaller apertures, improving debris removal and fractionation efficiency.

The performance of a pressure screen is measured by the amount of pulp into the accept stream (capacity), its ability to remove unwanted debris (efficiency), and the power required to operate the rotor (power consumption).

⁶ A version of this chapter will be submitted for publication. Delfel, S., Ollivier-Gooch, C., Olson, J., and Gooding, R., “A numerical study of multi-element pressure screen rotor foils with in-flow cylinders”.

There are two types of screens in use in the industry – in-flow and out-flow screens. With an out-flow screen, the feed passes into the center of the cylinder and the accepts pass radially through the apertures outside the cylinder. An in-flow screen functions in the opposite manner, with the feed passing along the outside of the cylinder and the accepts passing through the apertures into the center. The rotor for an out-flow screen is therefore placed inside the cylinder, and it is placed on the outside of the cylinder for in-flow screens. The differences between in-flow and out-flow screens are illustrated in Figure 7.1. Foil rotors in out-flow screens have been the subject of numerous studies [1-15], but in-flow rotors have not been well studied. One study, however, suggested that in-flow screens have greater efficiency due to the use of centrifugal forces for the removal of high density particles in addition to the barrier removal of the screen cylinder [16].

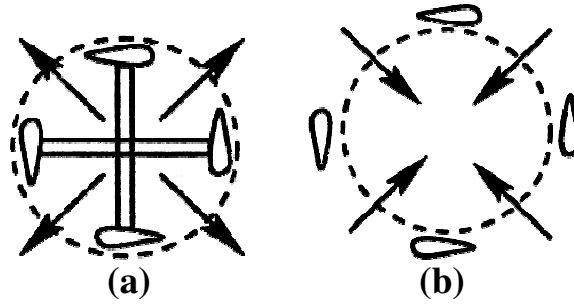


Figure 7.1: A schematic illustrating (a) out-flow screens and (b) in-flow screens.

A key non-dimensional parameter used in rotor design is the power coefficient, defined as

$$C_{Power} = \frac{Power}{\rho \cdot V_t^3 \cdot D^2} \quad (7.1)$$

where *Power* is the power consumption of the rotor, ρ is the fluid density, V_t is the tip speed of the rotor, and D is the cylinder diameter. In previous studies, the power coefficient has been found to be Reynolds number independent [17]. The power

consumption of the rotor is therefore dependent on the tip speed of the rotor cubed and the diameter squared.

Another key non-dimensional parameter is the pressure coefficient, defined as

$$C_p = \frac{P}{0.5 \cdot \rho \cdot V_t^2} \quad (7.2)$$

where P is pressure. The pressure coefficient has also been found to be Reynolds number independent [4, 18], meaning the magnitude of the pressure pulse generated by the rotor increases with the rotor tip speed squared. Therefore, by increasing the peak C_p generated by the rotor, the rotor can be slowed without reducing the magnitude of the pressure pulse generated by the foil, reducing power consumption without affecting screen capacity.

In previous work, it has been shown that there are two components to the pressure pulses generated by the rotor – a positive pressure component generated by the stagnation point near the leading edge and a negative pressure component generated by the upper surface of the foil [1-4, 13, 14]. It is desirable to minimize the strength of the positive pressure pulse since it will force unwanted debris through the apertures, reducing the efficiency of the screen. The strength of the negative pressure component has been shown to be directly linked to the capacity of the screen.

It has also been shown in out-flow studies that the geometry of the rotor foils affects the magnitude and shape of the pressure pulse [1-4, 6, 14]. It was found that increasing the angle-of-attack of the foil, or the angle of the foil with the tangent line, increases the magnitude of the negative pressure pulse and reduces the magnitude of the positive pressure pulse up to the point that the foil stalls, after which the negative pressure pulse diminishes. It was also found that increasing the camber, or curvature, of the foil increases both strength and width of the pulse. However, high camber foils were found to stall at very low angles-of-attack.

In order to achieve a high camber foil that can operate at a higher angle-of-attack, a novel multi-element (MEF) rotor for out-flow screens was developed in an earlier study [14]. The foil, shown in Figure 7.2 with key parameters defined, allows higher energy flow to pass from the lower surface to the upper surface of the foil, reenergizing the boundary layer and delaying stall. The foil was shown to have improved performance compared to other single-element rotors, both in terms of the pressure pulse generated and screen performance [14, 15, 19]. This study investigates, using computational fluid dynamics (CFD), the application of MEF rotors to in-flow screens.

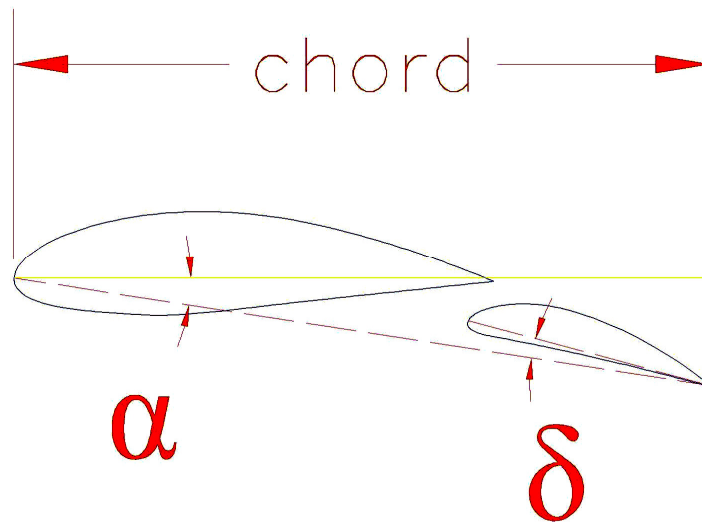


Figure 7.2: The multi-element foil (MEF) with angle-of-attack (α) and flap angle (δ) defined.

7.2 Numerical Method

The FLUENT 6.1 commercial solver was used to numerically solve the discretized Navier-Stokes equations for this study. The domain was modeled as shown in Figure 7.3,

which also shows a typical mesh used in the problem. The problem is assumed to be two dimensional, isothermal, and steady state. The standard $k-\varepsilon$ turbulence model with enhanced wall treatments was used to model turbulence in the flow. The $k-\varepsilon$ model was chosen as a reasonable balance between accuracy and computational costs. The methodology used in this work has been used successfully in previous out-flow rotor foil design studies [1-3, 14].

The boundary conditions used in the solutions are also shown in Figure 7.3. A rotating coordinate system spinning at the same speed as the rotor is set in the center of the domain, as the flow is steady in this reference frame. The outer wall and foil surfaces are set with zero velocity relative to the spinning coordinate system, while the inner wall, which represents the screen cylinder, is set with zero absolute velocity. All the edges have the no slip boundary condition. The domain is rotationally periodic at the periodic boundaries, representing a two foiled rotor. The fluid and geometric properties used in the study are summarized in Table 7.1.

Table 7.1: Fluid and geometric properties used in the study.

Fluid:	Water, 20° C
Cylinder Diameter:	0.40 m
Rotor Tip Speed:	20 m/s
Foil Chord Length:	0.1 m
Minimum Gap Between Foil and Cylinder:	5 mm

There several assumptions used in the modeling of the domain. First, water rather than pulp is used in the solutions (i.e. the consistency is 0.0%). Consistencies used in screening applications are typically very low (on the order of 1-2%), making the use of water in the simulations reasonable. Turbulent pulp suspensions in this consistency range have the same density and viscosity as water and it has been found in previous studies that increasing consistency reduces the magnitude of the pressure pulses generated by the

rotor, but the shape and trends of the pulses are not affected [4]. Another assumption is that the screen cylinder is modeled as a solid wall, corresponding to a slot velocity of $V_{\text{slot}} = 0$ m/s. This is meant to represent the critical design case when the cylinder plugs. It also significantly reduces the computational cost of the problem by eliminating the need to simulate the complicated flow through the apertures.

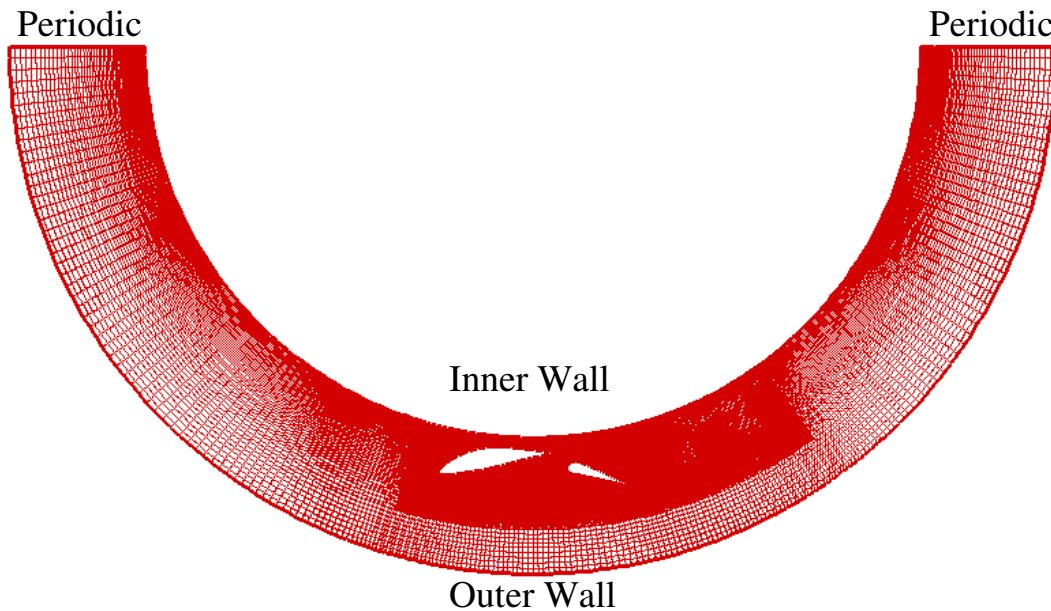


Figure 7.3: Computational domain, boundary conditions, and a typical mesh.

7.3 Results and Discussion

The pressure contours and streamlines for a NACA 8312 foil at varying angles-of-attack are shown in Figure 7.4. The NACA 8312 is a highly cambered foil that was found to generate the strongest and widest pressure pulse in previous studies out-flow screen studies [1, 3, 4]. As can be seen, the flow has separated from the upper surface of the foil and a vortex has formed even at a very low angle-of-attack. Additionally, at $\alpha = 1$ deg., there is leading edge separation on the lower surface of the foil. The separation in both cases is likely due to the angle of the incoming and outgoing flows as they follow the

curvature of the cylinder wall. This effectively reduces the angle-of-attack and increases the camber of the foil. In addition to reducing the strength of the pulse generated by the foil, these vortices will be large sources of drag, increasing the power consumption of the rotor. As the angle-of-attack is increased, the leading edge separation is eliminated, however the foil stalls further and the flow separation over the upper surface becomes even more pronounced.

Figure 7.5 shows pressure contours and streamlines for the MEF with varying flap angle at a constant angle-of-attack of $\alpha = 1$ deg. As can be seen, as with the NACA 8312, there is leading edge separation on the lower surface of the foil and the flap has stalled. Interestingly, though, increasing the flap angle causes a reduction in the leading edge separation and causes the negative pressure pulse to widen and intensify, even though the flow over the flap has stalled. At $\delta = 15$ deg. and above, the beginnings of vortex shedding can be seen.

The pressure contours and streamlines for increasing angle-of-attack at a constant flap angle of $\delta = 0$ deg. are shown in Figure 7.6. Increasing the angle-of-attack is shown to be effective in eliminating the separation from both the leading edge and the flap. This is due to the fact that high energy flow from the lower surface of the foil is allowed to pass through the slot between the main foil and the flap, reenergizing the boundary layer on the flap and delaying stall. Also, as the angle-of-attack is increased, the magnitude and width of the negative pressure pulse increases until the upper surface of the main foil begins to stall at $\alpha = 7$ deg. This is illustrated more quantitatively in Figure 7.7, which shows pressure traces along the cylinder wall for the MEF at a constant flap angle and varying angles-of-attack.

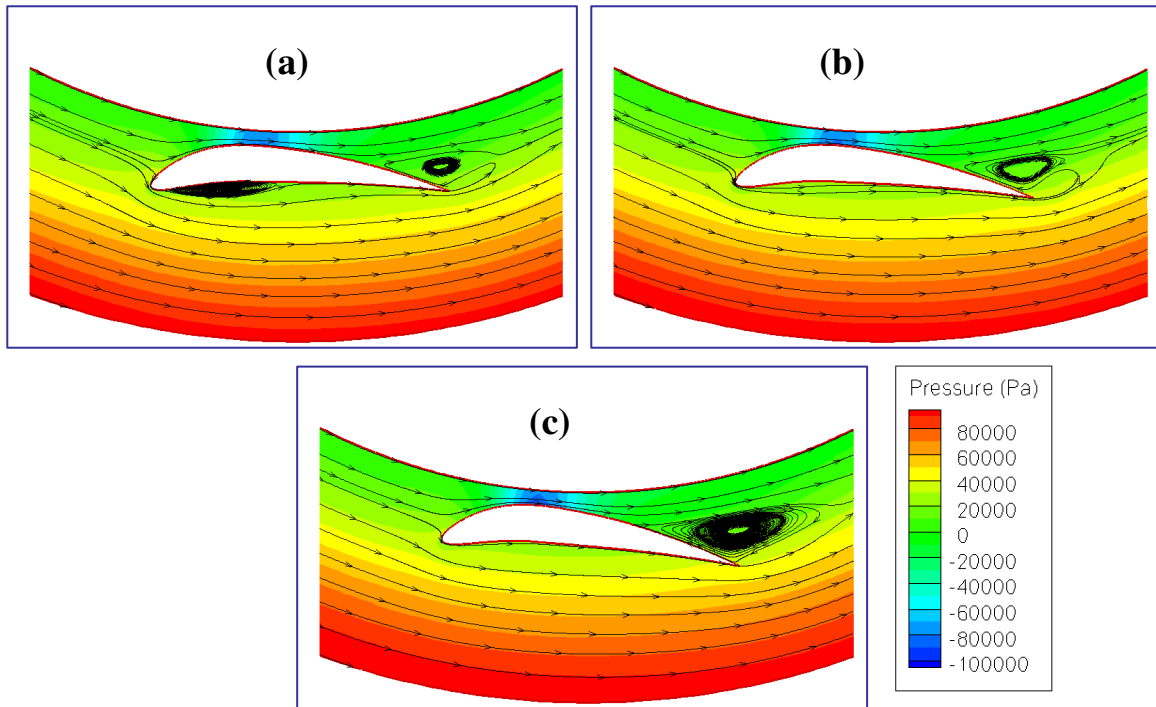


Figure 7.4: Pressure contours and streamlines for a NACA 8312 at an angle-of-attack of
 (a) $\alpha = 1$ deg., (b) $\alpha = 3$ deg., and (c) $\alpha = 5$ deg.

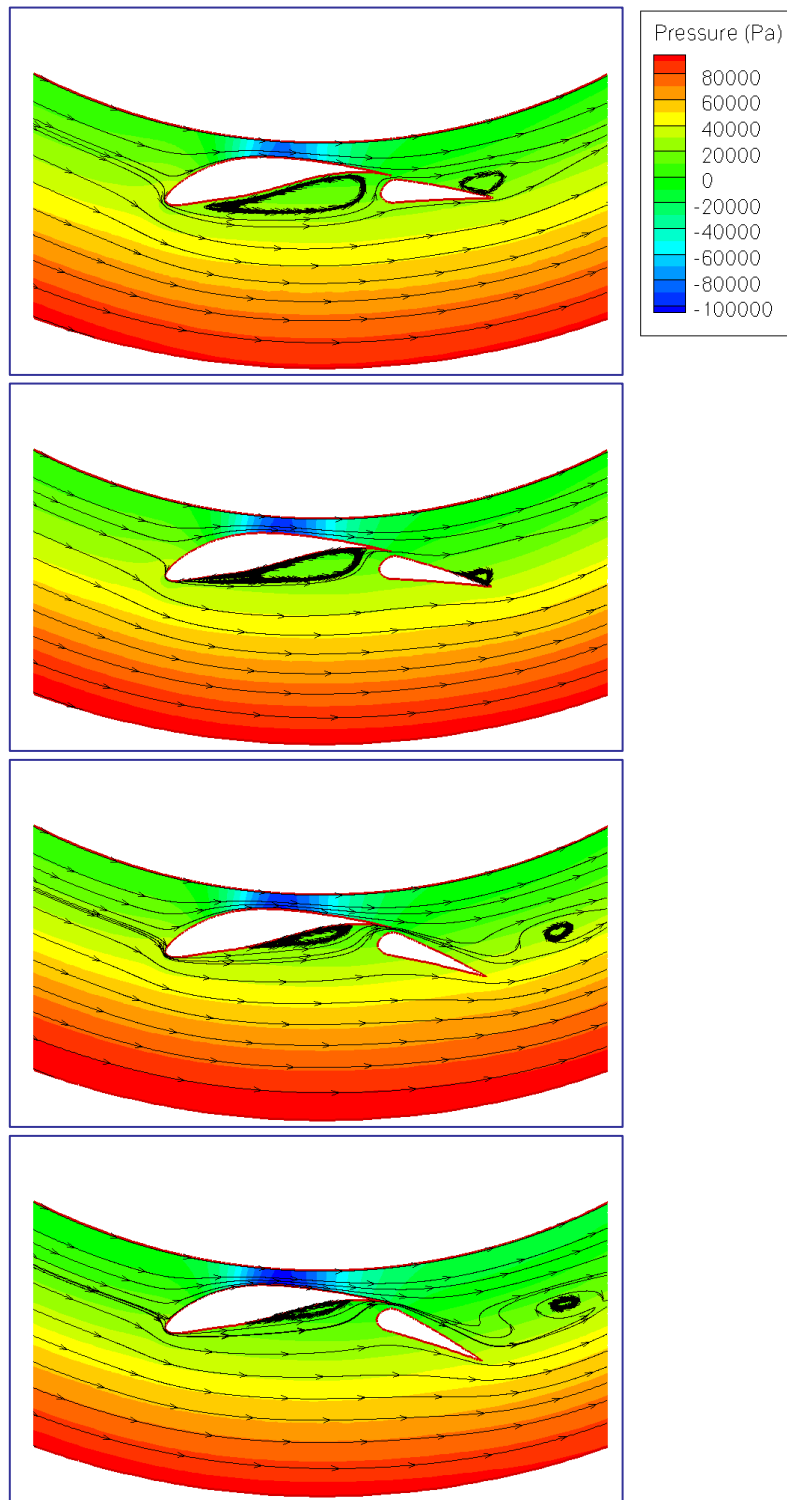


Figure 7.5: Pressure traces and streamlines for varying flap angles and a constant angle-of-attack of $\alpha = 1$ deg. The flap is at (a) $\delta = 0$ deg., (b) $\delta = 7$ deg., (c) $\delta = 15$ deg., and (d) $\delta = 22$ deg.

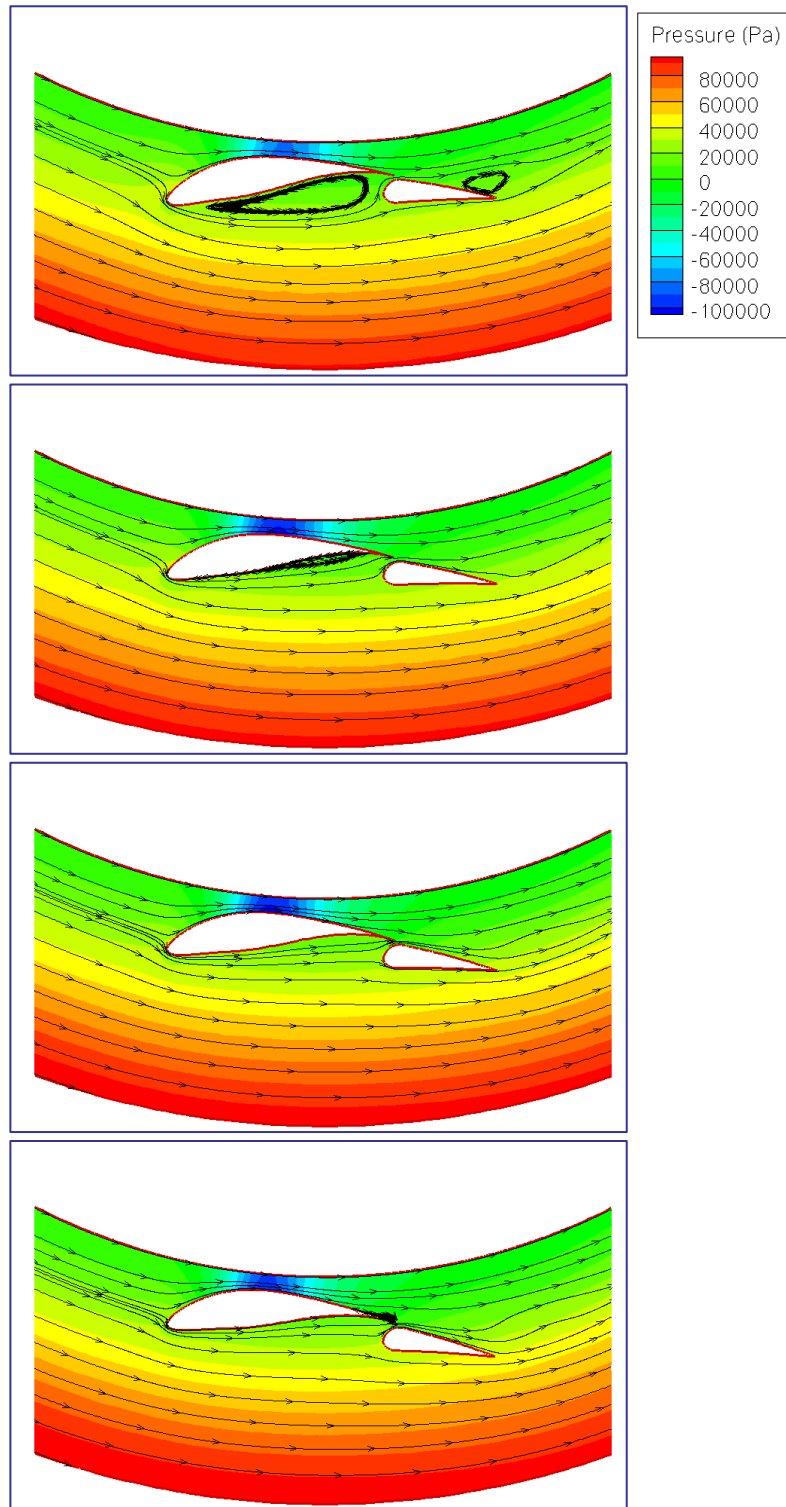


Figure 7.6: Pressure traces and streamlines for varying angle-of-attack at a constant flap angle of $\delta = 0$ deg. The angle-of-attack is (a) $\alpha = 1$ deg., (b) $\alpha = 3$ deg., (c) $\alpha = 5$ deg., and (d) $\alpha = 7$ deg.

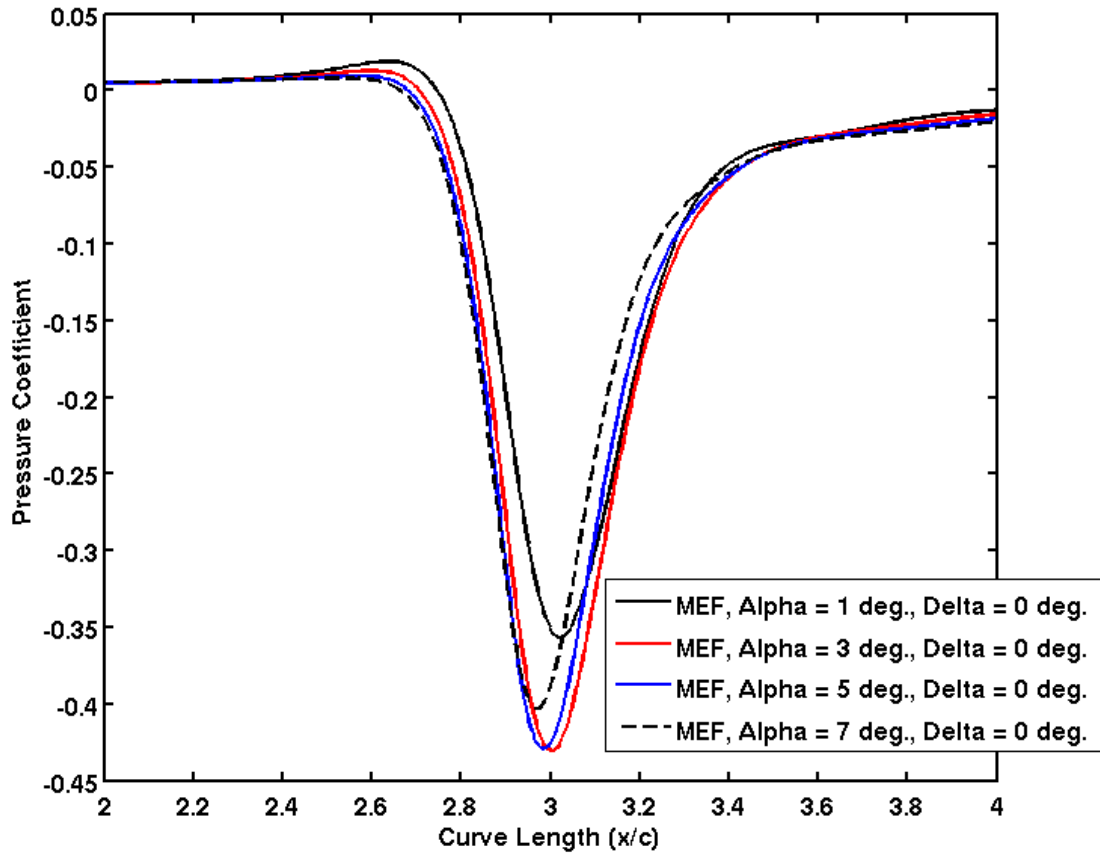


Figure 7.7: Traces of pressure coefficient on the cylinder wall for the MEF at varying angles-of-attack and a constant flap angle.

Figure 7.8 shows the effect of varying the flap angle on the minimum pressure coefficient along the cylinder at various angles-of-attack. An optimum flap angle is shown to exist for each angle-of-attack. This optimum flap angle is shown to decrease as angle-of-attack increases. All told, there is a 23% increase in the magnitude of the minimum wall C_p for the MEF compared to the best single-element configuration studied.

Similarly, Figure 7.9 shows the effect of varying the flap angle on the maximum pressure coefficient along the cylinder at various angles-of-attack. As can be seen, increasing the angle-of-attack and increasing the flap angle both reduce the magnitude of the positive pressure pulse on the cylinder. This is because the stagnation point at the leading edge of

the foil shifts towards the lower surface of the foil, preventing the positive pressure generated there from projecting onto the cylinder. The MEF is able to reduce the maximum wall C_p by 29%.

Finally, the integrated force coefficient as a function of flap angle, with lines of constant angle-of-attack, is shown in Figure 7.10. The two-dimensional force coefficient is found by integrating the pressure over the surface and is defined as

$$C_F = \frac{F}{0.5 \cdot \rho \cdot V_t^2 \cdot c} = \int C_p \frac{dx}{c} \quad (7.3)$$

where C_F is the force coefficient, F is the force (per m span), and x is the distance along the circumference of the cylinder wall. The force coefficient serves as a measurement of the width of the pulse in addition to the peak magnitude. Interestingly, the strongest force is generated at an angle-of-attack of $\alpha = 1$ deg., which was shown in Figure 7.6 to have both leading edge separation and separated over the flap. It is still unknown if screen capacity is driven more by the peak negative pressure generated by the foil or by the integrated force. Overall, the MEF was able to increase the magnitude of the force coefficient by 23% compared to the single-element foils studied.

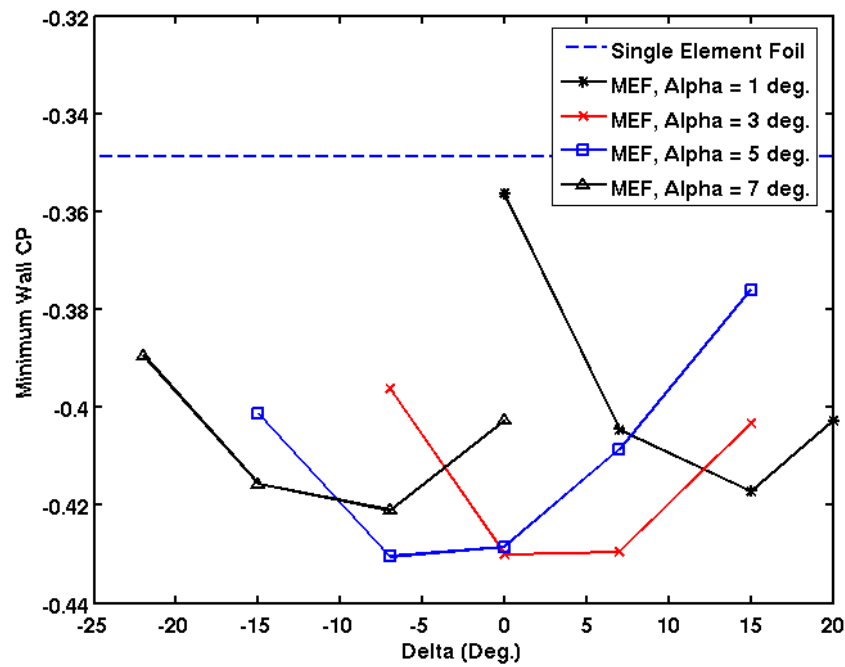


Figure 7.8: The effect of varying flap angle on the minimum C_p on the cylinder. The dashed line represents the best result for the NACA 8312 single-element foil.

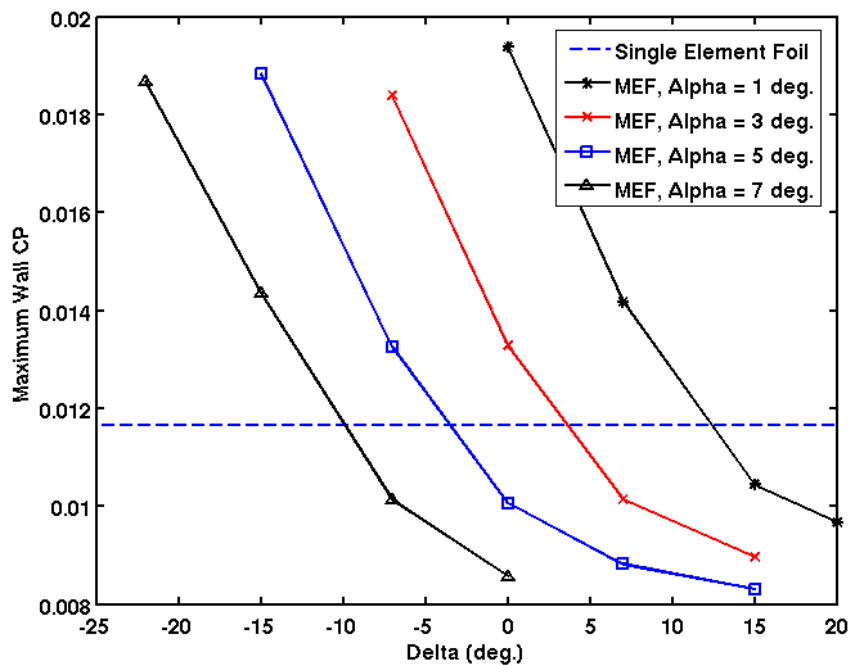


Figure 7.9: The effect of varying flap angle on the maximum C_p on the cylinder. The dashed line represents the best result for the NACA 8312 single-element foil.

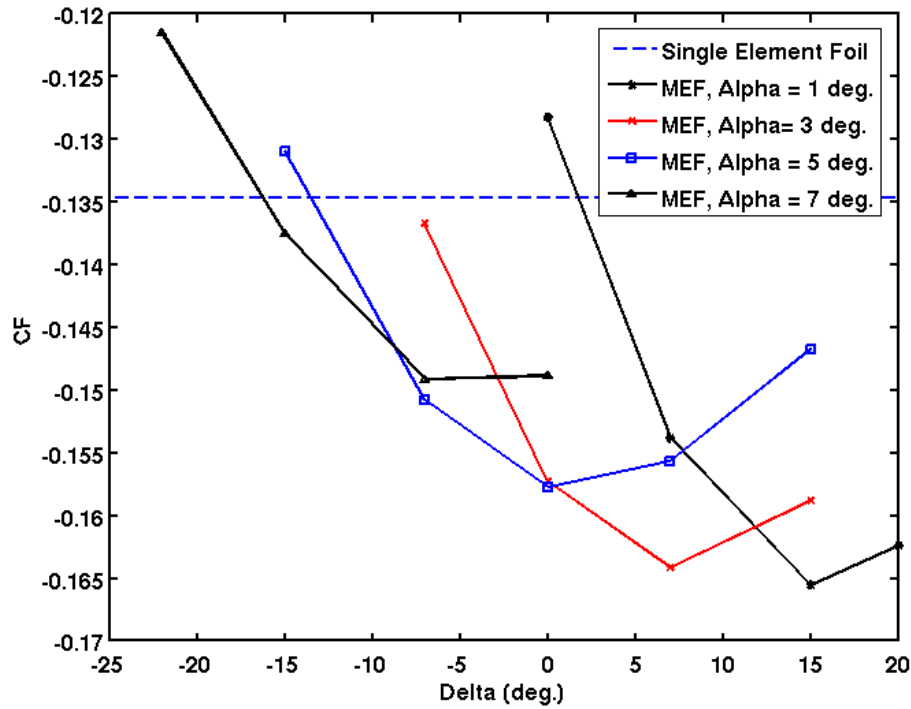


Figure 7.10: The effect of vary flap angle on the force coefficient on the cylinder. The dashed line represents the best result for the NACA 8312 single-element foil.

Based on the results in Figures 7.8, 7.9, and 7.10, an optimal configuration was selected at $(\alpha, \delta) = (3, 7)$ deg. This configuration, which is shown in Figure 7.11 with pressure contours and streamlines, results in a pressure pulse that is close to the maximum magnitude minimum wall pressure coefficient and force coefficient and has a low maximum wall pressure coefficient. Additionally, the flow is completely attached over both surfaces of the foil, which will reduce the drag on the foil, reducing rotor power requirements.

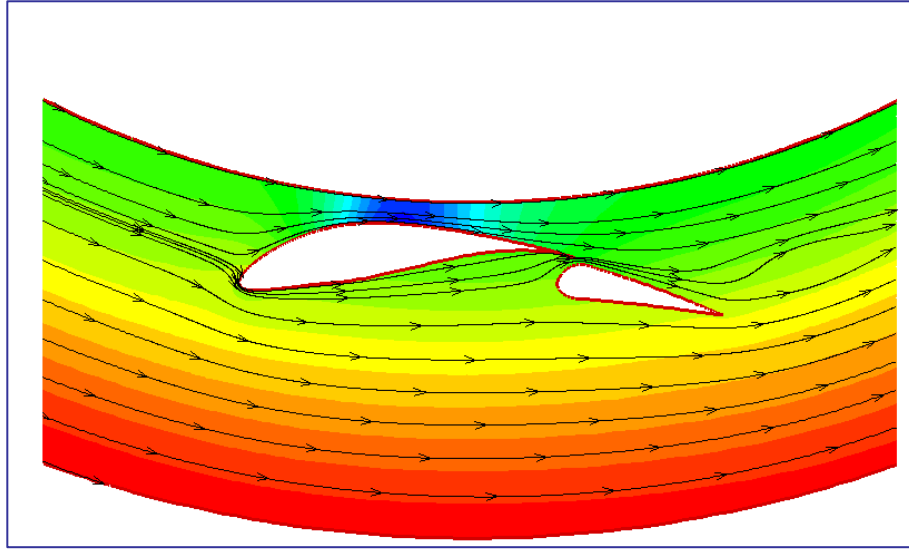


Figure 7.11: Pressure contours and streamlines for the MEF at $(\alpha, \delta) = (3, 7)$ deg., the optimum configuration.

7.4 Conclusions

The application of a novel multi-element rotor foil to in-flow pressure screens has been investigated using computational fluid dynamics. It was found that for single-element foils in in-flow screens it is difficult to eliminate the leading edge separation on the lower surface of the foil without stalling the foil. This is due to the curvature of the cylinder which effectively reduces the angle-of-attack of the foil while at the same time inducing separation at the trailing edge earlier than with an out-flow cylinder. The vortices generated by the separated flow would be a large source of drag, increasing the power consumption of the rotor.

The optimum configuration for the MEF was found to be at $(\alpha, \delta) = (3, 7)$. The MEF was shown to be capable of eliminating the leading-edge separation without stalling the foil. In addition to reducing the drag on the foil, this was shown to improve the pulse generated by the foil. The MEF was shown to increase in the magnitude of both the negative pressure pulse and the force coefficient by as much as 23% compared to the best single-element foil studied, while at the same time reducing the magnitude of the positive

pulse by 29%. These improvements in the pulse magnitude will allow the rotor to be slowed, further reducing its power consumption.

7.5 References

1. Feng, M., “Numerical Simulation of the pressure pulses generated by a pressure screen foil rotor”, M.A.Sc. Thesis, Dept. Mech. Eng., Univ. British Columbia, 2003.
2. Feng, M., Olson, J.A., Ollivier-Gooch, C.F., Xia, J., and Gooding, R.W., A computational fluid dynamic (CFD) tool for advanced pulp screen foil rotor design”, ABTCP Conf., Sau Paulo, Brazil, Oct. 2003.
3. Feng, M., Gonzales, J., Olson, J.A., Ollivier-Gooch, C., and Gooding, R.W., “Numerical simulation of the pressure pulses produced by a pressure screen foil rotor”, J. Fluid Eng., 127(2):347-357 (2005).
4. Gonzales, J., “Characterization of design parameters for a free foil rotor in a pressure screen”, M.A.Sc. Thesis, Dept. Mech. Eng., Univ. British Columbia, 2002.
5. Pflueger, C.D., Olson, J.A., and Gooding, R.W., “The performance of the EP Rotor in de-ink pulp screening”, Preprints 2007 Appita Conf.
6. Niinimäki, J., “Phenomena affecting the efficiency of a pressure screen”, 1999 Tappi Pulping Conf., 957-966.
7. Julien Saint Amand, F., and Perrin, B., “Fundamentals of screening: Effect of rotor design and fibre properties”, 1999 Tappi Pulping Conf., 941-955.
8. Julien Saint Amand, F., and Perrin, B., “Basic parameters affecting screening efficiency and fibre loss”, 2000 PTS-CTP Deinking Symposium, 26.1–26.22.
9. Wakelin, R.F., Blackwell, B.G., and Corson, S.R., “The influence of equipment and process variables on mechanical pulp fractionation in pressure screens”, 1994 Appita Conf., 611-621.
10. Wakelin, R.F., and Corson, S.R., “TMP long fractionation with pressure screens”, 1995 Int. Mech. Pulping Conf., 257-265.
11. Wakelin, R.F., and Corson, S.R., “Reject thickening behavior of TMP screening”, Pulp Paper Can., 99(1): 27-30, 1998.
12. Yu, C.J., “Pulsation measurement in a screen. Part I: Pulse signature and magnitude of S-shape rotor”, 1994 Tappi Engineering Conf., 767-782.
13. Atkins, M., “Axial variations and entry effects in a pressure screen”, Ph. D. Thesis, Dept. of Eng., Univ. of Waikato, 2007.

14. Delfel, S., Ollivier-Gooch, C., and Olson, J., "A numerical investigation into the effectiveness of multi-element pressure screen rotor foils", *J. Fluid Eng.*, 131(1): 011101-1, 2009.
15. Hamelin, M., Delfel, S., Olson, J., and Ollivier-Gooch, C.F., "High Performance Multi-Element Foil (MEF) Pulp Screen Rotor - Pilot and Mill Trials", *Paptac Annual Meeting Proc.*, Montreal, 2009.
16. Levis, S., "Screening of secondary fibers", *Progress in Paper Recycling*, 1(1): 31-45, 1991.
17. Olson, J.A., Turcotte, S., Gooding, R.W., "Determination of power requirements for solid core pulp screen rotors", *Nordic Pulp Paper Res. J.*, 19(2):213-217, 2004.
18. Pinon, V., Gooding, R.W., Olson, J.A., "Measurement of pressure pulses from a solid core rotor", *Tappi J.*, 2(10): 9-12, 2003.
19. Olson, J.A., Pflueger, C., Delfel, S., Ollivier-Gooch, C.F., Martin, P., Vaultot, F., and Gooding, R., "High Performance Foil Rotor Improves De-Ink Pulp Screening", *Progress in Paper Recycling*, 17(4), 2009.

Chapter 8

Influence of Cylinder Design and Other Factors on Capacity and Power Consumption in a Pressure Screen⁷

8.1 Introduction

Pressure screens are the most efficient, industrially practical way to remove contaminants from a pulp stream. Pressure screens are also the most effective method for separating fibre by length to enable targeted processing or use in high value specialty paper products. Through these processes, pressure screens increase the strength, optical properties and appearance of the end product in all forms of pulping and papermaking, including mechanical pulping, kraft pulping and recycling.

The two performance determining components of a pressure screen are the rotor and screen cylinder. Screen performance is described by capacity, i.e, the maximum accept pulp mass flow rate; contaminant removal or fractionation efficiency; and the rotor power consumption. The effect of cylinder design on efficiency and capacity has been investigated previously for both slotted screen cylinders and smooth holed cylinders [1-7], and power consumption has been shown to be related to rotor design, size and speed by Olson *et al.* [8]. However the effects of cylinder design, feed flow rate and screen inlet design on power consumption are not well understood.

Screen cylinders have specially designed aperture entry geometries, called contours, that enhance turbulence and redirect the cross flow into the aperture to increase the maximum capacity of the screen cylinder. The development of high performance contours have led to greatly reduced slot widths while maintaining a high maximum capacity. Smaller slots

⁷ A version of this chapter has been submitted for publication. Delfel, S., Olson, J., Martinez, M., Regairaz, A., Ollivier-Gooch, C., and Houvinen, A., “Influence of cylinder design and other factors on capacity and power consumption in a pressure screen”.

improve both the debris removal and fractionation efficiency of the screen [1, 4, 7, 9-12]. A typical contoured slot is shown in Figure 8.1 with key dimensions identified.

Previous studies of pressure screen power consumption have focused on the effects of the rotor design. Olson et al found through a series of pilot trials that the nondimensional power coefficient of the screen is independent of Reynolds number [8], with power coefficient defined as

$$C_{Power} = \frac{Power}{\rho V_t^3 D_t^2}, \quad (8.1)$$

where *Power* is the rotor power, ρ is the fluid density, V_t is the tip speed of the rotor, and D_t is the diameter of the tip of the rotor. The power consumption of the screen is therefore dependent on the rotor tip speed cubed. It was also found that the power coefficient was approximately linearly dependent on the capacity coefficient, where the capacity coefficient is defined as

$$C_q = \frac{Q_f}{V_t D_t^2} \quad (8.2)$$

where Q_f is the feed volumetric flow rate.

While a strong correlation between rotor speed and power consumption has been established, the effect of cylinder design on screen power consumption is not well understood. The objective of this work is to investigate the effects of pressure screen design and operation, especially cylinder wire shape and aperture type, on pressure screen power consumption and maximum capacity. The performance of cylinders with varying slot and hole designs were studied experimentally. Also, a theoretical model was developed to expand upon the work of Olson *et al.* and predict the power consumption of the pressure screen based on the geometry, flow conditions and operating parameters of the screen.

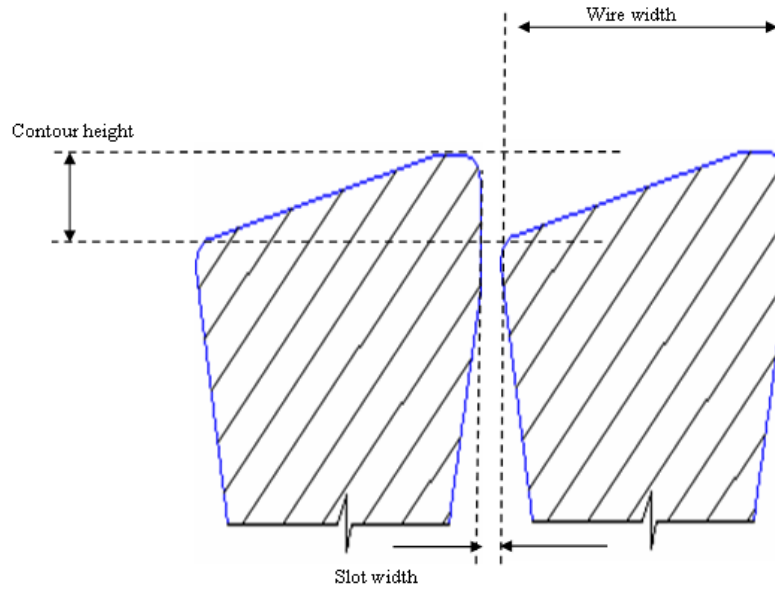


Figure 8.1: A typical contoured slot design with key dimensions identified [9].

8.2 Analysis

To better understand the impact of screen design and operation on power consumption, we developed a model of power consumption by considering a hydrodynamic mass and angular momentum balance through the screen.

For the mass and angular momentum balance, the screen was modelled as shown in Figure 8.2. For simplicity, the rotor for the analysis was assumed to be a solid core rotor, rather than a foil rotor. A control volume was considered for the internal volume of the screen, radially between the rotor and the cylinder and axially down the length of the screen. All three flows (feed, accept and reject) are considered and are assumed to be uniform. Additionally, the tangential flow in the screen is assumed to be moving at a uniform speed of

$$V_{avg} = \gamma \cdot V_t \quad (8.3)$$

where γ is the slip factor. The slip factor γ is determined empirically for each rotor and cylinder combination. It accounts for the variation in the swirling velocity of the flow in the cylinder due to losses and energy consumed by the complicated turbulent flows around the rotor, the wake, and in the vortices around the slots [12]. Typical values for γ are between 0.5 and 0.9.

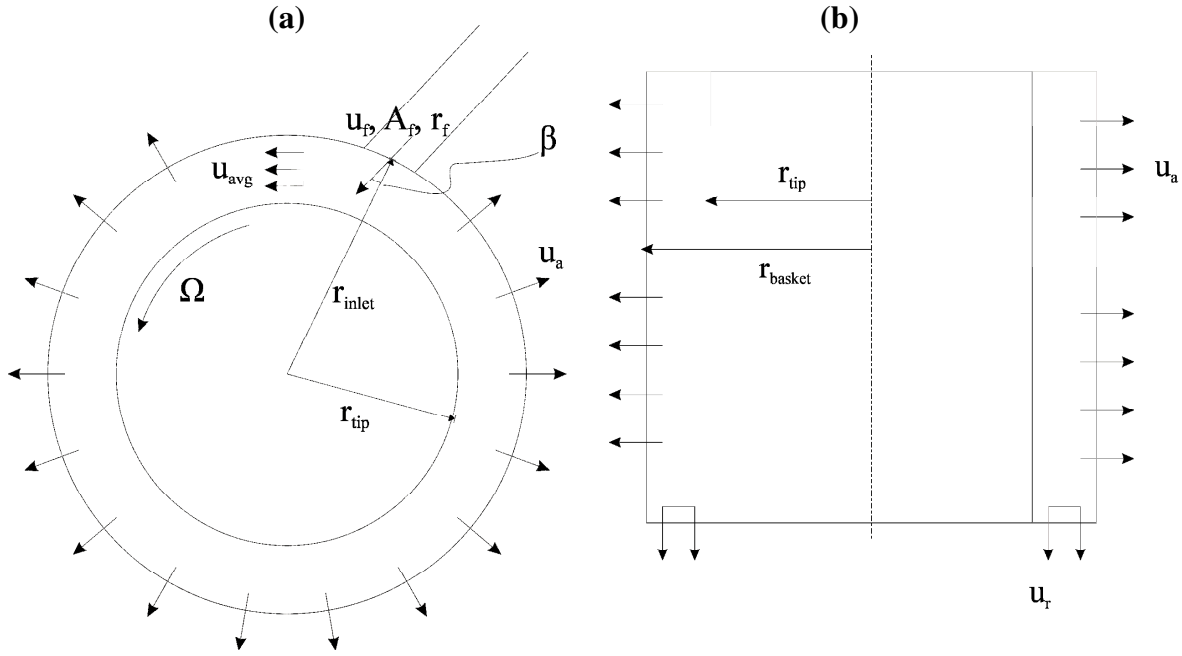


Figure 8.2: Top view (a) and side view (b) of the volume used for the analysis.

With the details of the analysis left to Appendix B, evaluating the continuity and angular momentum equations yields a concise relationship for screen power consumption, shown as equation 8.4. Equation 8.4 is given in terms of easily measured screen geometry and operating parameters:

$$Power = \Omega T = \rho \frac{V_t}{r_{tip}} Q_f [(r_{tip} + \frac{g}{2}) R_V \mathcal{W}_t - \frac{Q_f}{A_f} (r_{tip} + g) \sin(\beta)] + \frac{V_t}{r_{tip}} F, \quad (8.4)$$

where T is the torque applied to the rotor, r_{tip} is the radius of the tip of the rotor, g is the minimum gap between the rotor and the screen cylinder, R_V is the volumetric reject rate, A_f is the cross sectional area of the feed inlet, β is the inlet angle, and F is a friction term.

Expanding upon the power equation of Olson *et al.* in equation 8.1, the friction term F is assumed to be the torque caused by turbulent drag and bearing friction such that

$$F = C_D \frac{1}{2} \rho V_t^2 S r_{tip} + b, \quad (8.5)$$

where C_D is the drag coefficient, S is a reference area (typically the cross-sectional area of the screen), and b represents the torque due to bearing friction [8]. Based on the results in Figure 8.3, which shows rotor power as a function of tip speed for the rotor spinning in air, where the fluid density is very low, it can be seen that the no load rotor power consumption varies linearly with rotor tip speed. The parameter b is therefore assumed to be a constant.

Combining equations 8.4 and 8.5 yields the final power equation:

$$Power = \Omega T = \frac{\rho V_t Q_f}{r_{tip}} [(r_{tip} + \frac{g}{2}) R_V \mathcal{W}_t - \frac{Q_f}{A_f} (r_{tip} + g) \sin(\beta)] + C_D \frac{1}{2} \rho V_t^3 \pi r_{tip}^2 + \frac{V_t}{r_{tip}} b \quad (8.6)$$

By introducing several non-dimensional parameters and the assumption that, for large screens, $g \ll r_{tip}$, it is possible to simplify the equation further and solve for the non-dimensional power coefficient (as defined in equation 1). The dimensionless screen power equation becomes:

$$C_{Power} = C_q R_V \gamma - \frac{4C_q^2 \sin \beta}{\pi \hat{r}^2} + \frac{1}{8} \pi C_D + \frac{b}{4\rho V_t^2 r_{tip}^2}, \quad (8.7)$$

where \hat{r} is the inlet ratio. The inlet ratio is defined as

$$\hat{r} = \frac{r_f}{r_{tip}} \quad (8.8)$$

where r_f is the radius of the feed inlet. Since for pulp flows $b \ll 4 \cdot \rho \cdot V_t^2 \cdot r_{tip}^2$, equation 8.7 can further be simplified to

$$C_{Power} = C_q R_V \gamma - \frac{4C_q^2 \sin \beta}{\pi \hat{r}^2} + \frac{1}{8} \pi C_D \quad (8.9)$$

The most significant difference between the model in equations 8.6 and 8.9 and the results of Olson *et al.* is that rotor power is shown to be a function of the flow rate of the screen in addition to being cubically dependent on rotor tip speed. Also, Olson *et al.* found the power coefficient to be linearly dependent on the capacity coefficient, where as equation 8.9 shows C_{Power} to be a function of C_q squared. If the $\sin(\beta)$ term is small, however, the model becomes linearly dependent on the capacity coefficient and matches Olson *et al.*'s results [8].

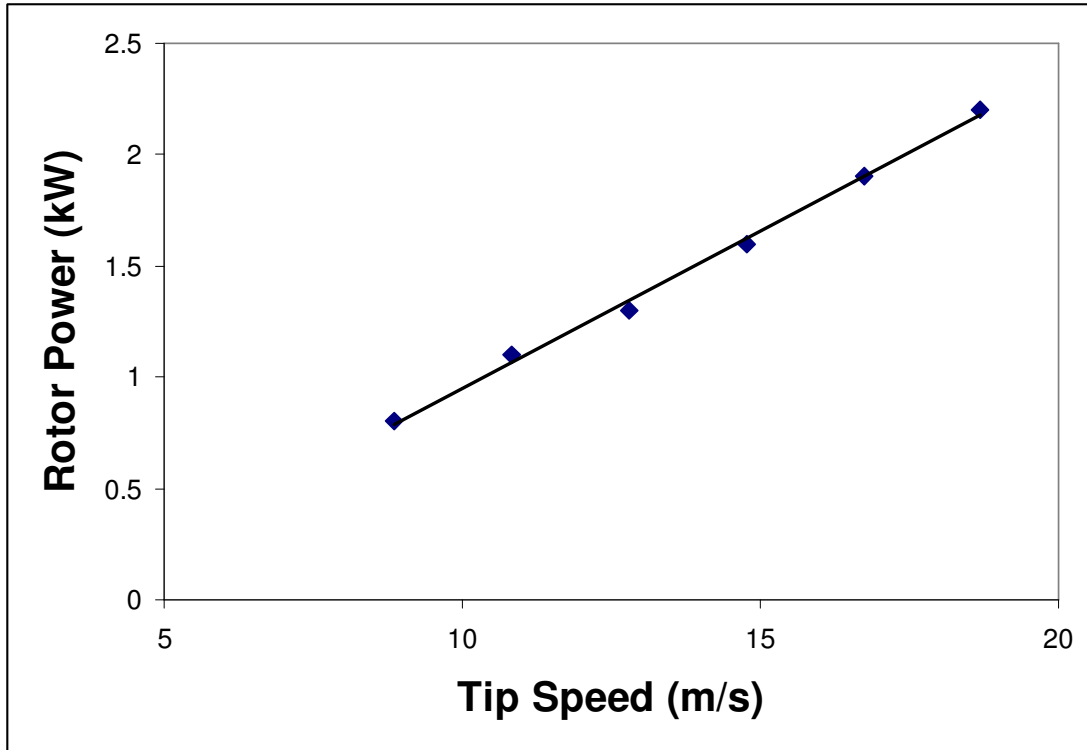


Figure 8.3: Experimental rotor power as a function of tip speed for the EP rotor in air with a linear least squares fit.

8.3 Experimental Procedure

The screen power consumption and capacity study was conducted using a laboratory MR8 pressure screen at the Pulp and Paper Centre at the University of British Columbia, shown in Figure 8.4. The screen is equipped with a variable frequency drive, allowing for adjustable rotor tip speeds as well as accurate measurements of rotor power consumption. The screen is also instrumented with magnetic flow meters on the accept and reject ports and pressure sensors on the feed, accept and reject ports. An AFT EP foil rotor was used in all cases with a constant gap between the rotor and screen cylinder of 5 mm.

A 50/50 hardwood/softwood kraft pulp mix was used to simulate a de-inked kraft pulp [13]. The screen was fed from a 1000 L feed tank, with the accept and reject streams

recirculating back to the feed tank. The pulp used was 2% consistency, which is within the range of consistencies found in industrial applications. Seven separate cylinder designs were tested – six different slotted cylinders and a 1 mm. smooth hole design. Table 8.1 shows the cylinders studied and their geometric properties. Cylinders A, B, C, E and F all have similar geometries to that shown in Figure 8.1, while cylinder D has a flattened top to the contour and cylinder G is the smooth hole design. Figure 8.5 shows how cylinder D varies compared to the other contoured slot geometries.

Each trial consisted of increasing flow rates of the screen at a constant rotor tip speed and volumetric reject rate ($R_V = 0.25$) until the screen plugged and a maximum slot velocity for the given configuration was found. The rotor tip speed was then decreased and the study was repeated. In this manner a “plugging line” representing the maximum capacity of each cylinder at a given rotor speed was found.

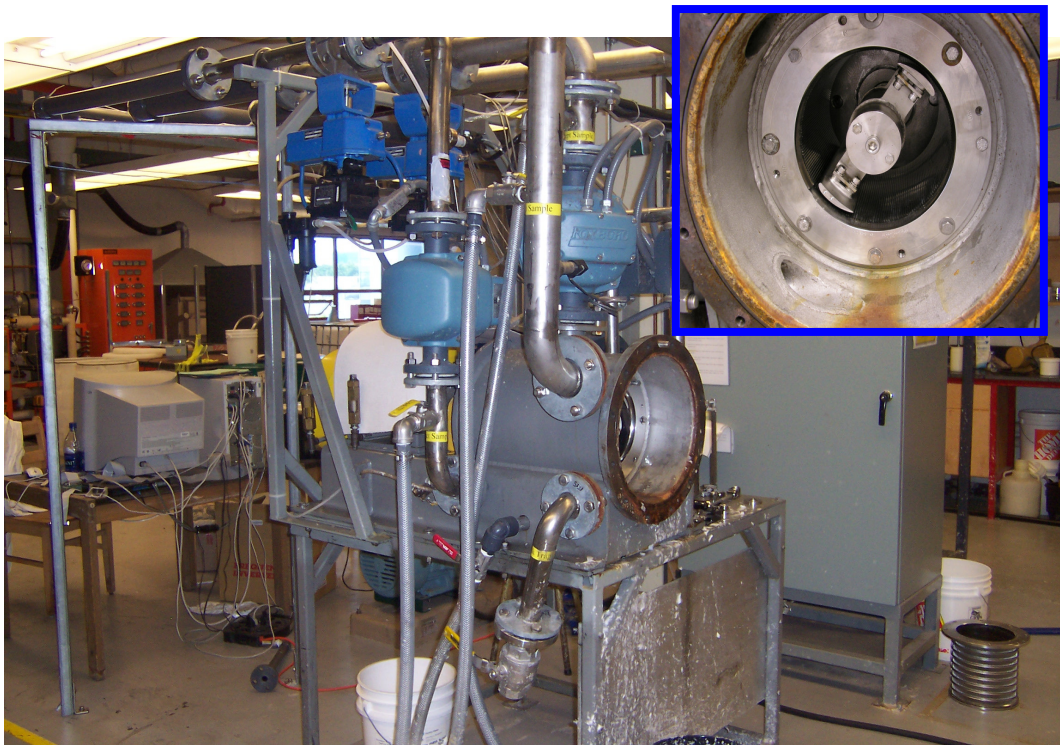


Figure 8.4: The UBC GL&V MR8 pilot pressure screen. The rotor and cylinder installation can be seen in the inset.

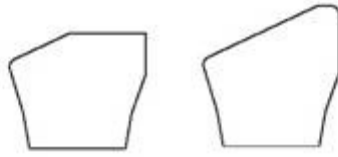


Figure 8.5: Schematic showing how cylinder D (left) varies compared to the other geometries.

Table 8.1: Wire geometries studied.

Cylinder Name	Contour Height (mm)	Contour Width (mm)	Slot Width/Diameter (mm)
A	0.6	3.2	0.15
B	0.9	3.2	0.15
C	1.2	3.2	0.15
D	0.6	3.2	0.15
E	0.6	2.3	0.15
F	0.6	2.3	0.10
G	n/a	n/a	1.00

8.4 Experimental Results

Figure 8.6 shows experimental results for slot velocity versus power consumption for cylinder A, which are typical for all cylinders measured. As can be seen, the maximum slot velocity increases with rotor power but approaches a maximum value at high rotor speeds. Also, it can be seen that increasing screen flow rates at a constant rotor speed and volumetric reject ratio leads to a reduction in rotor power consumption. At certain points, the rotor is using less power at higher rotor tip speeds and slot velocities. This is likely because at higher flow rates the pulp enters the screen with greater angular momentum,

meaning the rotor does not need to accelerate the flow as much to reach a steady state. This also generally supports the effectiveness of the model in equations 8.6 and 8.9, which show a dependence of rotor power consumption on the screen flow rates.

The compiled results for the performance of all cylinders tested are shown in Figure 8.7. Cylinder D had the best performance, with a greater than 20% higher slot velocity at a given rotor power than the other cylinders. Conversely, cylinder D used more than 40% less power at a given slot velocity. There is a weak trend indicating that lower contour height leads to lower power consumption at a given slot velocity, as shown by the results for cylinders A, B, and C. However, the lines for the three cylinders converge to a common maximum slot velocity and rotor power. It is also worth noting that the cylinder with a smaller slot width (cylinder F) was able to achieve similar slot velocities as the best 0.15 slot width cylinder, albeit at considerably higher rotor power. Smaller slot widths are generally desirable for both fractionation and debris removal. The smooth hole cylinder (cylinder G) had significantly lower capacity than the other cylinders, and rotor power did not have as strong an effect on maximum slot velocity as it did for the cylinders with contoured slots.

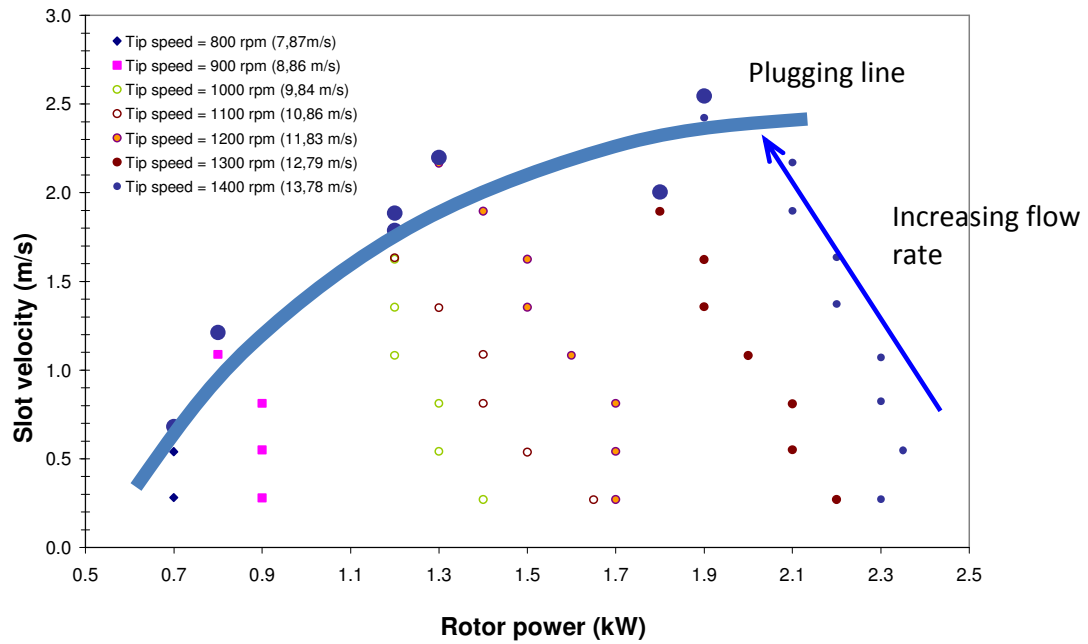


Figure 8.6: Slot velocity as a function of rotor power for cylinder A, showing a typical plugging envelope. Note the reduction in power as flow rates are increased for a constant rotor speed.

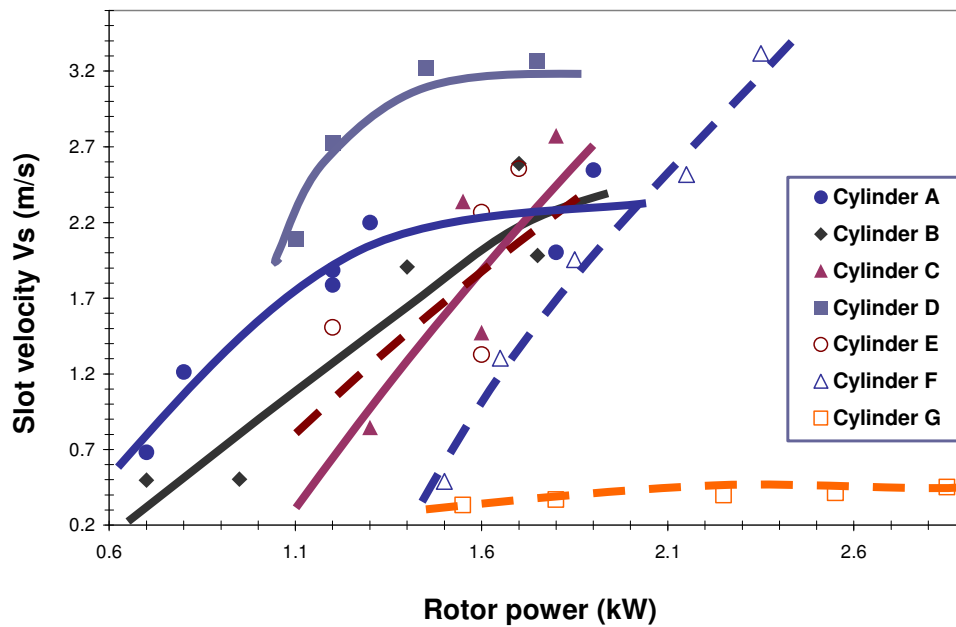


Figure 8.7: Maximum capacity envelopes for all cylinders studied.

The screen power model (equation 8.6) was compared with the experimental results above in order to determine its effectiveness. The physical parameters for the UBC MR8 screen with AFT EP rotor and cylinder A, as used in the analysis, are shown in Table 8.2. Note that equation 8.6 is used rather than equation 8.9 for the analysis, since the MR8 screen is small and the small gap assumption is not valid in this case.

Figure 8.8 shows the experimental and theoretical rotor power consumption plotted as a function of feed flow rate. Increasing feed flow rate can be seen to reduce the power consumption of the rotor for all of the tip speeds shown and the model fits the data well, both in terms of trends and magnitudes. Interestingly, it can be seen that the rotor power is less affected by increasing flow rates at lower tip speeds.

Similarly, the experimental and theoretical results for the effect of rotor tip speed on rotor power consumption at various feed flow rates are shown in Figure 8.9. Again the theoretical model agrees well with the experimental results, although the model does seem to slightly under predict rotor power consumption at the lowest flow rate.

Finally, Figure 8.10 shows all experimental rotor power results for cylinder A plotted as a function of theoretically predicted rotor power. The model is shown again to perform well in predicting rotor power.

Table 8.2: Physical parameters for the UBC MR8 pressure screen with an AFT EP rotor and wire cylinder with 0.6mm contour height and 3.2mm wire width.

Fluid Density (ρ , kg/m ³)	1000
Inlet Angle (β , deg.)	90
Friction Loss Coefficient/Slip Factor (γ)	0.5
Rotor Tip Radius (r_{tip} , m)	0.094
Feed Inlet Area (A_f , m ²)	5.03×10^{-3}
Gap (g , mm)	5.0

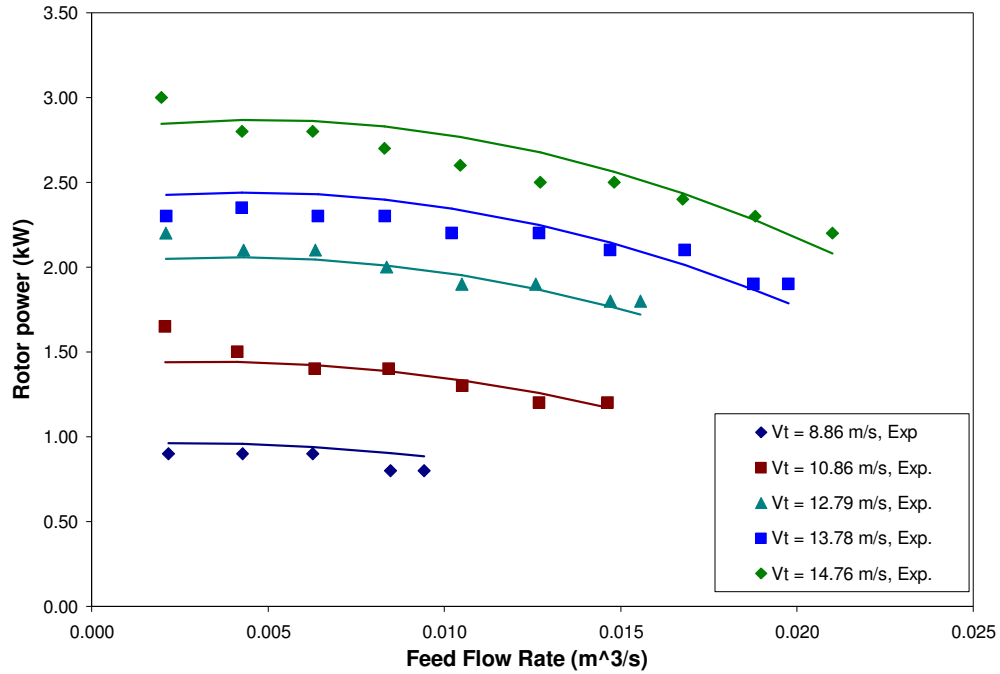


Figure 8.8: Experimental and theoretical rotor power as a function of feed flow rate for cylinder A at various rotor tip speeds. The curves represent results from equation 5.

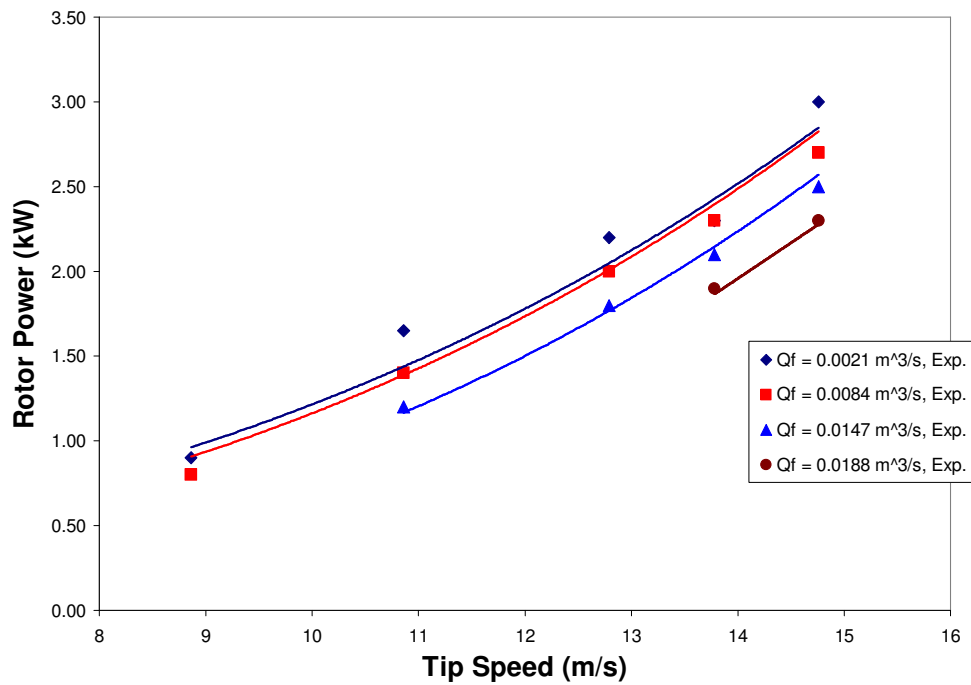


Figure 8.9: Experimental and theoretical rotor power as a function rotor tip speed for cylinder A at various feed flow rates. The curves represent results from equation 5.

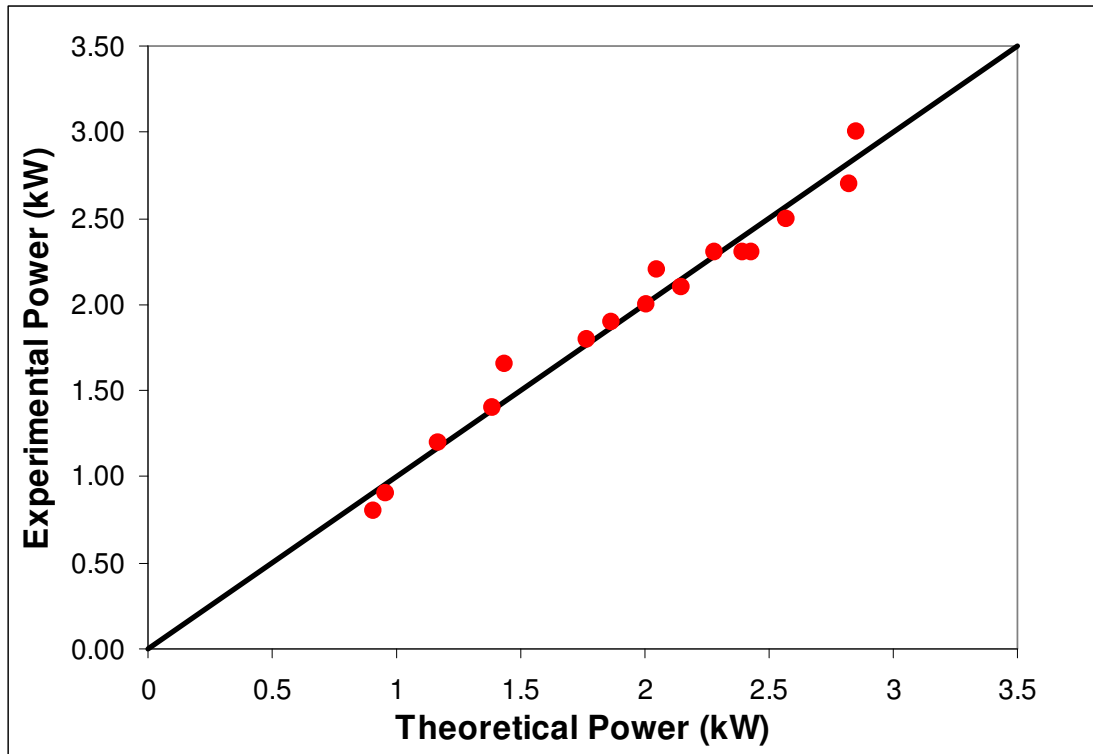


Figure 8.10: Measured rotor power for cylinder A vs. theoretically predicted rotor power.

8.5 Conclusions

The effect of cylinder design on pressure screen power consumption and maximum capacity was studied experimentally. It was found that, in some cases, cylinder design can have a significant effect on power consumption. There appears to be a small dependence of rotor power consumption on cylinder contour height. Also, cylinder D, with the flattened top, performed the best, using more than 40% less power than the other screens at a given slot velocity. Maximum slot velocity was not as strongly affected by rotor power for the cylinder with smooth holes as with the contoured, slotted cylinders.

A predictive model of power consumption was also developed to provide power estimates over a wide range of screen operating conditions. The model includes the

effects of varying rotor tip speed, flow rates, and screen geometry. The model predicted both trends and magnitudes well.

8.6 References

1. Kumar, A., Gooding, R.W., and Kerekes, R.J., "Factors controlling the passage of fibres through slots", *Tappi J.*, 81(5): 247-254, 1998.
2. Sloane, C.M., "Kraft pulp processing – pressure screen fractionation", *Appita J.*, 53(3): 220-226, 2000.
3. Frejborg, F., Giambrone, J., "Improvements of new and old screens in cleaning efficiency at maintained or increased capacity", *Proc. Tappi Pulping Conf.*, Seattle, p.529-532, 1989.
4. Halonen, L., Ljokkoi, R., and Peltonen, K., "Improved screening concepts", *Proc. Tappi Conf.*, p.207-212, 1990.
5. Niinimäki, J., Dahl, O., Kuopanportti, H., and Ammala, A., "The effect of surface properties on pressure screening – the selection of expedient screen basket for GW application", *Paperi ja Puu*, 80(8): 601-605, 1998.
6. Gooding, R.W., and Craig, D.F., "The effect of slot spacing on pulp screen capacity", *Tappi J.*, 75(2):12-16, 1992.
7. Martinez, D.M., Gooding, R.W., and Roberts, N., "A force balance model of pulp screen capacity", *Tappi J.*, 82(4): 181-187, 1999.
8. Olson, J.A., Turcotte, S., Gooding, R.W., "Determination of power requirements for solid core pulp screen rotors", *Nordic Pulp Paper Res. J.*, 19(2): 213-217, 2004.
9. Mokamati, S.V., "Effect of aperture geometry on the steady flow through the narrow apertures in a pulp screen: numerical and experimental study, PhD thesis", University of British Columbia, Canada, 2007.
10. Gooding, R.W., and Kerekes, R.J., "Consistency changes caused by pulp screening", *Tappi J.*, 75(11):109, 1992.
11. Yu, C.J., and DeFoe, R.J., "Fundamental study of screening hydraulics-1", *Tappi J.*, 77(8): 219-225, 1994.
12. Gooding, R.W., "The passage of fibres through slots in pulp screening", M.A.Sc. thesis, University of British Columbia, Canada, 1986.

13. Julien Saint Amand, J., and Perrin, B., “Fundamentals of screening: Experimental approach and modelling”, Proc. Tappi Pulping Conference, Montreal, p.1019-1031, 1998.

Chapter 9

Conclusions and Recommendations for Future Work

9.1 Introduction

This chapter summarizes the conclusions of the individual studies involved in this thesis. Additional analysis is also conducted in order to relate the findings and conclusions of the individual chapters to each other and draw broader conclusions. Finally, this chapter will offer recommendations for future work.

9.2 Discussion and Analysis

It was shown in this thesis that varying the geometry of the MEF changes the shape and magnitude of the pressure pulse generated by the foils. It was also shown that varying the MEF geometry can improve the performance of the pressure screen as a whole, but no direct measurements of how changing the shape and magnitude of the pressure pulse affects overall pressure screen performance have been made. Insight into how the pressure pulse shape and magnitude affects overall pressure screen performance can be obtained, however, by comparing the experimental MEF pressure pulse measurements in Chapter 3 with the pilot plant pressure screen performance data for varying MEF configurations in Chapter 4. In the laboratory pressure pulse study, the pressure pulses from 16 different MEF rotor configurations were measured in a Belloit MR8 pressure screen at a variety of tip speeds and flow rates. In the pilot plant trial, conducted at FP Innovations – Paprican Division screening pilot plant using a Hooper PSV 2100 pressure screen, the maximum capacity, power consumption and thickening of the pressure screen was studied for 12 different MEF configurations.

There are a number of differences between the pressure pulse study and the pilot plant study which must be highlighted and taken into consideration. The details of the two

studies are outlined in Table 9.1. First, the two studies used different sized pressure screens and rotors. It was shown in Chapter 6 that increasing the cylinder diameter slightly reduces the magnitude of the pressure pulse generated by the rotor. Also, water was used in the pressure pulse study ($C = 0.0\%$), while 1.5% consistency de-ink kraft pulp was used in the pilot plant trial. Atkins found that varying consistency has no effect on the magnitude or shape of the pressure pulses, but Gonzales and Pinon found that increasing consistency reduces the magnitude of the pressure pulse, but its shape and trends for varying geometry were unaffected [3, 4, 7].

Table 9.1: Trial details of the two experiments.

	Laboratory Pressure Pulse Experiment	Pilot Plant Trial
Consistency:	0.0%	1.5%
Cylinder Diameter:	20.32 cm	28.60 cm
Cylinder Height (span):	22.86 cm	15.20 cm
Foil Chord Length:	60 mm	90 mm
Foil Clearance Gap:	5 mm	2.5 mm
Angles-of-attack:	0, 2, 4, 6 deg.	0, 2.5, 5 deg.
Flap Angles:	12, 17, 22 deg.	10, 15, 20 deg.

A typical pressure pulse from the rotor measured in Chapter 3 is shown in Figure 9.1. The goal is to determine which of the key features of the pressure pulse has the greatest effect on the overall pressure screen performance: the magnitude of the negative peak, the magnitude of the positive peak, or the width of the pressure pulse. The width of the pulse is described by the total force on the cylinder, which is the integral of the pressure, or

$$F = \int P dx, \quad (9.1)$$

where P is the pressure and x is the distance along the cylinder wall.

Because the experiments were conducted at slightly different foil configurations (angles-of-attack and flap angles), surfaces of minimum and maximum pressure coefficient and integrated force coefficient were created. The pressure and force values at the foil configurations used in the mill trials were then interpolated from the surfaces. It was necessary to extrapolate the pressure pulse data at $\delta = 10$ deg. since the lowest flap angle in the pressure pulse study was $\delta = 12$ deg. Because the flap angle is not far from the lowest measured flap angle and there is a good coverage of values for the surfaces, the extrapolated values should be reasonable approximations.

Surfaces of the minimum and maximum non-dimensional pressure coefficient and the non-dimensional force coefficient were created rather than pressure because, as discussed in Chapter 3, the non-dimensional pressure coefficient was found to be Reynolds number independent for fully attached turbulent flows. The non-dimensional pressure coefficient C_P is defined as

$$C_P = \frac{P}{\frac{1}{2}\rho V_t^2}, \quad (9.2)$$

where ρ is the fluid density and V_t is the rotor tip speed. The non-dimensional force coefficient C_F is defined as

$$C_F = \frac{F}{\frac{1}{2}\rho V_t^2 c} = \int C_P \frac{dx}{c} \quad (9.3)$$

where c is the foil chord length. The pressure values at the tip speeds used in the pilot plant study were then solved for using equation 9.2 and 9.3. The surfaces, shown in Figures 9.1, 9.2, and 9.3, were generated using the data for $V_t = 13$ m/s. For reference, a surface of maximum slot velocity as a function of MEF flap angle and angle-of-attack at $V_t = 16$ m/s is also shown in Figure 9.5.

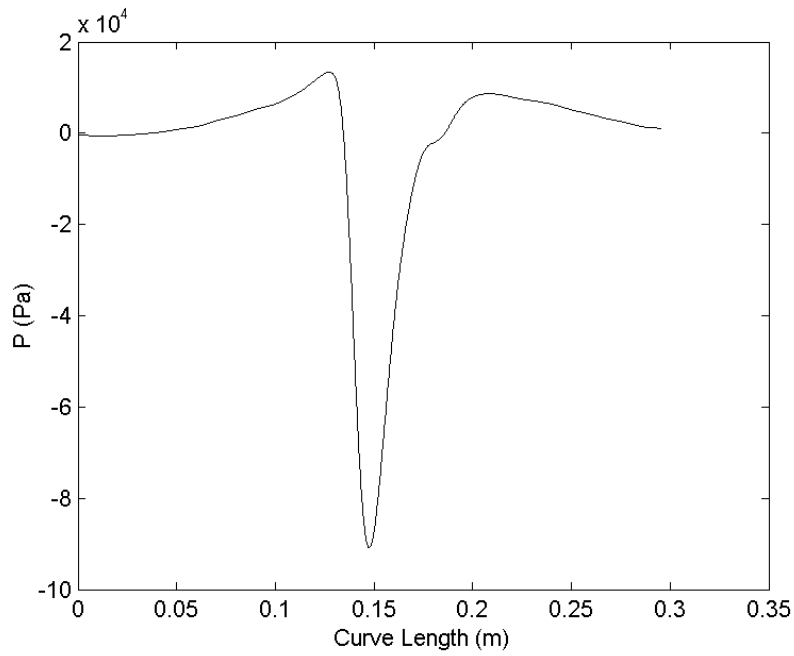


Figure 9.1: A single averaged pressure pulse measured at the cylinder wall representative of the pressure pulse data. The pulse shown is an ensemble average of 500 individual pulses.

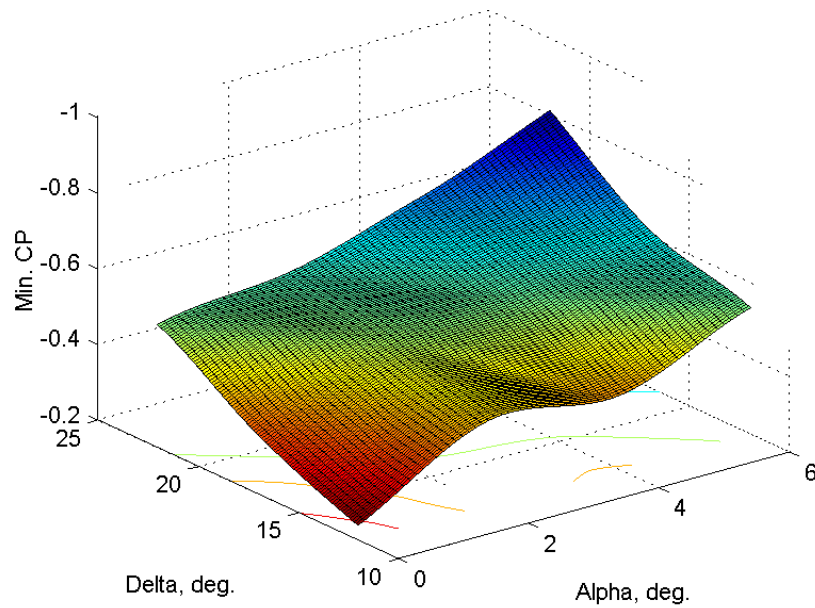


Figure 9.2: Minimum C_p at the cylinder wall as a function of foil configuration. The surface was constructed using 12 separate measurements.

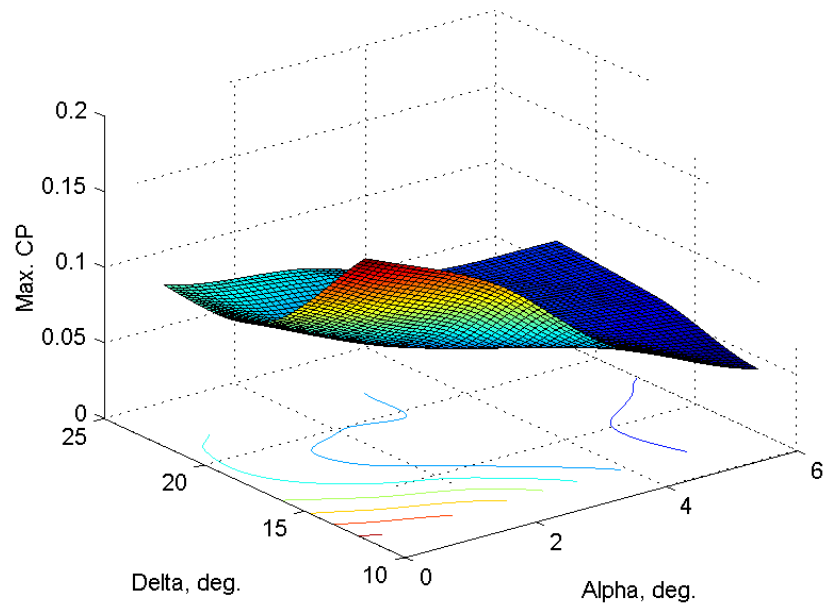


Figure 9.3: Maximum C_p at the cylinder wall as a function of foil configuration. The surface was constructed using 12 separate measurements.

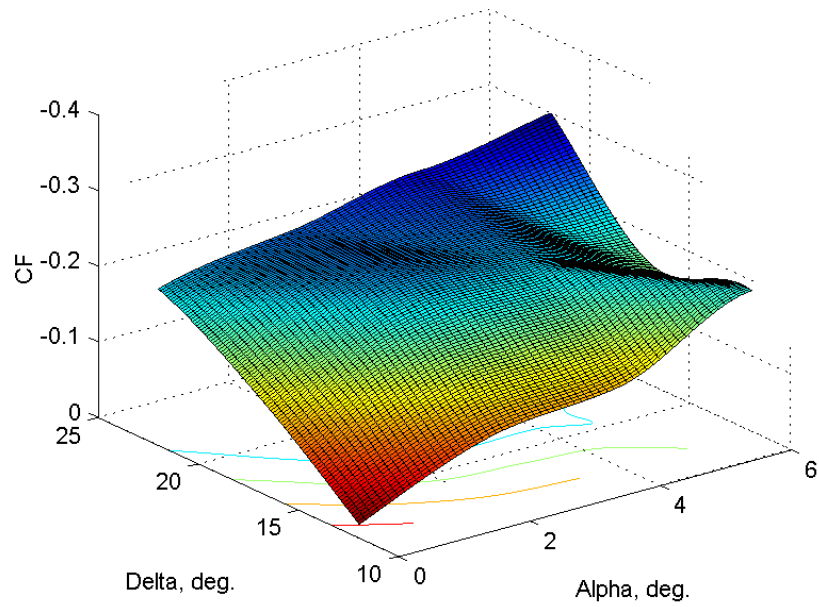


Figure 9.4: Integrated C_f at the cylinder wall as a function of foil configuration. The surface was constructed using 12 separate measurements.

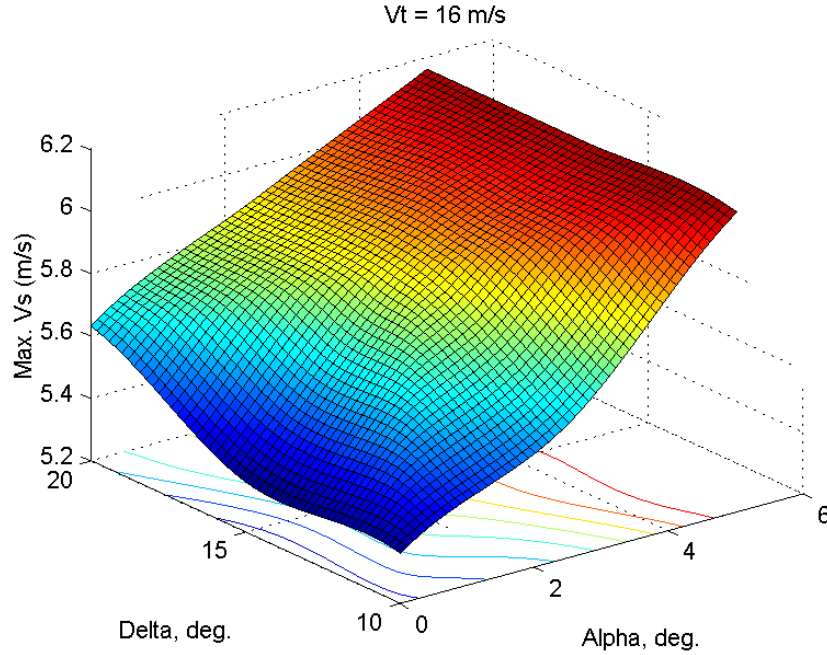


Figure 9.5: Maximum slot velocity as a function of foil configuration at $V_t = 16$ m/s. The surface was constructed using 9 separate measurements.

Maximum slot velocity is shown as a function of minimum pressure for all tip speeds measured in Figure 9.6, with the data colored by tip speed and with a linear best fit curve, in a least squared sense. There is clearly a strong linear correlation between the magnitude of the minimum pressure and the maximum obtainable slot velocity, with a correlation coefficient of $S = -0.8173$. It is interesting to note, however, that the quality of the fit of the curve appears to vary with tip speed, which implies that capacity is not solely dependent on minimum pressure.

In order to further explore this, Figure 9.7 shows the maximum slot velocity as a function of minimum pressure at individual tip speeds with linear best fit curves. The slope of the curves and the correlation coefficients are shown in Table 9.2. The correlation coefficients are all still very high, varying from $S = -0.8097$ to $S = -0.8863$. Interestingly, however, the magnitude of the slopes of the curves decrease as tip speed is increased. This implies that the maximum slot velocity of the cylinder becomes less dependent on the minimum pressure generated by the rotor as tip speed is increased. This may be, as

discussed in Chapter 6, due to the increase in pulse frequency as tip speed is increased. Increasing pulse frequency was shown to increase the capacity of the cylinder at a given pressure pulse magnitude.

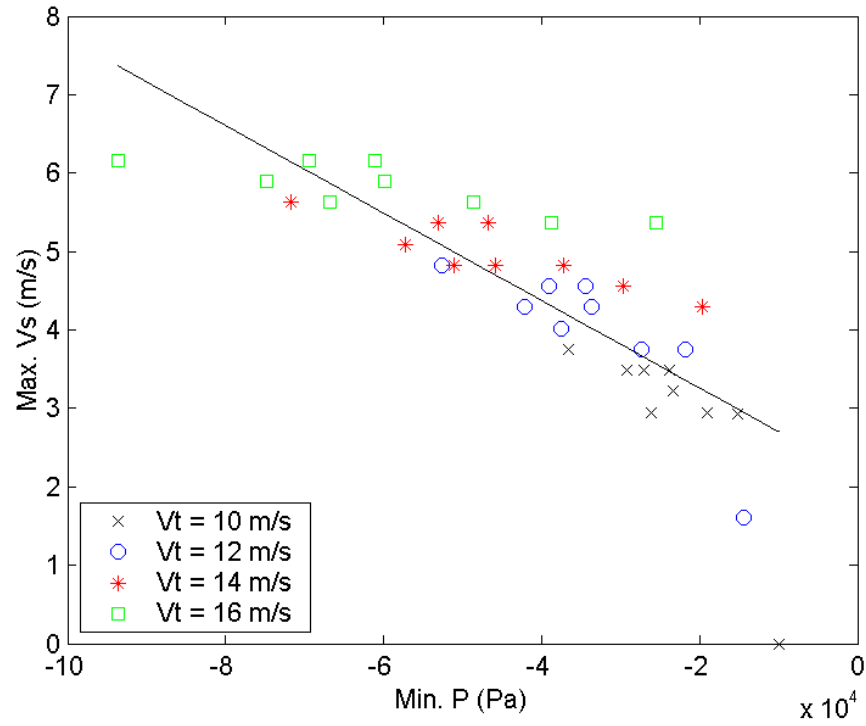


Figure 9.6: Maximum slot velocity as a function of minimum pressure at all tip speeds.

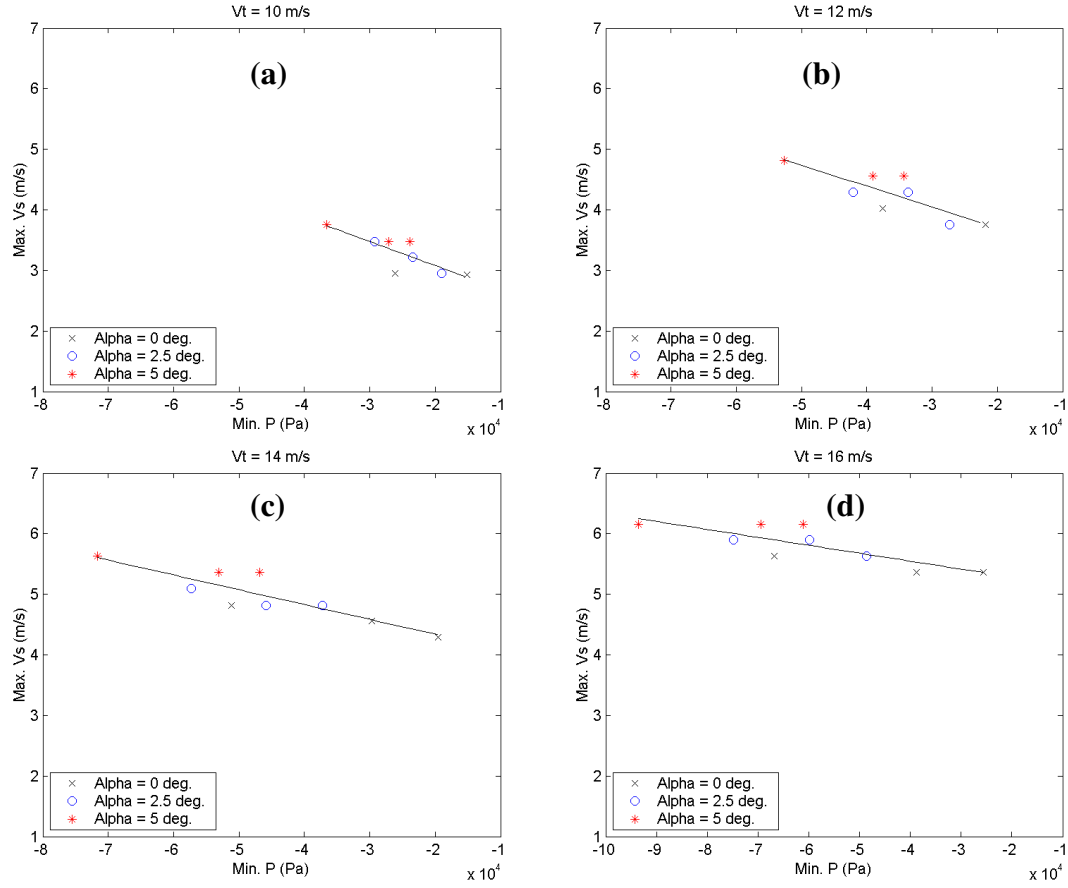


Figure 9.7: Maximum slot velocity as a function of minimum pressure at (a) $V_{tip} = 10$ m/s, (b) $V_{tip} = 12$ m/s, (c) $V_{tip} = 14$ m/s, and (d) $V_{tip} = 16$ m/s.

Table 9.2: Slope of the best fit curve, m , and correlation coefficient, S , of maximum slot velocity as a function of minimum pressure at various tip speeds.

V_t (m/s)	m (m/s/Pa)	S
All	-5.575E-05	-0.8173
10	-3.955E-05	-0.8203
12	-3.463E-05	-0.8262
14	-2.446E-05	-0.8863
16	-1.312E-05	-0.8097

Maximum slot velocity is shown as a function of maximum pressure for all tip speeds in Figure 9.8. No discernable trend can be seen for all tip speeds and the correlation coefficient is very low at $S = 0.1795$. Clear linear trends for maximum slot velocity as a function of maximum pressure can be seen at individual tip speeds, however, as shown in Figure 9.9. Increasing the maximum pressure can be seen to reduce the maximum slot velocity of the cylinder, with correlation coefficients vary from $S = -0.8739$ to -0.9586 . The correlation coefficients and slopes of the best fit lines for maximum slot velocity versus maximum pressure are shown in Table 9.3. Similar to what was seen with minimum pressure, the magnitude of the slope of the best fit curve, and therefore the dependence of maximum slot velocity as a function on maximum pressure, decreases as tip speed increases. Again, there is likely some factor associated with tip speed, such as pulse frequency, affecting the maximum slot velocity of the cylinder and its dependence on the maximum pressure generated by the rotor.

It is important to note that, as shown in Figures 9.2 and 9.3, it is difficult to decouple the reduction of the maximum pressure pulse from increasing the magnitude of the negative pressure pulse – i.e., the configurations that yield the strongest negative pressure pulse also produce the weakest positive pressure pulse. This likely contributes to the results seen in Figure 9.9, where the lowest magnitude maximum pressure yields the highest screen capacity. Because of this, and because there is no discernable trend for maximum slot velocity versus maximum pressure for all tip speeds, as shown in Figure 9.8, maximum pressure cannot be considered the primary factor controlling maximum slot velocity.

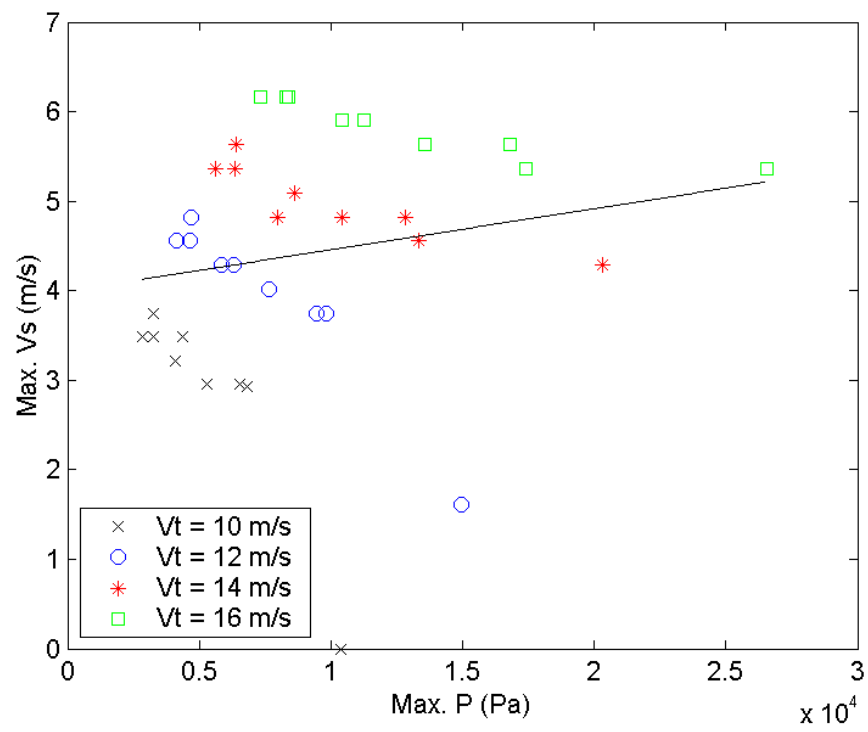


Figure 9.8: Maximum slot velocity as a function of maximum pressure at all tip speeds.

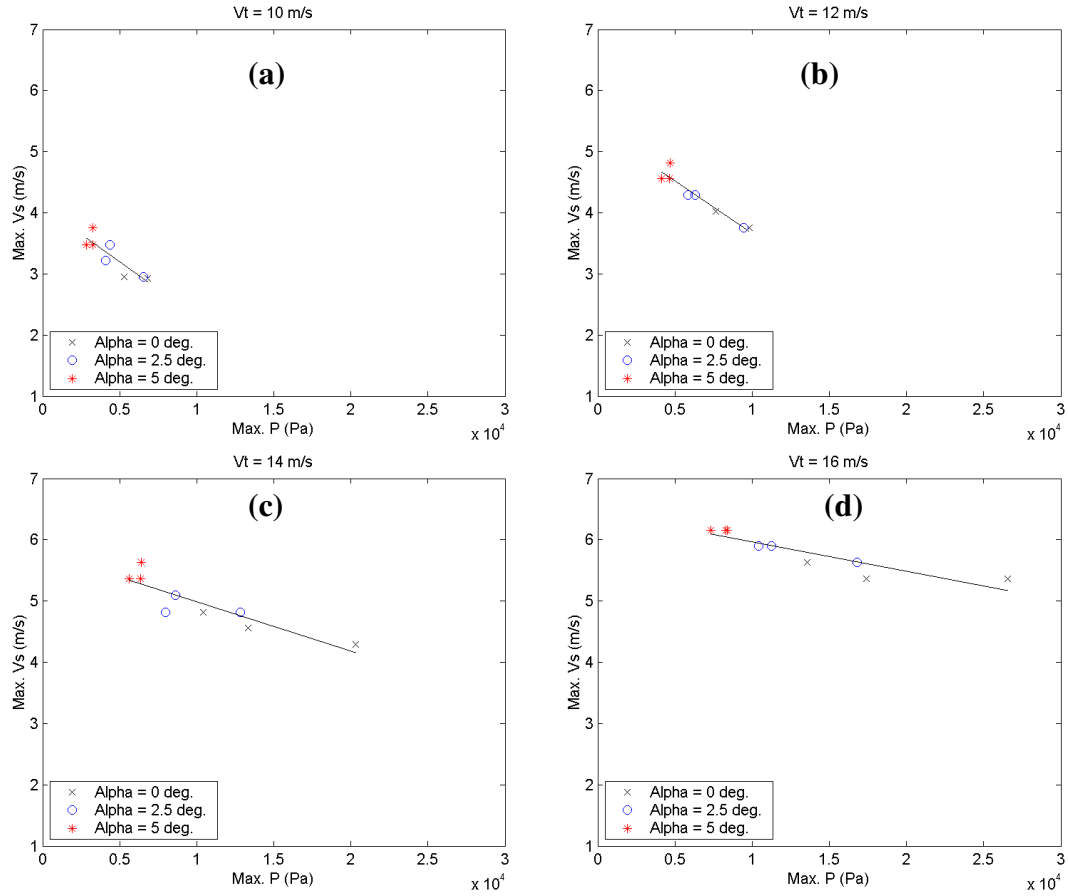


Figure 9.9: Maximum slot velocity as a function of maximum pressure at (a) $V_t = 10$ m/s, (b) $V_t = 12$ m/s, (c) $V_t = 14$ m/s, and (d) $V_t = 16$ m/s.

Table 9.3: Slope of the best fit curve, m , and correlation coefficient, S , of maximum slot velocity as a function of maximum pressure at various tip speeds.

V_t (m/s)	m (m/s/Pa)	S
All	4.585E-05	0.1795
10	-1.801E-04	-0.8739
12	-1.717E-04	-0.9586
14	-8.046E-05	-0.8885
16	-4.801E-05	-0.9032

Finally, maximum slot velocity is shown as a function of integrated force at the screen wall at all tip speeds in Figure 9.10. Increasing the magnitude of the force generated by the foil, which is a measure of not only the peak pressure but also the width of the pressure pulse, can be seen to increase the maximum capacity of the screen. The correlation is not as strong as was seen with the minimum pressure, however, with a correlation coefficient of $S = -0.6814$.

Again, the correlation improves when individual tip speeds are looked at, as shown in Figure 9.11. The correlation coefficients at the individual tip speeds for maximum slot velocity as a function of force, as summarized in Table 9.4, vary from $S = -0.7749$ to -0.8277 . Again, the slope of the best fit curves decreases as tip speed increases, indicating that maximum slot velocity is partially dependent on an outside factor related to tip speed, such as pulse frequency.

The integrated force is also inherently coupled with the minimum pressure value, as increasing the minimum value will increase the integrated area under the curve. This is illustrated clearly in Figures 9.2 and 9.4, which show that the maximum magnitude minimum pressure and force values occur at the same foil configuration. This makes it difficult to isolate the effects of increasing pulse width, and the integrated force, from increasing the magnitude of the minimum value. Because the correlation coefficients for maximum slot velocity as a function of minimum pressure were higher at each individual tip speed as well as for all tip speeds, the minimum pressure generated by the rotor is likely more of a determining factor for screen capacity than the integrated force.

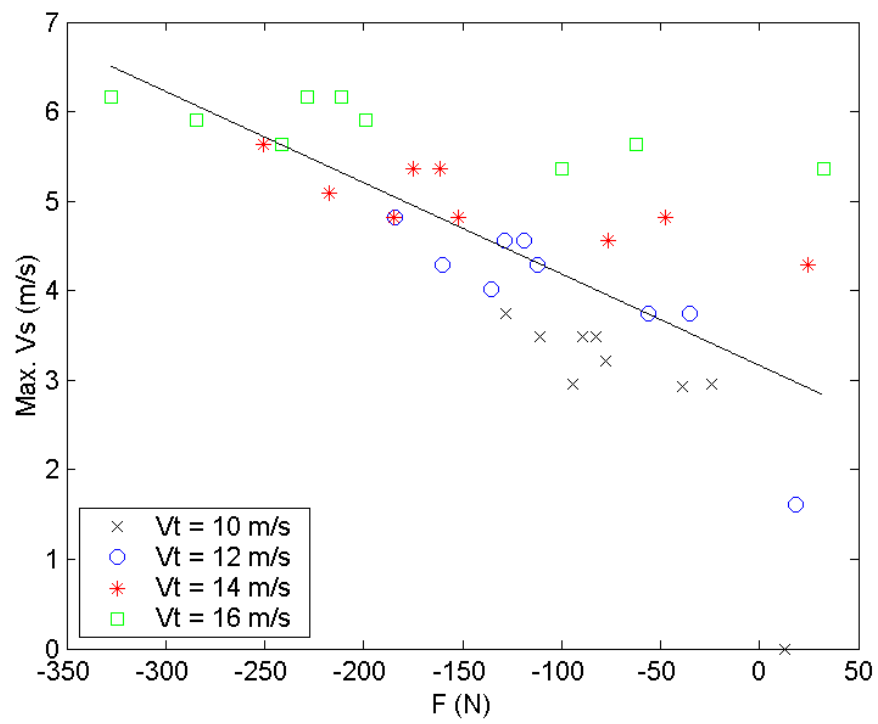


Figure 9.10: Maximum slot velocity as a function of integrated force at all tip speeds.

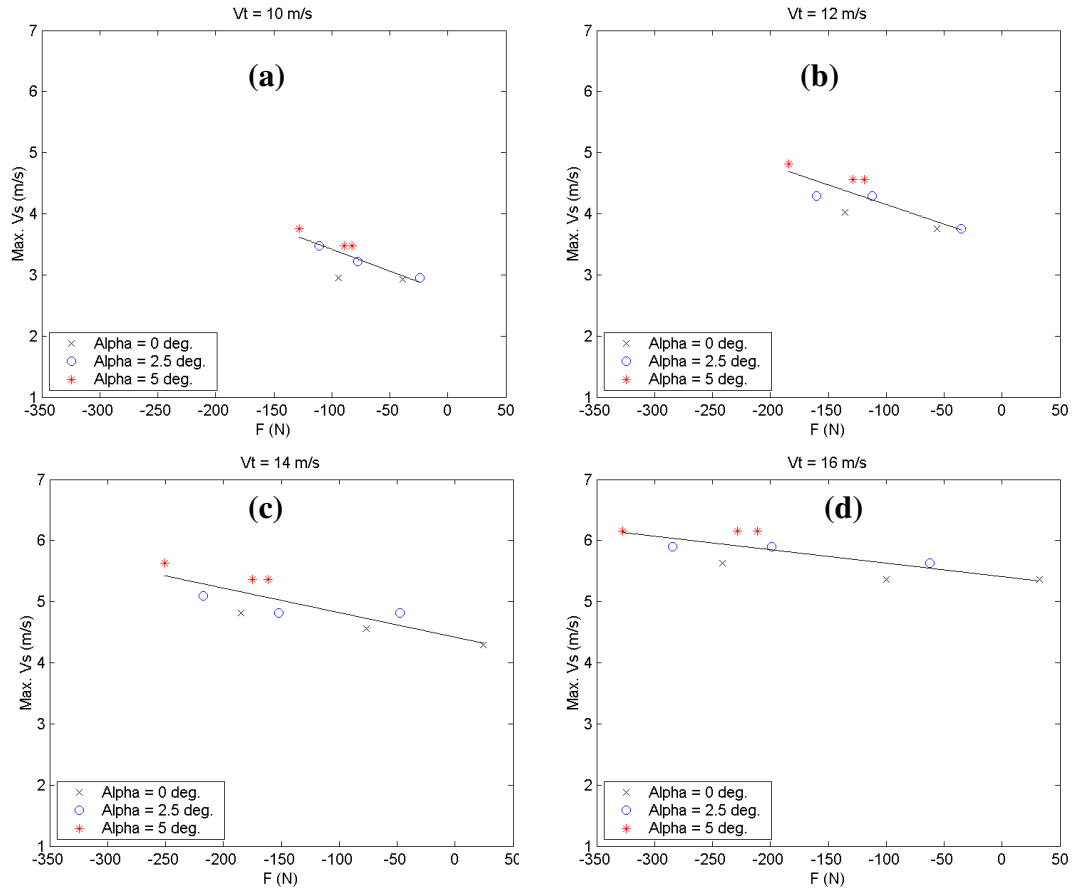


Figure 9.11: Maximum slot velocity as a function of integrated force at (a) $V_{tip} = 10$ m/s, (b) $V_{tip} = 12$ m/s, (c) $V_{tip} = 14$ m/s, and (d) $V_{tip} = 16$ m/s.

Table 9.4: Slope of the best fit curve, m , and correlation coefficient, S , of maximum slot velocity as a function of integrated force at various tip speeds.

V_t (m/s)	m (m/s/N)	S
All	-1.021E-02	-0.6814
10	-7.106E-03	-0.7842
12	-6.425E-03	-0.8156
14	-4.013E-03	-0.8277
16	-2.205E-03	-0.7749

Based on these results, it can therefore be concluded that the magnitude of the minimum pressure is the dominant feature of the pressure pulse in determining the maximum capacity of a pressure screen. The integrated force coefficient, used as a measure of the width of the pressure pulse, was shown to be of slightly less importance and increasing the magnitude of the positive pressure pulse was shown to reduce the maximum slot velocity of the screen at a given tip speed. The hypothesis presented in Chapter 1 is therefore shown to be valid: the goal in pressure screen rotor design should be to increase the magnitude of the minimum pressure generated by the rotor at a given rotor tip speed, allowing for an increase in the capacity of the pressure screen without an increase in rotor power consumption or, based on the power equation of Olson *et al.* and the equation developed in Chapter 8, allowing for a reduction in rotor tip speed and power consumption without reducing the maximum capacity of screen.

9.3 Conclusions

This thesis investigated, through a series of seven numerical and experimental studies, the hydrodynamics of pressure screen foil rotors. The effect of the rotor design on overall pressure screen performance was also studied, and a high performance multi-element foil rotor was developed. The MEF rotor was developed from CFD simulations, to laboratory experiments, to pilot plant trials, and finally to full scale mill trials. Other factors affecting the pressure pulses generated by the rotor, such as the number of foils on the rotor, the diameter of the cylinder, and the slot velocity were also investigated numerically and experimentally. Additionally, the effect of varying the geometry of the rotor's foils on the overall capacity and power consumption of the pressure screen was investigated experimentally. Factors affecting the rotor power consumption were also investigated, including the rotor tip speed, the flow rates, the diameter of the pressure screen, and the geometry of the feed inlet. Finally, the effect of varying the shape of the pressure pulse on the maximum capacity of the pressure screen was examined by comparing the results from laboratory pressure pulse experiments and a pilot plant trial.

Specifically, the conclusions of this thesis are:

1. It was shown using CFD that varying the multi-element foil rotors are capable of generating a higher magnitude and wider negative pressure pulse than a single-element foil rotor while at the same time reducing the magnitude of the positive pressure pulse. Increasing the foil angle-of-attack and flap angle both caused the magnitude of the negative pressure pulse to increase and the magnitude of the positive pressure pulse to decrease up to the point that the foil began to stall. After this point, the magnitude of the negative pressure pulse would diminish. This matches well with previous studies of single-element foils, which found that increasing the foil angle-of-attack and camber would cause an increase in the magnitude of the negative pressure pulse and a reduction of the positive pressure pulse [1-3]. It was also found that the positioning of the flap with respect to the main foil effects the magnitude of the pressure pulse and that an optimum flap position exists.
2. The numerical pressure pulse results were verified experimentally using a laboratory pressure screen and the CFD results were shown to capture the shape and magnitude of the negative pressure pulse well for cases where the flow was fully attached. The CFD model used under predicted the magnitude of the positive pressure pulse, however. It was also found that the CFD simulations over predicted flow separation over the foils and that the MEF foil could in fact achieve a higher magnitude negative pressure pulse than was predicted numerically. The MEF was found experimentally to produce a 126% higher magnitude negative pressure pulse and a 39% lower magnitude positive pressure pulse than a single-element foil rotor. The reason the CFD simulations over predicted flow separation and under predicted the positive pressure pulse compared to the experimental results is likely due to the use of a solid wall boundary for the cylinder wall, rather than modeling the flow through the slots. The use of a solid wall boundary would cause the stagnation point at the leading edge of the foil, which causes the positive portion of the pressure pulse at the cylinder wall, to move towards the lower surface of the foil. It would also prevent

low momentum flow from the slots from entering the domain, which prevent flow separation over the foils.

3. The magnitude of the pressure pulses generated by the foils was found experimentally to be dependent on the tip speed of the rotor squared and the non-dimensional pressure coefficient was found to be Reynolds number independent for fully attached turbulent flows. This verifies results from previous authors who observed the same phenomenon using a laboratory pressure screen and CFD [1-4].
4. Increasing slot velocity was found experimentally to have no effect on the magnitude of the pressure pulses generated by the rotor for cases where the flow was fully attached. Increasing slot velocity did cause the tip speed at which flow separation occurs to increase, however, which causes a reduction in the pressure pulse magnitude.
5. It was found in pilot plant trials that varying the geometry of a foil rotor can increase the capacity of a pressure screen at a given rotor power consumption or, similarly, reduce the power required by the rotor for a given capacity. Increasing both the angle-of-attack and the flap angle of the MEF was found to increase the maximum capacity of the screen at a given rotor tip speed. Overall, the MEF was found to increase maximum capacity of the screen by as much as 31% at a given rotor power consumption compared to a single-element foil rotor. Conversely, the MEF was shown to reduce the power consumption of the rotor by 26% compared to the single-element foil without affecting capacity.
6. The MEF was shown in a mill trial to use 42% less power than the existing state-of-the-art OEM rotor. The screen running the MEF rotor also had improved stickies removal efficiency.

7. The effect of varying the pulse frequency on rotor performance was studied numerically and experimentally by varying the number of foils on the rotor. It was found using CFD that adding foils to the rotor decreased the velocity of the mean flow relative to the foils, which decreases the magnitude of the pressure pulses generated by the foils. This is because of the added drag on the fluid from the additional foils, which increases the mean rotational speed of the fluid. This effect is similar to that observed by other researchers, who found that the magnitude of the pressure pulse generated by the rotor decreased along the axial length of the pressure screen as the fluid was accelerated by drag on the rotor [5-7]. These results were supported by results from a pilot plant study that showed a two foil rotor had increased capacity and reduced power consumption compared to a three foil rotor with identical foil geometry.
8. The effect of varying cylinder diameter on the pressure pulses generated by the rotor was studied numerically. It was found that, at a given pulse frequency, increasing the diameter of the cylinder causes a slight reduction in the magnitude of the pressure pulse generated by the rotor. It was also found that increasing the cylinder diameter reduced the optimal flap angle of the MEF.
9. The hydrodynamics of in-flow pressure screen rotors and the application of the MEF rotor to in-flow pressure screens were investigated using CFD. The curvature of the cylinder was found to cause the flow around a single-element foil to separate over the lower surface of the foil at the leading edge at low angles-of-attack. The curvature of the cylinder also caused the flow to separate from the upper surface of the single-element foil at the trailing edge even at low angles-of-attack. The MEF was capable of eliminating the flow separation over both the upper and lower surfaces of the foil, which led to a 23% increase in the magnitude of the negative pressure pulse compared to the single-element foil studied. The optimal angle-of-attack for the MEF with an in-flow cylinder was significantly higher than that found for out-flow cylinders, while the optimal flap angle was significantly lower.

10. The power equation developed by Olson *et al.* [8] was expanded upon through an angular momentum balance to include the effects of flow rate and the geometry of the inlet to the screening chamber. In addition to being dependent on rotor tip speed cubed, as shown by Olson *et al.*, rotor power consumption was found to decrease with feed flow rate squared for screens in which the feed flow enters the screen tangentially, and to increase linearly with increasing feed flow for axially fed pressure screens. The effectiveness of the power equation was validated using experimental results from a laboratory screen with a tangential feed.
11. The effect of cylinder contour geometry on rotor power consumption was also investigated experimentally using a laboratory pressure screen. Varying the geometry of the wire in a wedge wire cylinder was found to affect the rotor power required to operate the screen at a given slot velocity, with a weak trend of increasing contour height causing an increase in rotor power. One wire geometry used as much as 40% less rotor power at a given slot velocity than other geometries studied.
12. Finally, increasing the magnitude of the minimum pressure generated by the rotor was found to have the highest correlated affect on increasing the maximum capacity of a pressure screen. Increasing the magnitude of the maximum pressure generated by the rotor was found to have the lowest correlated affect on the maximum capacity of a pressure screen when all tip speeds were considered, and was found to decrease the maximum capacity at a given tip speed.

9.2 Recommendations for Future Work

In order to advance pressure screen rotor design beyond the work in this thesis, researcher should provide a better understanding of the mechanisms that cause the cylinder in a pressure screen to plug, either experimentally or analytically. This will provide future pressure screen rotor designers with better criteria for their designs. Direct

measurements of the effects of varying the magnitude and shape of the pressure pulses generated by the rotor on the overall performance of an industrial pressure screen should be made, specifically the effects on maximum capacity, fractionation efficiency and contaminant removal efficiency. Additionally, an optimal balance of the frequency of the pulses and the magnitude of the pulses should be investigated. This thesis found that increasing the frequency of the pulses by adding foils to the rotor decreased the performance of each individual foil and increased rotor power consumption but increased the maximum slot velocity of the screen at a given pressure pulse magnitude.

Finally, an improved, computationally efficient, CFD model should be developed for pressure screen rotor design. The model used in this thesis was sufficiently inexpensive computationally, but was overly conservative in predicting the foil configuration at which flow separation would occur. The greatest improvements in predicting flow separation would likely come from modeling the flow through the slots. An improved model will allow for the development of more aggressive foil configurations and for the application of optimal shape design methods.

9.3 References

1. Feng, M., Gonzalez, J., Olson, J.A., Ollivier-Gooch, C., Gooding, R.W., “Numerical simulation and experimental measurement of pressure pulses produced by a pulp screen foil rotor”, J. Fluids Eng., 127(3): 347-357, 2005.
2. Feng, M., “Numerical Simulation of the pressure pulses generated by a pressure screen foil rotor”, M.A.Sc. Thesis, Dept. Mech. Eng., Univ. British Columbia, 2003.
3. Gonzales, J., “Characterization of design parameters for a free foil rotor in a pressure screen”, M.A.Sc. Thesis, Dept. Mech. Eng., Univ. British Columbia, 2002.
4. Pinon, V., Gooding, R.W., Olson, J.A., “Measurements of pressure pulses from a solid core screen rotor”, Tappi J., 2(10): 9-12, 2003.
5. Gooding, R.W., “The passage of fibres through slots in pulp screening”, M.A.Sc. thesis, University of British Columbia, Canada, 1986.
6. Yu, C.J., “Pulsation measurement in a screen. Part I: Pulse signature and magnitude of S-shape rotor”, 1994 Tappi Engineering Conf., 767-782.
7. Atkins, M., “Axial variations and entry effects in a pressure screen”, Ph. D. Thesis, Dept. of Eng., Univ. of Waikato, 2007.
8. Olson, J.A., Turcotte, S., Gooding, R.W., “Determination of power requirements for solid core pulp screen rotors”, Nordic Pulp Paper Res. J., 19(2): 213-217, 2004.

Appendix A

Numerical Methods

A.1 Introduction

Computation fluid dynamics is used extensively throughout this thesis to solve the discretized Navier-Stokes equations. In order to aid in the reproduction of the results in this thesis, this appendix offers additional information about the numerical methods used beyond what was discussed in the individual chapters. Most details on CFD are out of the scope of this study, however, and are left to the references [1-4].

In this thesis, the FLUENT 6.1 commercial solver was used to solve the discretized Navier-Stokes equations. As discussed in the individual chapters, the problem is assumed to be isothermal, two-dimensional and steady state, reducing the Navier-Stokes equations to the continuity and x- and y- momentum equations:

$$\frac{\partial u}{\partial x} + \frac{\partial v}{\partial y} = 0 \quad (A1)$$

$$u \frac{\partial u}{\partial x} + v \frac{\partial u}{\partial y} = -\frac{1}{\rho} \frac{\partial P}{\partial x} + \nu \left(\frac{\partial^2 u}{\partial x^2} + \frac{\partial^2 u}{\partial y^2} \right) \quad (A2)$$

$$u \frac{\partial v}{\partial x} + v \frac{\partial v}{\partial y} = -\frac{1}{\rho} \frac{\partial P}{\partial y} + \nu \left(\frac{\partial^2 v}{\partial x^2} + \frac{\partial^2 v}{\partial y^2} \right) \quad (A3)$$

There are three main methods used to spatially discretize these PDEs: finite differences, finite volumes, and finite elements. FLUENT is a second-order finite volume solver,

meaning the domain is divided into small control volumes. Control volume averages are then found for each flow variable and the fluxes at the control volume faces are found through second order spatial interpolation from the control volume centers.

A.2 Turbulence Modeling

Turbulent flows contain small scale velocity fluctuations that are too computationally expensive to solve for directly. In industrial CFD applications, the Navier-Stokes equations are therefore modified either with Reynolds-averaging or filtering to remove small scale phenomena. Large eddy simulation (LES) uses a filtering approach, but requires considerably more computational resources than averaging approaches. A Reynolds-averaged Navier-Stokes (RANS) turbulence model is therefore used.

RANS models separate the variables in the Navier-Stokes equations into mean and fluctuation terms. The two dimensional, steady state, isothermal Reynolds averaged Navier-Stokes equations, in Einstein notation for convenience, are

$$\frac{\partial \bar{u}_i}{\partial x_i} = 0 \quad (\text{A4})$$

$$\bar{u}_j \frac{\partial \bar{u}_i}{\partial x_j} = -\frac{1}{\rho} \frac{\partial \bar{P}}{\partial x_i} + \frac{1}{\rho} \frac{\partial}{\partial x_j} \left(\mu \frac{\partial \bar{u}_i}{\partial x_j} - \rho \overline{u'_i u'_j} \right) \quad (\text{A5})$$

where \bar{u} is the mean velocity and u' is the velocity fluctuation. The term $\overline{u'_i u'_j}$ is an additional term, referred to as the Reynolds stresses, which require closure. RANS models provide closure for the Reynolds stresses by modeling turbulent properties, via the Boussinesq, or eddy viscosity, hypothesis, with additional transport equations. The Boussinesq hypothesis states that the Reynolds stresses are proportional to the local rate of strain tensor and an eddy viscosity term, making the momentum transfer due to turbulence analogous to molecular shear [3, 5]. The physics of turbulence are in fact quite different than molecular viscosity, however the eddy viscosity approximation has

been found to perform well in a wide range of simple shear flows [3]. A number of different RANS models have been developed, with each model having particular strengths and weaknesses depending on the type of flow being simulated.

Mahon and Zhang studied the performance of several RANS models in simulating the flow around a single- and double-element inverted foil in ground effect [6, 7]. They found that all of the models studied predicted both the surface pressures and wake velocity profiles well compared to wind tunnel data. For the single element foil, the $k-\omega$ SST model was found to be the best for predicting the surface pressure on the foil and the realizable $k-\varepsilon$ model was best at predicting the wake velocity profile. For the double-element foil, the realizable $k-\varepsilon$ model had the best performance for both surface pressures and wake velocity profile. The majority of numerical pressure screen rotor studies have used the $k-\varepsilon$ turbulence model [8-11]. Atkins had success in using the $k-\omega$ SST model, which has been found to have better performance in some cases with rotating flows and with flows with streamline curvature [12]. This study therefore investigated the standard $k-\varepsilon$ and $k-\omega$ SST models.

The $k-\varepsilon$ model solves additional transport equations for the turbulent kinetic energy, k , and turbulent dissipation rate, ε , to provide closure for the Reynolds stresses. The $k-\omega$ model is similar to the $k-\varepsilon$ model, but the second transport equation solved is for the specific dissipation rate ω , which is the ratio of ε to k (i.e. $\omega = k/\varepsilon$). The $k-\omega$ SST model blends the standard $k-\varepsilon$ and $k-\omega$ models, using the $k-\omega$ model close to wall boundaries and the $k-\varepsilon$ model for the bulk flow [3, 4].

As discussed in Chapter 2, there was little difference in the results from the $k-\varepsilon$ and $k-\omega$ SST models. Results from the $k-\varepsilon$ model matched the experimental pressure pulse data slightly better than those from the $k-\omega$ SST model. Because of this, and also because of the history of its use in the literature, the $k-\varepsilon$ model was used for the bulk of the numerical studies in this thesis. The default values for the turbulence model tuning parameters were used in all cases.

A.3 Domain Discretization and Boundary Conditions

Figure A1 shows how the cross-section of a pressure screen with a foil rotor was modeled and a typical mesh. All mesh generation was done using Gambit, the commercial pre-processing package for FLUENT. The meshes used were hybrid structured/unstructured multi-block meshes. Very fine C-meshes were created around the foils in order to achieve adequate resolution of the boundary layers and wake. Both the $k-\varepsilon$ and $k-\omega$ SST turbulence models require the first mesh point at a boundary to be at a wall unit of $y^+ \approx 1$. In order to reduce computational costs, a coarser structured mesh is used in the far field away from the foils. An unstructured block is used to blend the two structured meshes. The use of the unstructured block also makes it easier to generate new meshes as small changes to the geometry are made – the C-meshes around the foils and in the wake can be modified without changing the coarser far field mesh.

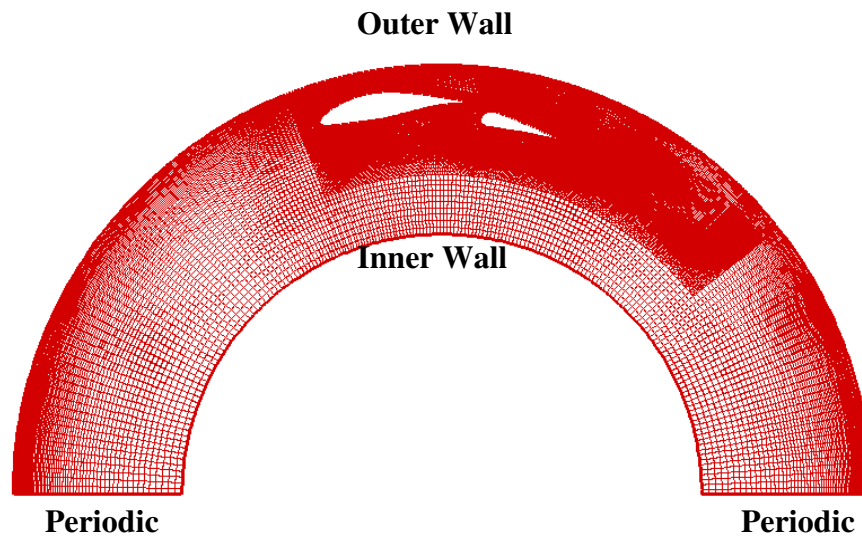


Figure A1: Computational domain and a typical mesh.

One of the most difficult aspects of the mesh generation is in creating the mesh in the slot between the two foils, especially when the gap between the two foils is small. This was accomplished by blending a block from near the trailing edge of the main foil with a block at the leading edge of the flap so that mesh lines parallel to the main foil become perpendicular mesh lines for the flap, as shown in Figure A2. Other important features

are a reduction in the aspect ratio of the control volumes at the leading and trailing edges of both foils in order to capture the stagnation point, high stream-wise gradients in the flow, and the point of flow separation.

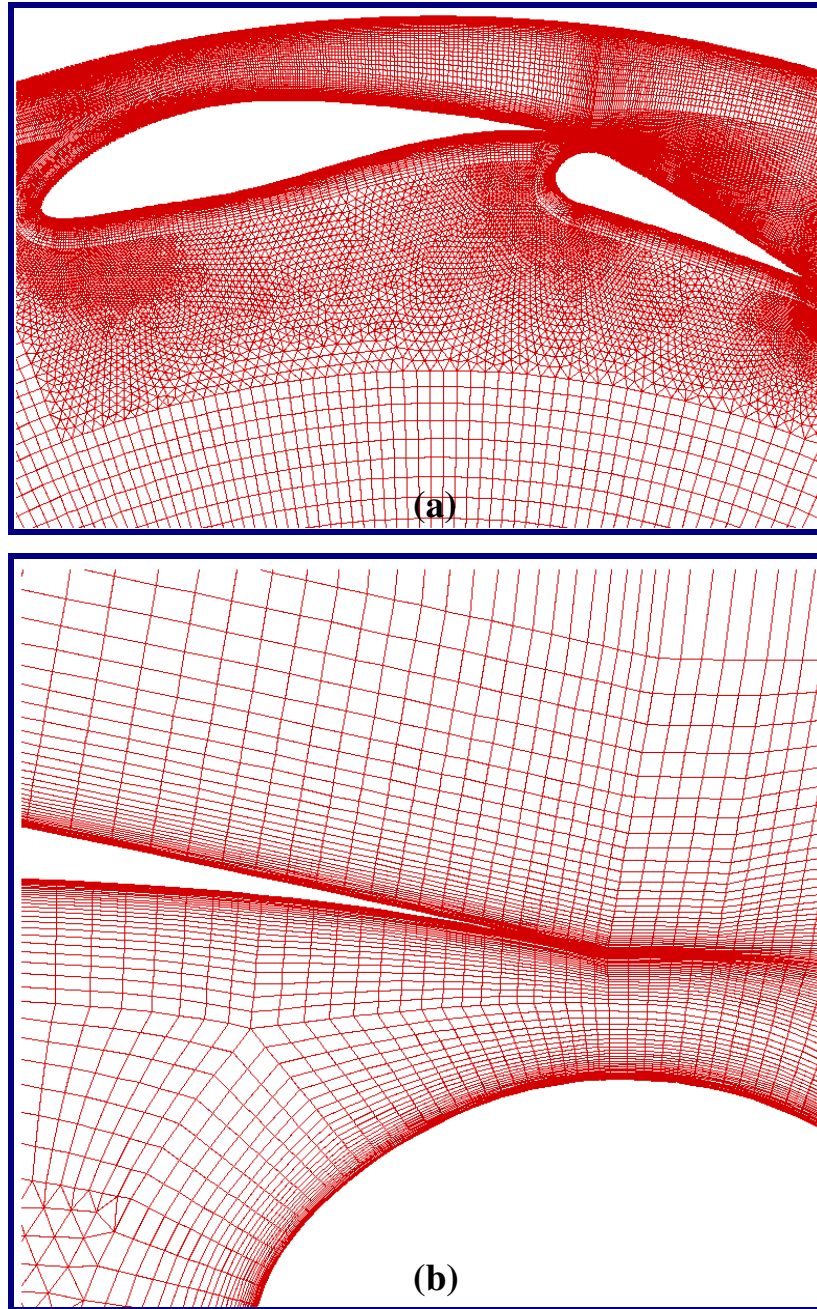


Figure A2: Details of key areas of the mesh: (a) the C-meshes around the foils and, (b) the mesh in the slot between the two foils.

Full grid independence studies were conducted for each major change in geometry, such as cylinder diameter or foil type. Grid independence was checked by comparing geometrically similar meshes of varying size. Geometrically similar meshes are meshes with the same general structure and control volume aspect ratios, skewness, etc. The number of control volumes required for grid independence varied with the size of the domain (i.e. the cylinder diameter) and the foil chord length, but was typically around 70,000 to 80,000 volumes.

The boundary conditions used in the model are also shown in Figure A1. The inner wall, which represents the inner rotor core, and foil are set at zero relative velocity to a coordinate system placed at the center of the cylinder rotating at the same angular velocity as the rotor. A rotating coordinate system is used because the flow is steady when viewed from this frame of reference. The outer wall, which represents the cylinder, is set at zero angular velocity in the absolute coordinate system. All wall boundaries have no-slip boundary conditions. The domain is rotationally periodic in order to represent a two-bladed rotor. The number of foils on the rotor is varied by changing the locations of the periodic boundaries.

The cylinder was modeled as a solid wall and the complex flow through the slots was not considered. This is meant to represent the critical design case of a plugged cylinder and also greatly reduces computational costs. Another simplification is that water (consistency of 0.0%) was used as the fluid in the simulations. There are conflicting results in the literature on how consistency affects the magnitude of the pressure pulses generated by the rotor. Atkins found that increasing the feed consistency has no effect on the pressure pulse magnitude [12]. Pinon and Gonzales found using a laboratory pressure screen that increasing feed consistency causes a reduction in the magnitude of the pressure pulse [13, 14]. They found that varying consistency did not affect the trends for varying geometry and operating conditions on the pressure pulse magnitude and shape, however. Additionally, the consistencies in screening applications are very low, on the order of 1-2%, and turbulent pulp suspensions in this consistency range have been found

to behave as a Newtonian fluid with the same density and viscosity as water [14]. These results make the use of water a valid assumption.

A.4 Convergence Criteria

Convergence of the solutions were determined using the normalized residuals of continuity, x- and y- momentum, and the turbulence equations (k and either ε or ω). The minimum pressure on the cylinder wall was also used as a criterion since the pressure pulse was the primary focus of the studies. The solution was deemed to be converged when the continuity residuals had reached approximately 10^{-6} and all other residuals had reached approximately 10^{-8} , and when all of the convergence criteria were no longer changing with iteration count. This generally took 30,000 to 50,000 iterations, depending on the domain size and rotor tip speed.

A.5 References

1. Chung, T.J., “Computational Fluid Dynamics”, Cambridge University Press, 2002.
2. Wilcox, D.C., “Turbulence Modeling for CFD”, DCW Industries, Inc., 2006.
3. Pope, S.B., “Turbulent Flows”, Cambridge Press, 2000.
4. Fluent, Inc., “Fluent user’s guide”, 2003.
5. White, F.M., “Viscous Fluid Flow”, McGraw Hill, Inc., 1991.
6. Mahon, S., and Zhang, X., “Computational analysis of pressure and wake characteristics of an aerofoil in ground effect”, J. Fluids Eng., 127(3): 290-298, 2005.
7. Mahon, S., and Zhang, X., “Computation analysis of a inverted double-element airfoil in ground effect”, J. Fluids Eng., 128(6): 1172-1181, 2006.
8. Feng, M., Gonzalez, J., Olson, J.A., Ollivier-Gooch, C., Gooding, R.W., “Numerical simulation and experimental measurement of pressure pulses produced by a pulp screen foil rotor”, J. Fluids Eng., 127(3): 347-357, 2005.
9. Feng, M., “Numerical Simulation of the pressure pulses generated by a pressure screen foil rotor”, M.A.Sc. Thesis, Dept. Mech. Eng., Univ. British Columbia, 2003.
10. Karvinen, R., and Halonen, L., “The effect of various factors on pressure pulsation of a screen”, Paperi ja Puu, 2: 80-83, 1984.
11. Wikstrom, T., and Fredriksson, B., “Hydrodynamics in a pressure screen – consequences on the separation process”, 5th Research Forum on Recycling, 197-202, 1999.
12. Atkins, M., “Axial variations and entry effects in a pressure screen”, Ph. D. Thesis, Dept. of Eng., Univ. of Waikato, 2007.
13. Pinon, V., Gooding, R.W., Olson, J.A., “Measurements of pressure pulses from a solid core screen rotor”, Tappi J., 2(10): 9-12, 2003.
14. Gonzales, J., “Characterization of design parameters for a free foil rotor in a pressure screen”, M.A.Sc. Thesis, Dept. Mech. Eng., Univ. British Columbia, 2002.

Appendix B

Details of Analysis

B.1 Introduction

This appendix provides additional details on the analysis conducted in Chapter 8.

B.2 Analysis

For steady flows, the continuity equation in integral form is

$$\oiint_S \rho \vec{u} \cdot \hat{n} dS = 0, \quad (\text{B.1})$$

Evaluating the integrals gives us simply

$$\rho A_f u_f - \rho A_S u_S - \rho A_R u_R = 0, \quad (\text{B.2})$$

where A_f is the cross sectional area of the feed inlet, u_f is the flow velocity at the feed inlet, A_S is the total open area of the screen cylinder, u_S is the average slot velocity, A_R is the cross sectional area of reject outlet, and u_R is the flow velocity at the reject outlet.

The integral form of the angular momentum equation is

$$T = \oiint_S (\vec{r} \times \vec{u})(\rho \vec{u} \cdot \hat{n}) dS + \vec{F} \quad (\text{B.3})$$

Evaluating the integrals and simplifying, equation B.3 becomes

$$Power = \Omega T = \rho \frac{V_t}{r_{tip}} Q_f [(r_{tip} + \frac{g}{2}) R_v k V_t - \frac{Q_f}{A_f} (r_{tip} + g) \sin(\beta)] + \frac{V_t}{r_{tip}} F \quad (B.4)$$

where $Power$ is the rotor power, Ω is the angular velocity of the rotor, T is the torque applied to the rotor, Q_f is the volumetric feed flow rate, r_{tip} is the radius of the tip of the rotor, g is the minimum gap between the rotor and the screen cylinder, R_v is the volumetric reject rate, k is the friction loss coefficient, V_t is the tip speed of the rotor, β is the inlet angle, and F is the torque due to friction. Following the work of Olson *et al.* and the results in Figure 8.3, which shows rotor power consumption as a function of tip speed for the rotor spinning in air, where the fluid density is very low, the friction term F is assumed to be due to turbulent drag on the rotor and friction from the bearings [1].

The friction term F is therefore of the form

$$F = C_D \frac{1}{2} \rho V_t^2 S r_{tip} + b, \quad (B.5)$$

where C_D is a rotor dependent non-dimensional drag coefficient, S is a reference area (typically the cross-sectional area of the screen), and b is a constant determined by the slope of the line in Figure 8.3. Combining equations B.4 and B.5, the final power equation becomes

$$Power = \Omega T = \frac{\rho V_{tip} Q_f}{r_{tip}} [(r_{tip} + \frac{g}{2}) R_v k V_{tip} - \frac{Q_f}{A_f} (r_{tip} + g) \sin(\beta)] + C_D \frac{1}{2} \rho V_{tip}^3 \pi r_{tip}^2 + \frac{V_{tip}}{r_{tip}} b \quad (B.6)$$

B.3 References

1. Olson, J.A., Turcotte, S., Gooding, R.W., "Determination of power requirements for solid core pulp screen rotors", *Nordic Pulp Paper Res. J.*, 19(2): 213-217, 2004.